CERN / LHCC 99–4
ALICE TDR 2
5 March 1999

A L I C E

Technical Design Report

of the

Photon Spectrometer (PHOS)

Spokesperson
J. Schukraft

PHOS Project Leader
V. Manko

Technical Coordinator
W. Klempt

Engineering/Integration Coordinator
L. Leistam

Resources Coordinator
J. de Groot

Cover design by Fabienne Marcastel

Printed at CERN
March 1999

ISBN 92-9083-138-3

ALICE Collaboration

Alessandria, Italy, Facoltà di Scienze dell'Università:
G. Dellacasa, L. Ramello, E. Scalas, M. Sitta and C. Soave.

Aligarh, India, Physics Department, Aligarh Muslim University:
N. Ahmad, S. Ahmad, T. Ahmad, W. Baritak, M. Irfan and M. Zafar.

Athens, Greece, Nuclear and Particle Physics Division, University of Athens:
A.L.S. Angelis, A. Kapogiannis, G. Mavromanolakis and A.D. Panagiotou.

Athens, Greece, Institute of Nuclear Physics, NRC Demokritos:
K. Kalfas.

Bari, Italy, Dipartimento di Fisica dell'Università and Sezione INFN:
N. Colonna, D. Cozza, D. Dell'Olio, D. Di Bari, D. Elia, R.A. Fini, B. Ghidini, V. Lenti, L. Liberti, R. Loconsole, V. Manzari, E. Nappi[1)], F. Navach, F. Posa, S. Stucchi and G. Tomasicchio.

Bari, Italy, Politecnico and Sezione INFN:
F. Corsi, D. De Venuto, M. Di Ciano, R. Dinapoli, G. Gramegna, A. Grimaldi, P. Lamanna, C. Marzocca, G. Matarrese and E. Monno.

Beijing, China, China Institute of Atomic Energy:
Shuhua Zhou.

Bergen, Norway, Department of Physics, University of Bergen:
E. Andersen, K. Fanebust, H. Helstrup, A. Klovning, O.H. Odland, D. Röhrich and T.F. Thorsteinsen.

Bhubaneswar, India, Institute of Physics:
A.K. Dubey, D.P. Mahapatra and S.C. Phatak.

Birmingham, United Kingdom, School of Physics and Space Research, University of Birmingham:
I.J. Bloodworth, D. Evans, G.T. Jones, P. Jovanović, J.B. Kinson, A. Kirk, O. Villalobos Baillie and M.F. Votruba.

Bratislava, Slovakia, Faculty of Mathematics and Physics, Comenius University:
J. Braciník, V. Černý, J. Ftáčnik, V. Hlinka, M. Ivanov, R. Janik, R. Lietava, M. Pikna, J. Pišút, N. Pišútová, B. Sitar, P. Strmeň and I. Szarka.

Budapest, Hungary, KFKI Research Institute for Particle and Nuclear Physics, Hungarian Academy of Sciences:
E. Denes, B. Eged, Z. Fodor, G. Harangozo, T. Kiss, G. Palla, G. Rubin, J. Sulyan, L. Szendrey, J. Sziklai, D.L. Tarjan, Z. Varga, B.N. Vissy and J. Zimanyi.

Cagliari, Italy, Dipartimento di Fisica dell'Università and Sezione INFN:
C. Cicalo, A. De Falco, M.P. Macciotta-Serpi, A. Masoni, S. Mauro, G. Puddu, P. Randaccio, S. Serci, E. Siddi and G. Usai.

Calcutta, India, Saha Institute of Nuclear Physics:
P. Bhattacharya, S. Bose, Sukalyan Chattopadhyay, N. Majumdar, A. Sanyal, S. Sarkar, P. Sen, S.K. Sen and B.C. Sinha.

Calcutta, India, Variable Energy Cyclotron Centre:
Subhasis Chattopadhyay, M.R. Dutta Majumdar, M.S. Ganti, T.K. Nayak, R.N. Singaraju, M.D. Trivedi and Y.P. Viyogi.

Catania, Italy, Dipartimento di Fisica dell'Università and Sezione INFN:
A. Badalà, R. Barbera, U. Becciani, C. Caligiore, M. Gulino, S. Ingrassia, A. Insolia, F. Librizzi, D. Lo Presti, D. Nicotra, A. Palmeri, S. Panebianco, G.S. Pappalardo, L. Pappalardo, C. Petta, N. Randazzo, S. Reito, F. Riggi, A.C. Russo, G.V. Russo, M. Russo, G. Saccà and A. Sciuto.

CERN, Switzerland, European Laboratory for Particle Physics:
J. Bächler, A. Bajeli[2)], J.A. Belikov[3)], V. Berejnoi[4)], J.-C. Berset, R. Brun, M. Burns, J. Buytaert, M. Campbell, E. Cantatore, W. Carena, F. Carminati, J. Christiansen, D. Collados, C. D'Ambrosio, M. Davenport, J. de Groot, A. Di Mauro, R. Divià, C. Eisenberg, C. Engster, J. Espirito Santo, M. Fageda, H.G. Fischer, M. Flammier, F. Formenti, D. Fraissard, E. Futo[5)], E. Gaumann, M. Goossens, B. Goret, T. Grassi, C. Gregory, M. Hoch, P.G. Innocenti, A. Jachołkowski, W. Klempt, A. Kluge, K. Knudson, G. Lecoeur, J.C. Legrand, L. Leistam, P. Lenoir, Y. Lesenechal, C. Lourenço, A. Malinine, P. Martinengo, M. Mast, T. Meyer, H. Milcent, R. Monnin, M. Morel, A. Morsch, M. Mota, L. Musa, B. Perrin, L. Pigni, F. Piuz, E. Quercigh, J. Raynaud, H. Renshall, A. Rivetti, K. Šafařík, J.-C. Santiard, J. Schukraft, E. Schyns, W. Snoeys, P. Sonderegger, M. Spegel, D. Swoboda, P. Szymanski, G. Tabary, J. van Beelen, H. van der Velde, P. Vande Vyvre, A. Vascotto, D. Vranic, S. Wenig, P. Wertelaers, T. Williams and K. Zelazowski.

Chandigarh, India, Physics Department, Panjab University:
M.M. Aggarwal, A.K. Bhatia, V.S. Bhatia, R. Chugh and V. Vashisht.

Clermont-Ferrand, France, Université Blaise Pascal and IN2P3:
J.P. Alard, A. Baldit, N. Bastid, G. Blanchard, M. Brossard, J. Castor, T. Chambon, P. Crochet, F. Daudon, A. Devaux, P. Dupieux, B. Espagnon, J. Fargeix, P. Force, L. Lamoine, F. Manso, S. Mayade, V. Ramillien, G. Roche, O. Roig, L. Royer, P. Saturnini and G. Savinel.

Coimbra, Portugal, Departamento de Física, Faculdade de Ciências e Tecnologia:
R. Ferreira Marques, P. Fonte[1)] and A. Policarpo.

Columbus, U.S.A., Department of Physics, Ohio State University:
T.J. Humanic, M. Lisa, G. Lo Curto, B.S. Nilsen, G. Paić, D.M. Reichhold and E. Sugarbaker.

Copenhagen, Denmark, Niels Bohr Institute:
I. Bearden, H. Bøggild, J. Gaardhøje and B. Nielsen.

Cracow, Poland, Henryk Niewodniczanski Institute of Nuclear Physics, High Energy Physics Department:
J. Bartke, E. Gładysz-Dziaduś, E. Górnicki, M. Kowalski, K. Papiernik, A. Rybicki, P. Stefański and Z. Wlodarczyk[6)].

Darmstadt, Germany, Gesellschaft für Schwerionenforschung (GSI):
A. Andronic, R. Averbeck, C. Blume, P. Braun-Munzinger, A. Deusser, A. Devismes, J. Eschke, P. Foka, C. Garabatos, B. Kolb, J. Lühning, U. Lynen, A.M. Marin, D. Miskowiec, W.F.J. Müller, C. Neyer, A. Sandoval, H. Sann, H.R. Schmidt, H. Stelzer, W. von Rüden and A. Wörner.

Frankfurt, Germany, Institut für Kernphysik, Johann-Wolfgang Göthe Universität:
C. Bormann, P. Buncic, M. Gaździcki, J. Günther, S. Lange, R. Renfordt, G. Roland, R. Stock and H. Ströbele.

Gatchina, Russia, St. Petersburg Nuclear Physics Institute:
V. Guersenchtein, B. Komkov, V. Mylnikov, V. Nikouline, V. Samsonov, S. Volkov and A. Vorobiev.

Heidelberg, Germany, Max-Planck-Institut für Kernphysik:
F. Ceretto, C. Fuchs, J. Rak and J.P. Wurm.

Heidelberg, Germany, Institut für Hochenergiephysik, Ruprecht-Karls Universität[‡)]:
F.O. Lesser, V. Lindenstruth and A.G.E. Mass.

Heidelberg, Germany, Physikalisches Institut, Ruprecht-Karls Universität:
H. Appelshäuser, S. Esumi, K. Filimonov, P. Glässel, B. Lenkeit, N. Herrmann, M.J. Richter, W. Schmitz, J. Stachel, H. Tilsner, J.P. Wessels, T. Wienold and B. Windelband.

Ioannina, Greece, University of Ioannina, Department of Physics:
X. Aslanoglou.

Jaipur, India, Physics Department, University of Rajasthan:
A. Bharti, S.K. Gupta, R. Raniwala and S. Raniwala.

Jammu, India, Physics Department, Jammu University:
S.K. Badyal, A. Bhasin, A. Gupta, V.K. Gupta, L.K. Mangotra, B.V.K.S. Potukuchi, N.K. Rao and S.S. Sambyal.

JINR, Russia, Joint Institute for Nuclear Research:
P.G. Akichine, V.A. Arefiev, V.I. Astakhov, A.A. Baldine, A.M. Baldine, V.D. Bartenev, B.V. Batiounia, I.V. Boguslavsky, M. Bondila, Z.V. Borissovskaia, A.V. Chabounov, G.S. Chabratova, I.A. Chichov, V.I. Datskov, V.K. Dodokhov, L.G. Efimov, A.G. Fedounov, O.A. Golubitsky, B.N. Guouskov, O.I. Iouldachev, V.G. Kadychevsky, I.E. Karpunina, A.D. Kovalenko, V.L. Lioubochits, V.I. Lobanov, G.I. Lykasov, E.A. Matiouchevski, K.V. Mikhailov, D.P. Mikhalev, I. Minaev, P.V. Nomokonov, A.N. Parfenov, I.V. Pouzynin, V.N. Pozdnyakov, A.B. Sadovski, S.V. Semashko, A.E. Senner, I.A. Shelaev, A.V. Sidorov, N.V. Slavine, R.V. Slepnev, G.P. Tsvineva, A.S. Vodopianov, M.B. Yuldasheva, S. Zaporozhets and A.I. Zintchenko.

V. Diomkin[7)], V. Kuznetsov[7)], V. Shestakov[7)], A. Vasiliev[7)] and A. Zhakovksy[7)].

Ts. Baatar[8)], B. Khurelbaatar[8)] and R. Togoo[8)].

K.G. Akhobadze[9)], A.K. Djavrishvili[9)], T. Grigalashvili[9)], E.S. Ioramashvili[9)], A.V. Kharadze[9)], L. Khizanishvili[9)], T.V. Khuskivadze[9)], L.V. Shalamberidze[9)] and N. Shubitidze[9)].

V. Djordjadze[10)], N. Grigalashvili[10)], Z. Menteshashvili[10)], M. Nioradze[10)], M. Tabidze[10)] and Y. Tevzadze[10)].

Jyvaskyla, Finland, Department of Physics, University of Jyvaskyla and University of Helsinki:
J. Aysto, V. Ruuskanen and W. Trzaska.

Kharkov, Ukraine, National Scientific Centre 'Kharkov Institute of Physics and Technology':
G.L. Bochek, V.F. Boldyshev, I.F. Chervonny, A.N. Dovbnya, V.I. Kulibaba, N.I. Maslov, S.M. Potin, I.M. Prokhorets and A.F. Starodubtsev.

Kharkov, Ukraine, Scientific and Technological Research Institute of Instrument Engineering:
V.N. Borshchov, S.K. Kiprich, O.M. Listratenko, G. Protsay, V.E. Starkov and M. Zamirets.

Kiev, Ukraine, Department of High Energy Density Physics, Bogolyubov Institute for Theoretical Physics, National Academy of Sciences of Ukraine:
T. Hryn'ova, D.E. Kharzeev, V. Palshin, O. Pavlenko, A. Velytsky and G. Zinovjev.

Košice, Slovakia, Institute of Experimental Physics, Slovak Academy of Sciences and Faculty of Science P.J. Šafárik University:
J. Fedoršin, M. Hnatič, A. Jusko, B. Kocper, I. Králik, A. Kravčáková, F. Kriváň, I. Kuľková, M. Lupták, G. Martinská, B. Pastirčák, L. Šándor, J. Urbán, S. Vokál and J. Vrláková.

Legnaro, Italy, Laboratori Nazionali di Legnaro:
R.A. Ricci.

Lisbon, Portugal, Departamento de Física, Instituto Superior Técnico:
J. Barbosa, P. Branco, R. Carvalho, J. Seixas and R. Vilela Mendes.

Lund, Sweden, Division of Cosmic and Subatomic Physics, University of Lund:
L. Carlen, S.I.A. Garpman, H.-A. Gustafsson, P. Nilsson, A. Oskarsson, L. Osterman, I. Otterlund, D. Silvermyr and E.A. Stenlund.

Lyon, France, Institut de Physique Nucléaire de Lyon (IPNL), IN2P3-CNRS et Université Claude Bernard Lyon-I:
M.Y. Chartoire, M. Chevallier, B. Cheynis, D. Essertaize, E. Galichet, E. Gangler, M. Goyot, J.Y. Grossiord, R. Guernane, A. Guichard, D. Guinet, G. Jacquet, P. Lautesse, M. Miguet and S. Tissot.

Marburg, Germany, Fachbereich Physik, Philipps Universität:
F. Eckhardt, V. Friese and F. Pühlhofer.

Mexico City, Mexico, Centro de Investigación y de Estudios Avanzados:
R. Hernández Montoya, G. Herrera Corral, L. Magana, H. Mendez and L.M. Montaño.

Minsk, Belarus, Institute for Nuclear Problems, State University:
A.A. Lobko.

Moscow, Russia, Institute for Nuclear Research, Academy of Science:
K.A. Chileev, S.N. Filippov, Ju.K. Gavrilov, M.B. Goloubeva, M.N. Gotra, F.F. Gouber, T.L. Karavitcheva, A.B. Kourepin, V.D. Laptev, A.I. Maevskaya, V.I. Razine, A.I. Rechetine, N.M. Sobolevsky and N.S. Topilskaia.

Moscow, Russia, Institute for Theoretical and Experimental Physics:
A.N. Akindinov, S.V. Boiarinov, V. Golovine, I.G. Grichouk, A.B. Kaidalov, M.M. Kats, I.T. Kiselev, S.M. Kisselev, E. Lioublev, M. Martemianov, A.N. Martemiyanov, P.A. Polozov, S.A. Pozdniakov, V.S. Serov, A.V. Smirnitski, M.M. Tchoumakov, I.A. Vetlitski, K.G. Volochine, L.S. Vorobiev and B.V. Zagreev.

Moscow, Russia, Russian Research Center 'Kurchatov Institute':
V. Antonenko, S. Beliaev, R. Cherbatchev, I. Doubovik, S. Fokine, M. Ippolitov, K. Karadjev, A.L. Lebedev, V. Lebedev, V.I. Manko, G. Mguebrichvili, T. Moukhanova, A. Nianine, S. Nikolaev, S. Nikouline, O. Patarakine, D. Peressounko, I. Sibiriak, A. Vasiliev, A. Vinogradov and M. Volkov.

Moscow, Russia, Moscow Engineering Physics Institute:
V. Grigoriev, V. Kapline, V. Loguinov and M. Strikhanov.

Münster, Germany, Institut für Kernphysik, Westfälische Wilhelms Universität:
D. Bucher, T. Peitzmann, K. Reygers, R. Santo, H. Schlagheck and M. Wahn.

Nantes, France, Laboratoire de Physique Subatomique et des Technologies Associées:
L. Aphecetche, T. Bernier, A. Boucham, S. Bouvier, L. Conin, J.P. Cussonneau, H. Delagrange, D. D'Enterria, B. Erazmus, S. Giliberto, B. Guillet, H.H. Gutbrod, M.S. Labalme, P. Lautridou, F. Lefèvre, M. Le Guay, L. Luquin, L. Martin, G. Martinez, V. Métivier, M.J. Mora, P. Pichot, A. Rahmani, O. Ravel, T. Reposeur, F. Retiere, P. Rivoalan, C.S. Roy, D. Roy, Y. Schutz and A. Tournaire.

NIKHEF, The Netherlands, National Institute for Nuclear and High Energy Physics:
M. Botje[11)], A. Buijs[12)], J.J.F. Buskop[11)], A.P. De Haas[12)], P.K.A. De Witt Huberts[11,12)], R. Kamermans[11,12)], P.G. Kuijer[11,12)], G. Nooren[11)], C.J. Oskamp[12)], A. Van Den Brink[12)], N. Van Eijndhoven[12)] and J. Visschers[11)].

Novosibirsk, Russia, Budker Institute for Nuclear Physics:
A.R. Frolov, I.N. Pestov and M.A. Tiounov.

Oak Ridge, U.S.A., Instrumentation and Controls Division, Oak Ridge National Laboratory:
C.L. Britton, W.L. Bryan, J.W. Walker and A.L. Wintenberg.

Orsay, France, Institut de Physique Nucléaire, Université de Paris-Sud:
L. Bimbot, P.F. Courtat, R. Douet, B. Genolini, H. Harroch, D. Jouan, L. Kharmandarian, Y. Le Bornec, M. Mac Cormick, J. Peyré, J. Pouthas, R. Sellem and N. Willis.

Oslo, Norway, Department of Physics, University of Oslo:
A.K. Holme, L.M. Ingebrigtsen, G. Løvhøiden, B. Skaali, T.S. Tveter and D. Wormald.

Padua, Italy, Dipartimento di Fisica dell'Università and Sezione INFN:
F. Antinori, F. Brandolini, N. Carrer, M. Morando, A. Pepato, F. Scarlassara, G. Segato, F. Soramel and E. Zanoni.

Prague, Czech Republic, Institute of Physics, Academy of Science:
J. Mareš, E. Mihoková, M. Nikl, K. Píška, K. Polák and P. Závada.

Protvino, Russia, Institute for High Energy Physics:
A.M. Blik, M. Bogolyubsky, G. Britvitch, S. Erine, G.V. Khaoustov, I.V. Kharlov, V.N. Kolossov, V. Lichine, S.A. Sadovski, V.D. Samoilenko, P.A. Semenov, V.I. Suzdalev, V. Tikhonov and A. Zviagine.

Řež u Prahy, Czech Republic, Academy of Sciences of Czech Republic, Nuclear Physics Institute:
V. Hanzal, J. Hošek, I. Hřivnáčová, V. Kuschpil, A. Kugler, V. Petráček, M. Šumbera, A. Tlustý, V. Wagner and D. Zákoucký.

Rome, Italy, Dipartimento di Fisica dell'Università 'La Sapienza' and Sezione INFN:
S. Di Liberto, M.A. Mazzoni, F. Meddi, D. Prosperi and G. Rosa.

Saclay, France, Centre d'Etudes Nucléaires, DAPNIA/SPhN:
A. Baldisseri, H. Borel, I. Chevrot, J. Gosset, F.M. Staley and Y. Terrien.

Salerno, Italy, Dipartimento di Fisica Teorica e S.M.S.A., Università di Salerno and Sezione INFN:
G. Grella, M. Guida, G. Romano and T. Virgili.

Sarov, Russia, Russian Federal Nuclear Center (VNIIEF):
S. Abramovitch, V. Basmanov, V. Ianowski, R. Ilkaev, L. Ilkaeva, A. Ivanov, A. Khlebnikov,
E. Kolokolnikov, V. Matiev, S. Nazarenko, V. Pounine, S. Poutevskoi, I. Selin, M. Tarasov,
I. Vinogradov, S. Zhelezov and A. Zhitnik.

St. Petersburg, Russia, Institute for Physics of St. Petersburg State University, Mendeleev Institute for Metrology and Meson Scientific Association:
L.Y. Abramova, V.S. Alexandrov, V.M. Baratov, A.A. Bolonine, M.A. Braun, V.M. Dobulevitch,
G.A. Feofilov, O.N. Godissov, S. Guerassimov, S.N. Igolkine, M.I. Ioudkine, A.A. Kolojvari,
V. Kondratiev, I.A. Novikov, S.V. Potapov, O.I. Stolyarov, T.A. Toulina, F.A. Tsimbal, F.F. Valiev,
V.V. Vetchernine, L.I. Vinogradov and L.F. Vitouchkine.

Strasbourg, France, Institut de Recherches Subatomiques:
L. Arnold, M. Ayachi, J. Baudot, J.D. Berst, J.P. Blondé, D. Bonnet, J.P. Coffin, W. Dulinski,
M. Germain, G. Guillaume, L. Hebrard, Y. Hu, F. Jundt, C. Kuhn, J. Lutz, A. Michalon, F. Rami,
C. Suire and A. Tarchini.

Trieste, Italy, Dipartimento di Fisica dell'Università and Sezione INFN:
V. Bonvicini, A. Gregorio, A. Rachevski, A. Vacchi, L. Valentincic and N. Zampa.

Turin, Italy, Dipartimenti di Fisica dell'Università and INFN:
B. Alessandro, R. Arnaldi, S. Beolé, G. Bonazzola, E. Botta, L. Busso, P.G. Cerello, E. Chiavassa,
P. Cortese, F. Daudo, N. De Marco, A. Feliciello, M. Gallio, G. Giraudo, P. Giubellino,
A. Marzari-Chiesa, M. Masera, G. Mazza, P. Mereu, B. Minetti, O. Morra, A. Musso, D. Nouais,
A. Piccotti, G. Piragino, L. Riccati, E. Scomparin, F. Tosello, E. Vercellin and A. Werbrook.

Warsaw, Poland, Soltan Institute for Nuclear Studies:
D. Czerwinski, A. Deloff, K. Karpio, S. Kozak, L. Lukaszek, H. Malinowski, T. Siemiarczuk,
G. Stefanek, L. Tykarski and G. Wilk.

Warsaw, Poland, University of Technology, Institute of Physics:
J. Buryk, J. Grabski, P. Kindziuk, A. Kisiel, P. Leszczynski, A.M. Maliszewski, J.M. Mazur,
T.J. Pawlak, W.S. Peryt, J. Pluta, M. Przewlocki, S. Radomski, A.M. Roszczewski, M. Sarzynski,
P. Skowronski, P. Stepien and P. Szarwas.

Wuhan, China, Institute of Particle Physics, Huazhong Normal University:
X. Cai, Y. Hu, F. Liu, L. Liu, H. Wang and D. Zhou.

Yerevan, Armenia, Yerevan Physics Institute:
R. Asatryan, M. Atayan, R. Avakian, V. Danielyan, V. Gavalian, A. Grigorian, S. Grigoryan,
H. Gulkanyan, R. Hakobyan, V. Kakoyan, S. Mehrabyan, L. Parlakyan, R. Shahoyan and H. Vardanyan.

Zagreb, Croatia, Ruder Bošković Institute:
D. Ferenc, A. Ljubičić and T. Tustonic.

[1)] Also at CERN, Geneva, Switzerland
[2)] On leave from Seasoft, Catania, Italy.
[3)] On leave from JINR, Dubna, Russia.
[4)] On leave from IHEP, Protvino, Russia.
[5)] On leave from Budapest University, Hungary.
[6)] Institute of Physics, Pedagogical University, Kielce, Poland.
[7)] Research Centre for Applied Nuclear Physics (RCANP), Dubna, Russia.
[8)] Institute of Physics and Technology, Mongolian Academy of Sciences, Ulaanbaatar, Mongolia.
[9)] Institute of Physics, Georgian Academy of Sciences, Tbilisi, Georgia.
[10)] High Energy Physics Institute, Tbilisi State University, Tbilisi, Georgia.
[11)] Foundation of Fundamental Research of Matter in The Netherlands.
[12)] Utrecht University, Utrecht, The Netherlands.
[‡)] Applying to join ALICE.

Acknowledgements

It is a pleasure to acknowledge the contribution given to the preparation of this TDR by: S. Burachas, Yu. Drakine, T-E. Hansen (AME AS), S.M. Ignatov, M. Koutcheriaeva, R. Livermore (AME AS), V. Lizourenko, S. Maridor, E. Nygård (IDE AS), M. Purschke, V.D. Ryzhikov, E. Shapovalova, G. Tamulaitis, M. Terekhin and Al. Vasiliev.
The collaboration wishes to thank all the technical and administrative staff (in particular S. Barras and S. Stappers) involved during the preparation of this TDR. We also thank R. Cook, M. Guarisco, M. Jouhet, J. Navarria, S. Leech O'Neale and G. Prost, from the Desktop Publishing Service, for their professional help with the editing.

Contents

1 Introduction

1.1 The ALICE experiment

ALICE (A Large Ion Collider Experiment) [1] is an experiment at the Large Hadron Collider (LHC) optimized for the study of heavy-ion collisions, at a centre-of-mass energy $\sim$ 5.5 TeV. The prime aim of the experiment is to study in detail the behaviour of matter at high densities and temperatures, in view of probing deconfinement and chiral-symmetry restoration.

The detector consists essentially of two main components: the central part, composed of detectors mainly devoted to the study of hadronic signals and dielectrons in the pseudorapidity range $-1 < \eta < 1$, and the forward muon spectrometer, devoted to the study of quarkonia behaviour in dense matter. The layout of the ALICE set-up is shown in colour Fig. I.

The major technical challenge to the experiment is imposed by the large number of particles created in the collisions of lead ions. There is a considerable spread in the currently available predictions for the multiplicity of charged particles produced in a central Pb–Pb collision. The design of the experiment has been based on the highest value, 8000 charged particles per unit of rapidity, at mid-rapidity. This multiplicity dictates the granularity of the detectors and their optimal distance from the colliding beams.

The central part of the ALICE detector also includes an electromagnetic calorimeter, PHOS, devoted to the study of photon signals.

1.2 The electromagnetic calorimeter PHOS

PHOS (PHOton Spectrometer) is an electromagnetic calorimeter of high granularity consisting of 17 280 detecting channels of lead-tungstate crystals, $PbWO_4$ (PWO), of $2.2 \times 2.2 \times 18$ cm^3 dimensions, coupled to large-area PIN-diodes with low-noise preamplifiers.

It will be positioned on the bottom of the ALICE set-up, and will cover approximately a quarter of a unit in pseudorapidity, $-0.12 \leq \eta \leq 0.12$, and 100° in azimuthal angle. Its total area will be ~ 8 m^2, and the total crystal volume will be ~ 1.5 m^3.

The PHOS electromagnetic calorimeter is optimized for measuring photons (of $\sim$0.5–10 GeV/c), π^0's (of $\sim$1–10 GeV/c) and η mesons (of $\sim$2–10 GeV/c). Measurement of higher momenta particles will also be feasible, although not with optimal energy resolution.

The PHOS calorimeter uses the other ALICE detectors for event characterization (e.g. centrality) and in studies of multi-particle correlations (e.g. collective flow effects, where the reaction plane has to be determined using data obtained with the tracking detector). Otherwise, data obtained with the PHOS detector can be analysed independently.

1.3 Physics goals

1.3.1 Introduction

The photon spectrometer PHOS provides unique coverage of the following physics topics:

- thermal and dynamical parameters of the initial phase of the collision, in particular the initial temperature, via direct single photons and di-photons;
- jet quenching as a probe of deconfinement, studied via high p_T π^0;

- signals of chiral-symmetry restoration.

In addition, the neutral-pion transverse-momentum spectra and Hanbury-Brown and Twiss correlations will provide important constraints on the dynamical evolution of the hadronic phase, up to the freeze-out stage.

1.3.2 Direct single photons

Directly radiated thermal photons, as dileptons, have long been considered as an interesting penetrating probe to study the early phase of the hot and dense matter produced in ultra-relativistic nucleus–nucleus collisions. Single direct photons are expected at high transverse momentum, p_{T}, from well-known hard QCD processes, but they should also be produced in the p_{T} region below several GeV/c due to *thermal radiation* of the hot and dense matter [2]. Since the mean free path of the produced photons is considerably larger than the size of the finite nuclear system, photons produced throughout all stages of the collision will be observable in the final state. Thus, it is believed that the emitted photons should provide information about the initial conditions of the hot dense system and thereby provide evidence for the possible formation of a Quark-Gluon Plasma (QGP).

The *thermal photons* radiated from the QGP and later stages should be observable in the medium-p_{T} range (around 1–5 GeV/c), where they are expected to dominate over the prompt QCD photons [3]. At very high momenta, direct photons originate mainly from *initial hard processes* and can be used to extract parton distribution functions in nuclei (in particular from p–A reactions).

Because of the large background arising from hadronic decays (mainly π^0 and η), a precise measurement of the rates and p_{T} spectra of these mesons is vital in order to extract the direct photon component. The predicted signal of thermal photons is of the order of a few per cent of the total inclusive photon yield, very likely increasing with increasing p_{T}. The largest uncertainty originates from the unknown meson p_{T} spectra. It will, in general, be more favourable at high initial energy density and, indeed, might be much more clearly observable at the large densities predicted for the LHC. Other estimates [4] predicted a direct photon signal relative to background photons of more than 10 % for $p_{\mathrm{T}} > 3$–4 GeV/c.

The search for direct photon production in ultra-relativistic nucleus–nucleus collisions has been a major emphasis of the WA80 and WA98 experiments at the CERN SPS. For central S–Au collisions at 200·A GeV, as studied in the WA80 experiment, the measured photon excess at each p_{T}, averaged over the range $0.5\,\mathrm{GeV}/c \leq p_{\mathrm{T}} \leq 2.5\,\mathrm{GeV}/c$, corresponds to 5.0 % of the total inclusive photon yield, with a statistical error of $\sigma_{\mathrm{stat}} = 0.8\,\%$ and a systematic error of $\sigma_{\mathrm{syst}} = 5.8\,\%$ [5]. The preliminary results from the WA98 data analysis on photon production in Pb–Pb collisions at 158·A GeV show, for transverse momenta above 1 GeV/c, excess photon yields of $\sim 20\,\%$ beyond those attributable to resonance decays, which were observed consistently, with different photon identification criteria, both for peripheral and central events [6].

The search for direct photons will be based on the positive experience of the CERN WA80/WA98 Collaborations. The direct-photon excess will be determined on a statistical basis for selected classes of events. The inclusive photon yields will be measured at different transverse momenta and for several centrality event classes. They are to be compared with the photon yields for the same event classes expected from radiative decays of long-lived resonances, including π^0, η, ω, η', which will be calculated via simulation. The direct-photon excess will then be determined from the difference between the measured and simulated distributions.

The input for the simulation will be based on the yields of the π^0 and η mesons, measured with the same apparatus (PHOS), the main source of the background, contributing $\sim 97\,\%$ of their total amount. This method has the advantage that it is free of cross-section normalization errors, since photon pairs and single photons are simultaneously observed in the same experiment, although some extrapolation in rapidity is required. Additional minor contributions from other radiative decays (e.g. ω and η') will be obtained from an event generator or other data.

As a figure of merit, the production of single photons is generally expressed in terms of γ/π^0, since photons from π^0 decay form the dominant source of background photons, and therefore the π^0 yield sets the scale for the sensitivity of the direct-photon search. Many factors, influencing systematic errors, will cancel in the γ/π^0 ratio.

The neutral mesons will be reconstructed via their $\gamma\gamma$ decay branch. In Pb–Pb collisions at the LHC energy, the number of particles produced in each collision is very high, and so is the combinatorial background in the two-photon invariant mass spectrum due to many possible photon pairs. Therefore, the meson yields can be determined only inclusively. The true π^0 and η yields will be extracted from the respective mass peaks, which sit on the combinatorial background. The combinatorial background will be evaluated by a technique known as event mixing (for more details see Chapter 4). This technique was succesfully applied in the analysis of the CERN-SPS photon data, obtained by the WA80/WA98 experiment (see e.g. Refs. [7–9]). It was shown that the event-mixing technique works with values of the signal-to-background ratio as low as a few tenths of a per cent, for statistics of a few million events, with a small systematic error in the determination of the combinatorial background.

1.3.3 Direct di-photons

Recently, thermal di-photons have been reconsidered as a probe for the early stages in ultra-relativistic heavy-ion collisions [10,11]. They are produced in the plasma phase by quark–antiquark annihilation and thus bear a similarity to thermal di-leptons. However, while thermal di-leptons are stronger in the region of the ρ mass, thermal di-photons seem to be favoured at high masses. Up to at least $M_{\gamma\gamma} = 5\,\mathrm{GeV}/c^2$ thermal production of di-photons is expected to dominate over prompt production, at the LHC [11].

The measurement of di-photons (as di-leptons) has the advantage that the mass spectrum is only influenced by the temperature of the emitting medium during the collision history, with an emphasis on the early stages, while the momentum spectra of single photons carry influences from both temperature and collective flow. Di-photons would therefore yield complementary information on the initial stages. As di-photons and di-leptons have different sensitivities to various phases of the collision, a simultaneous measurement of both should yield additional insight into the early dynamics of the collision.

The di-photons have to be extracted from an enormous combinatorial background. While this background can be estimated by event-mixing procedures, the signal will very likely only be visible for large transverse momenta. A simple study in Ref. [11] indicates that the di-photon signal might be measurable at LHC with a p_T cut of $3\,\mathrm{GeV}/c$ on the individual photons.

1.3.4 π^0 transverse-momentum spectra

Neutral-pion transverse-momentum spectra will be measured in a broad range, in particular in the high p_T region, where the resolution of the photon spectrometer is superior to the momentum resolution of the tracking system for charged particles. These broad-range spectra, which will be measured with a high statistical precision ($\sim 1\,\%$ for π^0's and $\sim 10\,\%$ for η's), should provide important information both on final- and initial-state contributions to particle production. It has been shown at SPS energies that the π^0 momentum spectrum measured in a p_T range of $\sim$ 0.4–4 GeV/c offers additional constraints on hydrodynamical scenarios related to the shape of the freeze-out hypersurface [12]. Of course, these spectra are indispensable for a precise measurement of direct photons, since they allow to predict the contribution of background decay photons in the total photon momentum spectrum.

Large E_T partons or jets are considered good probes of the dense matter formed in ultra-relativistic heavy-ion collisions [13]. The specific transverse-energy loss of partons should be significantly stronger if dense partonic matter is produced [14], which would lead to the suppression of high-p_T particle production (*jet quenching*).

The parton energy loss can be studied by comparing inclusive high-p_T pion production to perturbative QCD calculations. Such a comparison to neutral-pion spectra in 158·A GeV Pb–Pb collisions [9] has

recently been performed [15]. No evidence for parton energy loss has been found in these reactions. As a possible deconfined volume would be larger at collider energies, it is of high interest to study high-p_{T} hadron production in the ALICE experiment. As this signal is directly sensitive to deconfinement, the measurement nicely complements that of charmonium production. The identification of neutral pions in the PHOS detector is limited in momentum through the minimum opening angle of the decay photons. The granularity of PHOS should allow a good identification up to $p_{\mathrm{T}} = 30$ GeV/c with very good efficiency ($\sim 90\%$).

1.3.5 Chiral-symmetry related signals

1.3.5.1 Disoriented chiral condensates

Disoriented chiral condensates (DCCs) may be formed in high-energy heavy-ion collisions [16]. If the system undergoes a non-equilibrium transition to the chirally asymmetric phase, domains with a net isospin may survive. These would be forced to radiate off a large number of soft pions carrying this isospin. As a consequence, DCC formation will reflect itself in unusually large fluctuations of the number of neutral pions relative to the total number of pions. It is up to now still uncertain how large such domains will be, and how frequently they might occur.

The PHOS detector, in combination with the charged-particle detectors of ALICE, allows DCCs to be searched for by investigating the event-by-event fluctuations of the ratio of photons to charged particles, similarly to the search performed in Ref. [17]. The limited acceptance will only allow these fluctuations to be studied in relatively small regions of phase space. However, this will not limit the capabilities fundamentally, since DCCs are much more likely to only appear in a limited phase-space region. It will mainly affect the statistical significance of the measurement. To allow the study of soft particles, which should dominantly carry the effect, an efficient charged-particle veto for the photon detector is mandatory. Detailed Monte Carlo simulations will be performed to understand the achievable sensitivity of the ALICE detector to such fluctuations.

1.3.5.2 U(1)-restoration

There has been considerable discussion [18, 19] on whether in heavy-ion collisions not only the SU(2) chiral symmetry but also the U(1)$_A$ symmetry would be restored. Because the U(1)$_A$ anomaly is responsible for the large η' mass, a possible restoration would influence this mass and implicitly, because of the coupling between η and η', also the mass of the η meson. Such a reduced mass would not show up as a measurable quantity, because of the long lifetime of these mesons, but would strongly increase the production rate. A precise measurement of η and possibly η' production is therefore another important goal of the PHOS detector. As the measurement of these heavier mesons depends very sensitively on the geometrical acceptance, this would require the largest possible PHOS coverage.

Recently, more exotic signatures of U(1)$_A$ restoration, like the possibility of 'parity odd bubbles', have been proposed [20]. Such phenomena would allow processes that are normally forbidden, like the decay $\eta \rightarrow \pi^0\pi^0$. The PHOS detector should allow such exotic processes to be searched for.

1.3.6 Hanbury-Brown and Twiss correlations in π^0–π^0 and γ–γ systems

The study of particle interferometry — of identical particle correlation (or HBT correlation) — is of great interest in heavy-ion collisions because in expanding systems the momentum correlations contain information about its dynamical evolution (see e.g. the collection of original articles [21] and some recent reviews [22–24]). We therefore envisage to enlarge the study of HBT in ALICE to neutral pions, and if possible to direct photons.

The $\pi^0 - \pi^0$ correlations are not distorted by the Coulomb interaction, an advantage compared to the charged pion ones. The neutral pion correlation function $C_2(Q)$ is however strongly influenced at

small Q by resonance decays such as $\eta \to 3\pi^0$, $\eta' \to 2\pi^0\eta$, and other final state interactions. An added complication is the fact that it is not possible to reconstruct the individual π^0's in heavy ion collisions due to the large combinatorial background. It turns out that this is not an insurmountable difficulty because the $\pi^0 - \pi^0$ correlations survive in the π^0 decay gammas. It was shown [25] that it is possible to reconstruct the π^0 source size, and its 'coherence' factor, from the correlation function of decay gammas (for more information see Chapter 4). As for the direct gammas, they could yield information on the early stages of the system created in the collision, since they are not subject to the multiple interactions which affect the pions. However, the presence of decay gammas would obscure the correlation function unless the direct gammas in some p_T region would represent a sizable part of the spectrum (of the order of 35 % or more).

1.4 General design considerations

1.4.1 Introduction

The PHOS electromagnetic calorimeter is optimized to measure photons in a p_T range of $\sim$ 0.5–10 GeV/c, π^0's in a p_T range of $\sim$ 1–10 GeV/c, and η's in a p_T range of $\sim$ 2–10 GeV/c, providing the best possible energy and position resolution in order to narrow the π^0 and η mass peaks and thus increase the peak-to-background ratios.

In addition to photons, the PHOS register also charged and neutral hadrons: pions, kaons, protons, neutrons, antineutrons. The hadron rejection will be achieved by a cut on the shower width and lateral shape. For additional rejection of the charged hadrons a charged-particle veto detector (CPV) is placed in front of the PHOS detector.

1.4.2 Lead-tunsgstate crystals

It is expected that in central Pb–Pb collisions an extremely high number of particles will be produced. The highest estimate for the number of charged particles produced per unit of rapidity, at midrapidity, is 8000, leading to a total rapidity density of $\sim$ 16 000 (counting the π^0 decay gammas rather than the π^0's).

The expected high multiplicity environment for central Pb–Pb collisions requires small cell cross-section and, hence, implies the use of a very dense active medium with the smallest possible Molière radius, a high segmentation of the calorimeter, and the largest possible distance to the vertex.

Therefore, lead-tungstate ($PbWO_4$) crystals have been chosen as the material for the PHOS detector. This crystal has also been chosen by the CMS Collaboration for their electromagnetic calorimeter [26], though the requirements of the two experiments are rather different.

1.4.2.1 Properties of the lead-tungstate crystal

The use of the lead-tungstate (PWO) crystal for electromagnetic calorimetry has been extensively studied in recent years and very significant progress has been made towards its use in large calorimeters [27]. Some of its physical and chemical properties are given in Table 1.1.

Lead tungstate (PWO) is a fast scintillating crystal with a rather complex emission spectrum, consisting of two emission components: a blue component peaking at 420 nm (2.9 eV) and a green component peaking at 480–520 nm (2.5 eV). The light yield of this crystal at room temperature is low if compared with other heavy scintillating crystals (e.g. BGO). However, it depends strongly on temperature, as shown in Fig. 1.1.

1.4.2.2 Working temperature of the PHOS calorimeter

The temperature coefficient is ~ -2 % per °C in a broad temperature range. At a temperature of -25 °C, the light yield will be increased by about a factor of 3 compared to room temperature (20 °C) and fur-

Table 1.1: $PbWO_4$ properties.

Density	8.28 g/cm^3
Radiation length	0.89 cm
Interaction length	19.5 cm
Molière radius	2.0 cm
Melting point	1123 °C
Hardness	4 Moh
Refractive index along	
ζ axis ($\lambda = 632$ nm)	2.16
Hygroscopicity	none
Chemical activity	inert

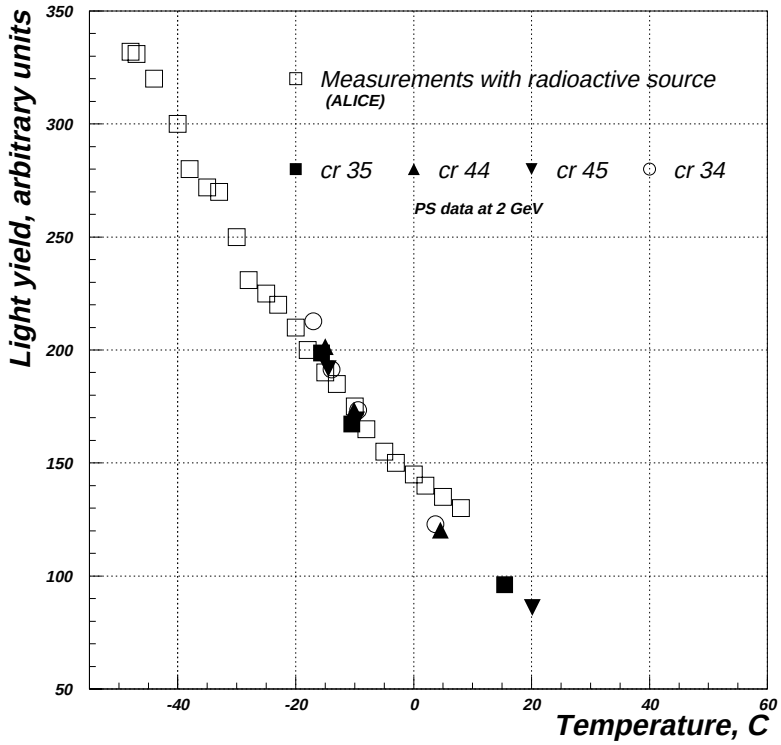

Figure 1.1: Light yield of $PbWO_4$ crystals vs. temperature.

thermore the electronic noise of the photon detector will be reduced. Both effects will lead to improved energy resolution.

We have chosen $-25\,^\circ$C as the working temperature for the PHOS, which can be obtained easily and economically. This temperature should be stabilized to ~ 0.3–$0.4\,^\circ$C in order to keep constant the light yield and the detector gain factors, with a precision of $\sim 1\,\%$. In order to ensure the identical performance of different areas of the PHOS spectrometer, a homogeneity of the temperature field of $\sim 1\,^\circ$C will be sufficient. The temperature instability in time, of the light yield, will be corrected for in the off-line data analysis, using the data of the temperature field measurement in the crystal array. The inhomogeneity of the temperature field will be taken into account in the detector gain factors by calibrating each detector at the working temperature of the stabilized regime.

1.4.2.3 Crystal transverse size

In order to have adequate position resolution and to allow separation of overlapping showers, the transverse cell size should be of the order of the Molière radius R_M [28].

The PWO crystal, with a Molière radius of 2.0 cm, for the PHOS calorimeter placed at $R = 4.6$ m, allows the transverse cell size to be made small enough to achieve a reasonable occupancy in central Pb–Pb collisions at the highest expected particle multiplicity ($dN/dy = 16\,000$).

Thus, we have chosen the cells of 2.2×2.2 cm^2.

1.4.2.4 Crystal length

The factors taken into account when choosing the crystal length were the energy resolution, and the cost and production capability.

The PHOS calorimeter is to be optimized for measuring photons of relatively low energies (in the range $\sim$0.5–10 GeV) with a good energy resolution. At such energies $\sim$15 radiation lengths ($\sim$14 cm) would be sufficient for good energy resolution. However, PIN diodes, which have been chosen as photodetectors, respond to charged particles traversing them, and the energy resolution can be spoiled by the shower punch-through effect.

It is obvious that the punch-through effect increases, whereas the cost decreases, with decreasing crystal length.

We have chosen 18 cm as a basic option for the crystal length. This value seems to be a reasonable compromise between the properties of the detector and the cost and production capability. It should be noted that with this length the measurement of photons and neutral mesons of higher momenta (e.g. for photon-tagged jet physics) will still be feasible, although the energy resolution will not be optimal.

In the test beam (see Section 2.4) we exposed an 18 cm length single crystal to 1, 2, 3 and 10 GeV electron beams. The amplitude spectrum obtained at 10 GeV is shown in Fig. 1.2. For this crystal length no significant tail is seen at 10 GeV.

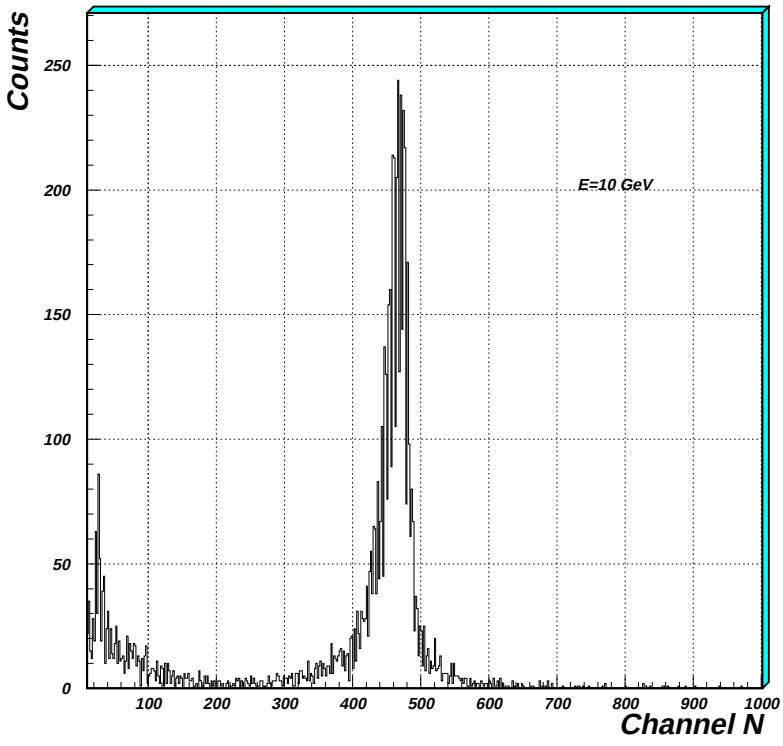

Figure 1.2: The spectrum of an 18 cm length single crystal at 10 GeV.

1.4.2.5 Radiation environment

The radiation load on the PHOS in the relatively low-luminosity ALICE experiment is of the order of 1 Gy/year, which is by many orders of magnitude lower than in the high-luminosity proton experiments, e.g. CMS. Thus the requirement on the PWO crystal tolerance to radiation is rather soft.

1.4.2.6 Requirement on the decay time

At the luminosity of the ALICE experiment the interaction rate is ~ 8 kHz. Thus, we have chosen a shaping time of 1.5 μs, which imposes a rather soft requirement on the PWO-crystal decay time.

1.4.3 Acceptance

The π^0 and η yields and spectra will be measured via their two-photon decays. The measurements of the neutral mesons with the PHOS calorimeter are limited in p_T from both low and high sides.

The high-p_T-side limits are determined by the granularity, which has to be chosen in accordance with the Molière radius of the PWO crystal. The granularity of PHOS should allow π^0's up to $p_T = 30$ GeV/c to be measured with a very good efficiency (~ 90 %) and with a lower efficiency for even higher p_T. As for η's, the p_T limits determined by the granularity are much higher.

The low-p_T limits are determined by the accessible opening angles, or for a given distance from the intersection point to the detector, R ($R = 4.6$ m for the PHOS), by the accessible distances between the two decay photons, i.e. by the detector area and configuration. A rough estimate of the required detector dimensions can be made from Fig. 1.3, where the efficiencies for detecting the π^0 (top) or η (bottom) mesons are plotted against the maximal accessible distance, assuming full coverage in azimuth.

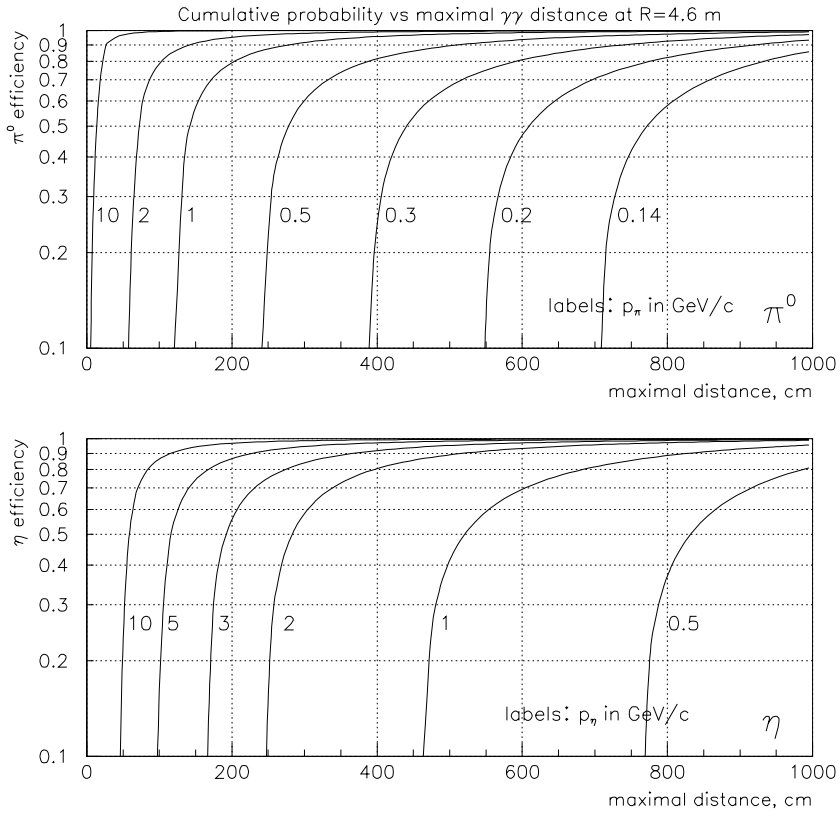

Figure 1.3: The efficiencies for detecting the π^0 (top) or η (bottom) mesons vs. the maximal accessible distance between the two decay photons (full coverage in azimuth is assumed).

As shown in Fig. 1.3, detecting π^0's of ~ 1 GeV/c momentum requires a detector ensuring an accessible distance of ~ 3 m between two hits, whereas detecting η's of ~ 2 GeV/c requires an accessible distance of ~ 6 m.

Thus, given the full PHOS area of ~ 8 m^2, a simple geometry with four identical rectangular modules has been chosen, and is shown in Fig. 1.4.

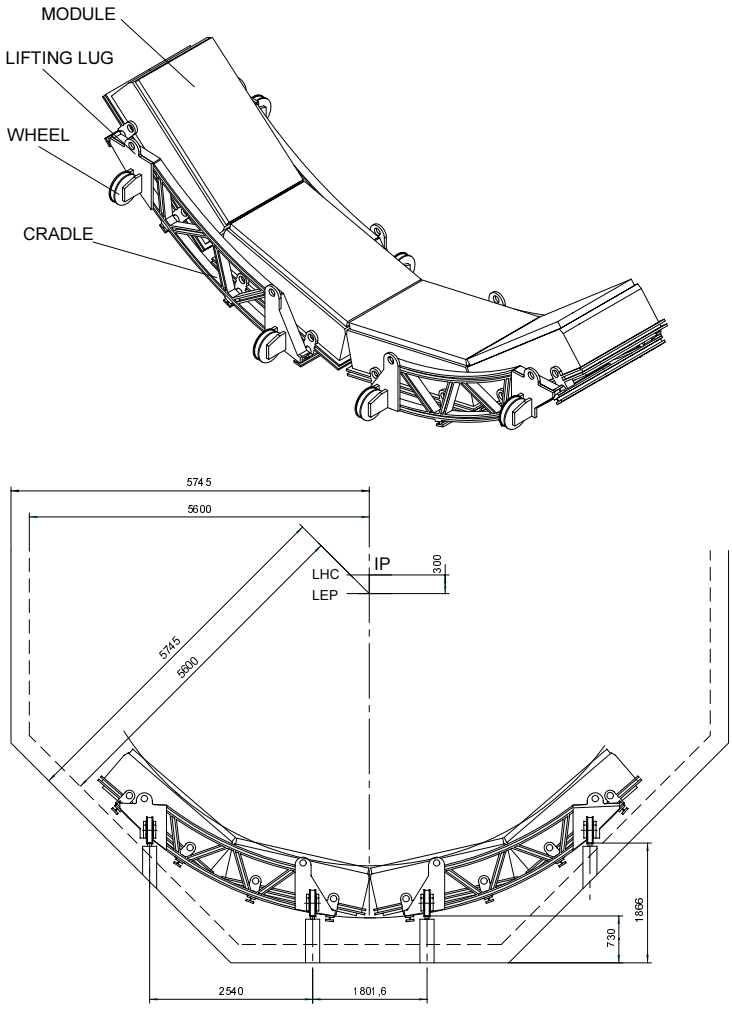

Figure 1.4: The configuration of the PHOS calorimeter.

The module has a size of 1×2 m^2. Each module faces the interaction point, so that the incidence angle will nowhere exceed $\sim 13^\circ$. This simple planar geometry facilitates the production of crystals, and the design and construction of the calorimeter.

The geometrical acceptance for π^0 and η mesons has been calculated by means of a Monte Carlo simulation. The only parameters entering this simulation are the detector boundaries (geometry) and the threshold for photon detection. The geometry of the configuration shown in Fig. 1.4, and a photon-energy threshold of 250 MeV, which corresponds to the minimum ionizing particle peak, were assumed in the simulation. The energy and position resolutions were also taken into account.

In Fig. 1.5 this acceptance is plotted against the transverse momentum. As can be seen from the figure, with the chosen configuration the minimal accepted p_{T} is ~ 0.5 GeV/c for both π^0 and η mesons. For the former it is determined by the chosen energy threshold, and for the latter by geometry.

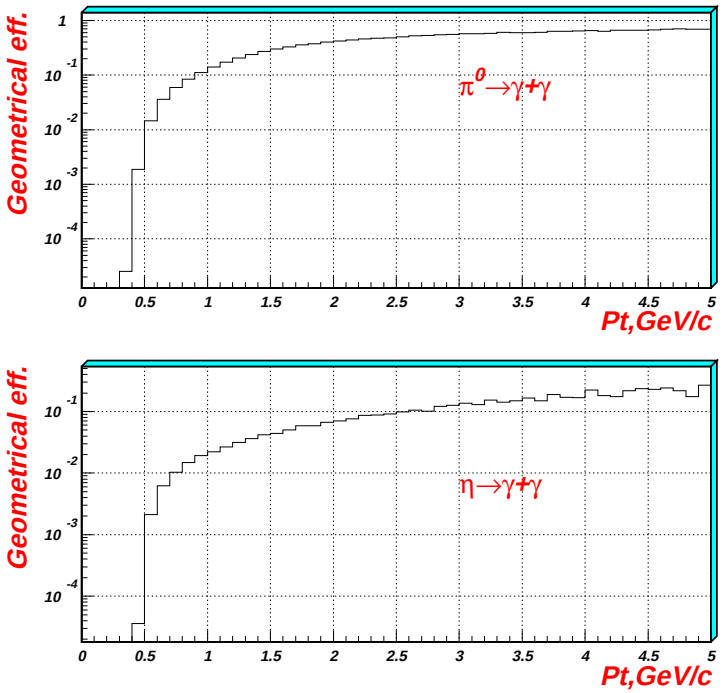

Figure 1.5: Geometrical acceptance for π^0 and η mesons vs. p_T for the PHOS calorimeter.

1.4.4 Energy and position resolution

The π^0 and η yields will be extracted from the $\gamma\gamma$ invariant mass spectrum, on top of a large combinatorial background (B). The signal fraction, $S/(S+B)$, in such a plot depends on the mass resolution, σ_M. A better mass resolution entails higher statistical significance and lower systematical error for the meson yields. The mass resolution depends on the energy and position resolution in the following way:

$$\frac{\sigma_M}{M} = \frac{1}{2}\sqrt{\frac{\sigma_{E_1}^2}{E_1^2} + \frac{\sigma_{E_2}^2}{E_2^2} + \frac{\sigma_\psi^2}{\tan^2(\psi/2)}}\,, \tag{1.1}$$

where E_1 and E_2 are the decay-photon energies and ψ is the opening angle between the two photons, whose error is determined by the position error.

The energy resolution can be parametrized as (E in GeV)

$$\frac{\sigma_E}{E} = \sqrt{\frac{a^2}{E^2} + \frac{b^2}{E} + c^2}\,, \tag{1.2}$$

where a is determined by the readout noise, b is the stochastic term, and the constant term c is due to detector and readout inhomogeneity and to the calibration error.

In the beam-test data analysis (see Chapter 2) the values of these parameters have been estimated as follows:

$$a = 0.03, \quad b = 0.03, \quad c = 0.01 \quad .$$

The position resolution can be parametrized by the following formula (E in GeV):

$$\sigma_{x,y} = \frac{A}{\sqrt{E}} + B\,. \tag{1.3}$$

In the beam test these parameters were found to be $A = 3.26$ mm and $B = 0.44$ mm.

It should be noted here that the parameters presented above, both for the energy and position resolution, correspond to normal incidence.

In spite of the varying incidence angles of the photons, the planar geometry of the PHOS has a very small effect on the energy and position resolutions, as was demonstrated in the beam tests (see Chapter 2) and by GEANT simulations (see Chapter 4).

1.5 Overview of the PHOS design and main R&D results

1.5.1 General structure of the PHOS detector

A conceptual design of the PHOS electromagnetic calorimeter will be described in detail in Chapter 3. It should be mentioned here that at the time of the engineering design study an electromagnetic calorimeter twice as wide as the one described in this report was being considered, and at the very beginning of 1999 a decision was taken to reduce the surface of the calorimeter by approximately a factor of two, owing to cost considerations. It was too late to perform a new engineering design and therefore some of the engineering drawings presented in Chapter 3 are those which have been produced in the course of designing the twice-as-wide detector. However, it should be stressed that, with the exception of obvious modifications of several dimensions of some large assembly units, this reduction does not otherwise change the chosen general structure or design of the vast majority of the components of the PHOS calorimeter.

1.5.1.1 Conceptual design of the PHOS mechanical structure

A modular structure has been chosen for the PHOS calorimeter. Its general view is schematically shown in Fig. 1.4. It will be positioned on the bottom of the ALICE set-up at a distance of 460 cm from the interaction point. The incidence angle of primary photons will be within the limits of $\pm 13^{\circ}$.

The PHOS calorimeter consists of four independent units, named *PHOS modules*, each of 4320 detecting channels. The module is assembled from detector blocks, *crystal strip units*, which are the main mechanical assembly units. Each strip comprises eight *crystal detector units* located in one row. Each unit is fastened to the strip with a thin titanium tape yoke. The crystal detector units consist of a lead-tungstate crystal of dimensions $22 \times 22 \times 180$ mm^3 coupled to a photodetector, which is a PIN photodiode of active area 16.1×17.1 mm^2, integrated with a preamplifier in a common body glued onto the end face of the crystal with optically transparent glue of a high refractive index.

In total, the PHOS electromagnetic calorimeter comprises 17 280 crystal detector units. Its total area will be ~ 8 m^2, the total crystal volume will be ~ 1.5 m^3, and their total weight will be ~ 12.5 t.

1.5.1.2 Cooling and thermostabilization system

The detector will operate at a temperature of $-25\,^{\circ}$C, stabilized with a precision of ~ 0.3–0.4°C. This will be achieved by using a cooling and thermostabilization system. The module is separated by thermo-insulation into two volumes, 'cold' and 'warm'. The strips with the crystal detector units will be located in the 'cold' volume, whereas the readout electronics will be located outside this volume. All six sides of the 'cold' volume will be equipped with cooling panels, and heat is removed by a liquid coolant pumped through the channels of these panels. As coolant a 1.2 propanedol-water solution has been chosen. The detector cooling system must transport the coolant over a distance of several tens of metres between the detector volume and the cooling system outside the L3 magnet. The scheme of this system uses two branches for cooling and one additional refrigerator for reserve, each branch involving a refrigerator, a heat exchange device, cooling panels for two detector modules, a volume for mixing the coolant, control and pumping devices. To better control the temperature a regulated heating source is foreseen. As a source of cold a two-staged cascade freon refrigerating machine has been chosen, operating with a refrigerant of type R134A.

Temperature monitoring will be provided by means of a temperature measurement system, based on resistive temperature sensors of wire or film type of thickness 30–50 μm, which will be inserted in the

gap between crystals. For reconstruction of the temperature distribution with an accuracy of $\sim 0.1^{\circ}$C, it will be sufficient to have two temperature sensors per 64 crystals. In addition, it is necessary to measure the temperature distribution over the cooling panel and the temperature of the coolant at the input and output of the cooling system. For this purpose standard resistive sensors will be used.

1.5.1.3 Readout electronics

The PHOS detector comprises four modules with a total of 17 280 channels. The data are digitized in 12-bit ADCs. Average event size is estimated to be 11 kbyte. This small event size means that the readout does not constitute a critical element of the detector.

The electronic chain includes preamplifiers, shapers, multiplexers, ADCs, buffer memories and zero suppression. The preamplifier is integrated with the PIN photodiode. The shapers, multiplexers and ADCs are mounted on cards placed in the 'warm' volume of the PHOS module. The cards containing the buffer memory and zero suppression are either placed in the same 'warm' volume or in crates under the PHOS supporting cradle.

1.5.1.4 PHOS trigger

The option of generating a PHOS trigger is currently under discussion. A trigger for level 1 (L1) may be generated from a fast summing of energy signals to find an energy deposition above a threshold in a cluster of adjacent modules. It may also be sufficient to trigger on a single high-energy cell. The current version of the front-end electronics of PHOS does not supply an energy signal sufficiently fast for a L1 decision. It will therefore require a revised shaper design with a fast output energy signal in addition to the current low-noise energy signal that has a peaking time at around 2 μs. For the energy summing circuitry a concept similar to the one developed for the PHENIX experiment will be studied [29].

1.5.2 LED monitoring system

The PIN photodiodes chosen as the photodetectors are very stable and, therefore, there is no need for monitoring their gain. Each preamplifier will have a calibration input for monitoring the gain of the readout electronics. The transparency of the lead-tungstate crystals and their optical contacts with the PIN diodes will be monitored by calculating the truncated mean of the spectrum of each crystal for a certain time and comparing it with previous measurements.

A common monitoring system to perform an overall monitoring of the PHOS detecting channels is needed for fast testing of the operational status of each channel, especially important during assembly of the modules, comissioning and cooling.

For this purpose a monitoring system using Light Emitting Diodes (LED) with stable current generators has been developed. A detailed description of the LED monitoring system is given in Chapter 3.

1.5.3 The charged particle veto (CPV) detector

In addition to photons, the PHOS calorimeter also responds to charged and neutral hadrons. The hadron rejection will be achieved by a cut on the shower width and lateral shape. For additional rejection of the charged hadrons a charged-particle veto (CPV) detector will be used.

The requirements on the CPV detector are the following:

- large-area modules of $\sim 200 \times 100$ cm^2;
- close to 100 % detection eficiency for charged particles;
- two-dimensional readout with localization accuracy of 3–4 mm;
- minimum amount of material, less than 5 % of X_0, electronics included;

- minimum dead-zone;
- low neutron sensitivity.

A detector based on known techniques of multiwire proportional chambers, filled with an Ar/CO_2 gas mixture, with pad readout, has been chosen as the baseline option for the CPV detector. A similar detector is proposed for the ALICE HMPID RICH detector [30]. It consists of four identical modules each connected with one of the PHOS modules. The CPV modules are located at a distance of ~ 5 mm above the PHOS modules.

A detailed description of the CPV detector design is given in Chapter 3, and the results of a simulation study of its performance are presented in Chapter 4.

It should be mentioned here that R&D is currently under way for another option of the CPV detector based on MICROMEGAS gas chambers. A preliminary design is presented in Appendix A.

1.5.4 R&D, prototypes, and test results

The PHOS electromagnetic calorimeter is optimized for measurements of photons of relatively low energies, up to ~ 10 GeV. The noise term in the energy resolution plays an important role at such low energies. Therefore, in the course of the PHOS R&D, a substantial effort was devoted to the improvement of the noise level of the photodetector unit consisting of a PIN photodiode and a preamplifier.

Studies of different ways of optimizing the crystal (PWO) growth technology and its subsequent mechanical treatment have also been carried out.

Studies of the optical and mechanical properties of the crystals, including the mechanism of their scintillation, were also a part of the PHOS R&D programme.

Significant efforts were devoted to develop methods for the crystal quality control. Different test benches for measurements of the crystal light yield and kinetics have been designed and constructed in the participating institutes. A large number of crystals have been measured with these test benches.

Several matrices of 3×3 and 5×5 crystals have been tested in the beam tests performed in 1996 and 1997. A 64-channel PHOS prototype has been constructed in the middle of 1998 and then tested using electron beams of different energies. A detailed report on the R&D and test beam results is given in Chapter 2. A brief summary of the main results is presented below.

1.5.4.1 Crystals

Crystal growth

An optimization of the PWO crystal growth and subsequent annealing and machining technology has been performed. Highly transparent crystals of large dimensions (boule diameter 30 mm and length up to 300 mm) have been grown at a pulling rate of 4–6 mm/hour and a rotation rate of 15–30 rpm. The duration of the technological process of crystal fabrication is 65–75 hours, consisting of 53–60 hours of crystal growth and 12–15 hours of crystal annealing.

Scintillation properties of the PWO crystals

Studies of the optical properties of the PWO crystals have been performed. Emission and transmission spectra, decay kinetics, light yield, radiation hardness and recovery processes were studied on small as well as full-size samples at different temperatures using different methods: with an excimer laser, with synchrotron radiation, and with radioactive sources.

The PWO emission spectrum consists of two components, peaking at 420 nm and at 480–520 nm.

In a light-yield measurement of a large batch (more than 200 crystals) of the full-size PWO crystals, performed using a ^{22}Na radioactive source, it was found that the crystals are rather uniform, the relative width of the experimental light-yield distribution being $\sim 10\,\%$. The mean value of the light yield, measured with the EMI-9814B photomultiplier, was found to be ~ 8 photoelectrons per MeV.

The temperature dependence of the PWO light yield has been measured using two independent methods: with the ^{22}Na radioactive source and with electrons of 2 GeV in the beam test. Both methods gave highly consistent results demonstrating a strong temperature dependence, with the temperature coefficient of the light yield being $\sim -2\,\%/^{\circ}$C in a broad temperature range.

In a kinetics study of the full-size crystals, performed with a ^{106}Ru radioactive source at room temperature, four components with decay constants of the order of 5, 15, 200 and 1000 ns were observed. However, it was found that more than 95 % of the total light integrated in 1000 ns is integrated in the first 100 ns.

1.5.4.2 R&D for PIN photodiodes

Beam tests with 10×10 mm^2 PIN photodiodes were carried out in 1996, using two prototypes of charge-sensitive preamplifiers. Based on the experience from these tests, an R&D programme was set up to develop a large-area PIN photodiode to maximize the light collection from the crystal cross-section of 22×22 mm^2, and a matching very-low-noise preamplifier for a diode with a high capacitance load, 150–200 pF. This programme was successfuly performed. In the middle of 1998 a large batch (~ 80) of the prototype large-area PIN diodes and low-noise preamplifier were delivered for test. The 1998 beam tests showed that the target energy resolution of the ALICE TP, mainly determined by the noise term, had been reached.

1.5.4.3 Beam tests

Different crystal test arrays (matrices of 3×3 and 5×5) equipped with different photoreadout PIN-preamplifier units, as well as different shapers, were tested in 1996 and 1997. A PHOS 64-channel prototype (a matrix of 8×8 crystals) was tested in 1998. The tests were carried out at the CERN SPS and CERN PS beam-lines X1, H6, T10 and T11, with electron beams in a broad energy range. A prototype of the CPV detector was tested at the CERN PS in the autumn of 1998.

The energy and position resolutions have been obtained by analysing the experimental beam-test data. The electromagnetic shower profile and the electron cluster size have been measured at different energies. The dependence of the energy and position resolutions on the incidence angle was studied. A preliminary study of the punch-through effects was performed at electron energies of 1, 2, 3 and 10 GeV. It was found that even at 10 GeV the tail due to this effect is small.

The 1998 beam test of the 64-channel PHOS prototype showed that the requirements on the energy resolution formulated in the ALICE TP are met. A summary of the results of the energy resolution studies from 1995 to 1998 is presented in colour Fig. VI.

1.5.5 Detector performance

The performances of the PHOS and CPV detectors have been simulated. The results are presented in Chapter 4. The following studies have been done via the simulations.

- The capability of extracting the π^0 and η peaks from the two-photon invariant mass spectra obtained with the PHOS in the high-multiplicity environment of central Pb–Pb collisions at the LHC energy has been investigated. The neutral mesons will be reconstructed via their $\gamma\gamma$ decay branch. In central Pb–Pb collisions at the LHC energy, the number of particles produced in each collision is very high, and so is the combinatorial background (B) in the two-photon invariant mass spectrum, due to the many possible photon pairs. Simulations have been performed to evaluate the capability of the event-mixing method in the ALICE experiment multiplicity environment. The event generator with the highest rapidity density expected in central Pb–Pb collisions, i.e. 8000 charged particles per unit rapidity, at midrapidity, has been used to produce π^0's and η's. In total

1.5 million such events were simulated. The REAL and MIXED two-photon invariant mass spectra were obtained. It was shown that a statistically significant signal is clearly seen, although the ratio $S/(S+B)$ is smaller than $\sim 0.2\,\%$.

- The PHOS occupancy in the ALICE experiment environment has been estimated under the highest particle densities currently predicted. Complete simulations of the radiation environment of ALICE have been performed using the GEANT and FLUKA simulation packages. The simulations show high fluxes of neutrons and low-energy gammas, which come mainly from the L3 magnet and from the absorber of the muon arm. 95 % of γ's and neutrons have energies below the cell noise of the single PHOS cell (10 MeV). About 90 % of γ's and charged pions with an energy higher than 250 MeV are due to primary particles. Taking into account the noise in the PHOS cells ($\sim$10 MeV), the occupancy of PHOS is found to be $\sim 15\,\%$, with the energy cut at 30 MeV.

- Since GEANT 3.21 does not include scintillator light processing, a method to simulate light propagation has been implemented, in order to evaluate the real performance of the detector. This method is based on a simplified approach to scintillation light propagation, where instead of tracking each single photon through a crystal only the average behaviour of the scintillation flash is taken into account.

- Based on these light propagation calculations, a lower limit on the values of the stochastic and constant terms of the energy resolution curve was found. These values are 2.48 % and 0.78 %, respectively. The PHOS prototypes with different gaps between crystals have been simulated. The results show almost no influence of gap width on the PHOS energy resolution for the photon energy range up to 10 GeV. These results are valid for the gap range 100–600 μm. The influence of the incidence angle on the energy and position resolutions has been studied.

- The first version of the PHOS reconstruction algorithm has been developed. The capability to unfold overlapping showers, to identify photons and to discriminate charged hadrons, neutrons and antineutrons has been studied using only the diagonal tensor elements of the electromagnetic shower form (dispersion cut).

  The possible use of a shower topology analysis has been investigated as well. This method uses full information about the shower shape and is very effective in suppressing the neutron and antineutron backgrounds.

- The performance of the CPV detector has been studied using a specially developed CPV reconstruction algorithm. The corresponding charged-particle suppression in the PHOS has been studied.

2 R&D, Prototypes, Test Results

Introduction

The PHOS electromagnetic calorimeter is optimized for measurements of photons of relatively low energies. The noise term in the energy resolution plays an important role at such low energies. Therefore, great efforts have been made in the course of PHOS R&D for improvement of the noise level of the photodetector unit consisting of a PIN photodiode with a preamplifier.

Studies of different ways to optimize the lead tungstate crystal growth technology have also been carried out. An extensive R&D programme for industrial technology of growing and subsequent machining of the lead tungstate crystals for high-energy physics was and is still being performed at the Bogoroditsk Techno-Chemical Plant in the framework of a special ISTC project.

Studies of optical and mechanical properties of the crystals and a mechanism of their scintillation were also a part of the PHOS R&D programme. Significant efforts have been made to develop methods for the crystal quality control. Different test benches for measurements of crystal light yield and kinetics have been designed and built. A few hundred crystals have been measured with these test benches.

2.1 Crystals

The lead-tungstate $PbWO_4$ (PWO) single crystals (colour Fig. II) have recently been considered as a very promising scintillator material in many applications where a high counting rate is required. High density and comparatively low manufactoring cost, in addition to fast luminescence decay, often compensate its comparatively low light yield at room temperature. In Technical Proposal [1] we have already identified PWO crystals as the most promising material for the PHOS detector and it will be used for the electromagnetic calorimeters of the CMS and ALICE detectors at CERN.

2.1.1 The growth of $PbWO_4$ crystal

To optimize the PWO crystal growth technology as well as the subsequent mechanical processing technology a special R&D programme has been performed at the Single Crystal Institute in Kharkov, Ukraine, with the participation of the ALICE collaboration. The methods and the results of these studies are published in Ref. [2]. A brief summary of these results is given below.

The state diagram of the PbO-WO_3 system reveals the existence of two congruently melting compounds: Pb_2WO_5 with melting point T_m at 899°C and $PbWO_4$ with T_m = 1123°C [3]. The high-temperature tetragonal β-modification of the $PbWO_4$ transforms to a low-temperature monoclinic α modification at 887°C. Inclusions of α modification and Pb_2WO_5 have to be carefully avoided when homogeneous monocrystals of β modification of the PWO are grown. We observed α modifications when the melt is kept in a supercooled state for a long time. The X-ray analysis of the crystallized melt from the supercooled state indicated the presence of 2% of α modification of the $PbWO_4$. Consequently, special attention has to be paid to heat removal conditions at the front point of crystal growth in order to grow homogeneous high-quality crystals. It is worth noting that the homogeneity of the crystals might be disturbed also by deviations from stoichiometry of the crystal when the melt is superheated. Consequently, the optimal melt temperature for the growth of the PWO, like that of BGO [4], is limited both from below (to avoid supercooling that increases the probability of formation of inclusions of the α-modification of $PbWO_4$ and the Pb_2WO_5) and from above (because of superheating that causes deviation from stoichiometry). The appropriate temperature range is determined by choosing optimal thermal

conditions of growth, by optimizing the growth regimes and by a special design of the crystalliser. Furthermore, the tetragonal crystal system of the $PbWO_4$ causes anisotropy of its crystallochemical and physical properties. We have measured the thermal conductivity of the crystal in different crystallographic directions and found that the thermal conductivity in [001] exceeds that in directions [100] and [101] by 10%. Consequently, the [001] direction is preferred as a growth direction because of the higher rate of heat removal from the crystallization front. Moreover, the light yield in such crystals is 5 to 10% higher than that in the crystals grown in other directions [5].

On the other hand, the anisotropy of mechanical properties of the PWO does not favor the crystals grown in the [001] direction. Cleavage planes, thoroughly investigated in PWO crystals in [6], are of crucial importance for mechanical processing of the boules. When the crystal is grown in the [001] direction, the cleavage plane [001], being perpendicular to the growing axis, plays a highly destructive role during the mechanical processing and easily causes ruptures of the crystal, especially if large blocks have to be fabricated. We did not succeed in reliably fabricating scintillator blocks of the necessary size from boules grown in [001]. The cleavage planes [101] and [112], important for mechanical treatment of crystals grown in the [100] direction, are not so destructive and large crystals blocks can be fabricated from such boules, though their scintillation properties are slightly worse than that of crystals grown in [001]. So we came to the conclusion that the [104] direction forming an angle of 19° with [001] is an optimal choice combining high quantum yield and thermal conductivity with passable mechanical properties.

Irrespective of the growth direction, growth of screw-shaped crystals was observed. We concluded that it was caused by misalignment between the growth axis and the axis of temperature distribution in the melt. The effect of screw shape is considerably enhanced by increasing the rate of crystal rotation as well as by excessive thermal screening of the crystal.

The modified structure of the crystallizer allowed us to fabricate homogeneous, highly transparent crystals with a diameter of 34 mm and a length of up to 300 mm at the pulling rate of 4–6 mm/h and rotation rate of 15–30 r.p.m. which were found to be optimal. The crystal diameter was controlled by weighting of the crystal. The duration of the technological process of crystal fabrication of 65–75 hours consisted of 53–60 hours of crystal growth and 12–15 hours of annealing in the growth chamber.

Some of the crystals in the early experiments had a slightly yellow colour even though the purity of the raw materials, technique of melt preparation and thermal conditions of the growth were identical for both colourless and yellow crystals. The yellow colour of the crystal is caused by the absorption band peaked at 430 nm. The band is due to excess of oxygen, in accordance with results of a detailed study of this band in Ref. [7]. Furthermore, the ratio of intensities of the green luminescence and the blue one was different in different samples. The detailed analysis of this phenomena led us to the conclusion that the atmosphere during the crystal growth and its subsequent thermal treatment is of crucial importance for the optical and radiative properties of the PWO. It was also observed that the intentionally chosen composition and pressure of the atmosphere in the process of preparing the mixture of raw materials and the melt also contribute to the shift of the luminescence band towards the blue region.

The study of the influence of annealing conditions and thermal treatment on the luminescence properties of PWO resulted in an increase in the light yield (LY) of 15–30% in comparision with that of as-grown crystals.

2.1.2 Scintillation properties of $PbWO_4$ crystals

We have performed a study of the optical properties of PWO crystals. Emission, transmission spectra, decay kinematics, influence of different doping on LY, radiation hardness and recovery processes of PWO crystals were investigated.

It is well known that the PWO emission spectrum consists of two emission components, a blue component (BC) peaking at 420 nm (2.9 eV) and a green component (GC) peaking at 480–520 nm (2.5 eV). The decay kinetics of the blue and green emission components have been described in Ref. [8].

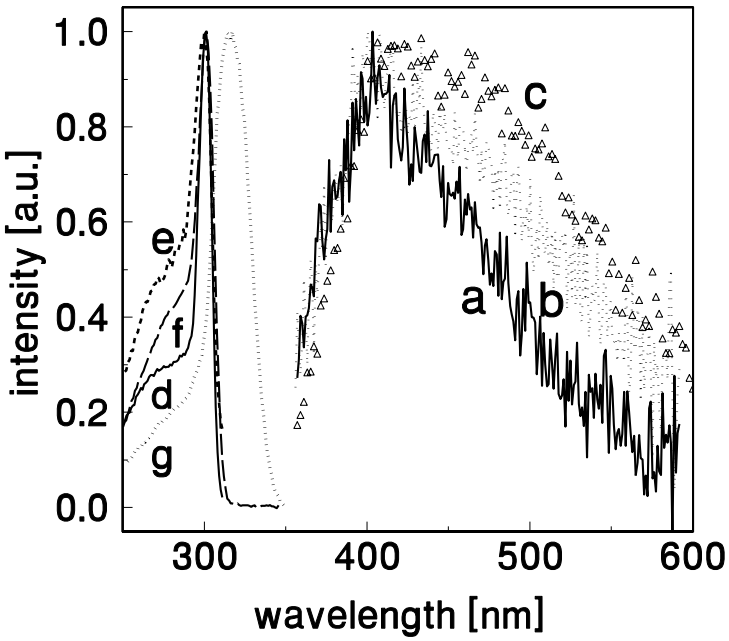

Figure 2.1: X-ray excited emission spectra of PWO1 (a),PWO2 (b) and PWO3 (c) at room temperature (RT). Excitation spectra at 80 K are given for PWO1, λ_{em}=400 nm (d), 500 nm (e) and PWO2, λ_{em}=400 nm (f), 500 nm (g).

Systematic measurements of transmission changes on large PWO crystal are reported in Ref. [9]. Nb-doping has been reported as an efficient tool in decreasing radiation damage of PWO crystals [10]. Also annealing PWO samples in different atmospheres and induced changes in the transmission spectra were used to further study the optical properties of defect centres in this material.

2.1.2.1 Emission spectra

The PWO samples used in the study of the emission spectra were produced in Prague, Institute of Physics –PWO1, Und1cz, La1cz, La2cz; in Turnov, CRYTUR Preciosa a.s., Czech Republic –PWO2; in Bogoroditsk BTCP plant, Russia –PWO3; the samples Und1jp, Und2jp, La1jp, La2jp grown by Furukawa Ltd. Iwaki, Japan.

The X-ray excited emission spectra of three typical samples, named PWO1, PWO2 and PWO3 are given in Fig. 2.1 (curves a, b, c) at room temperature (RT). The enhanced intensity in the green part of the PWO2 and PWO3 spectra shows evidence of the presence of a green emission component (GC), which is produced by the presence of Mo contamination at the level of 10–15 ppm (PWO2) and WO_3 centres (PWO3). The fact that no (or only a negligible) amount of the GC is present in the PWO1 spectrum can be derived from the absence of a characteristic excitation peak at about 310 nm of the GC at 80 K (compare excitation spectra at λ_{em} = 390 and 510 nm for PWO1, curves d), e) and PWO2, curves f), g), respectively. The temperature dependence of the blue and green emission components under X-ray excitation is given in Fig. 2.2 in the 80–300 K range for the PWO1 and PWO2 samples. The intensities of the BC and GC were obtained by calculating the area under the appropriate component spectrum at each temperature. For the PWO2 sample, the blue and green components were separated by subtraction of a suitably normalized PWO1 emission spectrum from the spectrum of PWO2. The BC intensity was normalized in both PWO1 and PWO2 to unity at 80 K (there is only a small difference in the absolute BC intensity in both samples given by slight differences in the sample shape and uncertainty in the experiment geometry), which make it possible to compare differences in their temperature dependencies. The values of the BC intensity above 180 K are systematically lower in PWO2 with respect to PWO1. The temperature dependence of

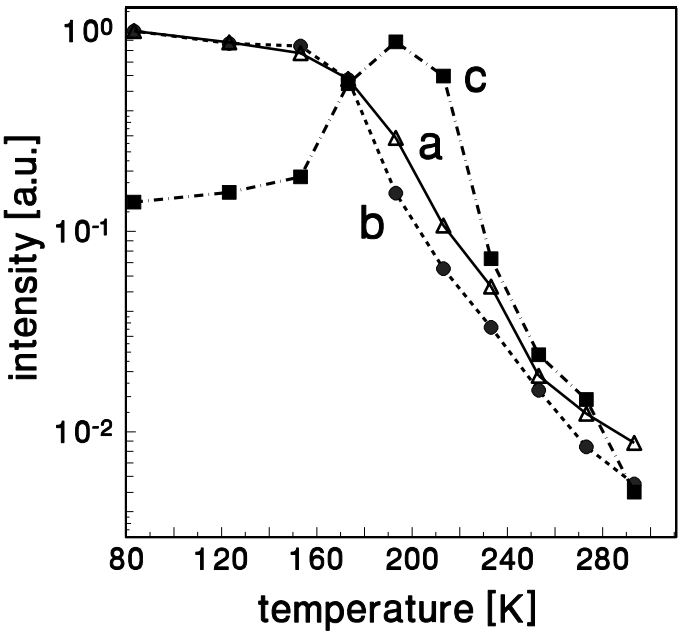

Figure 2.2: Temperature dependences of the blue emission component (curve (a) for PWO1, curve (b) for PWO2) and the green component (curve (c) for PWO2) constructed from the emission spectra under X-ray excitation (see text).

the BC and GC intensities at T in the range of 150–200 K can be explained by considering the energy transfer from the BC to GC [11]. The emission spectra of La, Lu, Y and Gd doped PWO samples do not show the presence of the green emission component.

2.1.2.2 Decay kinetics of lead tungstate crystals

The recent study of the kinetics of the PWO revealed some rather complicated features of the luminescence decay. The process is non exponential and can be conventionally divided into three characteristic time intervals [12]. During the first 5–10 ns after excitation the luminescent intensity rapidly decreases by two orders of magnitude. The subsequent decay is slower, however, after 50 ns only a very small fraction of the total luminescence is still observable. The characteristic decay time of this superslow component has been reported to be between 500 ns [13] and several microseconds [14].

The decay kinetics of lead tungstate crystals was studied by different methods at different participating Institutes.

Study of the decay kinetics with a laser

Studies of the PWO decay kinetics were performed with the same set of crystals as in Section 2.1.2.1. The decay kinetics of PWO was studied [15] and the co-existence of the decay kinetics of the 1st and 2nd order was observed in the blue emission decay as a result of thermal disintegration of the exciton excited state. An excimer laser was used (λ = 308 nm) in photoluminescence experiments. An energy transfer between the BC and GC centres was detected in the temperature dependences of emission spectra. This can be explained by considering energy exchange due to free charge carriers travelling through the conduction and valence bands [11]. A strong effect of La^{3+} doping on photoluminescence and spectrally unresolved scintillation decays was found. The decays are shortened with the increase of the La concentration. In the case of a multiexponential approximation for the decay curve (2.1) τ_{mean} can be calculated by Eq. 2.2:

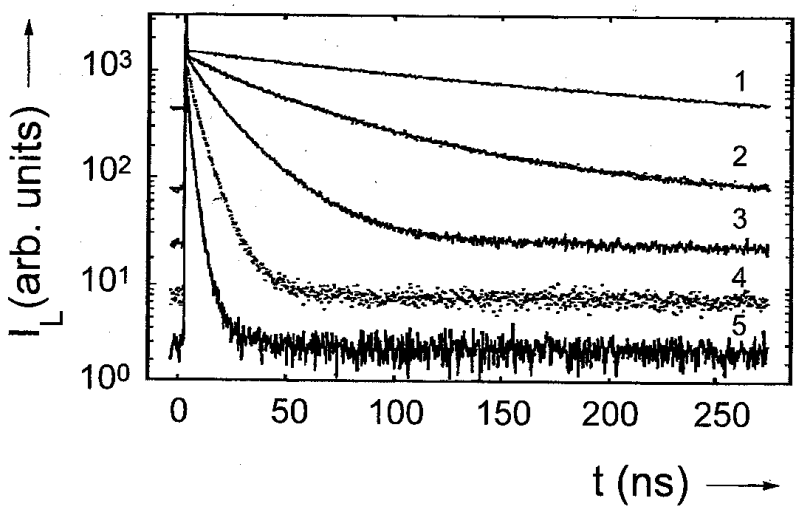

Figure 2.3: Decay of PWO luminescence at different temperatures: 200 K (1), 225 K (2), 247 K (3), 270 K (4) and 295 K (5).

$$I(t) = \sum_{i=1}^{4} B_i \cdot e^{-t/\tau_i} \tag{2.1}$$

$$\tau_{\text{mean}} = (\sum B_i \tau_i{}^2)/(\sum B_i \cdot \tau_i) \tag{2.2}$$

The values of τ_{mean} are shown in Table 2.3 on page 26.

Study of decay kinetics with synchrotron radiation

Two samples, N1 and N2, delivered by the Single Crystal Institute, Kharkov, Ukraine were tested [12]. The first one was cut from a boule, which was grown with a technology optimized to produce fast scintillators, with a high light yield, of a size $2 \times 2 \times 18$ cm^3. The second sample was grown and thermally treated in an atmosphere of nitrogen with an oxygen content of ~ 0.1 ppm. The time evolution of the luminescence during its initial decay was studied by short pulses (1 ns) of synchrotron radiation. Two characteristic quantum energies of the PWO emission spectrum were chosen for the study of the luminescence time evolution. The first quantum energy was 3.02 eV that corresponds to the peak of the BC band. The second point was 2.38 eV that corresponds to the region where the contribution of GC is maximal. The kinetics of luminescence at 3.02 eV is presented in Fig. 2.3 for several temperatures of the crystals. The studied temperature interval varies from 200 to 295 K. Since the luminescence of PWO is strongly quenched above 200 K, cooling of the sample below room temperature effectively increases the quantum yield. However, simultaneous slowing down of the luminescence decay is an undesirable result of cooling. So, a compromise between these two opposite trends has to be found in order to optimise the operational temperature of the PWO scintillator. The luminescence decay was parametrized by a sum of three exponentials with different decay constants τ_i and weight coefficients B_i. This gives us estimations useful for the comparison of decay rates at different wavelengths, in different samples etc. Results of such a parametrization are presented in Table 2.1 for the sample N2. For a probe quantum energy of 2.38 eV, the initial decay proceeds faster compared to the 3.02 eV quantum. However, it gets slower on the scale of tens of nanoseconds.

Table 2.1: Scintillating decays parameters of small PWO samples exited by synchrotron radiation

E_γ, eV	B_1	τ_1, ns	B_2	τ_2, ns	B_3	τ_3, ns
2.38	0.10	2.4	0.24	14.8	0.09	71
3.02	0.13	6.4	0.39	18.0	0.01	61

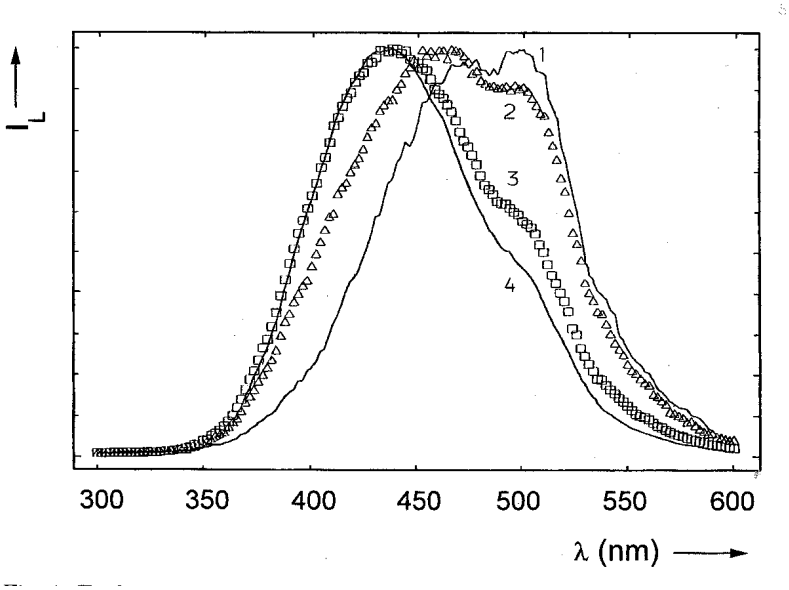

Figure 2.4: Evolution of the luminescence spectrum of the PWO crystal with temperatures: 250 K (1), 200 K (2), 175 K (3) and 150 K (4).

The relative intensity of the blue and green luminescence excited by synchrotron radiation strongly depends on temperature. The modification of the luminescence spectrum with increasing temperature is illustrated in Fig. 2.4. It demonstrates that the blue luminescence is quenched faster than the green one.

Measurement of the decay kinetics with a radioactive source

A test bench for measurement of the decay kinetics has been designed and constructed. It will be also used for the crystal quality control and certification of crystals.

The method consists in measurement of the time interval between the initial crystal excitation and the signal of a photomultiplier, detecting the crystal light. The photomultiplier works in the single photoelectron regime, which is achieved by attenuating the crystal light with a diaphragm.

A block diagram of one channel of the test bench is shown in Fig. 2.5. It has the following main components:

- A radioactive ^{106}Ru β-source with the maximal energy of 3.5 MeV. The source is placed inside a collimator which makes it possible to change the source intensity from 10 s^{-1} up to 10^5 s^{-1}.
- A start detector, S, which is a fast plastic scintillator of 1 mm thickness, coupled to the FEU-85 photomultiplier. The scintillator thickness is sufficient for producing ~ 50 photoelectrons.
- A stop detector, which is the Phillips XP1911 photomultiplier, with the attenuation diaphragm, D, in front of it.
- A specimen, i.e. a lead tungstate crystal, which is placed in between these two detectors.

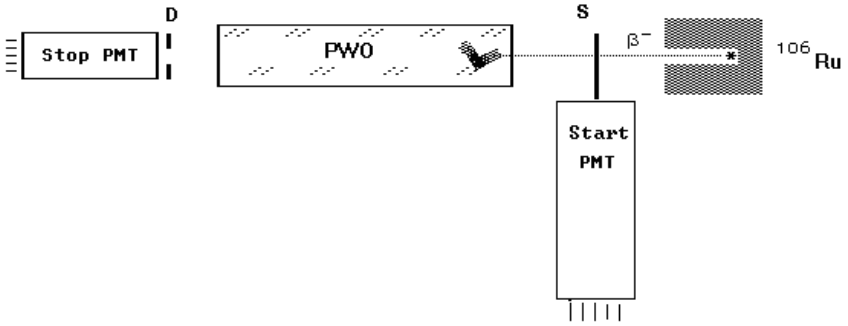

Figure 2.5: Block diagram of the ^{106}Ru crystal test bench for decay kinetics measurement.

The test bench allows one to simultaneously measure up to nine crystals arranged in a 3×3 matrix.

The test bench electronics comprises constant-fraction discriminators for the signals from the FEU-85 and Phillips XP1911 photomultipliers.

Two different methods of measurement of the start–stop time interval are used, depending on the interval duration, Δt, chosen for measurement. For $\Delta t < 200$ ns, the measurement is performed by a time-to-voltage convertor and a QDC block which allows to measure the decay curve with a bin size of ~ 0.1 ns. For large time intervals (up to $\Delta t \sim 20$ μs) the time is sampled by using a 100 MHz generator which makes it possible to have a bin size of 10 ns.

The time resolution of the test bench is mainly determined by the Phillips XP1911 photomultiplier working in the single photoelectron regime. Typically the time jitter for such a photomultiplier is ~ 300 ps, but in the one-photoelectron regime the time jitter increases and can be as large as ~ 800 ps. The additional timing uncertainties caused by the electronics are much lower: ~ 200 ps due to the discriminators and ~ 50 ps due to the TDC. Thus, the expected time resolution is ~ 900 ps.

With the maximal source intensity of 10^5 s^{-1}, the data-taking rate is determined by the data-acquisition system of the test bench, which allows us to reach an event rate up to 2×10^3 events/s. At this event rate one measurement takes 20 min on the average.

A sample of nine crystals delivered by Bogoroditsk Techno-Chemical Plant (BTCP) was measured with the test bench. The long and short time components were measured separately by using the two methods described above.

Typical decay curves are shown in Fig. 2.6 and Fig. 2.7. Four components with decay constants of the order of 5, 15, 200 and 1000 ns were needed to fit to the decay curves.

Thus, these curves were fitted with the following function:

$$I(t) = \sum_{i=1}^{4} (B_i/\tau_i) \times \exp\left(-\frac{(t-t_0)}{\tau_i}\right) \times \Theta(t-t_0) \tag{2.3}$$

Where, t_0 is the initial crystal excitation time, τ_i is is the i-th decay constant and B_i is the intensity of the i-th component.

The results are presented in Table 2.2. The systematic errors in the values of τ_i and B_i, which are typically larger than the statistical errors, are less than 10%. They were estimated by repeating the measurements and also by varying the fitting procedures.

As can be seen from the Table the timing properties of the crystals are rather uniform. The last column of Table 2.2 shows the ratio, R_{100}, of the charge integrated in the first 100 ns to the total charge integrated in 1000 ns. For all measured crystals this ratio was found to be ~ 0.95, which meets the kinetics requirement for the crystal, determined by the shaping time of the PHOS amplifier (~ 1 μs).

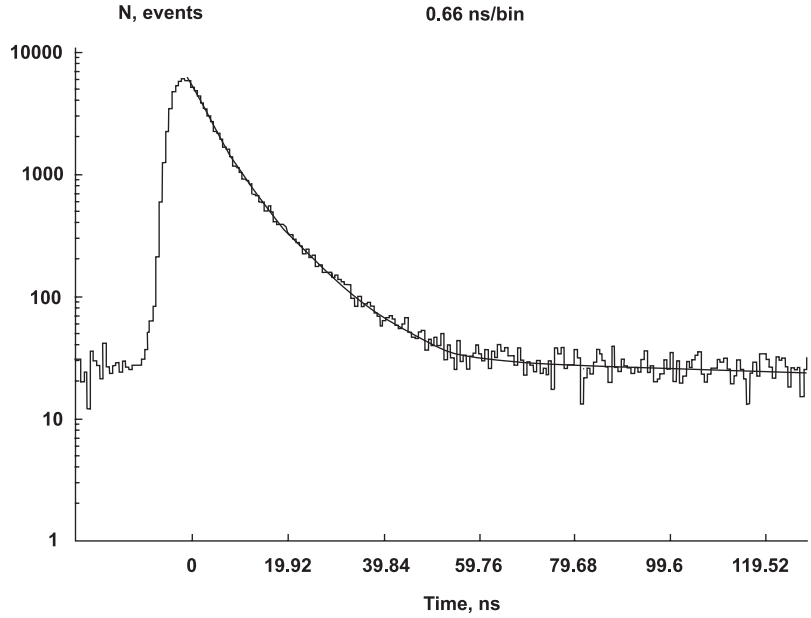

Figure 2.6: Typical scintillating decay time distribution (short component measurements).

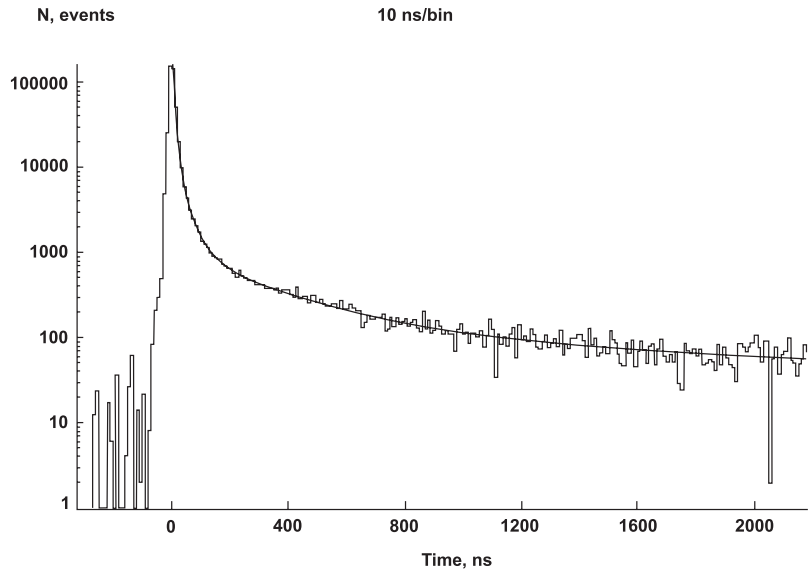

Figure 2.7: Typical scintillating decay time distribution (long component measurements).

2.1.2.3 Light yield of small samples

There are essentially two extreme situations, in which the light yield (LY) of PWO must be measured:

a) The small sample limit – the minimum sample dimensions are restricted by the requirement to get reasonably high absorption of the photons in the sample, i.e. a well-defined photopeak. For commonly used radioisotopes of ^{22}Na, ^{60}Co, etc. this requirement determines a minimum volume of the sample of about $1 \times 1 \times 1$ cm^3. The scintillation light produced in such a small sample has a rather high probability to reach the detector (low escape and reabsorption probability), so that such a measurement shows an intrinsic LY limit of a sample material and is of help for determining the scintillation light production mechanism.

b) The full-size limit – related to the full-size segment for HEP application e.g. $2 \times 2 \times 23$ cm^3. Additional escape and re-absorption losses lower the LY values measured with respect to an equivalent

Table 2.2: Scintillating decay time parameters for the measured samples (the crystal numbers are the factory ones).

Crystal number	B_1,% τ_1,ns	B_2,% τ_2,ns	B_3,% τ_3,ns	B_4,% τ_4,ns	R_{100}
209	40.6 ± 0.4	49.0 ± 0.7	5.81 ± 0.13	4.59 ± 0.07	0.929
	5.35 ± 0.16	17.5 ± 0.8	$118. \pm 5.$	$1550. \pm 50.$	
287	51.3 ± 0.5	50.1 ± 0.7	4.78 ± 0.06	3.81 ± 0.11	0.945
	4.82 ± 0.10	15.6 ± 0.7	$272. \pm 11.$	$2100. \pm 210.$	
149	86.0 ± 0.6	10.1 ± 0.3	2.29 ± 0.03	1.62 ± 0.07	0.977
	4.93 ± 0.08	12.6 ± 0.3	$310. \pm 20.$	$3040. \pm 990.$	
148	44.1 ± 0.4	41.6 ± 0.5	7.41 ± 0.11	6.91 ± 0.09	0.921
	5.73 ± 0.20	16.5 ± 1.2	$163. \pm 5.$	$1610. \pm 70.$	
191	82.7 ± 0.7	11.1 ± 0.2	3.48 ± 0.03	2.22 ± 0.06	0.967
	4.77 ± 0.11	11.3 ± 0.4	$213. \pm 11.$	$1590. \pm 230.$	
210	84.4 ± 0.6	9.36 ± 0.25	6.24 ± 0.04	not	0.958
	4.19 ± 0.10	9.65 ± 0.21	$268. \pm 11.$	seen	
145	60.2 ± 0.5	36.1 ± 0.5	6.72 ± 0.08	6.95 ± 0.11	0.922
	3.85 ± 0.19	8.8 ± 0.2	$204. \pm 7.$	$1760. \pm 90.$	
116	75.1 ± 0.4	18.2 ± 0.2	3.73 ± 0.06	2.99 ± 0.05	0.964
	5.43 ± 0.14	15.1 ± 0.9	$129. \pm 8.$	$940. \pm 70.$	
117	74.2 ± 0.4	19.1 ± 0.2	3.54 ± 0.03	3.14 ± 0.05	0.965
	6.21 ± 0.13	21.8 ± 1.7	$198. \pm 8.$	$2100. \pm 200.$	

small sample. Optimization of material, as for the lowest possible absorption losses in the spectral region where scintillation spectrum occurs, is of crucial importance.

A systematic comparison of the LY values among La-doped and undoped PWO samples was made in a small sample limit, see Ref. [16]. A correlation was found between shorter decay times and lower LY. This can be understood by assuming that the recombination (i.e. free-carrier-based) processes are strongly suppressed in the case of high La concentrations, which probably create new 'killer sites'. At these sites effective non-radiative recombination of free electrons and holes occurs (possibly close to La-dimers or La-small aggregates). Such a process inevitably leads to a strong decrease of LY. At intermediate La concentrations, the effect of τ_{mean} shortening is much more pronounced than the decrease of LY: this fact can be interpreted in terms of a generally faster free-carrier migration before radiative recombination. Also in the case of the blue emission centres, the speed of radiative processes based on recombination of free carriers depends strongly on the presence of traps [16]. These trap centres apparently capture temporarily free carriers at room temperature slowing down their migration and, consequently, the recombination decay components become slower as well. The observed LY values in Table 2.3 (i.e. for the case of small samples showing negligible GC intensity) together with the knowledge of their PL and SC decays gives the possibility to estimate the percentage of the immediate and recombination related scintillation light. It follows that a very fast immediate component (about 2–3 ns decay time at RT) contribute about 20–30% to the LY observed, while the rest is attributed to delayed radiative recombination processes.

2.1.2.4 Radiation damage processes in $PbWO_4$

The initial stage of γ-ray induced radiation damage of PWO is essentially a three-step process consisting of: (i) creation of hot electrons and holes by the interaction with high energy γ, (ii) their separation

Table 2.3: Calculated mean decay time values τ_{mean} of the photoluminesce (λ_{em} = 400 nm) and scintillation (spectrally unresolved) decays. The values of LY are measured at 15 ± 0.1°C and normalised to $T = 18$°C.

Sample	τ_{mean}, ns PL	τ_{mean}, ns SC	LY, ph.e/MeV	c_{La}, ppm
Und1jp	40.1	20.4	15.9 ± 0.1	< 1
Und2jp	34.4	21.1	16.5 ± 0.1	< 1
La1jp	9.3	3.7	11.1 ± 0.2	80
La2jp	2.2	2.4	4.0 ± 0.5	460
Und1cz	36.5	19.6	12.0 ± 0.1	< 1
La1cz	12.2	2.7	8.1 ± 0.1	55
La2cz	29.7	2.3	5.9 ± 0.2	$340 - 580$

during subsequent cooling down and diffusion processes and (iii) separate localization of both types of free carriers at suitable lattice sites (traps). Such sites might arise as a result of lattice distortions (dislocations, domain interfaces, etc.) or point defects (vacancies, impurity ions) or combinations of both of them. Colour centres might be created during (iii) as a result of a need for local re-creation of charge balance in the lattice (e.g. near to a monovalent or trivalent impurity ion at Pb^{2+} site in PWO, cationic and anionic vacancies, etc.). In case of PWO, one might expect in general the creation of F (two electrons in O vacancy), F^+ (one electron in O vacancy), O^-, Pb^+ and Pb^{3+} centres. Most of these centres are paramagnetic and some of them have also been detected in other scheelite tungstates by means of EPR, e.g. Pb^{3+} in $CaWO_4$ [17] and $(WO_4)^{3-}$ in several scheelites [18].

In general, no irreversible processes were observed during the irradiation of PWO up to high doses above 1000 Gy (e.g. formation of Pb colloids known from PbX2 compounds), because the initial transmission of the samples was always restored by heating to 200°C. This means that the stability of Pb^+ centres in the regular PWO lattice is strongly limited, because otherwise two electron capture in two steps at Pb^{2+} site becomes probable and subsequent creation of PbO and Pb-colloids might follow.

Transmission of the as-grown $PbWO_4$

Transmission of full-sized 20–23 cm long PWO segments was systematically reported in Ref. [9] and the presence of 350 nm and 420 nm absorption bands was very clearly demonstrated in many as-grown samples. In Ref. [9] a systematic decrease of the 350 nm band was noticed in Nb-doped crystals, while the 420 nm absorption band tended rather to increase after Nb doping. However, also in a few-centimetre-long undoped samples, these two bands can be well distinguished. These absorption bands clearly overlap the scintillation spectrum of PWO, which has two negative consequences: lowering of LY in full-sized samples and the spectrum inhomogeneity. The doping by stable trivalent dopants at the Pb site was found as a very efficient tool to reduce mainly the 350 nm absorption band in as-grown crystals, thus resulting in remarkable transmission improvement [19]. The effect was explained by the diminishing of hole centre concentrations (presumably ascribed to Pb^{3+} and O-like colour centres absorbing at 350 and 420 nm, respectively) by the excess Coulomb charge of La^{3+} ions introduced into the Pb sublattice. The remarkable improvement of transmission achieved for 15 cm long CRYTUR La- and Lu-doped crystals is displayed in Fig. 2.8.

Gamma-irradiation induced absorption changes

Considerable improvement of radiation resistance was found for La-doped crystal samples from three different laboratories [19]. The positive effect of La doping was explained in the case of improvement of transmission, namely that excess Coulomb charge introduced through a trivalent ion at a divalent

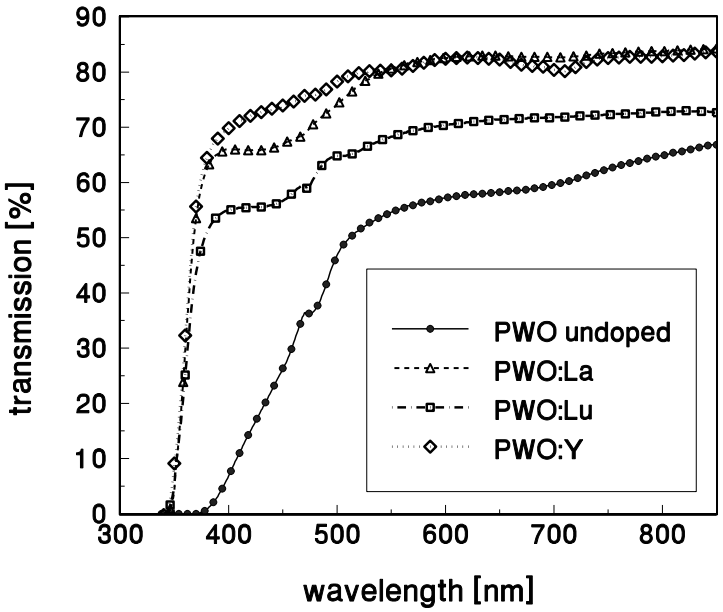

Figure 2.8: Transmission of 15 cm long PWO segments at RT for undoped, La doped, Y doped and Lu doped.

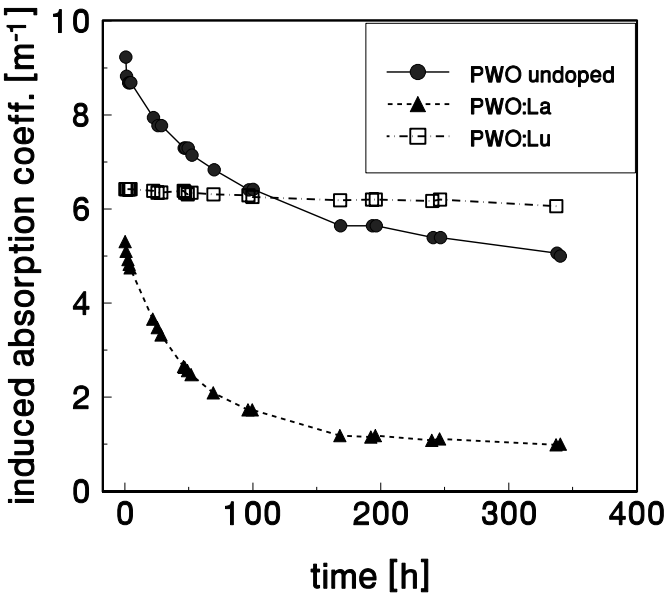

Figure 2.9: Recovery of the radiation damage for undoped, La- and Lu-doped $2 \times 2 \times 15$ cm^3 long CRYTUR crystals after a dose of 450 Gy.

lattice site reduces considerably the concentration of sites, which are able to localize temporarily holes created during irradiation. The dominant role of the hole centres in the radiation damage mechanism is based on the fact that the hole charge carriers have shown much higher mobility in electrical conductivity measurements [20].

Recovery processes at room temperature

The processes of spontaneous recovery of the induced absorption at room temperature (RT) are related to the stability of radiation-induced colour centres, i.e. to the thermal depth of related trapping centres. They are studies showing the possibilities for bleaching damaged PWO crystals. In Fig. 2.9, an example

of the spontaneous recovery (in the dark at RT) of three PWO crystals $2 \times 2 \times 15$ cm^3 (undoped, La- and Lu-doped) is given after the dose of 450 Gy [21]. It is evident that different doping influences thermal depth of the traps involved in the charge carriers' capturing and their subsequent release. Such an effect has no immediate explanation, because a tight spatial correlation between the doped ions and traps can not be a priori expected. On the other hand, it was recently found by EPR measurements that La doping enhances the cross-section of electron trapping at MoO_4 centres in PWO [22]. It was suggested that the depth of these electron traps is modified by Coulombic potential changes in the space regions of the PWO lattice, which contain La^{3+} ions. In this way one could propose that slight modification in Coulombic potential arises when different trivalent ions are used and consequently the depth of electron traps might become slightly different for various trivalent dopants.

2.1.2.5 Light yield measurements of full-sized crystals

Full-sized ALICE crystals ($2.2 \times 2.2 \times 16$ and $2.2 \times 2.2 \times 18$ cm^3) were delivered by Bogoroditsk Tecno-Chemical Plant (BTCP) in 1997. These crystals were tested with a test bench, specifically designed and built for measurements of the crystal light yields and kinetics. It allows one to simultaneously measure up to five crystals.

A block diagram of a single channel of the test bench is shown in Fig. 2.10. A ^{22}Na radioactive source is incorporated in the test bench. It emits either a positron (with the emission probability of 90%), which gives two annihilation photons of an energy of 0.511 MeV, or a photon of an energy of 1.275 MeV (the emission probability of 10%). The source is placed inside a cylindrical lead collimator.

The positron radiation branch is used for the measurements. The fact that two 0.511 MeV photons, moving in opposite directions, are produced, is used to make a trigger signal using one of the two photons, which is detected by a detector with a fast organic scintillator coupled to a photomultiplier FEU-85. The other photon produces a signal in the measured crystal coupled to a photomultiplier EMI-9814B, which was chosen for the light yield measurement. This choice was based on its high

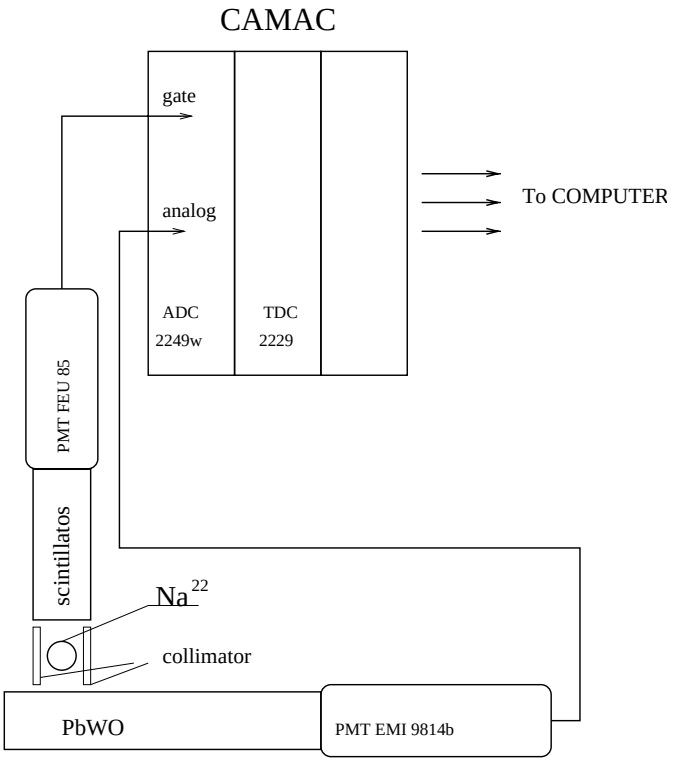

Figure 2.10: Block diagram of the test bench for light-yield measurements.

stability, a rather small width of the single-electron peak, a low level of the dark current and a good peak-to-valley ratio. This technique allows one to significantly decrease the noise level and, on the other hand, to simultaneously measure the pedestal signals using the radiation of the same radioactive source.

The output signals are transferred from the photomultipliers via long coaxial cables, of 5 metres length, to the data acquisition system. The signals from the measured crystals are digitized by means of charge-sensitive ADCs, (LeCroy 2249A), gated with the signal from the organic scintillator detector. The main DAQ computer is a PC/AT/XT-286 with a DOS operating system, running the CERN-BNL DTAKE data acquisition system. All information was recorded event-by-event and written to the Exabyte tape for offline analysis.

The measured crystals are wrapped in Tyvek. The Dow Corning optical grease Q2-3067 (refraction index n_{d} =1.5) is used for optical coupling of the crystal to the photomultiplier. The crystal detectors are placed inside a light-tight aluminium container.

The radioactive source is fixed to the trigger detector and both can be moved together along the crystal length, so that the measurements can be done for different positions of the irradiated crystal area. As a rule the measurements were being done with a 2 cm step.

A typical amplitude spectrum of the lead tungstate crystal is shown in Fig. 2.11. The pedestal peak is in channel 18 and is not shown in the figure. The single- and two-photoelectron peaks are clearly visible in the spectrum. The single-photoelectron peak position and width are the same for all measured crystals, since they are determined by the photomultiplier properties, and all measurements were done with the same photomultiplier in the same conditions. Therefore, the light yield calibration is based on the single-photoelectron peak.

The inclusive light yield spectrum is a superposition of the components corresponding to different numbers of photoelectrons, which should be well represented by Gaussian distributions, having a mean (μ_k) and a variance (σ_k^2), related to those of the one-photoelectron peak (μ_1, σ_1^2) in the following way:

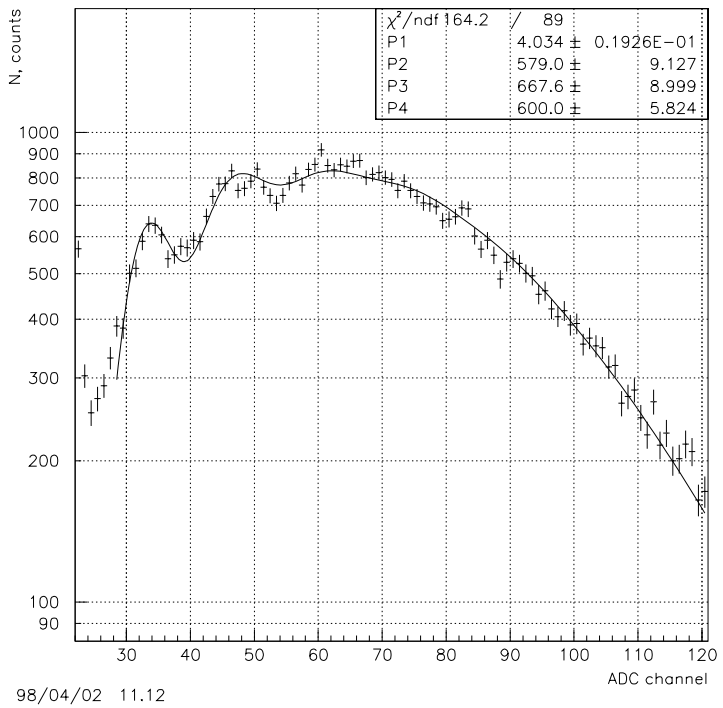

Figure 2.11: Typical ADC amplitude spectrum measured at midlength of the PWO crystals. The pedestals are not subtracted. The first peak corresponds to the single photoelectron, one can see also a two-photoelectron peak. The curve is the result of a fit (see text).

$$\mu_k = k \times \mu_1, \tag{2.4}$$

$$\sigma_k^2 = k \times \sigma_1^2, \tag{2.5}$$

where k stands for the number of photoelectrons of a given component.

The light yield spectrum produced by the low-energy annihilation photon has two components: one due to the Compton scattered photons and the other due to the photopeak. The Compton component mainly contributes to that part of the spectrum which corresponds to small numbers of photoelectrons, whereas the photopeak component mainly populates that part of the spectrum which corresponds to larger numbers of photoelectrons. Therefore, it is reasonable to assume that starting from some k the intensities of the components corresponding to different numbers of photoelectrons can be reproduced by a Poisson distribution. In this case the amplitudes of the two consecutive Gaussian distribution (A_k, A_{k-1}) can be readily related with the following formula:

$$A_k = A_{k-1} \times \frac{\lambda}{k} \times \sqrt{\frac{k-1}{k}}\ . \tag{2.6}$$

It was found that one can fit to the measured spectra with a single Poisson distribution starting from $k = 3$. The mean value of this Poisson distribution, λ, divided by photon energy 0.511 MeV represents the light yield of a given measured crystal in units of photoelectron/MeV.

Thus, the measured spectra are fitted with the following function:

$$f(x) = \sum_{k=1}^{15} A_k \cdot \exp\left(-\frac{(x - ped - \mu_k)^2}{2\sigma_k^2}\right). \tag{2.7}$$

Here *ped* stands for the pedestal peak position. It was assumed that equation 2.6 holds for $k \geq 4$. Four fit parameters were used: λ - the mean value of the Poisson distribution, A_1, A_2 and A_3 - the amplitudes of the Gaussian distributions corresponding to one, two and three photoelectrons respectively. For all other k the amplitudes were found by using Eqs. 2.6. For all $k \geq 2$ the mean (μ_k) and variance (σ_k^2) values were found by using Eqs. 2.4 and 2.5. For $k = 1$ the values of μ_1 and σ_1^2 were found in a special calibration run and they were not being changed in fitting to different crystal spectra.

For the majority of the measured crystals, the light yield measurements were done at four points along the crystal growth axis: at distances of 2, 4, 12 and 14 cm from the seed, in order to study the longitudinal homogeneity of the crystals and the light collection efficiency. The results of the measurements are shown in Fig. 2.12. One can see that the relative widths of the four light yield distributions are within 10%. Thus, the delivered batch of crystals turned out to be rather uniform. As for the longitudinal homogeneity, one can conclude that for this batch the differences of the light yields measured at different points are less than $\sim 5\%$ per full crystal length (20 radiation lengths), which should be sufficient for keeping the constant term in the energy resolution to $\sim 1\%$.

Owing to the thermal quenching of scintillation processes in the lead tungstate crystal, the crystal light yield should reveal a rather strong temperature dependence. This dependence has been measured with another test bench implemented with a ^{22}Na radioactive source. This test bench is in many aspects similar to the one used for light yield measurements described above. In addition, a cooling and thermostabilization system was implemented, which made possible high-precision measurement of the light yield temperature dependence in a broad-temperature range from room temperature down to -50°C. The results of the measurement are shown in Fig. 2.13. In the same Figure are presented the results obtained in the 1998 CERN PS beam test, when the same dependence of the lead tungstate crystal light yield on

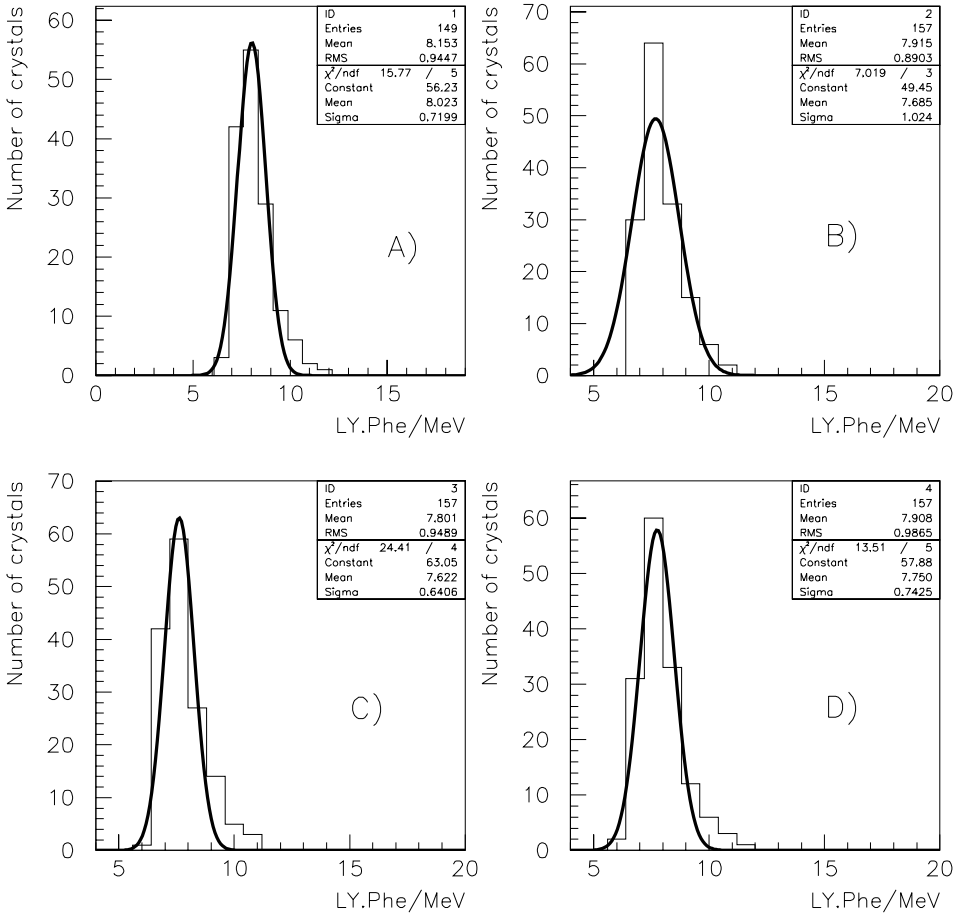

Figure 2.12: Mean values of LY for different points from the photomultiplier. A) 2 cm, B) 4 cm, C) 12 cm, D) 14 cm from the seed (photocathode). The curves are results of a Gaussian fit. Data was taken at room temperature.

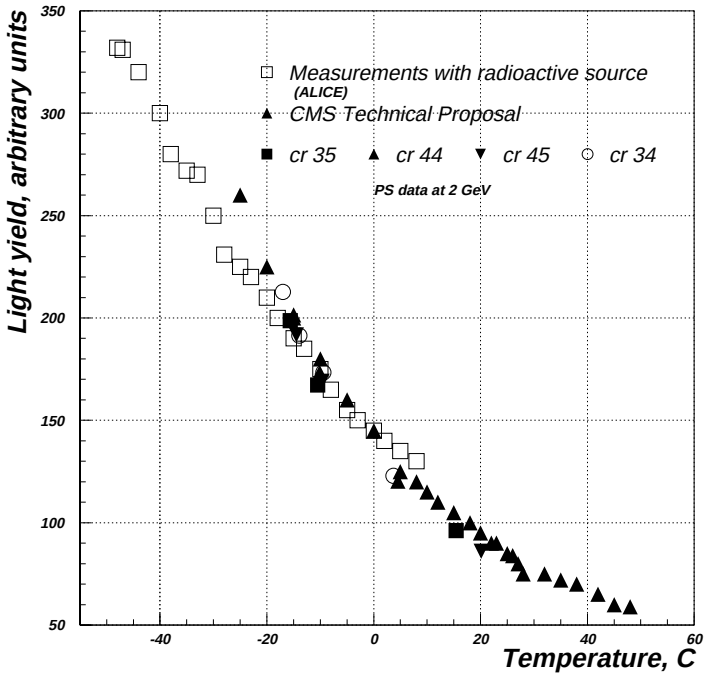

Figure 2.13: Temperature dependence of LY, measured with a radioactive source and with an electron beam.

the temperature was measured for four different crystals with an electron beam of energy 2 GeV (see Section 2.4). Also presented in this Figure are the published results from the CMS Collaboration [23]. The data of the three measurements are normalized at a temperature of $\sim 0^{\circ}$C.

A quite good agreement between the three different independent measurements is observed. The temperature coefficient of the light yield has a value of $-2\%^{\circ}$C in a wide region of temperatures. Therefore, in order to keep the crystal light yield and, therewith, the detector gain factors, constant with a precision of $\sim 1\%$, the temperature should be stabilized with a precision of ~ 0.3–0.4°C.

2.1.2.6 Transmission measurements with full-sized crystals

An optical test bench for measurements of the emission and transmission spectra of crystals was designed and built for optical transmission measurements performed with the crystals of a batch delivered by BTCP. These were La-doped crystals of a length of 16 cm. For each crystal the light transmission was measured in the direction perpendicular to the crystal growth axis at three different points along the crystal length: at a distance of 2 cm from the seed, at 2 cm from the opposite end and in the middle. A typical transmission spectrum is shown in Fig. 2.14. This particular spectrum was measured at the closest distance from the seed point. The transmission is zero for the light of wavelengths below ~ 340 nm, then a steep rise is observed in a range of 340–370 nm, followed by a plateau of $\sim 70\%$, corresponding to Fresnel losses. The results of the transmission measurements are summarized in Fig. 2.15. The two figures at the top (A and B) and the figure at the bottom left (C) show the distributions of the light wavelengths λ measured for each crystal at the value of 10%, 50% and 90% of the plateau transmission. The bottom right figure (D) shows the distribution of the plateau levels for these crystals.

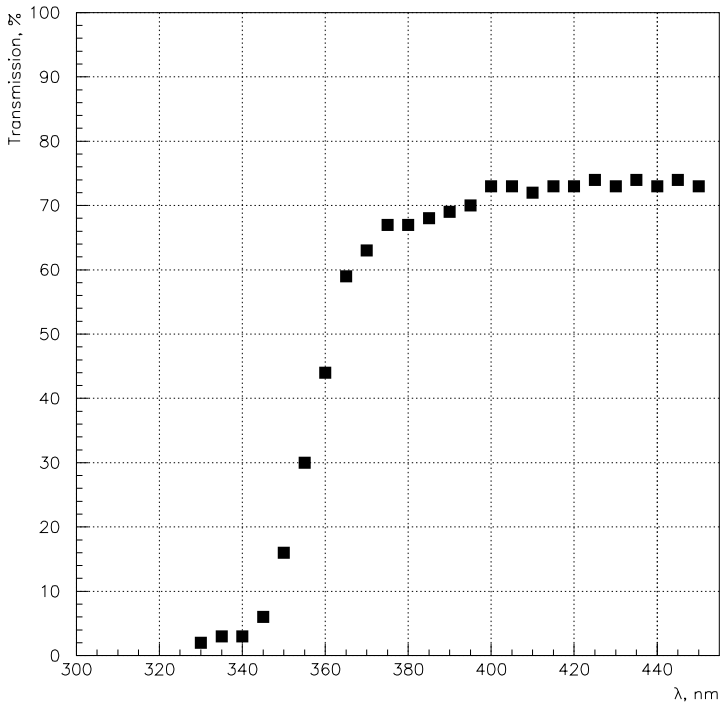

Figure 2.14: Typical transmision curve. The crystal was irradiated perpendicular to its axis at 2 cm from the seed.

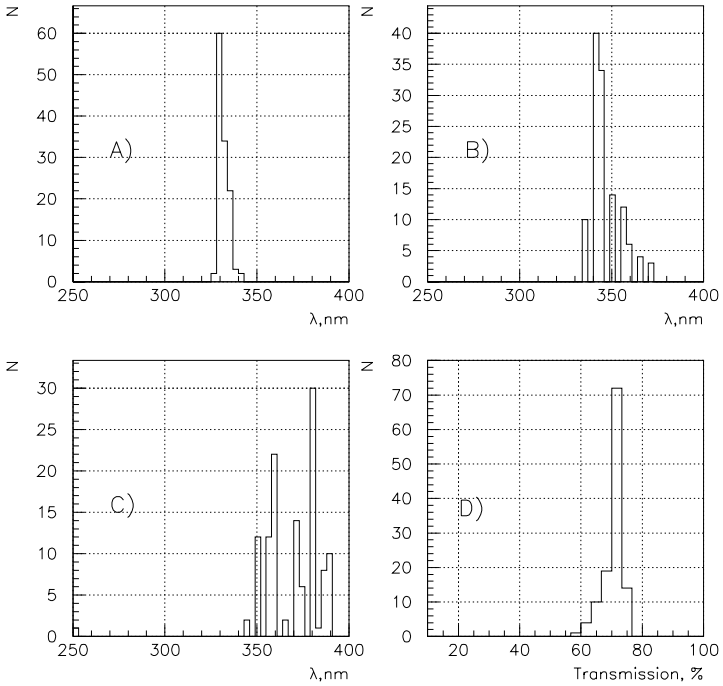

Figure 2.15: Summary of optical transmission measurements. A) distribution of λ at 10% level of plateau, B) distribution of the λ on half of plateau level, C) the λ distribution at 90% of plateau level, D) distribution of transmission, measured at plateau level.

2.2 R&D for PIN photodiodes

Two options for the photodetector were presented in the ALICE TP [1]: a PIN photodiode and a vacuum phototetrode (or photopentode). The PIN photodiode was considered to be the best candidate in terms of compactness, insensitivity to magnetic field and price. However, there are some disadvantages. PIN-diodes are sensitive to charged particles (punch-through effect) and have no intrinsic amplification, which requires a low-noise preamplifier and a shaper-amplifier in the readout chain. Because of the low light yield of the $PbWO_4$ crystals, the photodetector is the most critical element in the readout electronics for obtaining the required energy resolution for the PHOS.

Beam tests with 10×10 mm^2 PIN photodiodes were carried out in 1996, using two prototypes of charge-sensitive preamplifiers . Based on the experience from these tests, an R&D programme was set up to develop i) a large-area PIN photodiode to maximize the light collection from the crystal cross-section of 22×22 mm^2 and ii) a matching very low noise preamplifier for a diode with a high capacitative load of 150–200 pF.

The quantum efficiency of the PIN photodiode should have a maximum over the light emission distribution of the $PbWO_4$ crystals, which falls between $\sim$ 350 and $\sim$ 600 nm with a peak value around 450 nm. PIN-diods with preamplifiers, developed and tested during PHOS R&D, are shown in colour Fig. III.

2.2.1 The PHOS D–8501 photodiode

The company AME AS (Horten, Norway) has, in collaboration with the PHOS project, designed and produced a PIN photodiode optimized for the cross-section and spectral responsivity of the PHOS $PbWO_4$ scintillator crystal and the requirements of the PHOS readout electronics.

The photodiode chip has an active area of 17.1×16.1 mm^2 and is fabricated on n-type silicon material with a thickness of 280 μm. The wafer specific resistivity is between 3000 and 6000 Ωcm, which

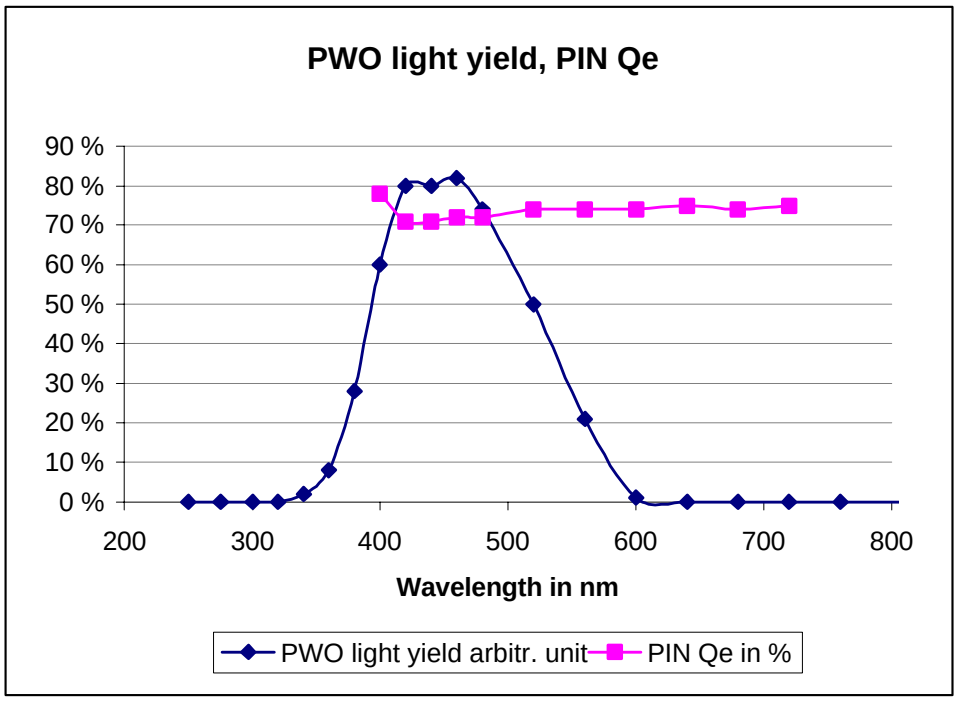

Figure 2.16: $PbWO_4$ crystal light yield and quantum efficiency (Qe) for the PHOS D8501 PIN photodiode.

corresponds to a typical depletion voltage of 70 V. In order to match the $PbWO_4$ emission spectrum the photodiode response is optimized with an epoxy coating for the spectral region from 400 to 500 nm. Typical quantum efficiency for the coated diode is $\geq$ 70–80% over the crystal light yield peak, see Fig. 2.16.

Special gettering techniques are employed in the production process to ensure low dark current and noise. The diode is operated in full depletion at 70 V with a typical dark current $<$ 5 nA, while the maximum dark current is specified to 10 nA at room temperature. The typical breakdown voltage is 120–500 V. The diode capacitance is $\sim$ 150 pF.

An oxide field plate is used to control the surface dark current. However, because of the large diode area this construction makes the chip sensitive to mechanical stress and damage during assembly. In order to make the chip mechanically more robust the construction will be modified in the following ways:

- The oxide field plate will be removed and replaced by a floating p-guard ring to control the surface dark current.
- A polyimide layer will be introduced as surface protection.

These modifications are based on experience from other high-reliability photodiode products developed and produced by AME.

2.2.2 The AE–9020 photodiode and charge amplifier assembly

The mechanical integration of the photodiode and the preamplifier is schematically shown in Fig. 2.17. The design and performance of the preamplifier is described in Section 2.3.2. The preamplifier PCB is separated from the diode in order to reduce the input stray capacitance.

The photodiode is glued onto a thick-film substrate frame. A miniature connector mounted on the substrate connects the diode to the preamplifier PCB. The amplifier output and bias and supply voltage

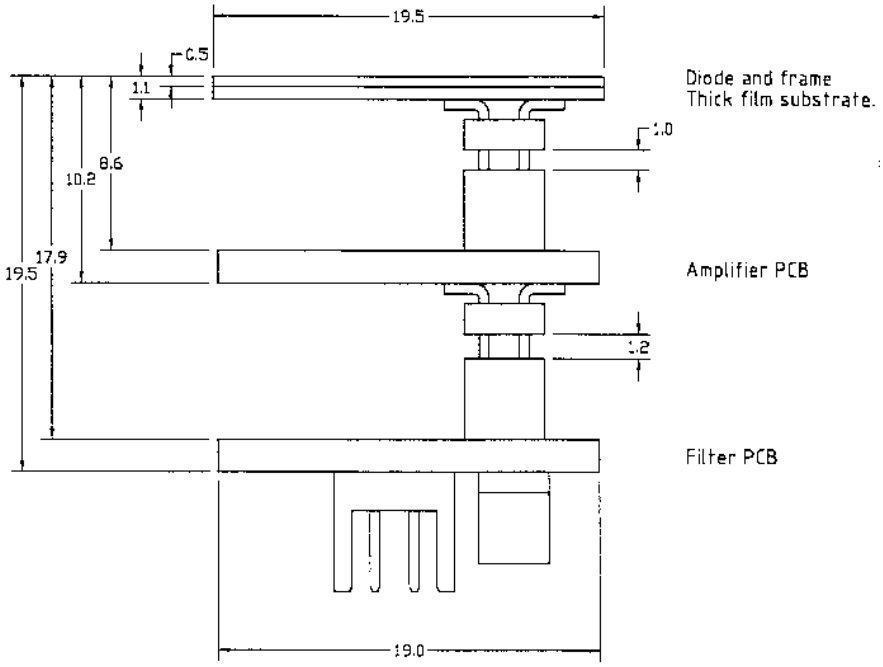

Figure 2.17: Mechanical layout of the AE–9020 photodiode and the charge preamplifier assembly.

lines are interconnected via a separate passive filter PCB to the external readout electronics and power supplies. Photographs of the PCBs are shown in Fig. 2.18.

2.2.2.1 Improvement of the photodiode - preamplifier assembly

The described assembly was used in the 1997 and 1998 beam tests at CERN (see Section 2.4) and was found to be an appropriate design for keeping the input stray capacitance to a minimum and thereby obtaining the low-noise characteristics of the photodetector. However, in order to have a good mechanical integration and also to minimize the costs of fabrication and mounting, a back-to-back interconnection of

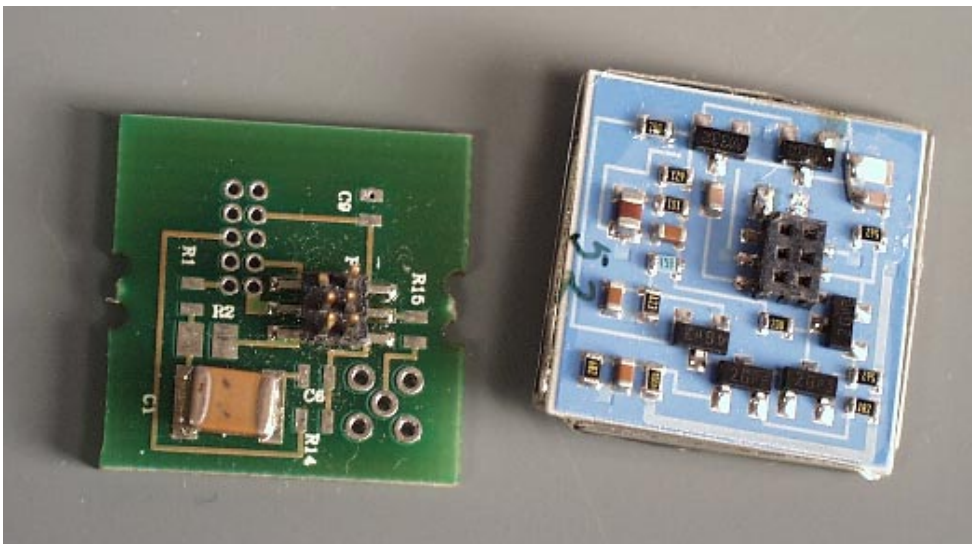

Figure 2.18: The filter and preamplifier PCBs of the AE–9020 assembly. The dimensions are 20×20 mm^2.

the photodiode and the preamplifier is preferable. The earlier problems related to input stray capacitance have been solved and the new and improved mechanical mounting depicted in Fig. 3.1 on page 68 will be used for the PHOS, see Chapter 3.

2.2.3 Assembly of eight channels into a crystal strip unit

Eight single-crystal channels with photodetector mounted on a common support constitutes the base assembly unit – a crystal strip unit (see colour Fig. IV) – from which a PHOS module is assembled, see Chapter 3. The mechanical structure of a crystal strip unit, with the PIN photodiode – preamplifier assembly extracted, is shown in Fig. 2.19.

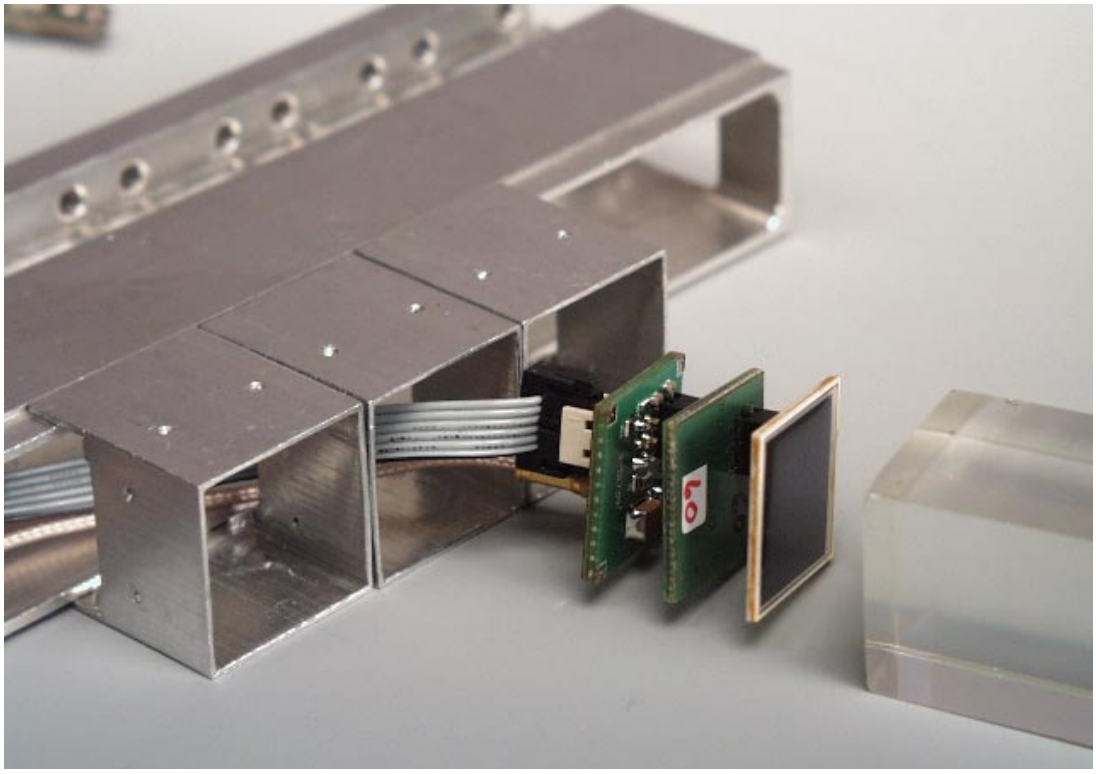

Figure 2.19: PIN photodiode and preamplifier assembly for a crystal strip unit.

2.3 R&D for the PHOS front-end electronics

The PHOS front-end and readout electronics chain (FEE) comprises a charge-sensitive preamplifier (CSP), a shaping amplifier, track-and-hold and multiplexing, and digitization in a 12-bit ADC.

In the description of PHOS in the ALICE TP [1], an option was presented to generate a fast timing signal from the CSP in order to collect time-of-flight information for antineutron subtraction. This feature has not been implemented in the current version of the CSP. (However, a fast energy signal generated by the shaper may have to be implemented if PHOS should participate in L1 trigger.)

Since the PIN photodiode – preamplifier stage is by far the most critical element for reaching the required energy resolution, the R&D work on this first stage has therefore been given priority.

During 1997–98, a low-noise preamplifier matched to the high capacitance of the D–8501 photodiode was developed and implemented in discrete circuits. This design was first verified in the 1997 beam test. An improved version was used to equip a full 8×8 crystal matrix in the 1998 beam tests.

As a possible alternative, a monolithic one-channel preamplifier chip has been developed by the company IDE AS (Oslo, Norway), and the first samples were delivered in December 1998, see Section 2.3.5. Tests of this chip are under way.

Prototypes of a shaping amplifier and an ADC have been developed and tested, see Sections 2.3.3 and 2.3.4.

2.3.1 Requirements for the PHOS FEE

A PIN photodiode is a device which converts light photons to an electrical charge. This charge is collected by the preamplifier which is a current integrator. At the preamplifier output appears a voltage signal with a fast rise time and a slow fall time. The preamplifier output is connected to the input of a shaper. The shaper has two functions: firstly, it amplifies the preamplifier output signal to an amplitude appropriate for the dynamic range of the ADC; secondly, a filter placed in the shaper increases the signal-to-noise ratio and changes the pulse to a quasi-Gaussian. In order to multiplex a number of channels to a common ADC, the amplitude of the shaper output signal is stored in an analog memory, gated by the L0 trigger track-and-hold (T/H).

2.3.1.1 Specifications for the preamplifier

In order to reach the required energy resolution for a PHOS channel, a noise level of ENC $< \sim 600\ e$ for the photodiode – preamplifier must be reached. This is a very low value taking into account the large diode capacitance of 150–200 pF. Other requirements are power consumption $<$ 200 mW and dimensions $20 \times 20 \times 20$ mm^3 or less.

2.3.2 Design and studies of the preamplifier

2.3.2.1 Circuit description

The circuit diagram for the CSP is shown in Fig. 2.20.

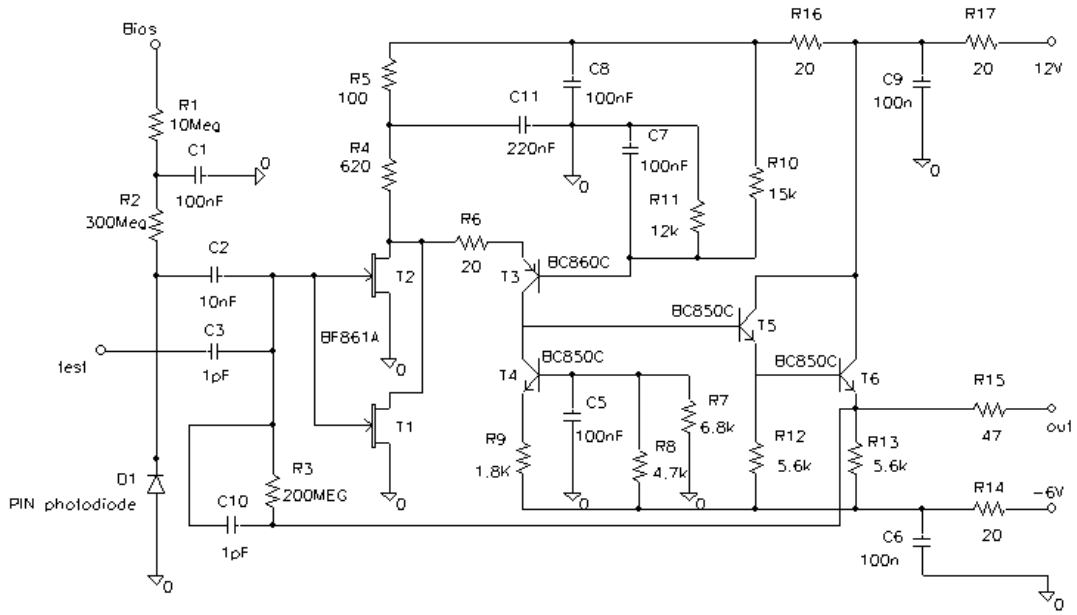

Figure 2.20: Circuit diagram for the PHOS preamplifer with two JFET input stage.

The preamplifier is an operational amplifier with a feedback capacitance C10 and field-effect transistors (JFET) T1 and T2 at the input. The resistor R3 is direct current feedback and determines the fall time of the output signal (200 μs for our case). The drain of T1 and T2 feeds the emitter of transistor T3, whose base potential determines the operation voltage of the JFETs. The operating currents of T1 and T2 are determined by the resistors R4 and R5. The characteristics of the JFETs determines the preamplifier noise level and the output-pulse rise time.

It is important that the charge sensitivity depends on the capacitor C10 only. To achieve this it is necessary that the CSP gain without feedback be approximately equal to 3000. To satisfy these requirements a scheme was chosen, where the current generator T4 is the load for T3. For circuit stabilization the CSP consist of two stages. The serial connection of the emitter followers T3 and T6 decreases the influence of output termination.

The power consumption is dependent on the choice of working points for the transistors. The CSP supply voltages are +12 V and -6 V. A more detailed description is given in Ref. [24].

2.3.2.2 Preamplifier noise sources

The various noise sources are the following:

- the noise developed in the first amplifying devices (FET) produces a voltage that can be represented by the Johnson noise in an equivalent serial resistor;
- noise coming from the detector leakage current and the input current to the first amplifying device;
- the parallel resistance noise arising from any resistor shunting the input circuit;
- the so-called flicker noise, $1/f$ noise;
- parallel lossy dielectric noise.

Figure 2.21 shows the equivalent input circuit for studying the energy resolution capabilities of the preamplifier. Expressions for the various noise terms are given in [24].

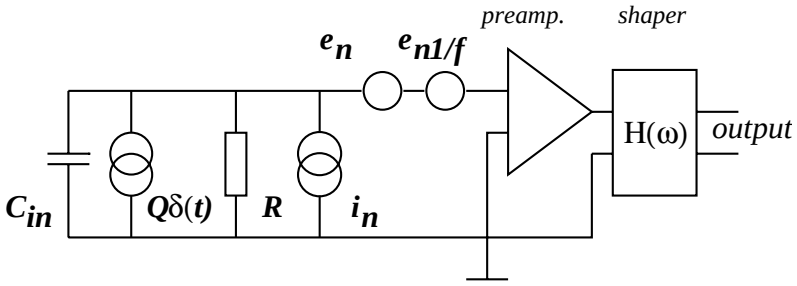

Figure 2.21: Equivalence circuit for studing the characteristics of the preamplifier.

For a detector signal approximated by an impulse of current containing charge Q, the signal at the input approximates a voltage step function of magnitude Q/C_{in}. The equivalent noise charge (ENC) of the system preamplifier – shaper is defined as the charge (in coulombs or numbers of electrons) that, when put into C_{in}, gives an output pulseheight equal to the r.m.s. value of the output noise voltage.

2.3.2.3 Calculations and measurements of equivalent noise charge (ENC)

The classical method of calculating the equivalent noise charge (ENC) is based on integrating the output response function in a frequency domain. If it is assumed that the response of the shaper to a sine wave

of frequency $\omega/2\pi$ is $H(\omega)$ and that a step input voltage has, at the output of the filter, a maximum amplitude $A_{\max}$, then

$$\mathrm{ENC} = \left[\frac{1}{2\pi A_{\max}^2}\int_0^{+\infty} Q^2(\omega)|H(\omega)|^2 d\omega\right]^{1/2}. \tag{2.8}$$

The shaper is of great importance in determing the energy resolution capabilities of the spectrometer and the associated electronics. With regard to the signal-to-noise ratio, a theoretical study by Den Hartog and Muller [25] shows that, considering the relative spectral distribution of serial and parallel noise, an optimal shaper exists. According to this work, the best signal-to-noise ratio is obtained with a shaper having a cusp-shaped response to a step input voltage.

The optimum value of the ENC is shown to be

$$\mathrm{ENC}_{\mathrm{cusp}} = \sqrt{4kTC_{\mathrm{in}}}\cdot\left(\frac{R_S}{R}\right)^{1/4}, \tag{2.9}$$

when the time constant of the shaper is optimized with condition that at the input the shaper keeps the differentiation chain with a time constant

$$\tau_1 = \tau_0 = C_{\mathrm{in}}\sqrt{R_S R}\,, \tag{2.10}$$

where τ_0 is the so-called noise corner time constant.

Among various shapers a single CR differentiation of time constant τ_1 and n stage RC integration of time constant τ_2 are widely used because of their good noise performances and ease of construction.

See Ref. [24] for a detailed calculation of the theoretical ENC.

Figure 2.22 shows the calculated and measured values of the ENC vs. the input capacitance for the preamplifier circuit of Fig. 2.20 on page 37. Figure 2.23 shows the calculated and measured values of ENC vs. shaping time constants. The agreement is very good.

Figure 2.24 shows the total noise measured at the shaper output for the 64 PIN photodiodes glued onto crystals, used in the 1998 beam test, at room temperature and cooled. At the operational temperature all channels have ENC lower than 600 e.

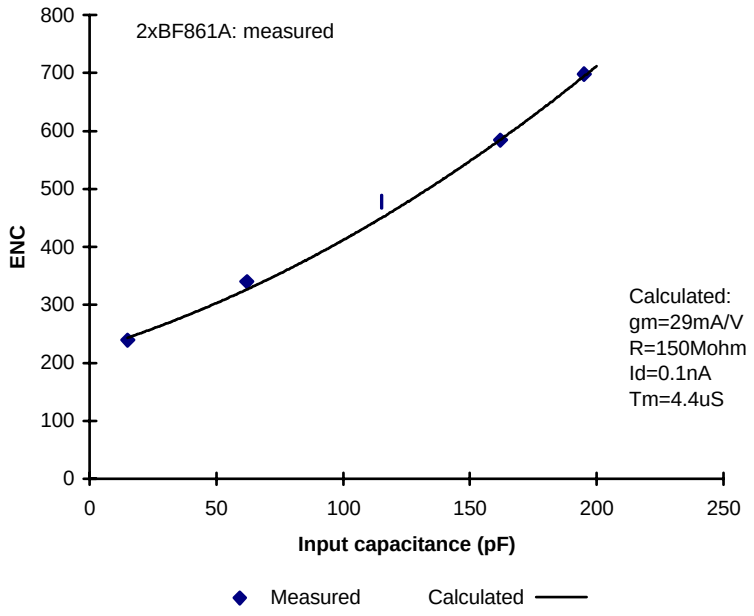

Figure 2.22: Calculated and measured noise in ENC (in e) vs. input capacitance for the preamplifier.

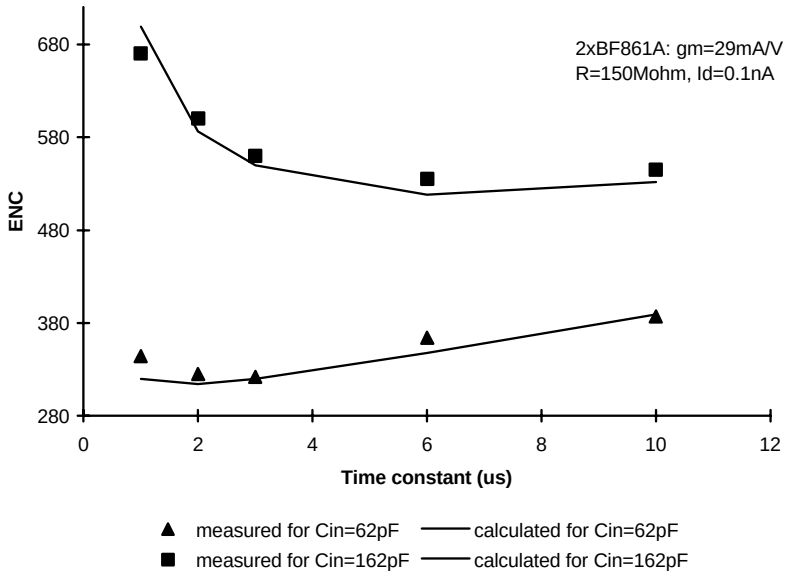

Figure 2.23: Calculated and measured noise in ENC (in *e*) vs. shaping time for two different values of the input capacitance.

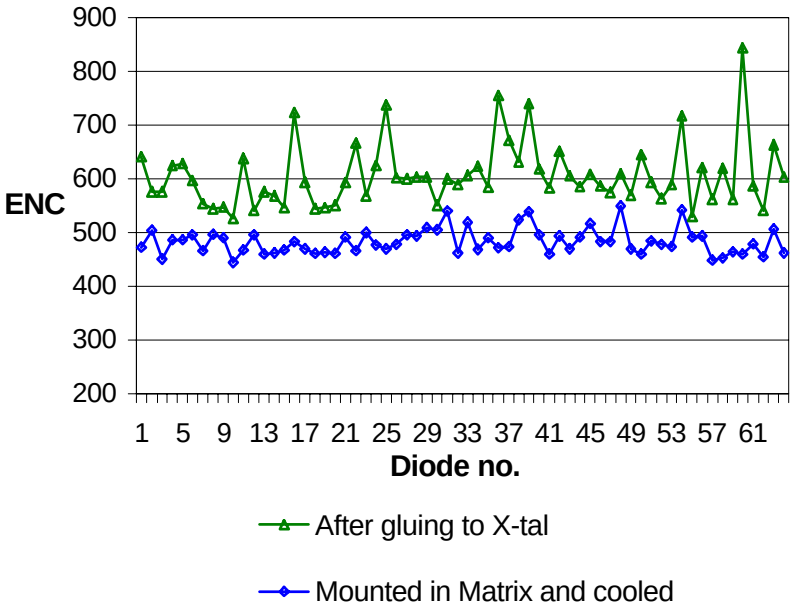

Figure 2.24: Total noise in ENC (in *e*) measured at the shaper output for the 64 PIN photodiodes used in the 1998 beam tests.

2.3.3 Design of a prototype shaper

The shaper is intended for the amplification of a preamplifier output signal and shaping of a pass-band for improving the signal-to-noise ratio.

The shaper circuit diagram is shown in Fig. 2.25. The shaper consists of three amplification stages A1, A2 and A4 (LF357N) with a gain equal to 7 for each stage. The measured equivalent noise referred to the shaper input is 12 μV (r.m.s.).

The input differentiator stage includes a ‘pole-zero’ compensation. Calculations for a PIN-diode having a capacitance of about 150 pF and a leakage current < 1 nA under cooling, give a noise corner

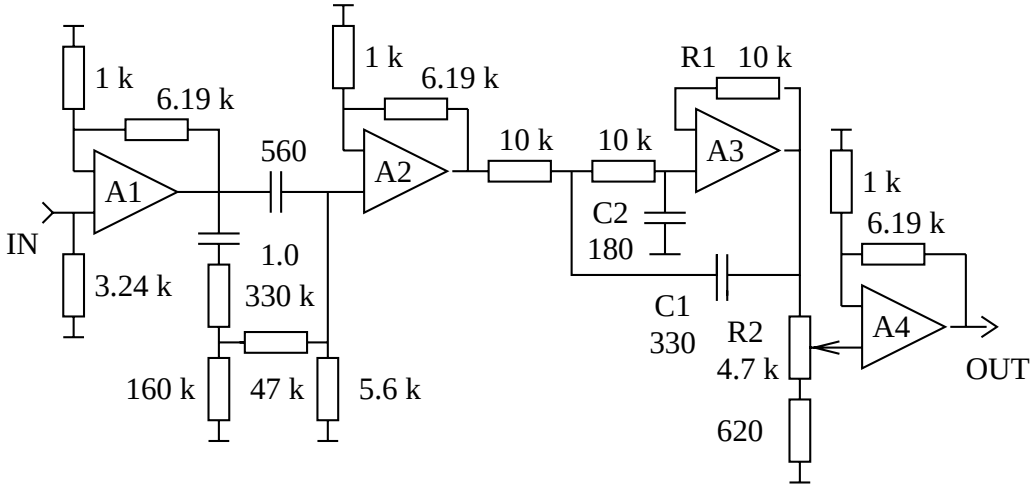

Figure 2.25: Circuit diagram for the PHOS prototype shaper.

time constant of 6 μs. For this value the optimum time constants of differentiation and integration are 3.36 μs. Furthermore the signal is amplified by A2 and is twice integrated by a second-order low-pass Sallen-Key filter. The value of the capacitor C2 is selected to be approximately one half of the value of the capacitor C1. This choice allows the fall time constant of the pulse to be shortened and thus the probability of pile-up to be reduced. The frequency correction of A3 is carried out with the resistor R1 and the input capacitance of A3. The falling edge of a pulse has no oscillations about a baseline. The actual gain is set by the resistor R2.

2.3.4 Design of an ADC prototype

In this section we describe the first version of an ADC developed for PHOS which was tested in the 1998 CERN beam test.

The ADC block diagram is represented in Fig. 2.26. The analog-to-digital conversion is carried out by the chip MAX 198 which is a multirange, fault-tolerant ADC, using successive approximation and internal input track-and-hold circuit to convert the input signal to a 12-bit digital output. The 12-bit parallel output format provides easy interface to microprocessors. The MAX 198 provides six analog input channels that are independently software programmable and requires only a single +5 V supply.

The signals to the MAX 198 pass through a linear gate and an analog memory, see Fig. 2.27. The linear gate consists of the resistor R1 and the switch S1 (1/4 chip DG412). The linear gate in an initial condition is closed and opened on a signal of the L0 trigger for 8 μs.

The analog memory is a peak detector which stores the pulse amplitude during the conversion of all 64 input channels. This time is 102 μs. The analog memory is implemented with two operational amplifiers AD823 (1 chip), 2 diodes 1N4448 and a switch S2 (1/4 chip DG412). The amplitude is stored on the capacitor Cm. The delay and jitter of the trigger arrival time will not influence the amplitude of the stored signal.

The capacitance C1 and switch S1 fulfil a role of a gated baseline stabilizer. After storing the input signals in the analog memory the control block generates a start-transformation signal. Since each MAX 198 multiplexes 6 inputs, 11 chips are used for the 64 channels. At the end of a MAX 198 conversion cycle, which lasts 12 μs, the chip generates a signal INT, on which the control block begins to read out the digitized values from the internal registers of the eleven MAX 198 circuits and stores them sequentially in the output memory. After all channels are read out, the control block starts a conversion cycle for the second input to the MAX 198s and so on. To digitize the signals in all 64 channels 6 cycles are needed.

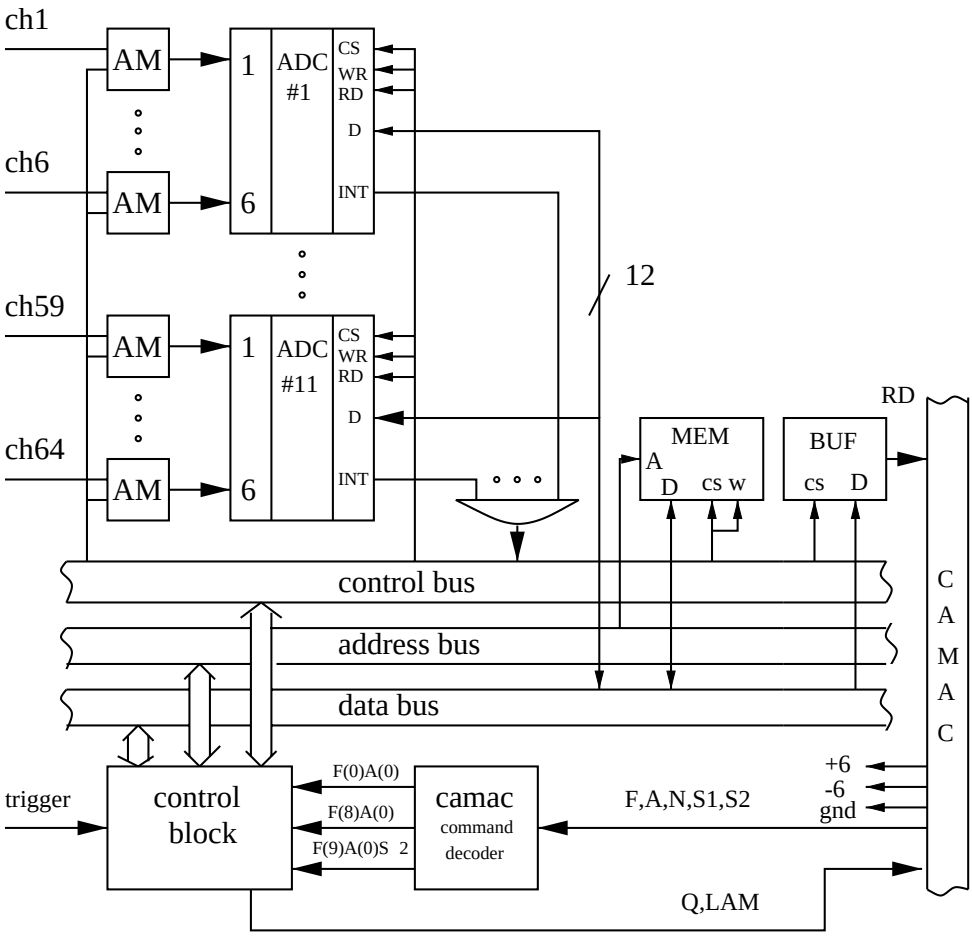

Figure 2.26: Block diagram of the PHOS ADC prototype.

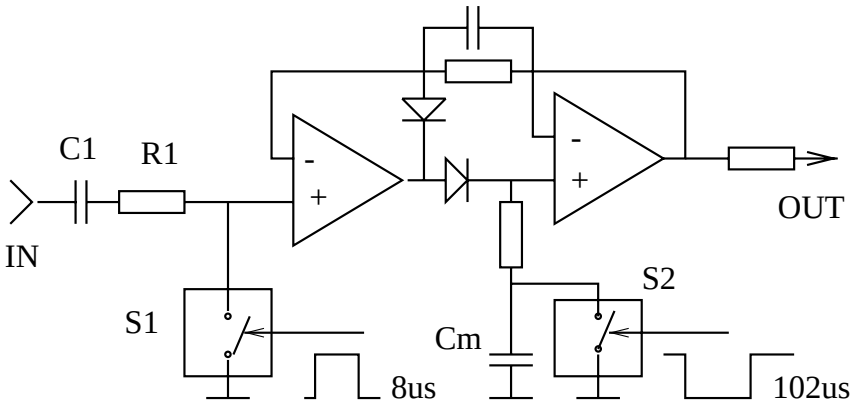

Figure 2.27: Circuit diagram of the linear gate and analog memory cell.

The first prototype has been implemented in a CAMAC module. At the end of digitization the control block generates a LAM on the CAMAC bus. On this signal the DAQ system reads out sequentially the ADC memory by means of 64 $\times$ A(0) F(0). At the end of reading the command A(0) F(9) resets the ADC.

The specifications and test results are:

1. number of inputs: 64, AC-coupled, R_{in} = 10 kΩ;

2. range: 0 to +4 V, peak detection;
3. strobe: NIM signal with $>$ 20 ns duration to initiate conversion;
4. data: 11 or 12 bit (set by jumpers) available on R1 to R12 dataway lines;
5. integral nonlinearity $<$ 0.12% for 1% to 100% of full scale;
6. differential nonlinearity: $<$ 14% for 11 bit and $<$ 30% for 12 bit full scale;
7. conversion time: 102 μs for all 64 channels;
8. influence of input counting rate on position and peak width: for a counting rate from 10 Hz up to 50 kHz the peak position is decreased by 1.1% and the sigma is increased by 20%;
9. supply voltages: +6 V, -6 V.

2.3.5 Development of a single-channel monolithic preamplifier chip

The preamplifier described in Section 2.3.2 draws $\sim$ 200 mW. For the full PHOS detector (17 280 chs) this implies a power consumption of $\sim$ 3.5 kW. A monolithic version of the PHOS preamplifier will significantly reduce the power dissipiation of the front-end electronics. Furthermore, the price for a large production volume will be less for a monolithic version.

The company IDE AS (Oslo, Norway) has developed a prototype of a monolithic single-channel, low-noise preamplier, with specifications that match the input capacitance and dynamic range of the PHOS photodiode.

The *Va_1chan* is a low-power charge-sensitive preamplifier-shaper circuit followed by a readout buffer. The chip has in addition an internal bias network.

The architecture of the chip is shown in Fig. 2.28. The bias voltages *vfs, vfp, pre_bias* and *sha_bias* are generated internally. If other settings than the default values are needed, they can be set with an external circutry.

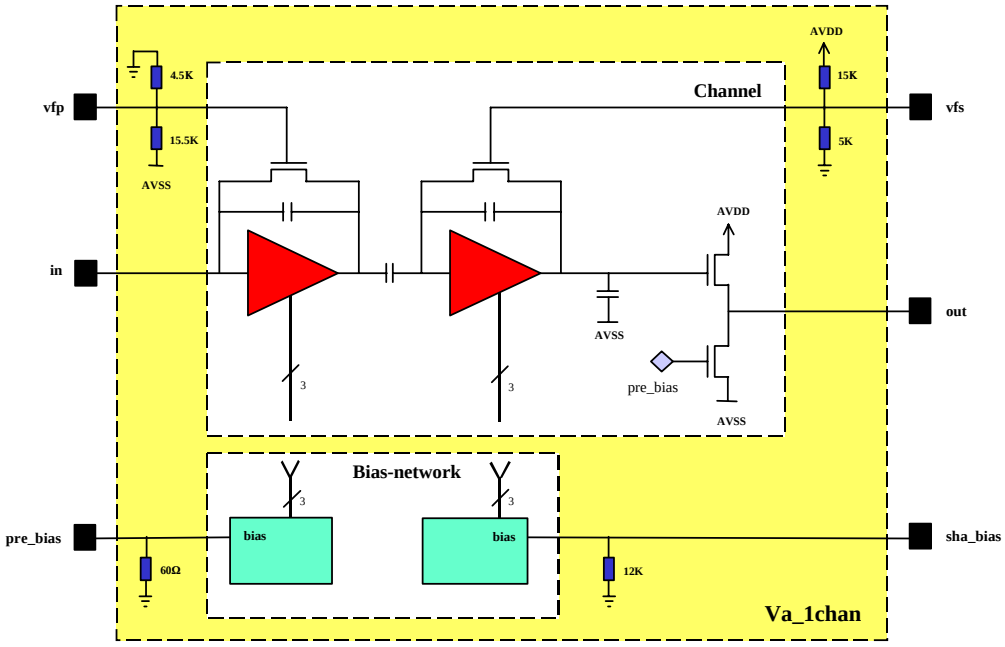

Figure 2.28: Principle of the *Va_1chan* with bias network.

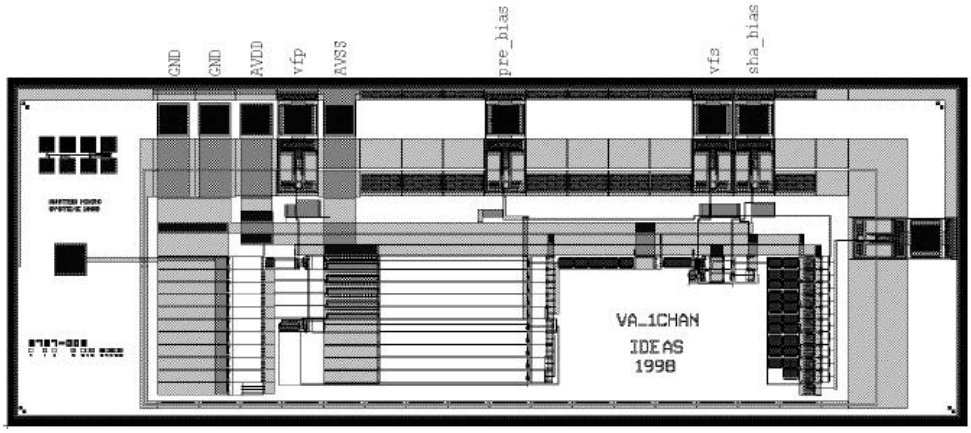

Figure 2.29: Geometry and layout of the *Va_1chan* chip.

The chip was produced in the AMS 1.2 μm BiCMOS BAE process. The dimensions are 3×1 mm^2, see Fig. 2.29.

The *Va_1chan* is designed for a large dynamic range of ~ 500 fC and with gain ~ 2 mV/fC. A noise slope ~ 2 e/pF and shaper noise ~ 250 e give a total noise of ~ 500 e at 200 pF input load. The output impedance of the readout buffer is ~ 100 Ω. Supply voltages are ± 2 V, with a power consumption of $\sim$ 20 mW.

A power consumption of $\sim$ 20 mW/channel will reduce the total power budget for the PIN-diode preamplifiers by a factor of 10, down to $\sim$ 350 W, compared with the discrete circuit version.

Tests of the *Va_1chan* chip have started (January 1999) and design of a shaper circuit is in progress.

2.4 Beam tests

2.4.1 Introduction

Different crystal test arrays (matrices of 3×3 and 5×5 detectors) equiped with different photo-readout PIN-photodiode-preamplifier units, as well as different shapers were tested in 1996 and 1997. A PHOS 64-channel prototype (a matrix of 8×8) was tested in 1998. The tests were carried out at the CERN SPS and CERN PS beam lines X1, H6, T10 and T11 with electron beams in a broad energy range.

2.4.1.1 Crystals

A batch of the crystals can be seen in colour Fig. II. They were optically polished, the tolerance in the transverse size was 50 μm and that in the length was 1 mm.

Most of the tested crystals were provided by Bogoroditsk Techno-Chemical Plant, Tula Region, Russia. Nine crystals were produced by the Single Crystal Institute, Kharkov, Ukraine. Five crystals have been provided by the CRYTUR s.a., Precioza, Czech Republic. Crystals of various lengths: 14, 16, 18 and 20 cm were used in the tests.

The crystals were visually inspected for mechanical imperfections, bubbles etc. Before testing in the beam, each crystal was evaluated according to its optical transparency and light yield measured with the test benches, which are described together the details of measurements in Section 2.1.2.

The crystals were wrapped in Tyvek.

2.4.1.2 Photo-readout units

The PIN photodiodes with preamplifiers were used as photodetectors. The noise term in the energy resolution plays an important role at relatively low photon energies, which are relevant for the ALICE experiment. Therefore, the photo-readout unit was the key issue in the PHOS R&D and it has passed through extensive testing during the last years.

1996 electronics

In 1996, different PIN-diodes provided by Recom Ltd, Moscow, Russia, as well as the AE9427, AE9012 and AE9012B (hybrid) diodes from AME AS, Norway, were used. The PIN-diodes of a sensitive area of 1.0×1.0 cm^2, with a typical dark current of 2–3 nA and a capacitance of about 50 pF, have been produced from 300 μm thick wafers.

Three different preamplifiers were used in the tests: those from Recom Ltd, Kurchatov Institute, Moscow, Russia and University of Bergen, Norway. The noise level for the preamplifiers was, in electron equivalents, ENC $\sim$ 600 e with a diode capacitance of 50 pF.

1997 electronics

At the end of 1996 it was decided to increase the sensitive area of the PIN photodiodes. An R&D programme has been carried out in the co-operation with the company AME (see Section 2.2.1). The area of the PIN-diode was increased by a factor of 2.72, to 1.6×1.7 cm^2.

In the fall 1997 sample PIN photodiodes with a large sensitive area (AE9724) were mounted on the AE9016 preamplifiers and were placed in metal shields of dimensions of $19.5\times19.5\times16$ mm^3. The PIN-diode was coupled to the crystal with the Meltmount Quick Stick optical glue, delivered by Cargille Labs, Cedar Grove, USA. This glue has the refraction index $n_{\mathrm{d}} = 1.704$ and the glue transmission spectrum matches the lead-tungstate crystal emission spectrum, as well as the PIN-diode quantum efficiency.

For the 1997 tests, there was substantial change in the preamplifier design. A surface-mounted preamplifier, integrated with a PIN photodiode on the same ceramic substrate, has been developed. The preamplifier with two JFETs in parallel on the input allows one to achieve the best possible noise level for PIN photodiodes with high input capacitance. The preamplifier has a power consumption of 150 mW compared to 220 mW in 1996. This is an important parameter for the PHOS because it is due to operate at -25°C.

Before the PIN photodiode was glued to the back side of the crystal, a test of the diodes and the preamplifiers was carried out. An ^{241}Am radioactive source was used to irradiate the PIN photodiodes. The width of the peak from the 59 keV gamma line was measured for each set of diode and preamplifier. The typical FWHM was between 6 and 10 keV.

After the preamplifier, the signals were transferred via coaxial cables of 2 metres length, to a shaping amplifier (shaper). The shaper was specially designed for the PHOS. A more complete description of the amplifier and shaper was given in Section 2.3.

The output signals were transferred from the shapers via long coaxial cables of 50 metres length, to the data acquisition system. The signals were digitized by means of peak-sensitive ADCs, these were AD811 (Ortec, Wilkinson type, 1mV resolution, 11-bit dynamical range), gated with a 5 μs strobe.

1998 electronics

For the 1998 tests new large-area PIN-photodiode-preamplifier units with improved topology were produced. For these units the typical FWHM of the ^{241}Am peak was 4–6 keV. Prior to the beam tests a series of electronic noise measurements were performed. The results of these measurements can be seen in Fig. 2.24 on page 40. The results indicate a 21% noise reduction for a temperature decrease of 45°C.

2.4.1.3 Beam test DAQ system

During the tests in 1996, the DAQ-system developed for the CERN WA98 [26] experiment was used. In the 1997 and 1998 tests, a specially developed DAQ-system for PHOS was used [27]. The main DAQ computer was running the CERN *Cascade* data acquisition system [28] adapted to the PHOS configuration.

All information was recorded on an event-by-event basis and written to the Exabyte tape for offline analysis.

The CAMAC modules were read via VME. A MVME147 VME crate processor, running the OS-9000 Real-Time kernel, was used for collecting all the events during one beam spill. The events were stored in two 256 Kbyte MVME201 memory modules and were read out by *Cascade* between the spills. The DAQ PC and the VMEbus were interconnected by a high-speed (200 Mbyte/s) SCI optical link. The length of the optical link was 10 m (100 m for some of the tests in the North Area).

The DAQ and slow control system is schematically shown in Fig. 2.30. The signals from the 64 preamplifiers (Section 2.3.2) of the PHOS matrix were fed to NIM shapers (Section 2.3.3). The CAMAC ADCs and registers were read out via a VME CBD 8210 CAMAC Branch driver.

The temperature of the matrix was continuosly monitored on a separate control PC.

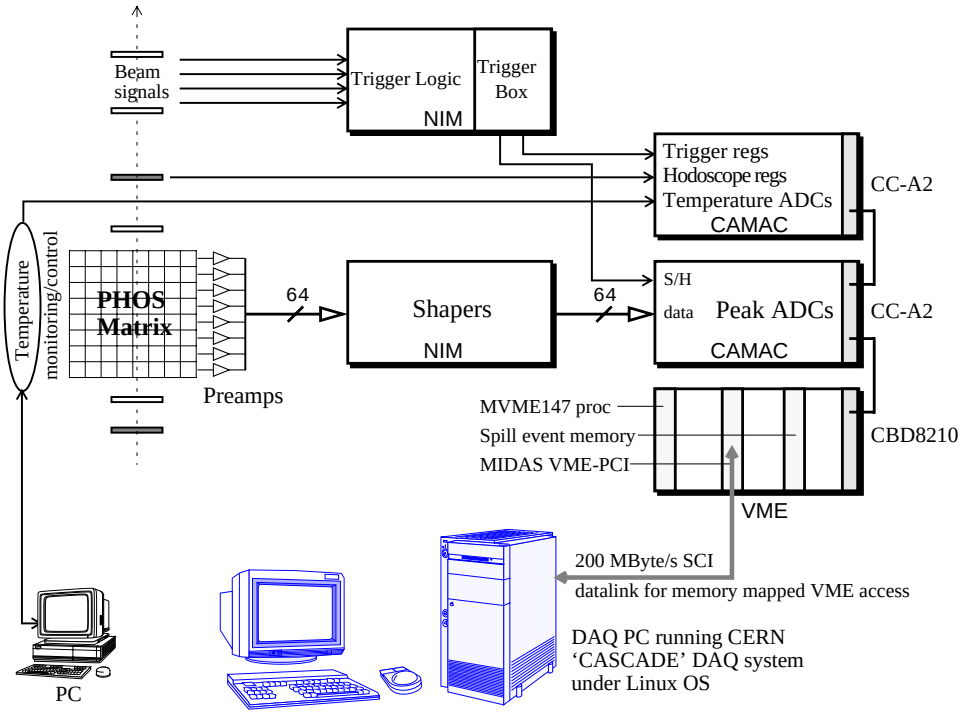

Figure 2.30: The DAQ system used in 1997–98 beam tests.

2.4.1.4 Cooling and temperature control

1996–1997

In 1996 and 1997 a common deep-freezer was used for cooling and thermostabilization. For monitoring temperature, seven T-sensors were glued with a thermoconductive glue to some of the tested crystals. These T-sensors were thermocouples calibrated with ice and boiling water. The change of the temperature in time was measured with a precision of $\sim 0.1^{\circ}$C. The peak-to-peak temperature fluctuations were typically of about 0.5°C in all measurement points. The temperature at the point near to the PIN-diode

was higher compared to the other points. The maximal temperature difference between the hottest and coldest points was less than 2°C.

1998

In 1998 a specially designed cooling and thermostabilization system was used for the PHOS prototype. Its detailed description is given in Section 3.3.1 of Chapter 3. A block diagram of the system is shown in Fig. 2.31. The tested prototype was placed inside a thermoinsulated container, which was cooled with a cooling liquid pumped through the Lauda Ultra Cryomate K90DW refrigerating machine. The temperature was monitored with 32 specially designed thermocouples of thickness of ~ 300 μm, installed at different positions in between the crystals. The relative errors of the temperature measurement were less than 0.05°C and the absolute ones were less than 0.2°C. The maximal temperature difference between the hottest and coldest points was less than 0.1°C.

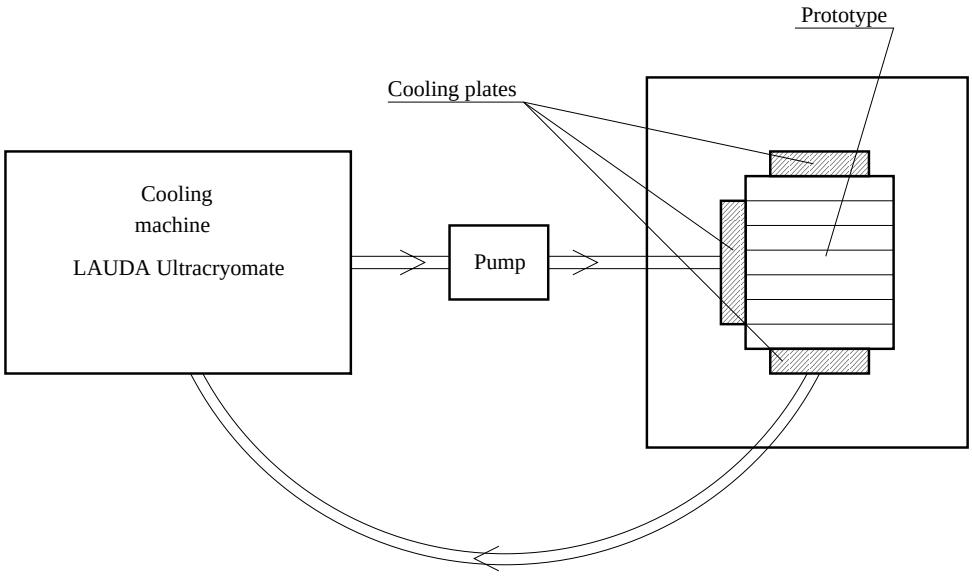

Figure 2.31: Block diagram of cooling and thermostabilization system.

2.4.2 The 1996 and 1997 beam tests.

The lead tungstate crystals of different lengths: 14, 16, 18 and 20 cm were tested in 1996 and 1997. All crystals had a cross-section of 22×22 mm^2.

The crystals were stacked in 3×3 or 5×5 arrays. The inactive material (Tyvek) was wrapped around the sides and the front. The effective thickness of the inactive material on the front sides of the crystals, which amounts to $\sim 0.1\%$ of the radiation length, would have just marginal influence at low incident energies, i.e. energy < 1 GeV, and can be neglected at higher energies. The gap between the stacked crystals was approximately 500 μm. The matrix was then placed into an aluminium light-tight thermoinsulated container. This container was installed in a deep-freezer and cooled down to -25°C.

A photo of the full 5×5 matrix can be seen in Fig. 2.32.

2.4.2.1 Experimental set-ups, beam-line counters and triggers

The 1996 beam tests were performed at the CERN SPS X1 beam line with electrons of energies from 3 up to 15 GeV. This beam line delivers almost pure electron beam, the content of hadrons in the electron beam is less than 0.5% for beams in the energy range 3–80 GeV. The beam intensity was $\sim 10^2$ electrons/spill at energy range 3–15 GeV. The momentum spread was of about 1%.

Figure 2.32: View of the 5×5 matrix, tested in 1997.

The 1997 beam tests were performed at the CERN PS T11 beam line with electrons of energies in a range of 0.4–2.2 GeV. This beam line delivers electrons, muons, protons and pions with energy ranging from 0.3 to 3.5 GeV. The beam intensity was up to 10^4 particles/spill during the spill length of 0.4 s with only a few per cent of electrons. The beam momentum spread was also of about 1%.

The experimental set-ups, trigger conditions and trigger counter set-ups were similar for both the SPS and PS tests. In Fig. 2.33 the layout of the 1997 PS beam test is shown. The freezer with the crystal matrix was installed on a remotely controlled X-Y moving platform. The matrix inclination angle could be changed by means of wedges to make measurements at different incident angles.

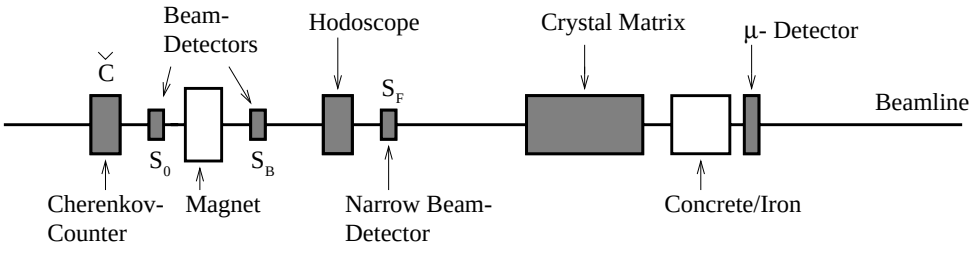

Particles from the PS accelerator
Energy=0-3 GeV

Trigger Combinations;

Beam= S_0 and S_B (s)

Electron= S_0 and S_B and $\check{C}$ and $\bar{\mu}$ (e)

Narrow Electron= S_0 and S_B and S_F and $\check{C}$ and $\bar{\mu}$ (ne)

Muon= S_0 and S_B and $\check{C}$ and μ (μ)

Narrow Muon = S_0 and S_B and S_F and $\check{C}$ and μ (nμ)

Hadron= S_0 and S_B and $\bar{C}$ and $\bar{\mu}$ (h)

Narrow Hadron = S_0 and S_B and S_F and $\bar{C}$ and $\bar{\mu}$ (nh)

Pulser= $\bar{e}$ and $\bar{\mu}$ and $\bar{h}$ and $\bar{s}$

Figure 2.33: Experimental set-up and trigger conditions for the PHOS 1997 PS test.

A series of thin scintillator beam counters and a Cherenkov counter were installed upstream of the crystal matrix. A *Narrow Beam* detector, S_f, was placed at 5 cm in front of the crystal matrix. The transverse size of this detector was 1.0×1.5 cm^2. The impact points of beam particles were measured with a 1.27 mm pitch scintillation hodoscope. Behind the crystal matrix an iron brick was situated in order to absorb possible charged particles passing through the crystals.

A list of possible triggers and the trigger logic can be seen in Fig. 2.33. To control the pedestals of the ADCs and the gains of the electronic chains, pulser and pedestal triggers were generated between the beam spill from the accelerator. In order to distribute the signal of a master pulser to all the preamplifiers, without introducing external cabling, a precision fan-out system was integrated in a separated block in close vicinity of the matrix.

2.4.2.2 Experimental details of the 1996, 1997 tests

Before the energy scan relative calibration was performed. Each detector was placed in the beam line and aligned with trigger counters. A calibration run with 5×10^3 events was performed. These events where taken with a narrow electron (*ne*) trigger at 5 GeV at the X1 beam and 1.6 GeV at the T11 beam. To speed up the relative calibration, the beam collimators were opened during the calibration runs. After the calibration the beam was centred on the central detector in the matrix and the energy scan was carried through. At the SPS the energy region for this scan was 3–15 GeV. At the PS the energy scan data were taken from 400 MeV to 2.2 GeV. During the energy scan runs the collimator slits were almost closed. Both the relative calibration and the energy scans were performed for each of the different sets of electronics, crystals and PIN-diodes that were tested.

2.4.2.3 Analysis of the experimental data

The analysis of the data starts with the relative calibration. A preliminary gain adjustment was achieved and calculated by means of the pulser signals in each detector (each crystal). After this procedure, the matrix was placed in the beam line and data were taken with the narrow electron (*ne*) trigger. The electron peak position was obtained for each detector from a Gaussian fit to the amplitude distribution. An example of such a fit is shown in Fig. 2.34, part C. The plots were filled only at narrow electron triggers, i.e. hit in the centre of the detector, which means a hit within the area of the S_f counter (1.0×1.5 cm^2). In addition to the narrow electron triggers, data were taken at pulser and pedestal triggers. The positions and the corresponding widths (σ_{ped} & σ_{puls}) of the pedestal and pulser signals were found. The electron peak positions, measured at the same energy in each detector, were then aligned relative to each other by introducing a set of intercalibration constants. These constants are calculated as ratios of the peak position in the central crystal to the peak positions in each crystal. Examples of single-module amplitude distributions are shown in Fig. 2.34, for 14 cm crystal length for different types of triggers. After the relative calibration, when all the detectors in the array were adjusted according to their relative gains compared with the central detector, the total energy deposited by the electromagnetic shower in the crystal(s) can be reconstructed. The deposited energy is reconstructed by summing the signals in the central 9 (3×3) crystals at each beam energy. An example of how the sum of the 9 central crystals is distributed, for electrons at beam energy 1 GeV, is shown in Fig. 2.34 D. The peak was fitted to a single Gaussian distribution, in the range of $\pm2\sigma$ around the peak position. Only one cut was applied on the data, the signal value should be greater then pedestal in order to be included in the summation of the signals in the 3×3 central crystals.

2.4.2.4 System stability

To check the stability of the system, the positions and widths (σ_{ped} & σ_{puls}) of the pedestal and pulser signals were checked throughout the data-taking periods. As an example, the value of the pedestal and

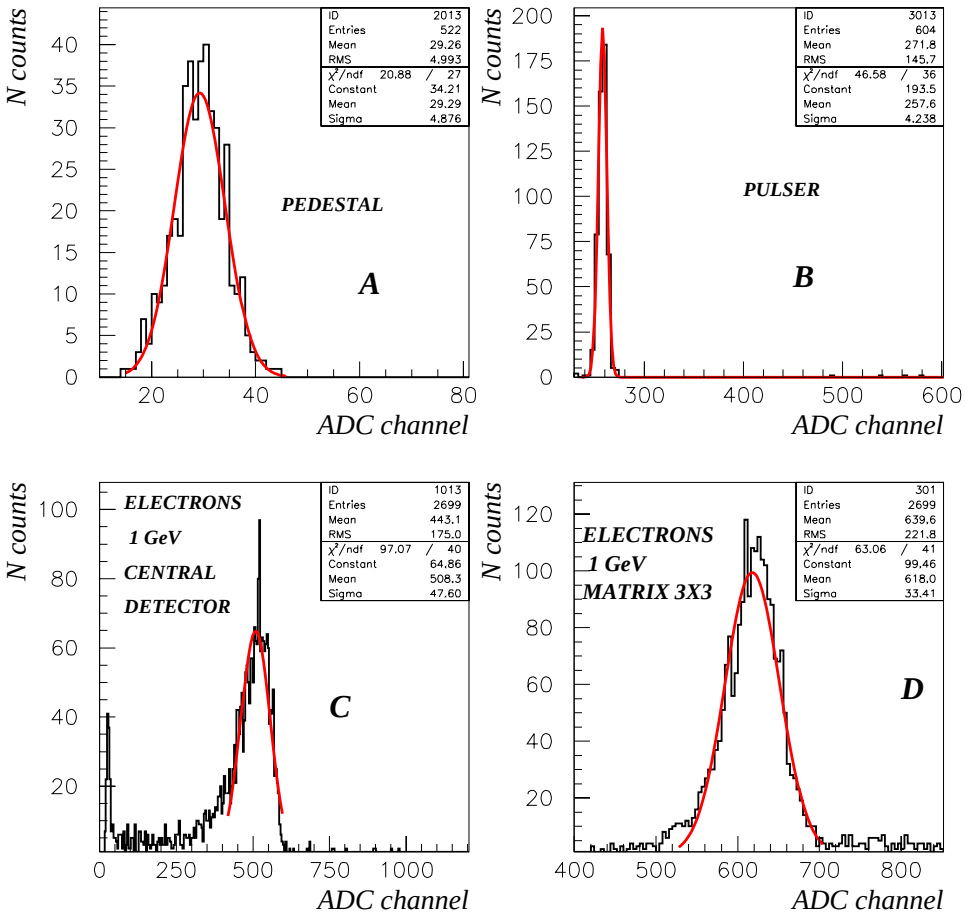

Figure 2.34: Examples of spectra, obtained during test with different kinds of triggers. A, B, C pedestal, pulser and narrow electron (*ne*) triggers for the central crystal in the matrix respectively; D sum over 3 × 3 crystals, *ne* trigger after relative calibration.

the pedestal width (σ_{ped}) for the central detector, during runs with 2.72 cm^2 PIN-diodes and 14 cm crystals, is shown in Fig. 2.35.

2.4.2.5 Energy resolution and linearity curves

The achieved linearity curve, i.e. the nominal beam energy versus the position of the peak, in ADC channels, is shown in Fig. 2.36.

As can be seen from this figure, the response of the $PbWO_4$ matrix in the energy range 0–2 GeV is linear. The results of the measurements up to 15 GeV also show the excellent linearity of the response of lead-tungstate crystals.

The energy resolution of an electromagnetic calorimeter can usually be parametrized as

$$\frac{\sigma_E}{E} = \sqrt{\left(\frac{b}{\sqrt{E}}\right)^2 + \left(\frac{a}{E}\right)^2 + c^2}\,, \tag{2.11}$$

where the energy E is in GeV, b represents the stochastic term, a represents the electronic noise and c represents the constant term. The stochastic term b takes into account the fluctuations in the electromagnetic showers and the variations due to photostatistics. The noise term a includes contributions from preamplifier noise, digitization noise and, in principle, pile-up noise, the latter was negligible in our tests.

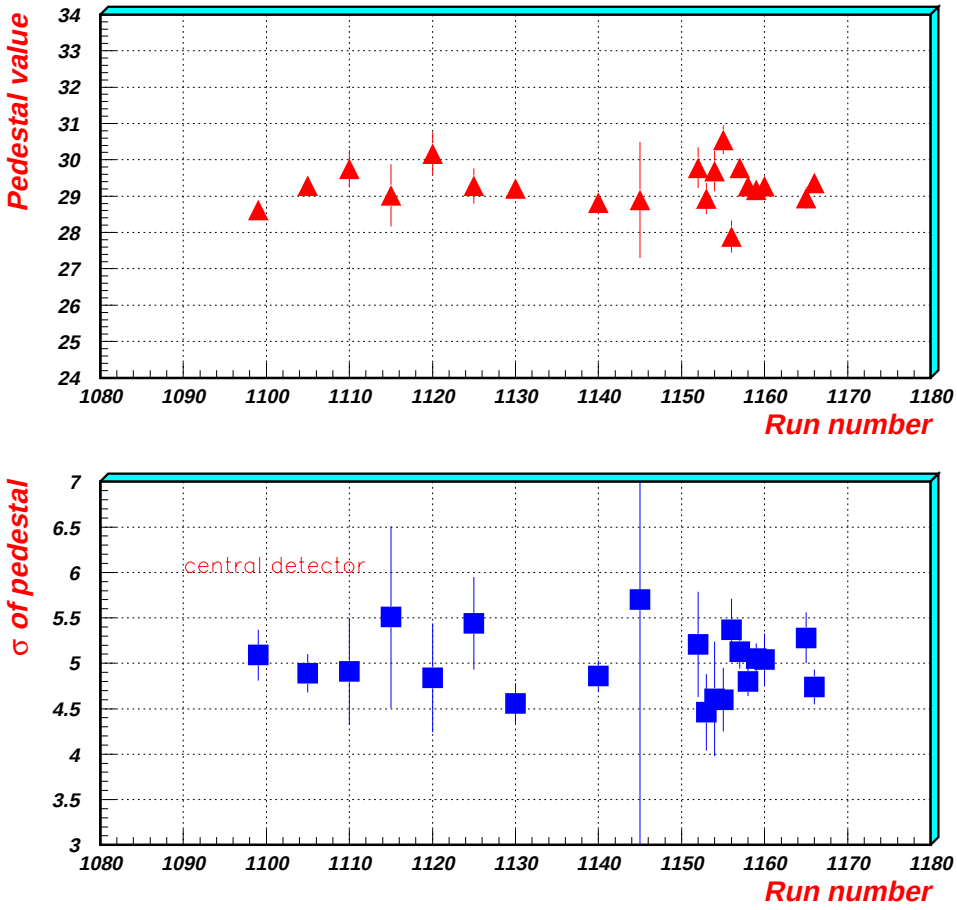

Figure 2.35: Pedestal position and width as function of run number. Sixty runs corresponds to approximately 60 hours of data taking.

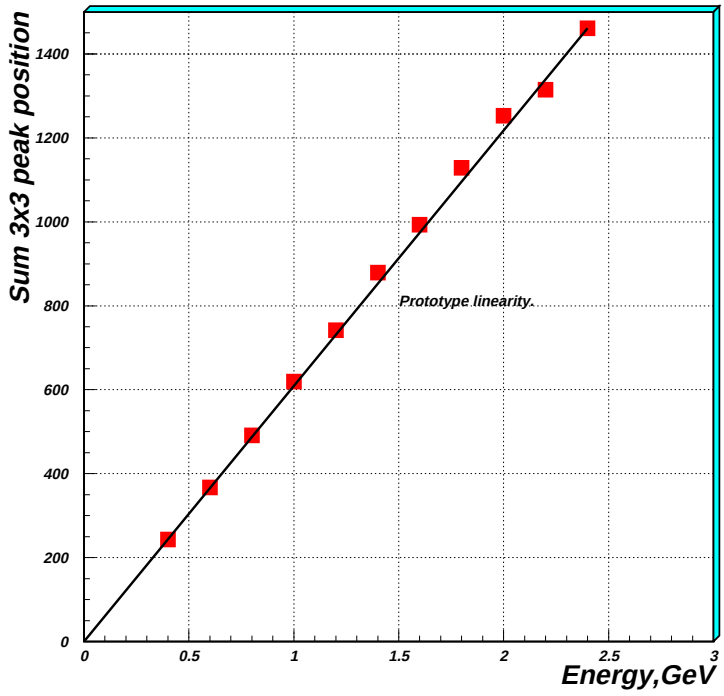

Figure 2.36: Linearity curve.

The constant term takes into account shower leakage at the back end of the crystals, intercalibration errors, non-uniformity in the light collection and geometrical effects. In colour Fig. VI the summary of our measured energy resolution is shown. No correction is done in order to adjust for the influence of the beam momentum spread. During the 1995 test, the influence of the electronic noise was the dominant factor. Because the number of measured points was small, the stochastic term was not found. In 1996 we improved the construction of the electronics and PIN-diodes and increased the number of measured points on the energy resolution curve. Fitting the 1996 measurements gives an equivalent noise term value of 66 MeV, and 0.033 and 0.01 for the stochastic and constant terms, respectively. A further inmprovement of electronic design and crystal quality in 1997 allowed us to achieve a noise term of 33 MeV. The statistical errors in the calculated terms are negligible. The noise term, a, can also be calculated independently from the fit of the energy resolution measurements; by means of a Gaussian fit to the distribution of the sum of the 3×3 central crystals at pedestal trigger the position and the width (σ_{ped}) were found. The gain factors for each detector were included here as well. The distribution was fitted with a Gaussian curve in the range of $\pm3\sigma_{ped}$ around peak position. An example of such a pedestal distribution and the fitted σ_{ped} are plotted vs. run number in Fig. 2.37.

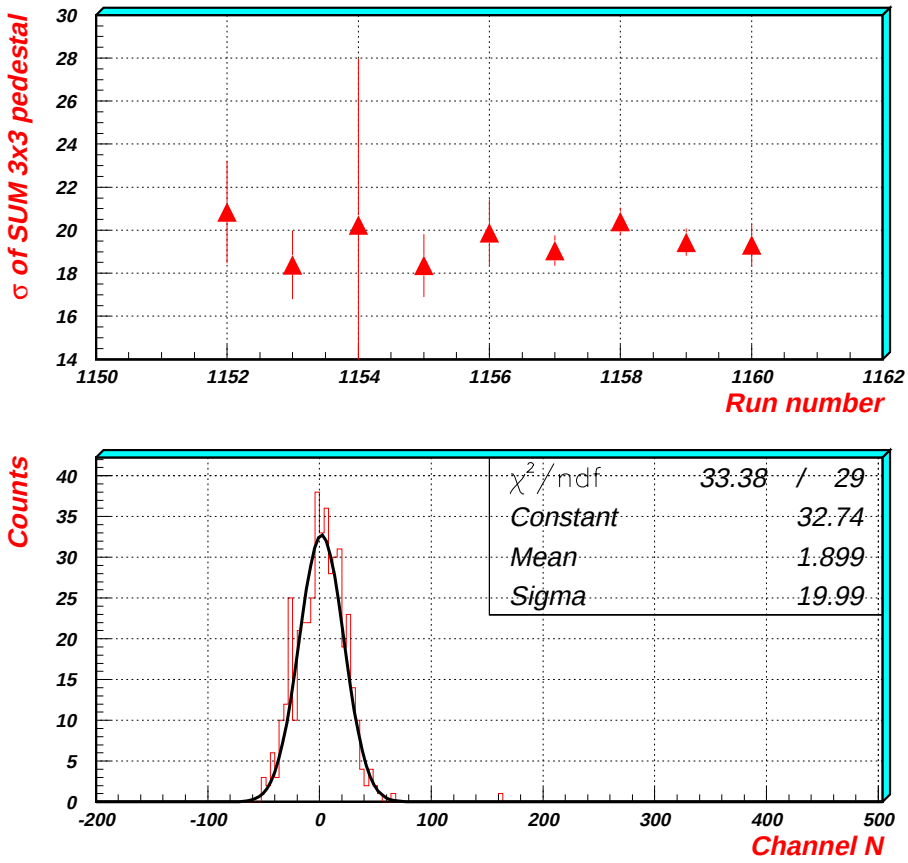

Figure 2.37: Pedestals for SUM 3×3.

The calculated σ_{ped} of this distribution is, as we see from Fig. 2.37 around 20 channels. This corresponds to $\approx$ 30 MeV and it is thus in agreement with the value $\approx$ 33 MeV, which was derived from the energy resolution curve fit.

The influence of pile-up and possible long time tails in the emission spectra of $PbWO_4$ on the noise term was investigated. The pedestals were taken during spill and between spills. The positions and width of pedestals are very similar in both cases. That gives a value for the uncorrelated noise level of 10–11 MeV/channel. (The same measurements was done during the 1998 test and we found a noise level of the order of 8–9 MeV/channel.)

The effect of the angle of incidence on the energy resolution for electrons was investigated in the tests as well. Data were taken with 0°, 3.5° and 8° angle between the axis perpendicular to the crystal surfaces and the axis of the beam line.

The data show that, at low energies, the optimal energy resolution was obtained with an angle of 3.5°. The improvement at 3.5°, at least compared to the energy resolution curves for 0° and 8°, is consistent with data from other experiments [23].

All data presented are not corrected for the beam dispersion and temperature variation during the beam tests (typically of about 0.5°C).

2.4.2.6 Cluster Size at different angles

The capability of particle identification in a finely granulated electromagnetic calorimeter is based on the finding that the lateral development of hadronic showers is different from that of electromagnetic ones [29]. Usually, a hadronic shower is wider and the energy is distributed over a larger number of detectors (crystals) compared to an electromagnetic one. Cuts in the shower width will thus allow one to distinguish between the different types of showers. Nonperpendicular incidence of particles on the detector surface will increase the number of involved crystals and will influence the shower width. The dependence of the electromagnetic cluster size on the angle of incidence for electrons with energies in the range from 0.4 GeV to 2 GeV has been studied. Mesurements were done for 0°, 3.5° and 8° angle of incidence. A comparision of 0° and 8° data is shown in Fig. 2.38 for 22 MeV (2σ) and 33 MeV (3σ) cuts. The data show that the number of fired detectors is only slightly increasing with increasing incident angle.

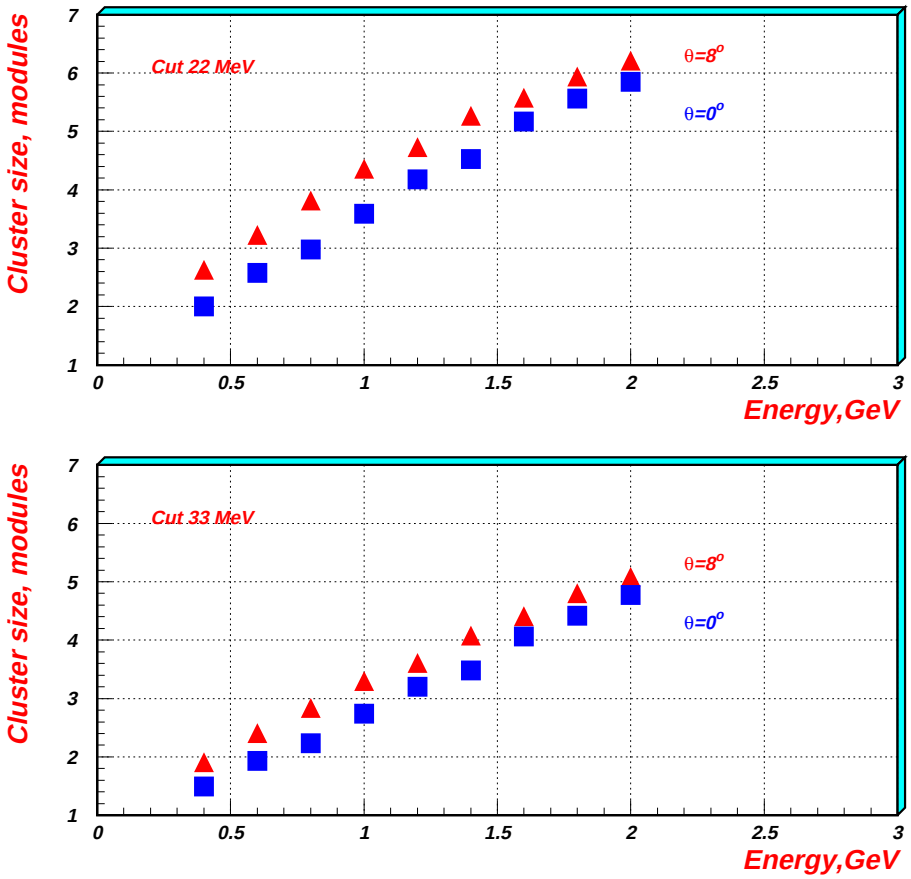

Figure 2.38: Electromagnetic cluster size for different energies.

2.4.2.7 Study of radiation hardness of the lead-tungstate crystals

Since the radiation load in the relatively low-luminosity ALICE experiment is by many orders of magnitude lower compared with the high-luminosity proton experiments (ATLAS and CMS), the requirement on the radiation hardness of the crystals is much softer as compared with that of the CMS experiment. However, during the 1997 PS tests, the influence of radiation doses from charged particles was estimated. For eight crystals the radiation dose accumulated during the tests was estimated to be ~ 3 Gy. It was observed that for this dose the light yield decrease is less than 1%, if any. Such a dose corresponds approximately to the estimated dose accumulated in ALICE during three years of operation.

2.4.3 The 1998 beam tests

In the very beginning of 1998, the mechanics, cooling and thermostabilization system of the 64-channel prototype were constructed. At the end of 1997, a new batch of lead-tungstate crystals of 18 cm length was delivered by BTCP and the AME AS company delivered 70 hybrid PIN-diode-preamplifier units by the summer of 1998.

Thus, the 64-channel prototype was constructed and tested in 1998. A photograph of the prototype can be seen in colour Fig. V.

2.4.3.1 The prototype description

The prototype comprises the basic components of the PHOS general structure as designed so far. A detailed description of the prototype will be given later in Chapter 3 (Section 3.3.2). The crystals are arranged in an 8×8 matrix. The basic assembly unit is a strip of eight detectors. Eight strips are attached to a cooling plate. An additional four cooling panels are mounted on the matrix, so that only the front side does not have a cooling panel. The design and performance of the prototype cooling and thermostabilization system are described in more details in Ref. [30]. Thirty-two thermocouples were installed inside the matrix volume to map the temperature field and to control its long-term stability. The ambient temperature was monitored as well. During the tests temperature variations of the order of 10°C were observed in the experimental test area and at the same time the long-term stability of the temperatures inside the prototype was $\sim 0.6^{\circ}$C. On the other hand, the temperature difference between the hottest and the coldest points inside the prototype was less than 0.1°C.

2.4.3.2 Experimental set-ups, beam-line counters and triggers

The 1998 beam tests were performed at beam lines T10 and T11 of the CERN PS and also at beam line H6 of the CERN SPS. The T10 beam line provides electrons, muons, protons and pions within the momentum rage of 1–7 GeV/c. The beam intensity was up to 10^4 particles/spill. The momentum spread of the beam was of about 0.5–1%.

The experimental set-ups were similar for both the SPS and PS tests. A photograph of the T10 layout is shown in Fig. 2.39. The prototype can be seen in the middle of the bottom part of the photo.

A block diagram of the T10 test experiment is shown in Fig. 2.40. The prototype was installed on a remotely controlled moving platform. A series of thin scintillation beam counters and two Cherenkov counters were installed upstream of the prototype. The *Narrow Beam* detector, S_f, with the transverse dimensions of 1.0×1.0 cm^2, was placed in front of the prototype. The incidence coordinates of beam particles were measured with a 1.27 mm pitch scintillation hodoscope, which has a spatial resolution of ~ 400 μm. Behind the prototype an iron block was installed to absorb the charged particles which passed through the crystals.

The H6 CERN SPS beam line test set-up is shown in Fig. 2.41 and includes the same set of scintillation counters. Instead of the threshold Cherenkov counter, a differential Cherenkov counter, CEDAR,

Figure 2.39: Photography of T10 test layout.

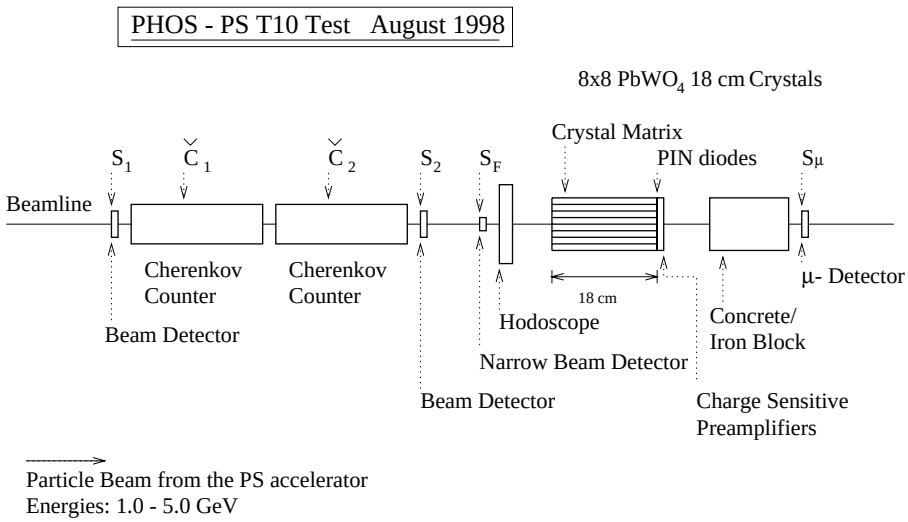

Figure 2.40: Diagram of the T10 set-up.

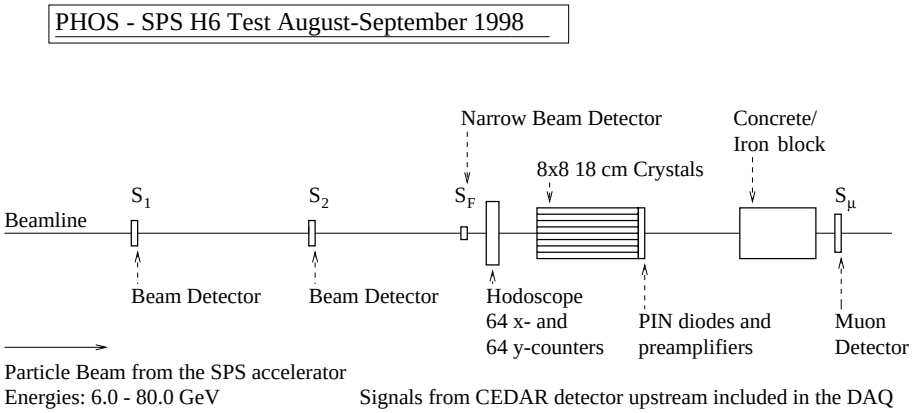

Figure 2.41: The experimental set-up for the PHOS SPS H6 Test August–September 1998.

was used at the H6 beam line. For all tests the trigger conditions were similar to those of the previous year's tests (see Fig. 2.33 on page 48).

2.4.3.3 Calibration

A preliminary gain adjustment was achieved by means of pulser signals in each detector of the prototype. Electronic gains were adjusted to obtain the same response to the pulser signals for all 64 channels. After this procedure, the prototype was exposed to the narrow electron beam. The electron peak position was obtained for each detector from a Gaussian fit of the amplitude distribution and the relative gain factors were calculated for all detectors.

2.4.3.4 Measurement of the temperature dependence of the light yield

In the course of cooling, the temperature dependence of the light yield was measured for four crystals, with electrons of an energy of 2 GeV. The results of this measurement are shown in Fig. 2.13 on page 31. In the same figure is shown the crystal light-yield temperature dependence measured earlier with the ^{22}Na radioactive source test bench (see Section 2.1.2). The beam data are in a good agreeement with the test bench measurement.

2.4.3.5 Position resolution

The coordinates of the incident particles were measured with high precision using the scintillation hodoscope. On the other hand, these coordinates were independently reconstructed in the analysis of the data obtained with the crystal matrix. Thus, by comparing the true coordinates as measured by the hodoscope with the reconstructed ones as obtained in the analysis, one can find the position resolution of the crystal matrix. The result is reported in Fig. 2.42. In the top figure the distribution of the difference

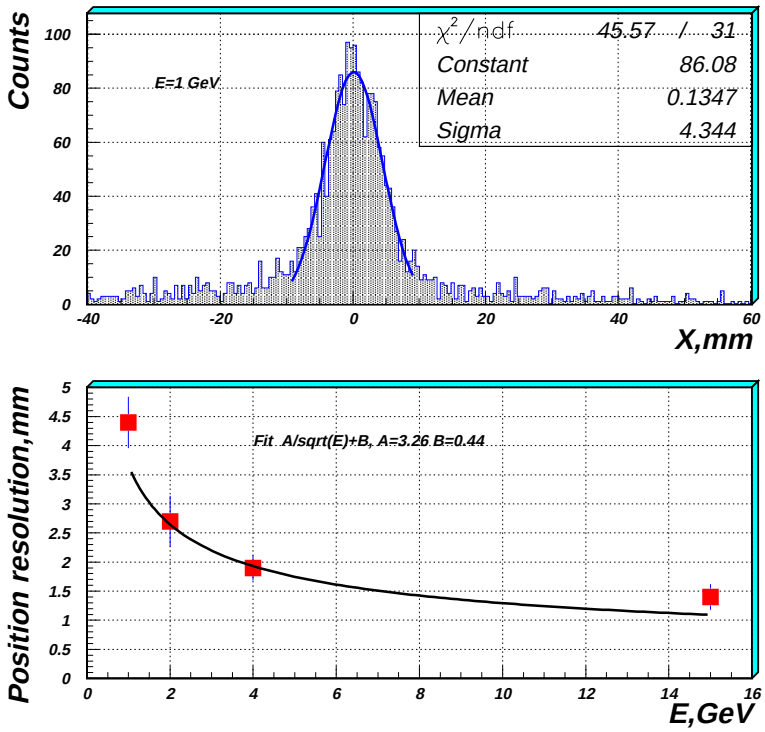

Figure 2.42: Position resolution.

between the true and reconstructed x-coordinate is shown together with the parameters of the Gaussian fit to this distribution.

In the bottom figure the σ parameter of the Gaussian fit is plotted vs. the electron beam energy. The dependence of the position resolution on the energy can be parametrized with the following formula:

$$\sigma = \frac{A}{\sqrt{E}} + B\,, \tag{2.12}$$

where the energy E is in GeV. The resulting fit curve is also shown in the bottom of Fig. 2.42, as well as the fit parameters.

2.4.3.6 The shower profile

One of the most important stages in the analysis of the data obtained with a finely granulated electromagnetic calorimeter is the reconstruction of photons from the detected showers. In particular, overlapping showers must be disentangled. The reconstruction procedure is based on the knowledge (see Chapter 4) of the photon shower profile.

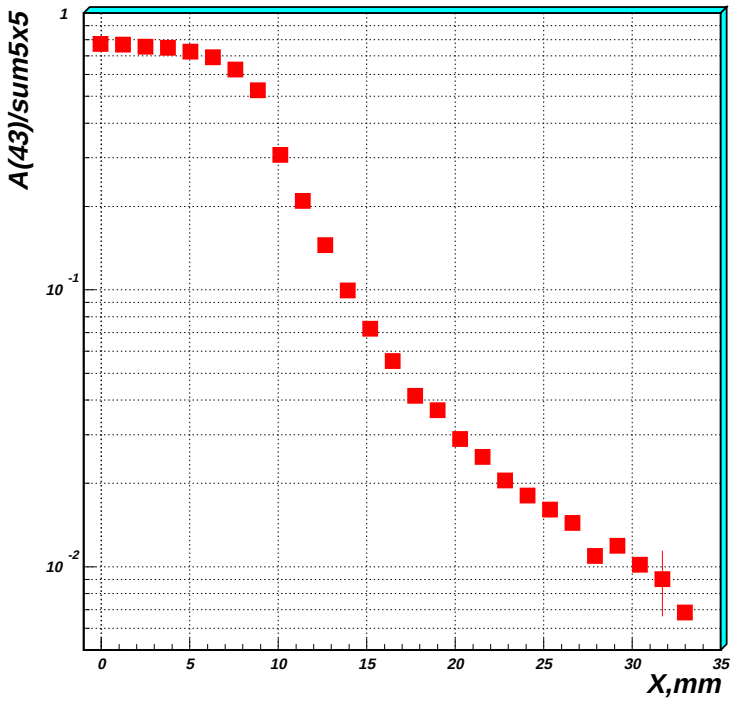

Figure 2.43: Shower profile for 15 GeV/c electrons.

Therefore, the 15 GeV/c electron shower profile has been determined using the 1998 SPS test data. It is shown in Fig. 2.43. It was observed that the result of GEANT simulation is in a good agreement with the experimental result (see Fig. 4.5 on page 119).

2.4.3.7 Energy resolution

After the calibration of the prototype, the energy scan was performed for 15 different zones of the crystal matrix, so that the beam was centred on different detectors in the prototype.

The energy resolution at different energies was determined from a Gaussian fit to the electron peaks obtained by summation of the gain corrected signals in the crystals of the 3×3 matrix around a given central detector. The distribution of the energy resolution values obtained for 15 different 3×3 crystal

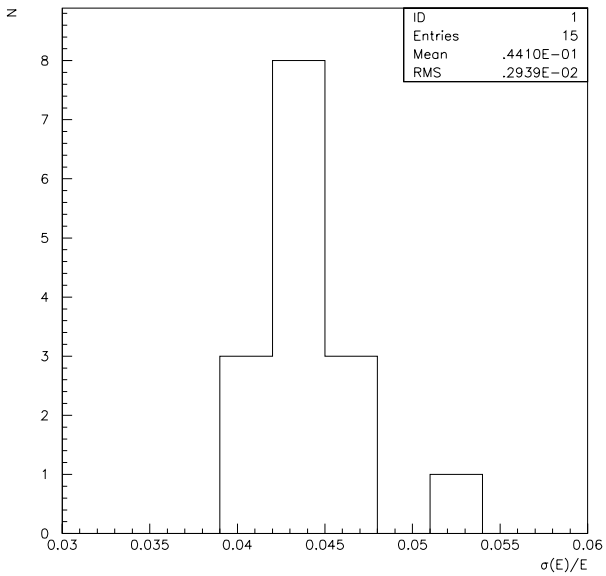

Figure 2.44: The distribution of energy resolution of 15 different matrix 3×3 inside 8×8 prototype. Data collected in the PS T10 beam line, with a 1 GeV electron beam.

arrays at an electron energy of 1 GeV is shown in Fig. 2.44. This plot demonstrates that the crystals are rather uniform, 14 out of 15 sample crystals having an energy resolution better than 4.8% at 1 GeV. The average value of the energy resolution at this energy is $4.4 \pm 0.3\%$, which meets the ALICE requirement. In colour Fig. VI the results of the 1998 energy resolution measurements at different energies are shown in comparison with the previous results. As one can see, the experimental points are very close to the curve which was aimed at in the Technical Proposal [1].

2.4.3.8 Study of the punch-through effect

PIN-diodes, which are proposed as photodetectors, have the disadvantage that they are sensitive not only to optical photons, but also to charged particles. Therefore, the electrons and gammas in an electromagnetic shower leaking through the rear end of the crystal can reach the sensitive volume of the PIN-diode and generate an electrical signal (punch-through or nuclear counting effect), which may worsen the energy resolution. A preliminary study of the significance of this effect was performed: a 18 cm long single crystal was exposed to 1, 2, 3 and 10 GeV electron beams at the T10 CERN PS beam line (the first three energies) and also at the H6 CERN SPS beam line (the last energy). The amplitude spectra obtained in this test are shown in Fig. 2.45. Some high-energy tails are visible at all energies. They might be explained partially by the punch-through effect and partially by muons and hadrons from the beam that were not completely rejected due to the trigger inefficiency. However, even at 10 GeV the tail is still acceptably small.

2.5 Prototype of the Control Module of the LED Monitoring System

2.5.1 Laboratory test

A prototype of the electronic control module of the PHOS LED monitoring system was designed and constructed. A block diagram for one LED channel is shown in Fig. 3.27 on page 96. The prototype includes two LED channels.

A laboratory test of the prototype has been performed with the aim of testing the stability of the LED light flash, as well as the ageing effect of the LEDs. The two LEDs were placed in front of two lead-

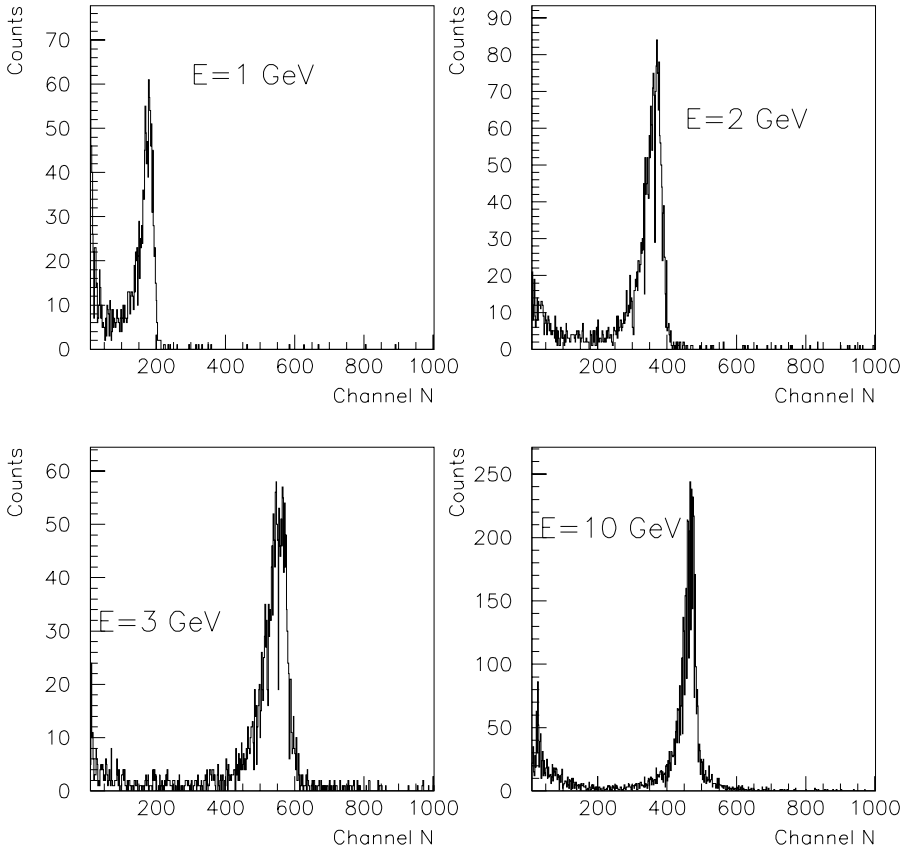

Figure 2.45: Single crystal spectra at different energies.

tungstate crystals. Behind each crystal a photodetector, which consisted of a PIN-diode, a preamplifier and a shaper, was mounted.

The output signal amplitudes were measured with charge-sensitive 12-bit ADCs based on the chip MQT200. The amplitude spectra were recorded every minute for a period of four weeks. For each spectrum 500 LED flashes were accumulated at a fixed flash rate.

In Fig. 2.46 a typical spectrum of the flashes of one of the two LEDs is shown as measured by the

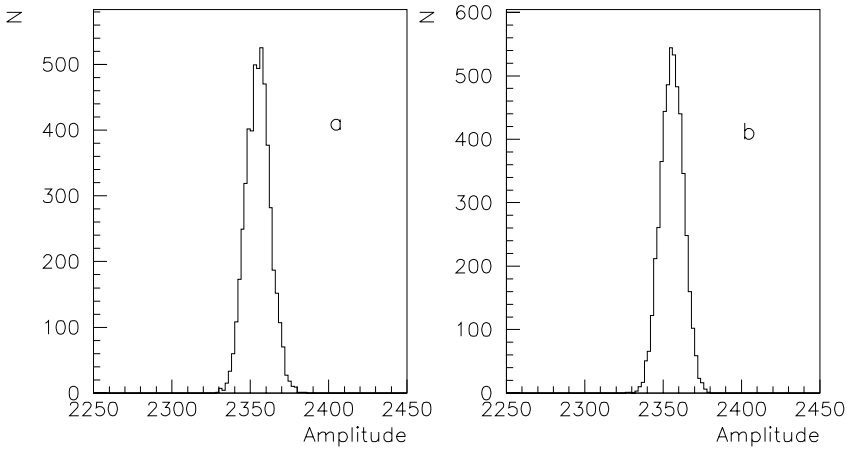

Figure 2.46: Amplitude spectra in one PHOS channel from a series of LED flashes separated by four hours: a) typical amplitude spectrum, b) the same spectrum after four hours.

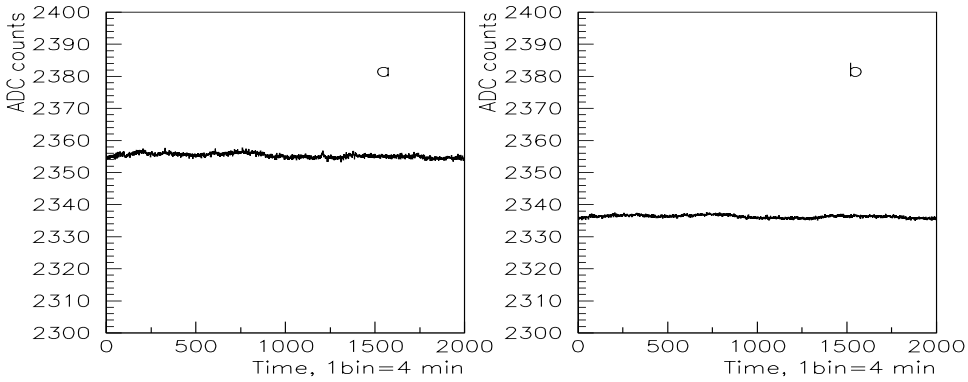

Figure 2.47: Time stability of two PINs irradiated by the same LED, 1 bin = 4 min.

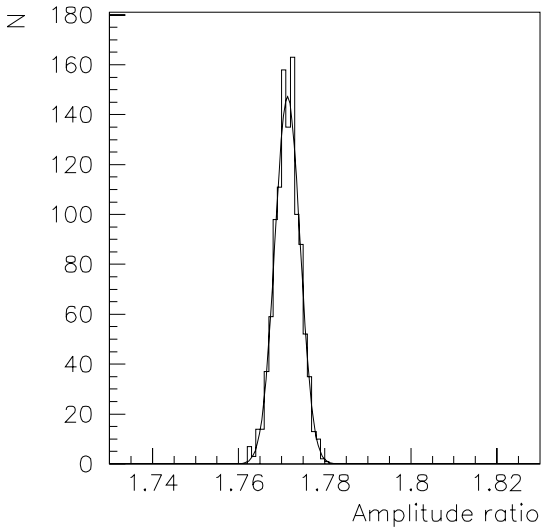

Figure 2.48: Ratio of amplitudes for two PHOS channels irradiated by different LEDs R = Amp(LED_1+PIN_1)/Amp(LED_2+PIN_2) during four days; the solid curve is a Gaussian fit with $\sigma_R/R = 1.5 \times 10^{-3}$.

photodetector. In Fig. 2.47 the result is shown of the stability measurements for the two LED channels carried out during four days, whereas in Fig. 2.48 the distribution of ratios of the amplitudes of these two channels (irradated by two different LEDs) is presented. It can be concluded that the stability of the LED flashes is of the order of 10^{-3}.

No ageing effect was observed for $\sim 10^8$ LED on/off switches.

2.6 CPV Prototype

A prototype of the Charged Particle Veto (CPV) detector was designed and tested at the CERN PS in the autumn of 1998.

2.6.1 Design of the prototype

The prototype is a plane structure of dimensions 18×18 cm^2 filled with eight proportional tubes with a cathode pad readout and GASSIPLEX chips [31] as front-end electronics. For more details see the engineering design in Fig. 2.49.

The cross-section (relative to the anode wires) of each tube is of a rhombic, almost square, shape. The wire pitch is 2.2 cm. The cathode pads are of the same transversal dimensions, of 2.2×2.2 cm^2, as

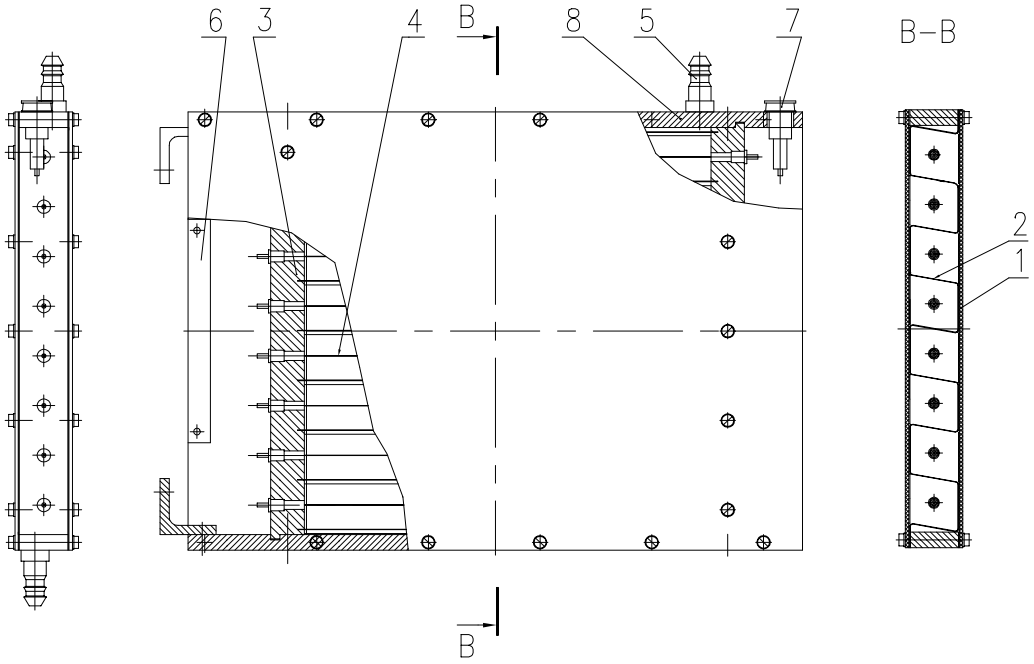

Figure 2.49: The CPV prototype.

the crystals of the PHOS.

The anode wires are of 50 μm diameter, the anode-cathode distance D is 1.1 cm. A gas mixture of 80% Ar + 20% CO_2 is used in the prototype.

2.6.2 Test results

The test of the CPV prototype was performed in September–October 1998 at the T10 and T11 PS beam lines with different particles (electrons, muons and hadrons) in a momentum range of 1–10 GeV/c.

The experimental set-up included scintillation and Cherenkov counters, as well as coordinate detectors: at the T10 beam line, 10 panels of Microstrip Silicon Detectors (MSD) with a strip pitch of 50 μm and a cross-section of 2×2 cm^2 and at the T11 beam line a scintillation hodoscope with plastic sticks of 1 mm width and a cross-section of 6.4×6.4 cm^2.

The CPV was placed perpendicular to the beam direction so that the anode wires were horizontally oriented. This direction was defined as the X-axis and the vertical direction was defined as the Y-axis.

The signals from the cathode pads were amplified by GASSIPLEX chips, then transferred to ADCs and the digitized data were stored on the DAQ computer disk.

2.6.2.1 The amplitude spectra and clusters

A minimum-ionizing particle produced signals in several pads which are grouped into a cluster elongated along the wires. Figure 2.50 shows typical spectra of the pad signal amplitudes at high voltage of 2050 V: in the left (a) for the pads of the maximal amplitude in a given cluster (the main pads) and in the right (b) for the adjacent pads.

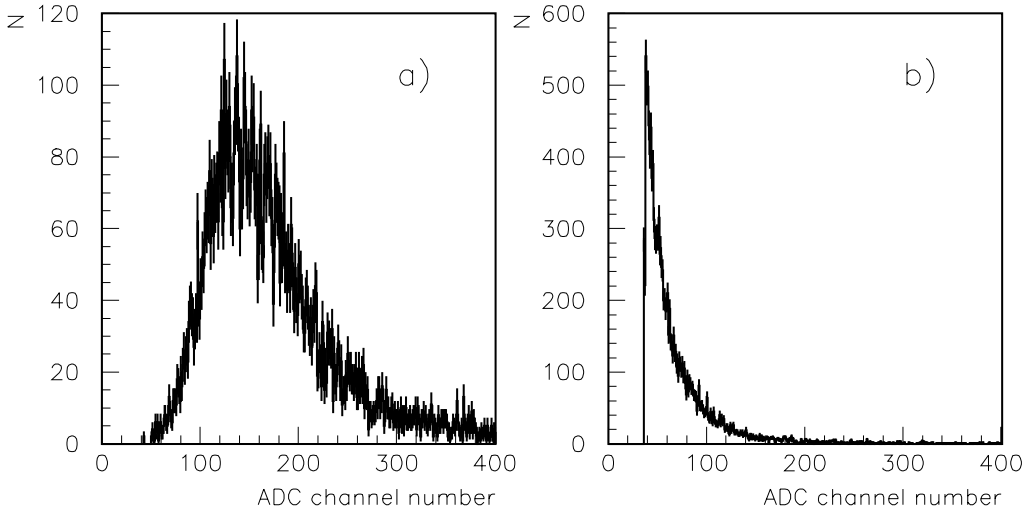

Figure 2.50: Amplitude spectra of the signals from the CPV cathode pads. Part (a) of the figure presents the results for the main pad with maximal amplitude in the registered cluster elongated along the anode wire direction; part (b) shows the analogous distribution for neighbouring pads (relative to the main pad) in the same cluster. The high voltage was 2050 V.

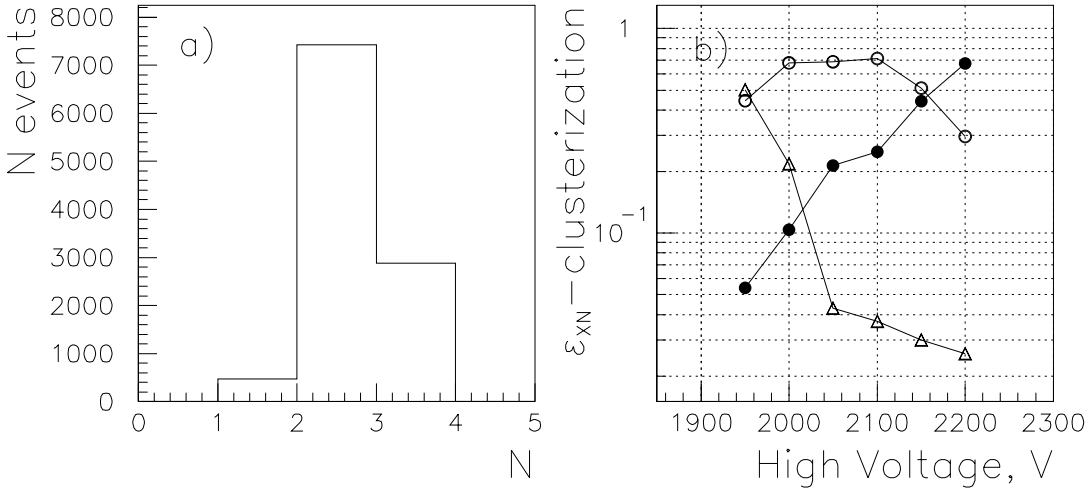

Figure 2.51: Cluster size distribution in pad numbers N along the wire direction at high voltage 2050 V (a), and dependence of the contribution ε_{XN} of the clusters with given N into the total sample on the high voltage applied (b); here triangles, circles and black points represent data for clusters with $N = 1$, $N = 2$ and $N = 3$ respectively.

The number of pads in one cluster (the cluster size, N) in most cases is between one and three. The percentage of the clusters of a given size depends on the high voltage. Figure 2.51 shows the cluster size distribution at 2050 V (a) and its dependence on high voltage (b).

As can be seen from the figure, the percentage of the clusters with $N > 1$ is increasing with high voltage and at 2050 V the relative number of one-pad clusters is less than 4%.

2.6.2.2 Charged particle detection efficiency

The result of the CPV prototype efficiency measurements are shown in Fig. 2.52, where the efficiency is plotted vs. high voltage. It is increasing with high voltage in a range of 1950–2000 V and then a plateau is observed at a level of $\varepsilon \simeq 0.99 \pm 0.016$.

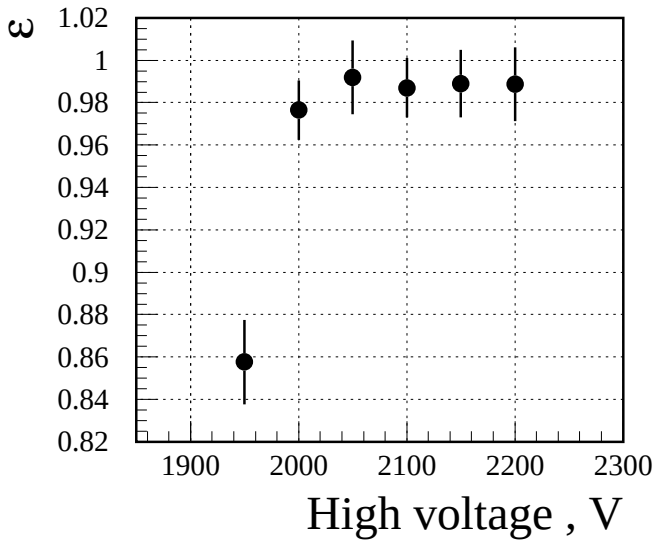

Figure 2.52: Charged particle detection efficiency in the CPV prototype as a function of the high voltage applied.

2.6.2.3 Position resolution

The position of an incident particle is to be determined by using a reconstruction procedure. The test data were used to determine the parameters needed for calculation of the pad response function used in the reconstruction procedure (for more details see Ref. [32]).

The coordinates of incident particles were measured with high precision using the beam-line coordinate detectors (MSD or the scintillation hodoscope). On the other hand, their x-coordinate (along the wires) were independently reconstructed in an analysis of the data obtained with the CPV detector. Thus, by comparing the true x-coordinate as measured by the coordinate detector and the reconstructed coordinate, one can find the position resolution of the CPV in the x-direction.

Figure 2.53 shows a scatter plot of the true (as measured with MSD) vs. reconstructed x-coordinate (a) and also the distribution of the difference between them (b) at 2050 V. A Gaussian fit to the latter distribution gives $\sigma_x = 1.25$ mm.

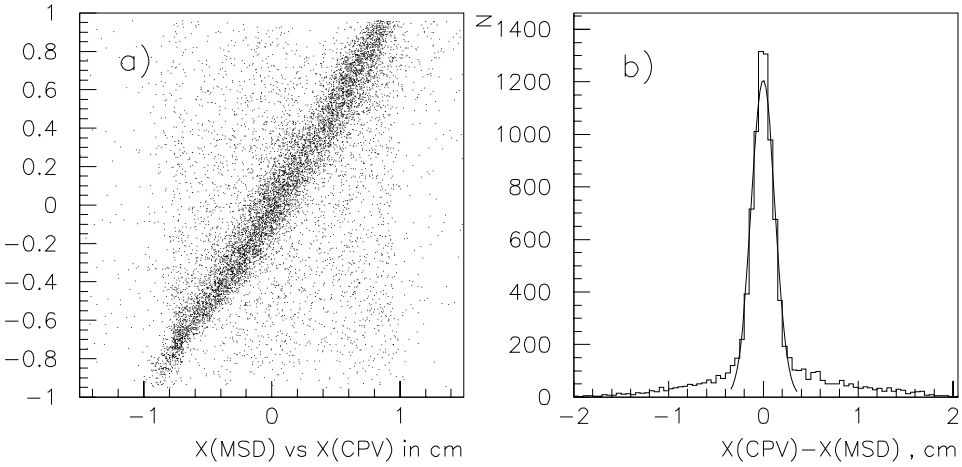

Figure 2.53: Correlation between measured x-coordinates of the hits for charged particles in the CPV and in the Microstrip Silicon Detector (MSD) (a) and distribution of the difference between the x-coordinate determined in the CPV and in the MSD (b); the solid curve represents the fit of the experimental data by a Gaussian distribution corresponding to $\sigma_x = 0.125$ cm. The high voltage was 2050 V.

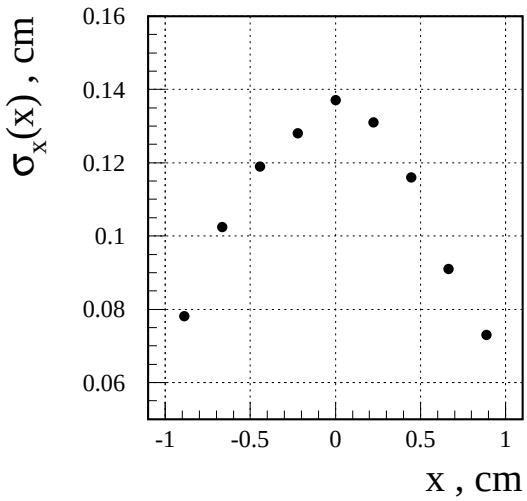

Figure 2.54: Dependence of the CPV spatial resolution σ_x on the *x*-coordinate of the charged particle hit on the pad plane. Here the local system coordinate is used with origin in the geometrical centre of the analysed pad. The high voltage was 2050 V.

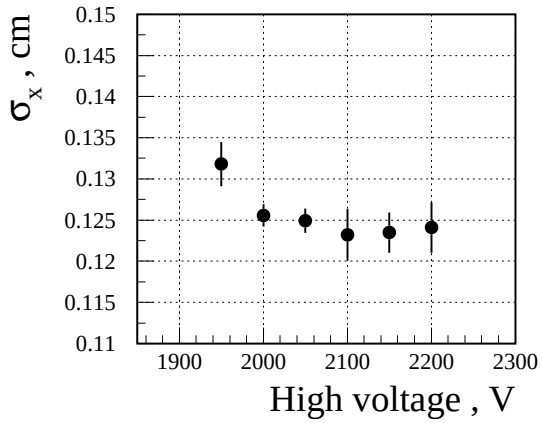

Figure 2.55: Dependence of the CPV spatial resolution σ_x on the high voltage applied.

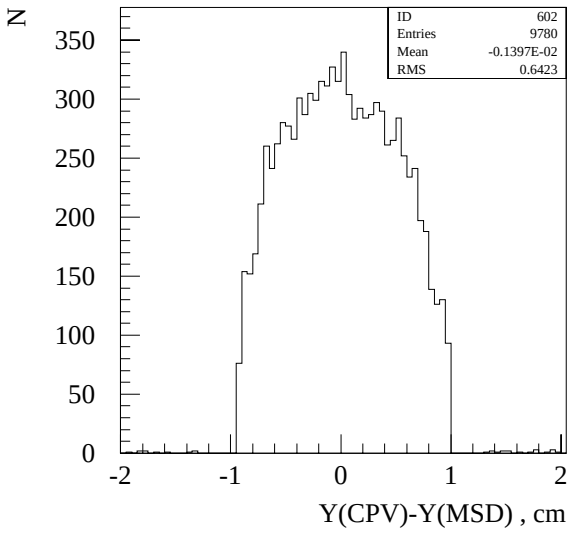

Figure 2.56: Distribution of the difference between the *y*-coordinates determined in the CPV and MSD. The high voltage was 2050 V.

The position resolution depends on the hit position relative to the main pad centre, as demonstrated in Fig. 2.54. It only slightly depends on high voltage, as shown in Fig. 2.55.

In Fig. 2.56 is shown the distribution of the differences between the true (MSD) and reconstructed (CPV) *y*-coordinates. The dispersion of the distribution, which has a value of 6.4 mm, is in a good agreement with the expectation for the *y*-position resolution ($22\ \text{mm}/\sqrt{12}$).

3 Description of the PHOS detector

Introduction

PHOS (PHOton Spectrometer) is a highly granulated electromagnetic calorimeter with 17280 detecting channels of lead tungstate crystals of 2.2×2.2 cm^2 cross-section, coupled to large area PIN-diodes with low noise preamplifiers.

It will be positioned on the bottom of the ALICE set-up, and cover approximately one quarter of a unit in pseudorapidity, $-0.12 \leq \eta \leq 0.12$, and 100° in azimuthal angle φ. Its total area will be ~ 8 m^2, the total crystal volume will be ~ 1.5 m^3 and the weight ~ 12.5 t.

The PHOS electromagnetic calorimeter consists of four independent units, named *PHOS modules*, each with 4320 detecting channels. A module is assembled from detector blocks (*crystal strip units*). Each strip consists of eight *crystal detector units.*

In order to reach the required energy resolution for the PHOS detector, the following conditions must be met:

- Crystals should have a high light yield. To achieve this the crystals will be operated at -25°C with a stability of $\pm 0.3^\circ$C. The temperature homogenity over the volume of the crystal will be better than 1°C;
- The ENC noise in the PIN photodiode unit should be less than 600 e$^-$;
- As shown by simulation studies the dead zones (gaps) between neighbouring crystals should not exceed 0.6 mm;
- The material in front of the detector must not exceed 5 % of a radiation length, which is equivalent to 4 mm of aluminium.

This chapter describes the individual elements and the integrated structure of the PHOS detector.

3.1 General mechanical structure

3.1.1 Crystal detector unit and strip unit

The crystal detector unit consists of one $PbWO_4$ crystal of 22×22 mm^2 cross-section and 180 mm length. The crystal is mounted with its front face oriented towards the interaction point. The showers of charged particles developed in the crystal by high-energy radiation are converted into scintillation light detected by a photodetector. The photodetector consists of a PIN photodiode integrated with a preamplifier in a common body glued onto the end face of the crystal with optically transparent glue.

As stated in Section 2.2.2.1 on page 35, an improved structure of the PIN photodiode-preamplifier assembly is now under study, and will be used in the PHOS detector. The photodiode itself will be better protected by means of a ceramic frame. The preamplifier will be attached directly to the rear of the frame. This arrangement is shown in Fig. 3.1. (The mounting will be the same if the *Va_1chan* preamplifier chip is used, see Section 2.3.5 on page 43).

The PIN photodiode is mounted on a ceramic substrate 0.65 mm thick. On this substrate the photodiode is surrounded by a ceramic frame with outer dimensions 19.5×19.5 mm^2. The frame is 0.5 mm high and 1.1 mm wide. The photodiode and bondings to ground and the preamplifer input are protected by an optical transparent epoxy layer. The preamplifier is mounted directly on the rear of the frame, using SMD technology. Power, bias voltage and the output of the preamplifier go through the connector P1.

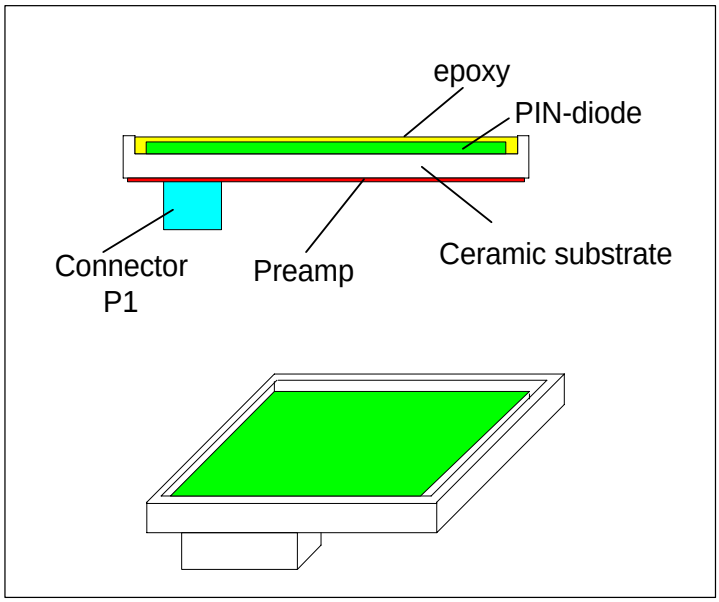

Figure 3.1: Mechanical mounting of PIN photodiode and preamplifier.

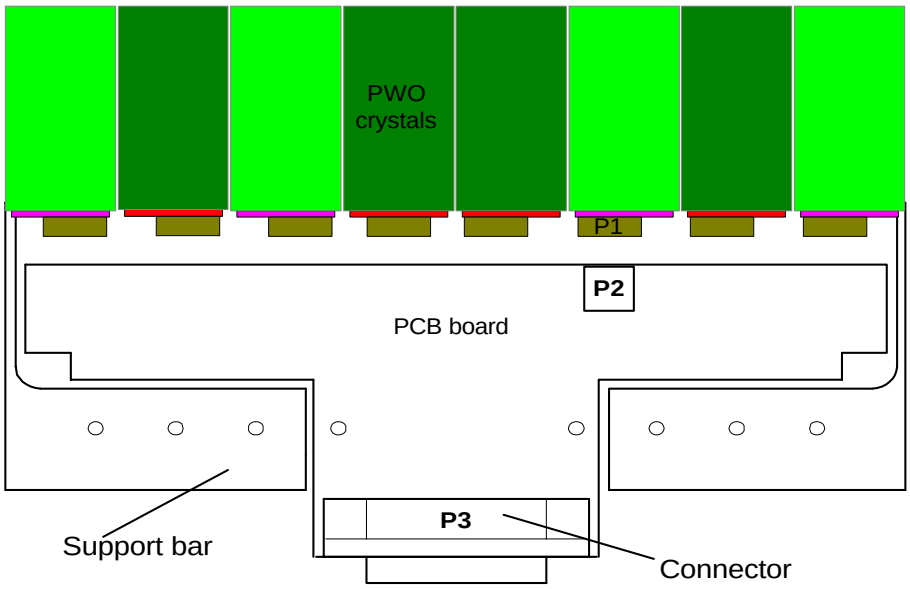

Figure 3.2: Mounting and electrical connections for a strip of eight crystals.

Figures 3.2 and 3.3 show the assembly and electrical connections for a strip unit of eight crystals. The PIN photodiode-preamplifier assembly is glued to the crystal and connected to an 8-unit PCB via the connectors P1 and P2 with a 40 mm long cable. The interconnection to the external electronics is routed on the 8-unit PCB from the P2 connectors to the P3 connector. P3 also provides connections for bias voltage, power, and temperature sensors.

A $PbWO_4$ crystal in assembly with a PIN photodiode, wrapped in paper, forms the basic *crystal detector unit*, from which the PHOS detector is constructed (see Fig. 3.4). The crystal detector units are placed in a thermally-insulated casing, cooled down to the operating temperature.

The crystal pitch is 22.6 mm, which includes the wrapping and attachment marked COVER in

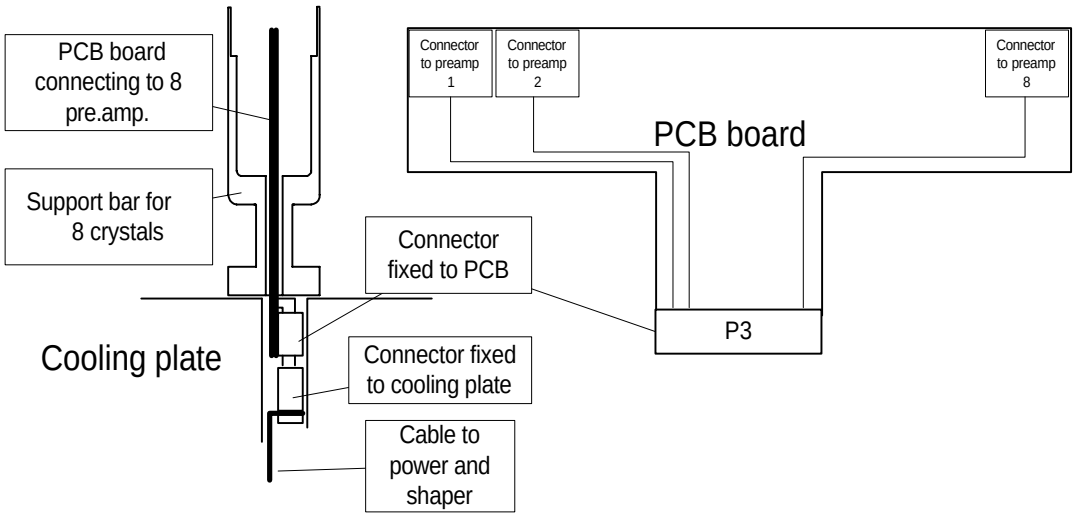

Figure 3.3: Mechanical details for the electrical assembly of a strip of eight crystals.

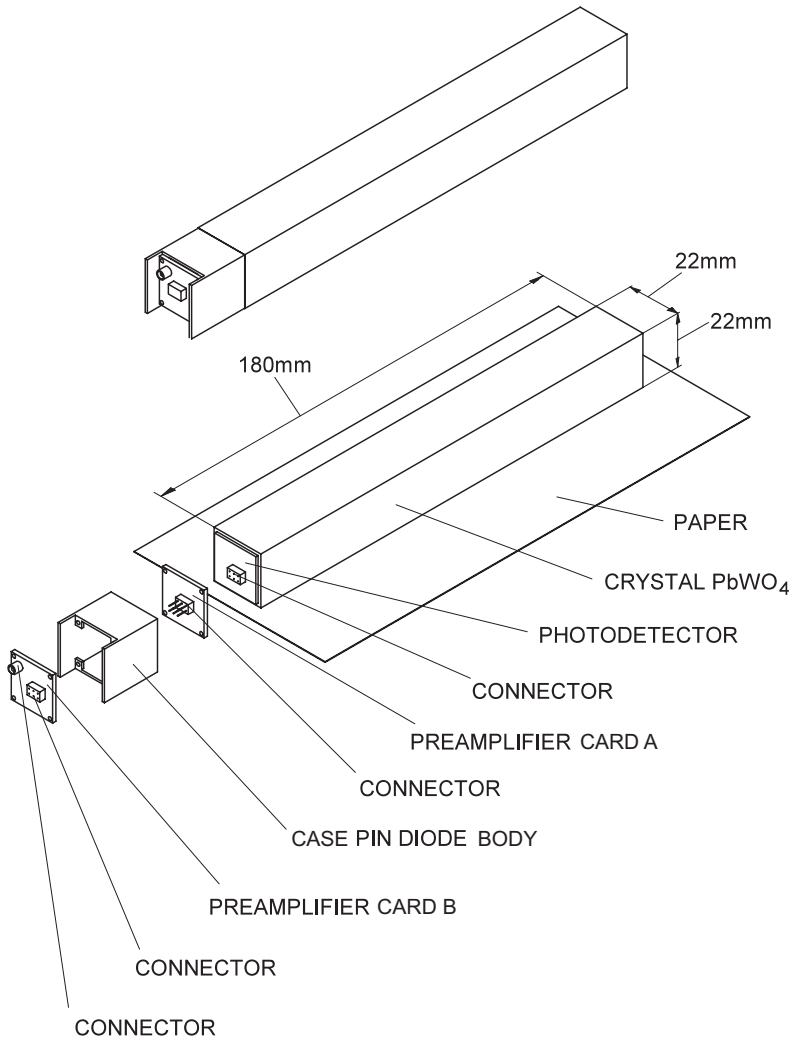

Figure 3.4: Crystal detector unit.

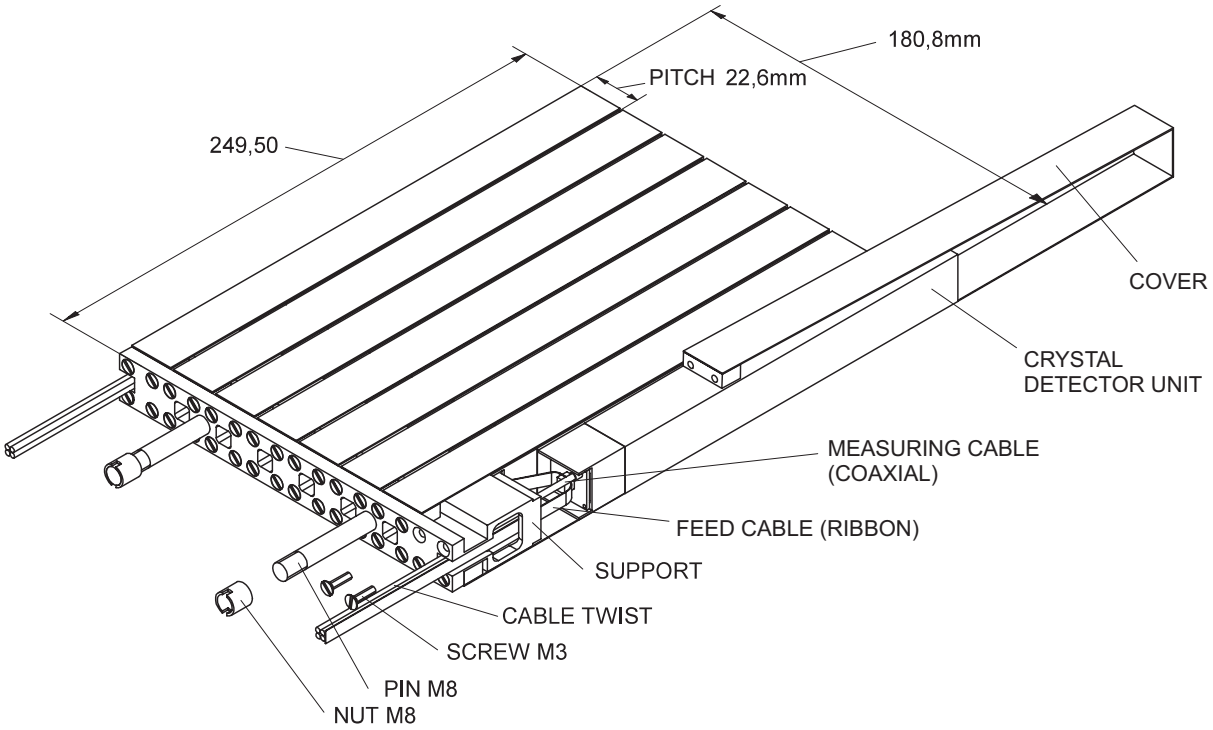

Figure 3.5: Crystal strip unit.

Fig. 3.5. The detector unit casing and crystal attachment cover have minimum thickness on the side of the radiation flow, equivalent to 3 mm of aluminium.

The crystal faces are oriented towards the interaction point.

A crystal strip unit consisting of eight crystal detector units located in one row (1×8 crystals matrix) is chosen as the main mechanical assembly unit (see Fig. 3.5).

The crystal strip unit has cable assemblies interconnecting the PIN photodiodes with the front-end electronics cards. The function of the front-end electronics includes amplification and shaping, buffering, multiplexing, digitization, pedestal substraction, data compression (zero suppression) and data transport.

The crystal strip unit was chosen as the basic assembly unit because of its convenience for manual assembly. The mass of a unit is about 7 kg. The fastening of the crystal units in the strip unit is made by tape yokes. The support material is aluminium. The yokes are made from titanium foils with two fastening brackets of stainless steel. The cable assemblies are placed in a groove of the aluminium support. The crystal strips are fixed by bolts to the aluminium support plate. The plate also constitues the bottom cooling plate.

3.1.2 PHOS detector module

The PHOS detector consists of four separate PHOS modules (Fig. 3.6). The PHOS module constitutes a thermo-insulated casing (thermostat). The module contains 90×6 strip units, with a total of 90×48 (4320) crystals. All crystal faces lay in the same plane. This modular construction conforms with the requirement that the radiation incident angle is smaller than $\pm 13^{\circ}$.

This module size of 2034×1084 mm^2 has a total mass of about 3.2 t, which can be handled by the crane facilities in the experimental area.

3.1.3 Power dissipation and cooling of the PHOS module

The power dissipated in the PHOS module originates from

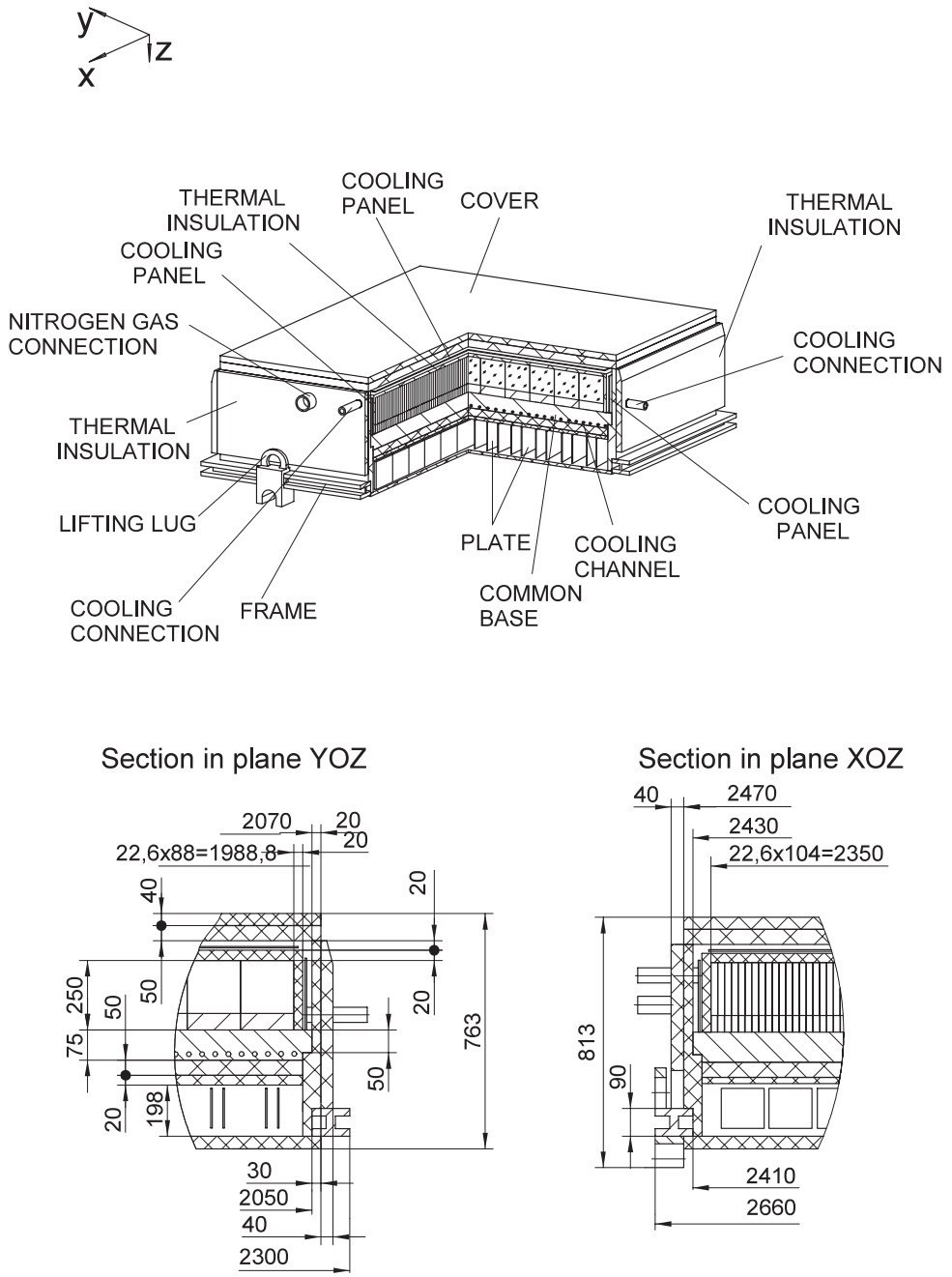

Figure 3.6: Conceptual design of a PHOS module. *This figure corresponds to the TP version of the PHOS detector, twice as wide as the present version.*

- PIN photodiode preamplifiers, ~ 0.2 W/channel, i.e. a total power of ~ 1 kW. (This will be reduced by a factor of 10 if the monolithic Va_1chan preamplifier is used;)
- Front-end electronics cards, ~ 0.5 W/channel, i.e. ~ 2.5 kW in total. The cards will be mounted in the 'warm' volume under the crystal assembly;
- Heat penetrating through the thermostat walls from the environment, with a postulated temperature of $+20^{\circ}$C.

The working temperature of -25°C in the crystals is provided by forced cooling. Heat is removed by coolant pumped through the channels of the cooling panels (Fig. 3.7). For the coolant, a 1.2 propanedol-

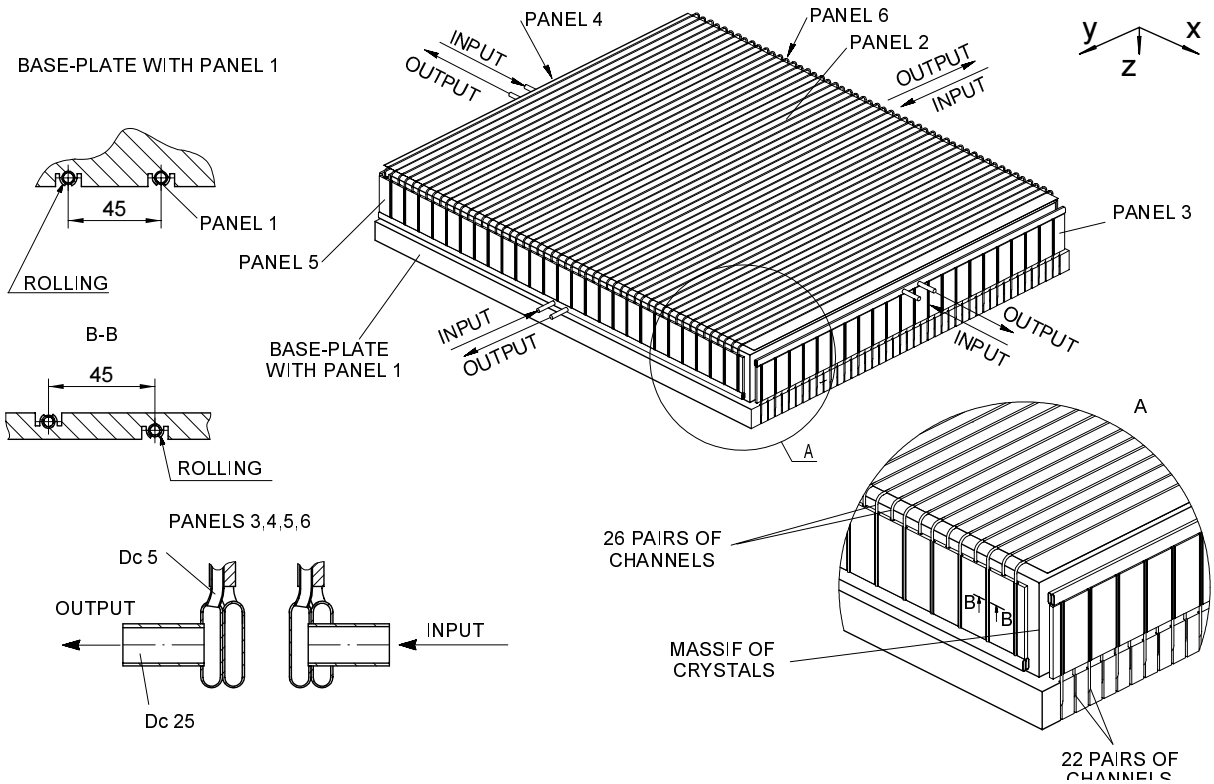

Figure 3.7: View of the cooling panels. *This figure corresponds to the TP version of the PHOS detector, twice as wide as the present version.*

water solution is chosen.

The PHOS module is separated by thermo-insulation into two volumes, 'cold' and 'warm'.

The required temperature homogeneity in all crystals can be achieved by a main heat flow direction along the crystal axis (axis *z*), and with a minimum flow along the planes perpendicular to the *z* axis (along *x* and *y* axes). This requires cooling panels along all six sides of the module. The cooling panels (see the numbers in Fig. 3.7) have two independent cooling tubes, allowing the coolant to flow in opposite directions. There is one flow through panels 5, 2, and 6 along axes *y* and *z* back and forth, and a similar flow through panels 3, 1, and 4 along the axes *x* and *z*.

The temperature gradient in the panels along the *x* and *y* axes should be minimized. This is achieved by a flow of coolant in different directions. Additional thermo-insulation is introduced between the cooling panels and the crystals.

The cooling panels are fabricated from aluminium plates with tubes through which the coolant is pumped.

A detailed description of the construction of the cooling panels and the flow of coolant is given in Ref. [1].

The PIN photodiode-preamplifier assembly, being an integrated part of the crystal detector unit, is included in the cold volume. The front-end electronic cards are operated at room temperature and are placed underneath in the 'warm' volume. To avoid moisture condensating on the PIN photodiodes and preamplifiers, the 'cold' volume is flushed with dry inert gas (nitrogen).

During detector operation the crystals should stay permanently at their working temperature. The front-end electronics can be accessed without unsealing the 'cold' volume.

The 'warm' volume has to be cooled to remove a power dissipation of $\sim$ 2.5 kW per module. The cooling media will be chilled water piped into the module.

The base plate, see Fig. 3.7, is a one-piece aluminium plate with coordinate holes for fixation of the crystal strip units with a pitch of 22.6 mm. Furthermore, there are holes in the plate for cable assemblies. The thickness of the plate is sufficient to ensure that the weight of the module will not distort the inter-crystal gaps, see Section 3.2.3 on page 78.

Aluminium is the chosen material, having good heat-conductivity λ = 200 W/m·K and fairly good mechanical characteristics with $\sigma_{0.2}$ = 80 MPa. With these material characteristics, the chosen geometry of the cooling tubes, and the strip support, one obtains a homogeneous temperature field that satisfies the operation of the crystals.

The PHOS module casing will be fabricated from fibreglass plastic with good mechanical characteristics $\sigma_{0.2}$ = 200 MPa and with heat conductivity λ = 0.3 W/m·K, i.e. a fairly good thermal insulator. In addition, the cooling space is insulated with thermo-insulating material 'Armaflex' with a thermo-conductivity coefficient $\lambda = 0.04$ W/m·K.

The PHOS module is supported by a metal frame with four lifting brackets, and with four bearings matching the support structure of the cradle. The frame has no thermal contact with the metal inside the 'cold' volume. The frame is made by welded aluminium profiles.

All the material of the PHOS module is non-magnetic.

3.1.4 Temperature measurement system

Calculations and measurements have shown that the temperature distribution in PHOS crystals is fairly homogeneous. For a matrix of 8×8 crystals, the experimental temperature gradient along the crystal axis and over the matrix cross-section appeared to be of the order of 0.5°C/m. For reconstruction of the temperature distribution with an accuracy better than 0.1°C it is sufficient to obtain temperature data at at distances of 10 mm from each of the crystal end faces, over a transverse grid of eight crystals.

Temperature sensors of thickness 30–50 μm will be inserted in the gap between crystals. A resistive sensor of wire or film type (PT100) is used. Thermocouples cannot be used because they require a cold junction reference measurement and complex connections. The temperature readout electronics will be integrated in the PHOS data acquisition system to supply temperature corrections on an event-by-event basis.

A temperature readout channel consists of a differential DC amplifier and an analog-to-digital converter. There are two temperature sensors per 64 crystals. In addition, it is necessary to measure temperature distribution over the cooling panel and the temperature of the coolant at the input and output of the cooling system. For this purpose, standard resistive sensors will be used. The readout of these channels will be of the same type as the ones in the crystal volume.

The temperature monitoring and control is part of the ALICE Slow Controls system. It will monitor the values from all the points described above. The feedback control will ensure stable conditions based on preset values for the working conditions.

3.1.5 Integration of the PHOS detector

The PHOS detector consists of four modules positioned along the arc of a circle with a radius of 4.6 m, within an angle of $\pm 53^\circ$. Each of the four PHOS modules will be positioned with its front face pointing towards the vertex, as shown in Fig. 3.8, implying a maximum incidence angle for the photons of $\sim 13^\circ$.

Each PHOS module is installed in the support cradle according to the following procedure. The crane lowers the PHOS module down so that a pair of pivots on the frame, being on the same axis, are inserted into sockets of the supporting platforms on the support cradle. When the crane moves down, the PHOS module rotates round the common axis of the first couple of pivots until the second pair of pivots find themselves in the sockets of the supporting platforms. Lifting is accomplished in the inverse sequence.

Additional adjustments of the PHOS module relative to the interaction point can be carried out by inserting shims between the pivots and the cradle platforms. The support cradle rests upon the rails

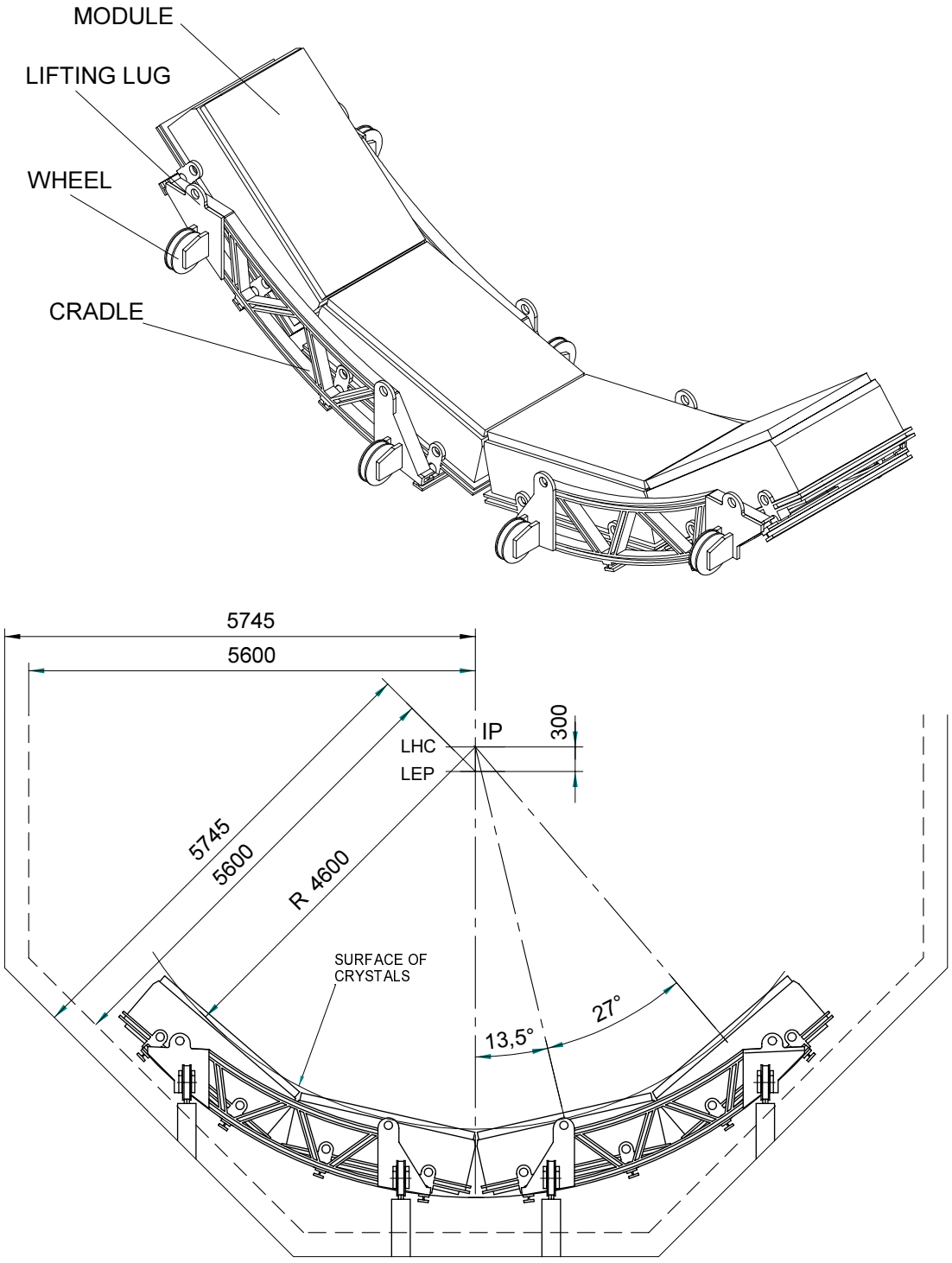

Figure 3.8: Mechanical structure of the PHOS detector.

fastened on the yoke of the L3 magnet. The complete detector is moved and removed to/from the final position by rolling the support cradles along the rails with the magnet L3 door open. When the detector is placed in the operational position, the number of maintenance operations that require a direct access to its units should be kept to a minimum.

Maintenance, repair, and testing of the detector units is accomplished in a special zone, to which the detector is transported from the operational zone by cranes with a load capacity of 40 and 65 t. For the

integration of the detector, the support has been constructed to allow the cradles to be fixed in different positions in pairs, symmetrically, relative to the vertical plane.

3.1.6 The cooling system

The detector cooling system must transport the coolant over a distance of several tens of metres between the detector volume and the cooling system outside the L3 magnet. This imposes restrictions regarding safety, i.e. toxicity, fire, and explosion. The scheme of the cooling system has been chosen based on the experience gained in experiments performed at VNIIEF and CERN on models of the PHOS detector. This is shown in Fig. 3.9.

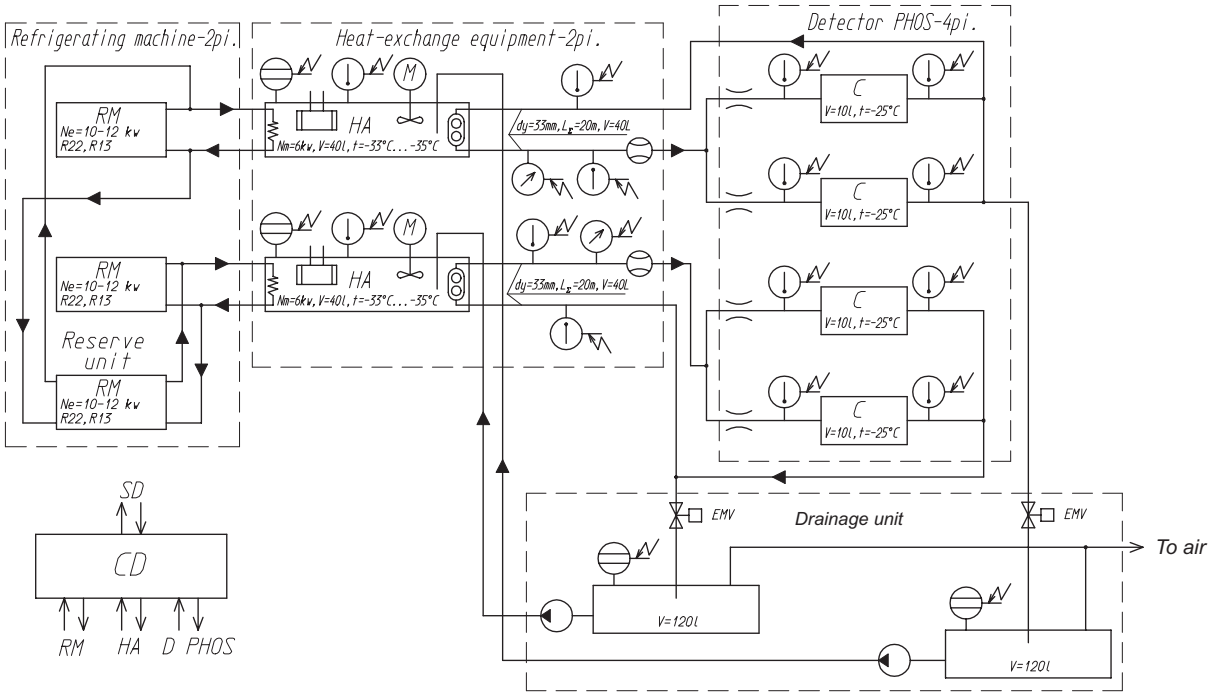

Figure 3.9: Scheme for the PHOS cooling system.

This scheme uses two branches for cooling and one additional refigerator in reserve. Each branch involves a refrigerator, a heat exchange device, cooling panels for two detector modules, a volume for mixing the coolant, control and pumping devices. To better control the temperature a regulated heating source is foreseen.

According to preliminary calculations, the amount of coolant is 100 l in each branch. This includes the coolant in the heat exchange device (up to 40 l), in the pipes (up to 40 l), and in the PHOS modules (up to 10 l in each). The heat exchange device has a volume defined by the heat transfer, the compensation for the dynamics during pumping, and compensation for temperature expansion. With a distance of 20 m between the heat exchange device and the detector, the velocity of the coolant is 2 m/s for a tube diameter of 33 mm. As a source of cold a two-stage cascade Freon refrigerating machine was chosen, in which both stages operate with a refrigerant of type R134A. A detailed description of the cooling system is given in Ref. [1].

The safety aspects related to the cooling system are presented in Chapter 5.

Based on calculations of the temperature fields in the crystals and the results from the PHOS beam test where the cooling and thermal stabilization of the crystal modules were measured, a solution of 1.2 propanedol in water was chosen as the coolant.

3.2 Engineering design study. Cradle and module simulations

All mechanical simulations were performed for the old version of the PHOS detector, which was twice as big in area compared to the final version.

A mechanical analysis of the PHOS detector design is based on the following principles, which specify the requirements on permissible values of stress and deformations in the elements of the detector:

- Any deformations of the PHOS mechanical support should not lead to additional loads transferred to the attachment of the crystal strip units;
- The primary fixation of crystals in strip units and fixation of the units in the module should preserve the required gap between the crystals. This should be maintained under operation and transportation of a module with an inclination up to 50° with respect to the horizontal plane;
- A change of temperature in the crystals within the limits of -25°C to $+25^\circ$C should not lead to excessive changes in the load on the fastening mechanism of the crystals, caused by temperature deformation of these elements;
- The total weight of the detector for transportation should not exceed 38 t (crane lift capacity restriction);
- Only non-magnetic materials are allowed.

Based on preliminary calculations and with respect to operational requirements, the main material selected for the supporting structures (PHOS module frame and PHOS support cradle) is an aluminium alloy (AMg-2M GOST 4784). The alloy has the following mechanical parameters $\sigma_{0.2} = 80$ MPa and $E = 0.7 \times 10^5$ MPa. It is widely used in industry for profile production, and has good welding properties. According to strength norms for structures of aluminium alloys (SNiP 2.03.06-85), a permissible stress of $\sigma \leq 53$ MPa and deformations $\delta \leq 0.5\,\%$ were selected.

3.2.1 Crystal detector unit

The fastening of a crystal detector unit in the crystal strip unit (Figs. 3.4 and 3.5), should provide a fixed minimum gap between crystals.

For the fastening it was decided to use a yoke made of thin metal tape. The crystal face rests on the PIN photodiode casing, the wall thickness of the casing being 0.8 mm (Figs. 3.4 and 3.5).

When fixing the crystals to the support, one has to take into account the following considerations for load limits and choice of tape material:

- The permanent deformation limit of the crystal;
- Displacement of the crystal with respect to the support caused by the weight of the crystal;
- The tape thickness should provide the most compact packing of the crystals in the PHOS module;
- The increase in the tape loading during cooling caused by the difference of the linear expansion coefficients of the tape material and the crystal should not lead to crystal destruction, and the stress in the tape should not exceed the floating limit;
- Only non-magnetic material should be used.

The maximum load on the crystal from the fixation was chosen to be 20 kg with a tape strength of up to 10 kg. Three materials were considered: aluminium alloy, titanium alloy, and stainless steel. The tape width was assumed to be 20 mm. Based on the design improvements during the test experiments the titanium tape was chosen.

3.2.1.1 Optical coupling of PIN photodiode and crystal wrapping

The refractive index of the $PbWO_4$ crystals is very high compared to the PIN photodiode window, $n_d = 2.29$ vs. $n_d = 1.5$, leading to loss in light transmission. An optical glue with an intermediate refractive index will decrease the transmission loss. Thus, the requirements for the optical coupling of crystal-PIN photodiodes are:

- The index of refraction should have a value between those of the $PbWO_4$ and PIN photodiode;
- It should have a good light transmission property within the range of the crystal emission spectra;
- It should be mechanically reliable during cooling and warming up processes;
- It should have stable long-term optical parameters (transparency, etc).

The properties of the optical couplants used are found in Table 3.1. The current choice for glue is Melt-Mount Quick-Stick (Cargille Laboratories, USA). For Quick-Stick we have performed measurements of optical transmission. The glue provides good matching of the decay emission spectrum of the $PbWO_4$, the transmission property of the glue itself, and the quantum efficiency of the PIN photodiode.

Table 3.1: Properties of optical glues.

Optical glue	n_d	Mechanical properties	Remarks
Dow Corning 3067	1.5	Poor	Low value of n_d
Epotec	1.5	Good	Low value of n_d
Quick-Stick	1.703	Good	High n_d

The wrapping of the crystal must provide high light collection efficiency (LCE) and optical insulation between the crystals. Different types of wrapping have been tested: white paper, Mylar, Tyvek, Teflon paper, and millipore filters. There is practically no influence from the type of wrapping on the LCE. This is explained by the high value of the refractive index of $PbWO_4$. The results are in good agreement with simulations (see Chapter 4). White Tyvek was chosen as the wrapping material.

3.2.2 Crystal strip unit

A row of eight crystal detector units constitute the basic assembly of a crystal strip unit. The dimensions of the strip unit support are determined by the size of the crystal, the photodiode-preamplifier assembly, and the connector and cable assembly.

The support is made from aluminium alloy, which has good heat conductivity, provides adequate transmission of the heat dissipated from the PIN photodiodes-preamplifiers to the supporting cooling plate, and low density.

The supports are fixed onto a common plate with two bolts (M8). The bolt dimension and tightening force are selected to prevent displacement of the crystal strip units with respect to the common plate in all the positions foreseen for detector testing and operation.

Calculation of the thermal conductivity between the support and the plate has shown that the thermal contact produced by the bolt pressure alone is not sufficient to provide the desired temperature homogeneity. However, increasing the bolt diameter and the number of bolts weakens the supporting plate. It is therefore, proposed to provide the required heat contact by a heat conducting paste introduced during assembling.

3.2.3 PHOS module

The main criterion for the calculation of the PHOS module's strength is the requirement of a fixed gap between neighbouring crystals. The main load taken into account is the weight of the module element of the PHOS. The design was carried out for the two PHOS modules in their operational position inside the support cradle.

In accordance with this concept, the following supporting scheme was developed. The casing (4-side frame), consisting of glass fibre reinforced plastic walls, are profiled so that inside the casing a shelf is made for the solid support plate (cooling) onto which the crystal strip units are installed. Outside the casing a shelf for the metal frame is constructed. The frame is for transferring the load from the casing to the support bearings in the cradle when in operational position. The support bearings are equipped with hooks for lifting and transportation of the module.

The glass fibre reinforced plastic was chosen because of its good mechanical characteristics and relatively good thermo insulating properties. For the solid metal plate, the aluminium alloy was chosen to meet the requirement for non-magnetic material with good heat conductivity, low density, and good properties for high-accuracy machining. Figure VII illustrates the values of stress and deformation for PHOS support elements in operational load and fastening conditions. One quarter of the plate, casing, and frame is shown. For the calculations the uniformly distributed loads were set from crystal mass over the whole plate. A uniform load along all parts of the support structure was considered, and the total load was transferred to the cradle over the four support brackets. The maximum calculated stress in the design elements does not exceed the permitted loads for the materials. The deformation of the bearing plate leads to a decrease in the gaps between the crystals by a value considerably less than the required gap of 0.1 mm.

3.2.4 Support cradle

The support cradle provides the support for the PHOS modules in operational position, during assembly, and for transport to the operational zone and to the service zone (Fig. 3.8).

The possibility of installating either two or four PHOS modules in different positions, symmetrically with respect to the vertical plane defined by the beam axis has been foreseen.

The maximum calculated stress and deformations in the elements do not exceed the permitted values for the materials. The divergence from the nominal position of the face plane of the crystals, caused by deformation of the cradle, is eliminated by inserting shims in the support cradle.

3.2.5 Prototypes

The crystal strip unit and the crystal detector unit elements were developed by constructing and testing prototypes. Fig. IV shows pictures of the crystal strip unit during assembly.

Figure V shows pictures of the prototype module, consisting of eight crystal strip units assembled into a matrix of 8×8 crystals, used during beam test experiments at CERN in 1997–1998.

3.2.6 Tests

The goals for the test of the crystal strip unit and the crystal detector unit elements mounted in a prototype test matrix are:

- Verification of the calculated mechanical design parameters;
- Testing of the assembly technique for the crystal and the photodetector;
- Improvements in the assembly technology;
- Control of dimensions during assembly and in test position.

Definition of load limits on crystals

To define the tolerable load on crystals, experiments were carried out by weight loading reference samples cut from crystals. Crystal destruction and inner defects were measured using ultrasonic and acoustic detectors. The measurements were carried out at +20 and -25 °C. The results are presented in Fig. 3.10. The load on a crystal (20 kg) does not exceed the limit at which changes in the crystals are observed.

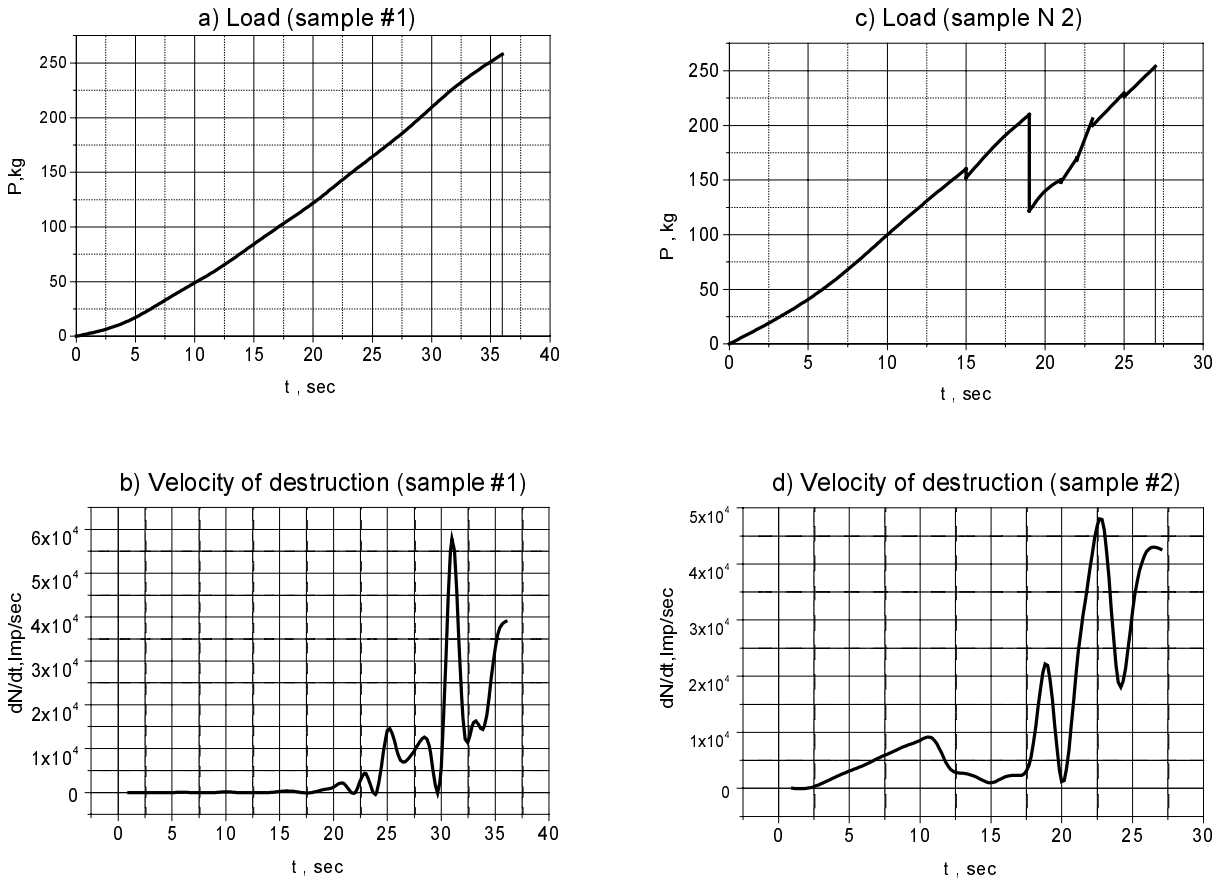

Figure 3.10: Load and velocity of destruction formation in crystals at a temperature of -25°C (sample #1) and $+20$°C (sample #2).

Gluing of PIN photodetector to crystal

The gluing of the PIN photodetector to the crystal by Quick-Stick was carried out by heating the elements under a flow of hot air. The position accuracy of the photodetector on the crystal is within 0.2 mm. A dose of 0.2 g of glue was used to ensure a stable joint with minimal glue thickness. The quality of the gluing was inspected visually through the the crystal face. Absence of bubbles was controlled after completion of gluing.

Assembly of a crystal detector unit

The assembly of this unit includes the wrapping of the crystals and mounting of the photodetector, together with the casing of the unit. The excess of soft glue around the PIN photodiode provides a soft layer for transmitting the load from the surrounding support to the crystal.

Assembly of a crystal strip unit

This assembly includes the fixation of the crystal detector units to the support bar by means of the take yokes. The assembly also places the cables inside the grooves made on the support.

Assembly of the prototype module

The reliability of the assembly of the crystal strip units onto the common plate were verified. The module was controlled after assembly. Its size in the plane perpendicular to the crystal's axis with a gap between the crystal strip units of 22.6 mm and with an accuracy of the coordinate holes in the plate of ± 0.05 mm, was 181×181 mm.

The absence of crystal breaking after completion of the test experiments with cooled crystals was verified.

3.2.7 Thermal calculations

The required energy resolution of the PHOS detector is achieved by operating the crystals at -25°C and with a temperature stabilization of $\pm 0.3^{\circ}$C. The detector includes systems which will provide cooling and thermostabilization of the crystals in the PHOS modules within these values.

3.2.7.1 PHOS module cooling and thermostabilization conditions

Operation in cooling mode

1. The PHOS modules are cooled down during 'no-beam' operation;
2. The PIN photodetectors and the detector front-end electronics are powered off;
3. The heat removed is mainly that of the inflow from outside and the heat stored in the structure elements.

Operation in thermostabilization mode

1. The PHOS detector is in the operational state;
2. Power dissipation from the PIN photodetectors in the 'cold' volume is 0.2 W per crystal detector unit, with a total power dissipation up to 1 kW in a PHOS module;
3. Power dissipation from the front-end electronics in the 'warm' volume is 0.5 W/channel, with a total power dissipation up to 2.5 kW in a PHOS module;
4. The heat flows in from outside in actual convection heat exchange conditions with the temperature inside the casing of -25°C and the air temperature outside the casing of $+20^{\circ}$C;
5. As the front-end electronics are located in the 'warm' volume the calculation of this heat flow may also be considered external;
6. The heat conductance is through the cables between the 'cold' and the 'warm' volumes.

The results of preliminary calculations of the temperature distribution show that a satisfactory homogeneity of the temperature field in the crystals is achieved by cooling the PHOS module on all sides. In Fig. 3.7 the arrangement of the cooling panels is presented.

3.2.7.2 Analysis of the PHOS cooling and heat-insulating system

All thermosimulations were performed for the old version of the PHOS detector which had twice as many detecting channels, and, hence twice as much area and power dissipation per module. The operation of the PHOS detector requires a good homogeneity of the temperature field in all PHOS module crystals with a high degree of stability. The temperature gradient in the crystal matrix should not exceed 0.2°C over a cluster of 5×5 crystals. However, a temperature gradient of several degrees along the z-axis is allowed. The time variation of the 'stable' temperature should not exceed 0.3°C.

Based on these criteria, the cooling system has to provide the maximum homogeneous heat absorption in panel 1 and in panel 2. In panels 3, 4, 5, 6 a temperature gradient along the z-axis is allowed. Power dissipation in the PIN photodetectors is homogeneous in the $x-y$-plane. The external heat flow through the walls essentially determines the temperature field homogeneity in the crystals. For this purpose the cooling panels are placed inside the casing along all of the walls. For additional reduction of fringe effects in the temperature distribution, the crystals are separated from panels 2, 3, 4, 5, 6 by an additional internal layer of heat insulation.

It is evident that the temperature field homogeneity also depends on the distance between the cooling channels. The homogeneity increases with decreasing distance (increase of channels), but this makes the design more complicated. According to the preliminary simulations a distance of 45.2 mm was chosen, one channel per row of two crystals.

Calculations and simulation of the the heat flow under cooling and thermostabilization conditions are described in detail in Ref. [1]. Results from these calculations for elements and rows of elements are displayed in Figs. 3.11 to 3.15 (the numerical values corresponding to the TP version of the PHOS).

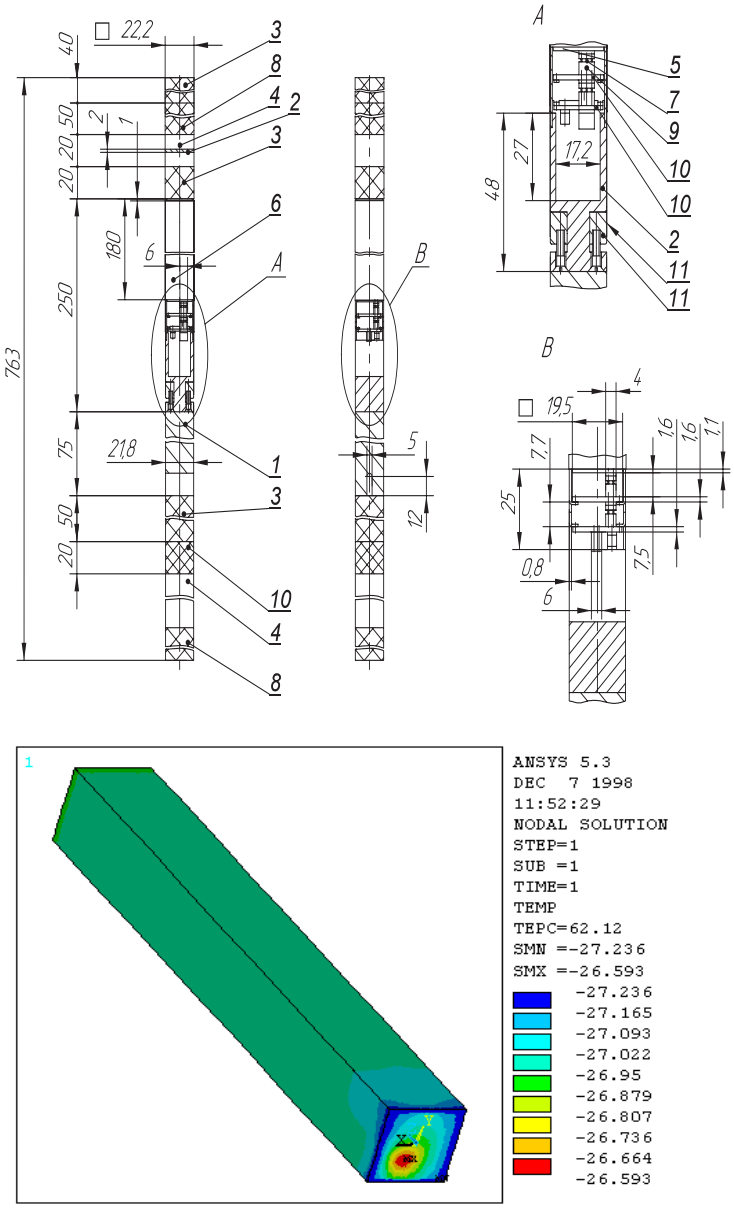

Figure 3.11: Temperature field in a crystal detector unit inside a PHOS module.

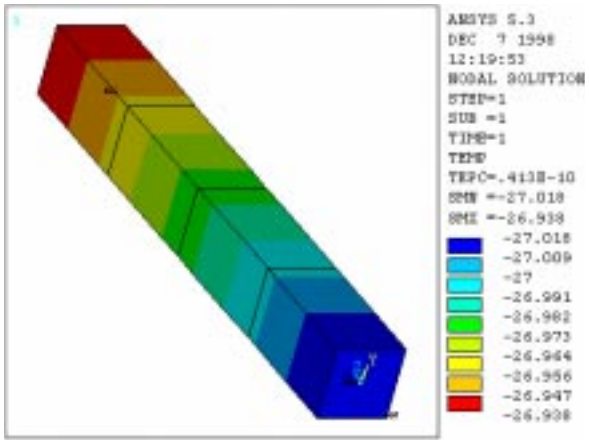

Figure 3.12: Temperature distribution in a simplified model of a crystal detector unit.

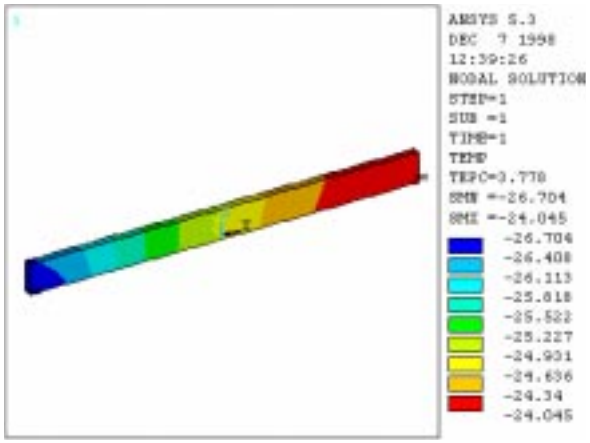

Figure 3.13: Temperature distribution for 2×104 crystal detector units allocated in two parallel rows.

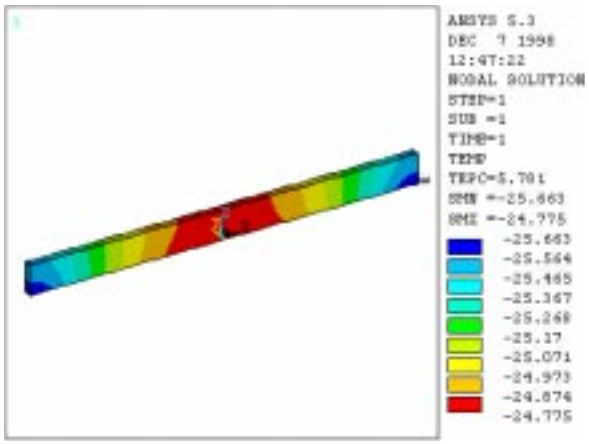

Figure 3.14: Temperature distribution over four parallel rows of crystal detector units with two cooling channels with opposite flow in panel 1.

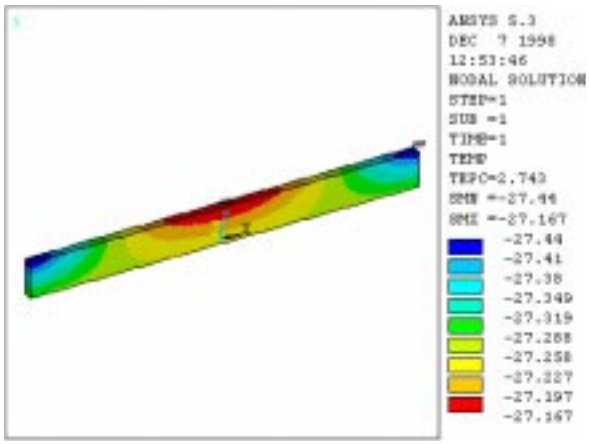

Figure 3.15: Temperature distribution for two rows with 2×88 crystal detector units along the *y*-axis and with opposite coolant flow in panel 2.

Figure VIII represents a simulation of a PHOS module model with regard to the heat flow through the flank sides and the heat removal in the cooling panels 3, 4, 5, and 6 (Fig. 3.7). The channels in panels 3, and 4 are an extension of the channels in panel 1, and the channels in panels 5, and 6 extend the ones in panel 2.

According to simulations it is necessary to keep the temperature of the coolant at the input of the cooling panels at -30°C. The coolant discharge for a PHOS module will constitute 0.6 kg/s, and the diameter of the input and output trunks should not be less than 25 mm. The heat power removed from the PHOS module will be 2.6 kW.

Assuming the refrigerator power value (without accounting for losses in the conducting trunks) to be 3 kW (obtained as a result of calculations in stabilization mode), the estimated time for cooling down the PHOS module to -25°C will be up to 30 h. This period is acceptable from the standpoint of the operation of the PHOS detector.

3.3 Engineering design study. Prototype test and simulation

3.3.1 Prototype

The cooling and thermostabilization system for the prototype module, consisting of 64 registration channels, was tested at a special experimental testbed at VNIIEF. Data obtained from these experiments were used for designing and manufacturing the prototype model. The cooling and thermostabilization system was finally verified in real operating conditions during beam tests at CERN. During the tests the alcohol-water mixtures of different concentrations were used as a cooling agent. The relevant properties of these mixtures: viscosity, thermoconductivity and thermocapacitance are very similar to those of 1.2 propanedol.

The experimental testbed

The testbed involves:

- Primary cooling machine with temperature monitoring and control system;
- Tank with coolant;
- Pump;
- Thermostat with cooling panels;
- Prototype module with 64 measuring channels;
- Temperature measurement system;
- Supporting cables and armature.

During the experiments at VNIIEF, the source of primary cooling was a climate chamber of the type Taimini-Subzero TABAI MF-81 (Japan), operated at temperatures down to -85°C.

The thermostat had five cooling panels, made from Al alloy and eight channels with $\varnothing$ 5 mm, length 170 mm, combined by a common collector with $\varnothing$ 12. Foam plastic was used as the thermo-insulating material in the thermostat. Armaflex was used for the pipelines of the cooling system.

Whilst working with the prototype module at VNIIEF, the $PbWO_4$ crystals were simulated with polystyrene samples, and resistors simulated the power dissipation of PIN photodectors. Experiments were carried out with ice freezing, as well as with an alcohol-water solution without ice with different concentrations.

Figure VIII represents the results of calculating the temperature distribution in the crystal assembly inside the thermostat. According to the experimental conditions at CERN, the coolant temperature at the input of the cooling panel was assumed to be -30°C, and its velocity 0.085 m/s.

In the experiments carried out at VNIIEF, a multi-channel measuring system based on modules in the CAMAC standard and a personnal computer were used. This system is analogous to that used in the beam tests at CERN. The block diagram of the system is illustrated in Fig. 3.16.

The multi-channel temperature measuring system comprises four groups of thermocouple sensors. Each group consists of seven thermocouples of Chromel-Constantan type with a thermistor temperature-controlled unit for cold junction temperature measuring. The design provides identical cold junction temperature for all thermocouple groups. As a cold junction temperature sensor a thermoresistor of special design is used. Signals from the thermocouples and thermoresistors are enhanced by amplifiers of type UT-8, implemented in the CAMAC standard.

In the beam test experiments the crystal temperature values are transmitted in parallel into the PHOS DAQ system. Therefore, the amplified signals are branched both to ADCs in the DAQ system and to a 32-input analog multiplexer of the temperature measuring system.

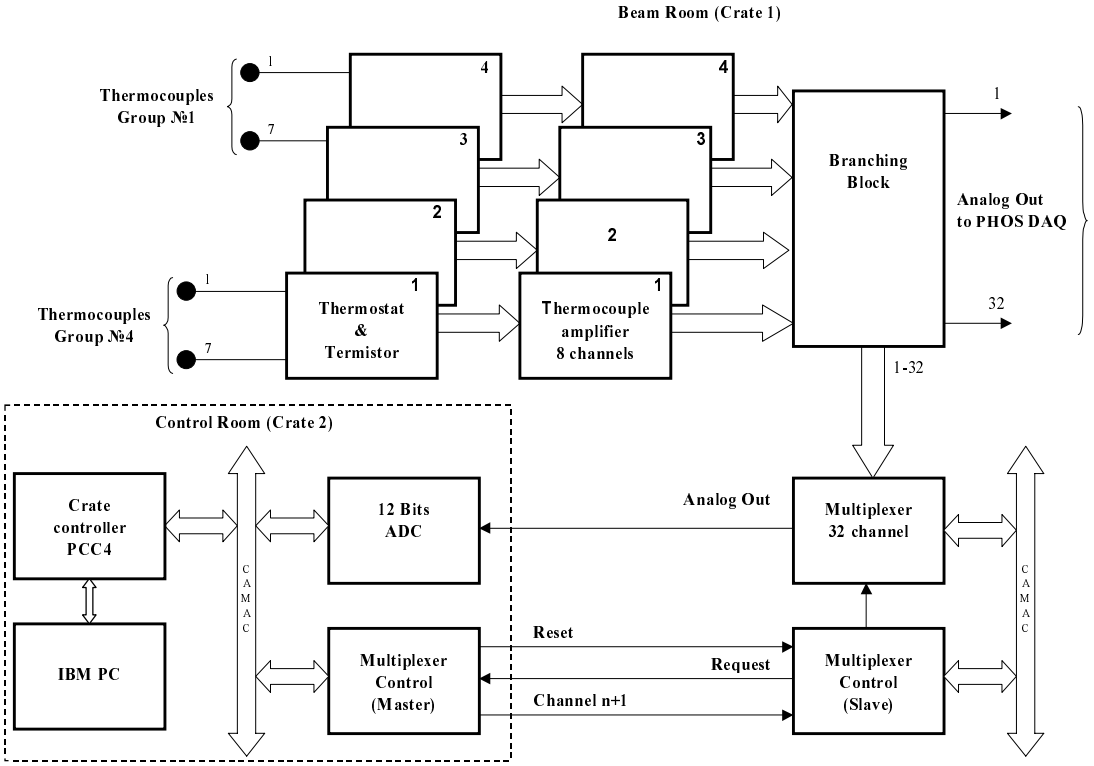

Figure 3.16: Block diagram of the temperature monitoring and control system.

In the beam test experiments the control room can be at a distance of 100 to 200 m from the experimental hall. To decrease the number of communication cables the temperature measuring system equipment is mounted in two crates. The crate in the experimental hall contains the thermocouple amplifiers, signal branching and multiplexing with slave control. The crate in the control room contains the rest of the CAMAC equipment: multiplexer with master control and integrating 12-bit ADC. The operation of the analog-to-digital converter and distant multiplexer is synchronized through control signals.

The temperature measurement system is controlled by an IBM PC. The software controls the multiplexer, receives data from the ADC and converts them into relevant temperature data. As for the thermoresistor measuring the cold junction temperature, a linear dependence of resistance vs. temperature is used. For thermocouples a dependence between thermo-E.M.F. and the temperature is described by a cubic spline, which is based on the standard table data (GOST R 50431-92). The software provides visualization of received data, storage on the computer hard disk, and a wide variety of mathematical operations on the data.

The system is intended for temperature measurements within the range from $-50°$C to $+50°$C. The measurement error in this range does not exceed $0.05°$C. The error is determined by the thermoresistance and the accuracy of the calibration of the thermocouple measuring channel. Using temperature reference points (water, mercury, and carbonic acid freezing points) the absolute accuracy of thermocouple measurements is about $0.1°$C.

3.3.2 Tests

For the beam tests at CERN a detector module with 8×8 crystals was assembled. The $PbWO_4$ crystals were initially tested at the Kurchatov Institute. The PIN photodiodes with preamplifiers are described in Chapter 2. The detector matrix was placed into the cooling thermostat (Fig. 3.17).

As a source of primary cold a refrigerating machine of type Lauda Ultra Kryomate (Germany) was used.

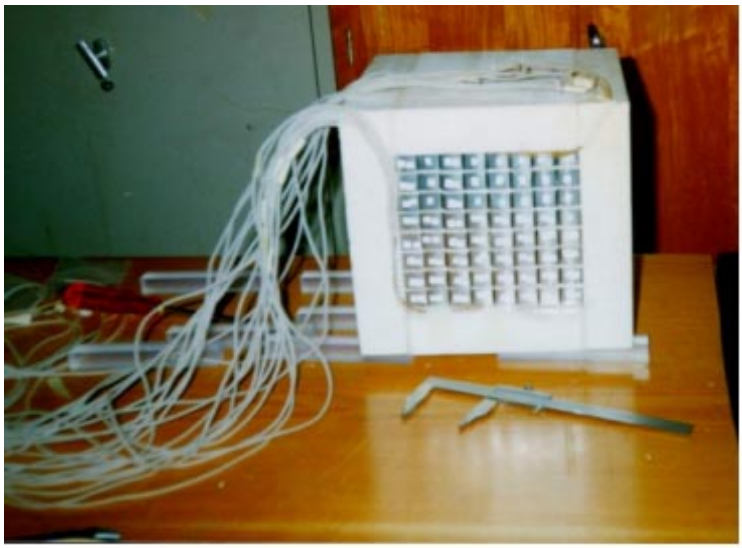

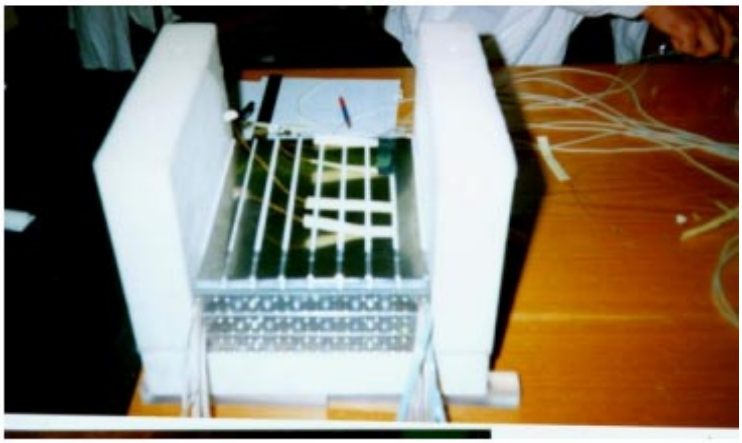

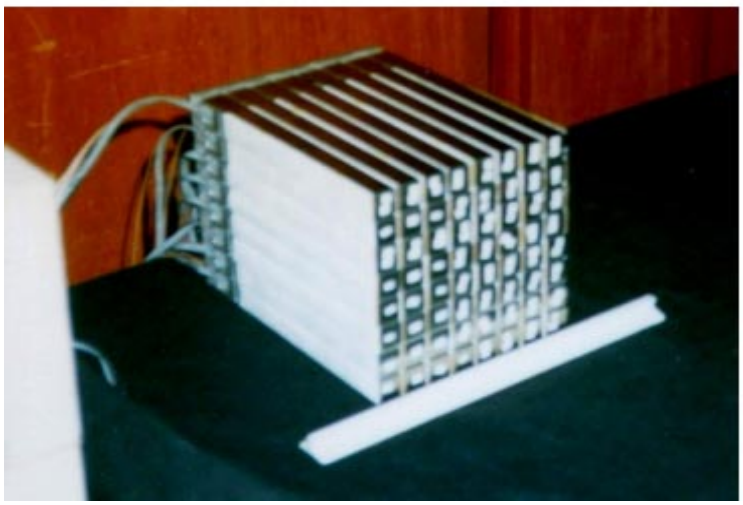

Figure 3.17: Assembly of the detector crystal matrix and mounting inside a thermal insulation box. From bottom to top: preassembling on the main cooling plane (bottom); assembly, strip unit by strip unit, the boxstrip (middle); final view of the matrix inside a thermal insulation box (top).

The tests were carried out at T10 and T11 at the PS, and H6 at the SPS. The temperature conditions in these experiments differed significantly.

The thermoresistor measuring channels were calibrated over the temperature range of 0 to 35°C, and the thermocouple over the range of −30 to +35°C. The ice melting point and other temperature points measured by a thermometer were used for calibration with an error of 0.2°C. After calibration the temperature control system provided a relative error of measurements better than 0.05°C, the absolute error was about 0.2°C. The comparatively high absolute error in the temperature measurement is insignificant because the main goal of the measurements was to determine temperature gradients in a rather narrow temperature range.

For temperature control in the detector matrix, 22 thermocouples of Chromel-constantan type and of special design were installed. The overall thickness of the thermocouple and electric insulation is about 0.3 mm. This allows insertion of thermocouples inside the module between the crystals without increasing the gap between them. The layout of thermocouples in the matrix of 64 crystals is illustrated in Fig. 3.18 and in Table 3.2.

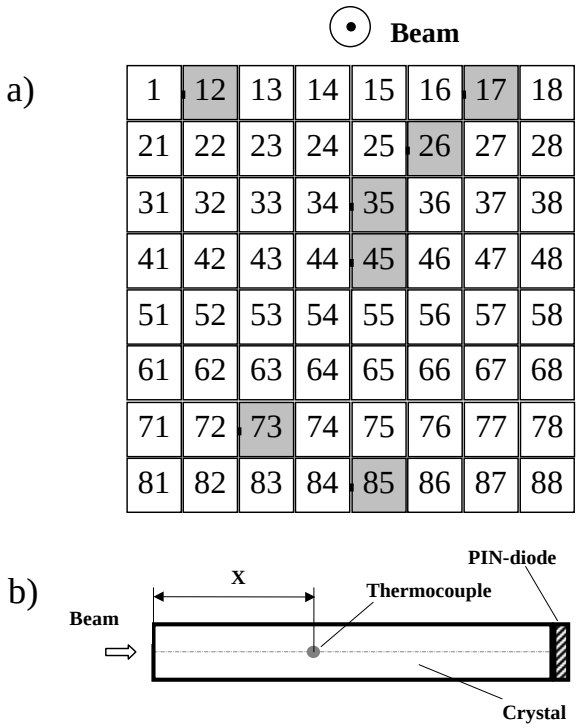

Figure 3.18: Thermocouples in the 64 crystal detector matrix module volume. a) Crystal matrix, crystals with thermocouples are shaded. b) Layout of thermocouples on the side of the crystal.

The air temperature in the experimental room was measured by thermoresistor sensors. The temperature of the coolant was measured by thermocouples at the input and output of the cooling system, as well as the temperature at two points on the surface of the main cooling panel. The thermocouples on the cooling panel were glued at distance of 10 mm from the input and output pipes. These data are required for further development of the cooling and thermostabilization system.

The thermostat with the crystal matrix was installed in the CERN PS T11 beam. After it was cooled down to ~ -27°C. The cooling was performed with PIN photodiodes, the preamplifiers powered on. The cooling mode was chosen such that the maximum temperature difference along the crystal axis did not exceed 10°C. With these conditions the time for reaching the stationary temperature state was about 50 h. After reaching the stationary state the temperature in the cooling system and the crystal matrix were maintained by the thermostabilization system.

Table 3.2: Positions of thermocouples in the 64 crystal detector matrix.

Crystal No.	Thermocouple No.	x (mm)
12	44	10
	43	90
	33	170
17	12	10
	22	130
	14	170
26	24	10
	17	70
	26	130
	16	170
35	32	10
	13	170
45	35	10
	25	70
	21	130
	11	170
73	31	10
	34	90
	42	170
85	37	10
	23	70
	15	170

During the test period at the PS accelerator the temperature in the experimental area oscillated by up to 7°C during the day.

In Figs. 3.19 and 3.20 data obtained in the stationary mode are presented. Figure 3.19a illustrates the temperature changes in the main cooling panel. One can observe rather rapid temperature oscillations of 0.2–0.3°C. These oscillations are due to changes in the coolant temperature during operation of the threshold thermostabilization system of the refrigerating machine. In addition, there is a slow temperature change of 0.8°C over a period of 50 h. The slow temperature drift is determined by the quality thermostabilization system of the refrigerating machine. The temperature difference at the input and output of the main cooling panel is about 1°C. This considerable temperature drop is caused by the low pumping velocity of the coolant, namely ~ 0.2 ml/min.

The results, shown in Figs. 3.19 and 3.20, fully characterize the homogeneity of the temperature distribution over the crystal matrix. They are the temperatures on the main cooling panel (Fig. 3.19a), temperatures on the different points on the surface of crystal #45, and their deviation from the mean value (Fig. 3.19b,c). Figure 3.20 presents the data for crystals #12, #73, #35, #45, #85, #26, and #17 in the matrix at distances of 10, 130, and 170 mm from the front plane. The data are represented in the $T - T_{\text{Mean}}$ form, for which the temperature gradients are more pictorial.

One can see that temperature inhomogeneity along the crystal #45 section does not exceed 0.06°C. The temperature inhomogeneity at $x = 10$, 130, and 170 mm is respectively, 0.1, 0.08 and 0.5°C. The temperature inhomogeneity in the crystal matrix volume at 130 mm from the front plane does not exceed 0.1°C.

In Fig. 3.20c three groups of curves with different temperatures are observed at X = 170 mm which

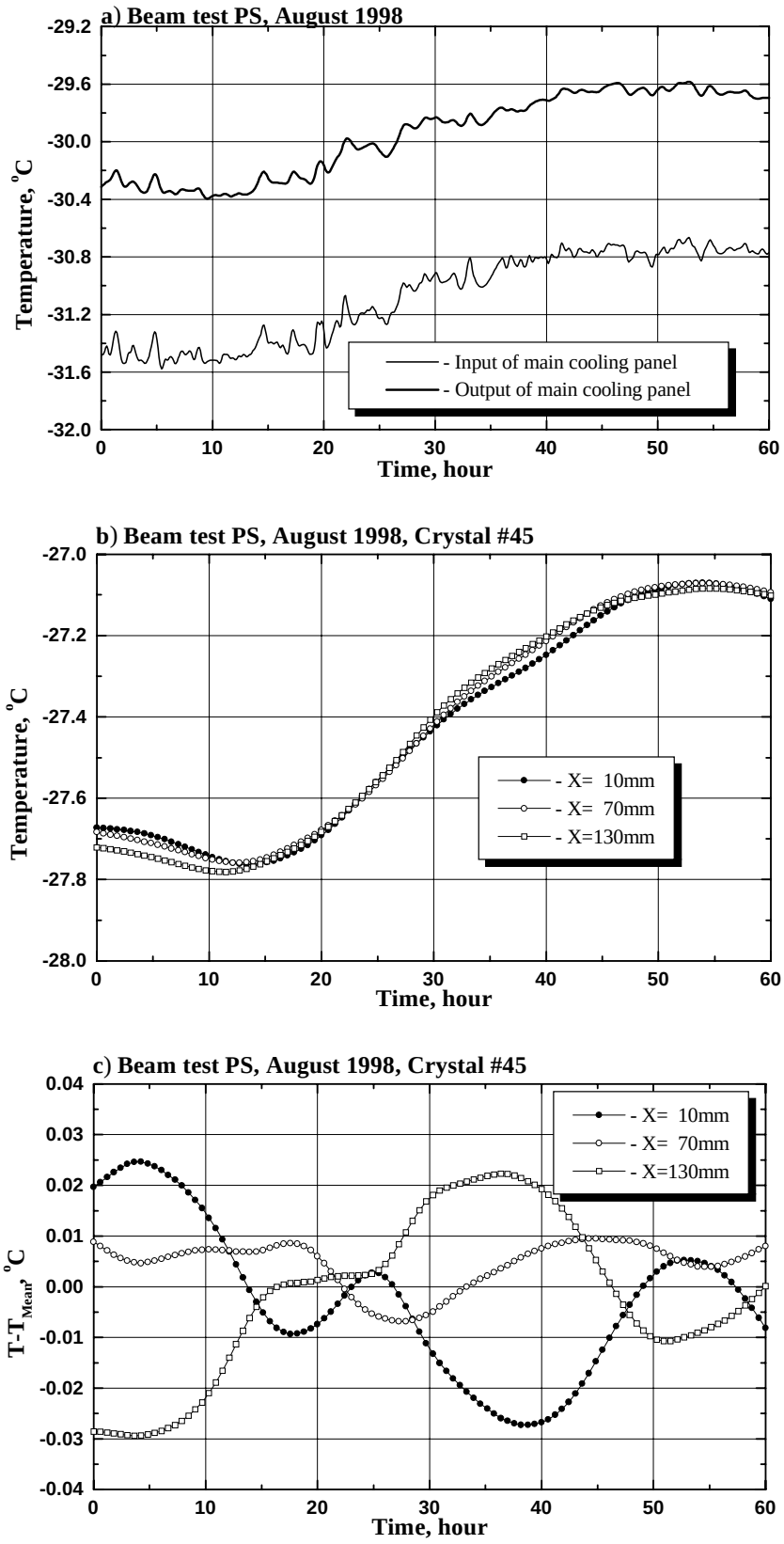

Figure 3.19: Stationary cooling mode of the detector matrix prototype in the beam test experiment at the CERN PS. a) Temperature on the main cooling panel. b) Temperature on the surface of the central crystal #45. c) Temperature difference over the crystal #45 relative to its mean value.

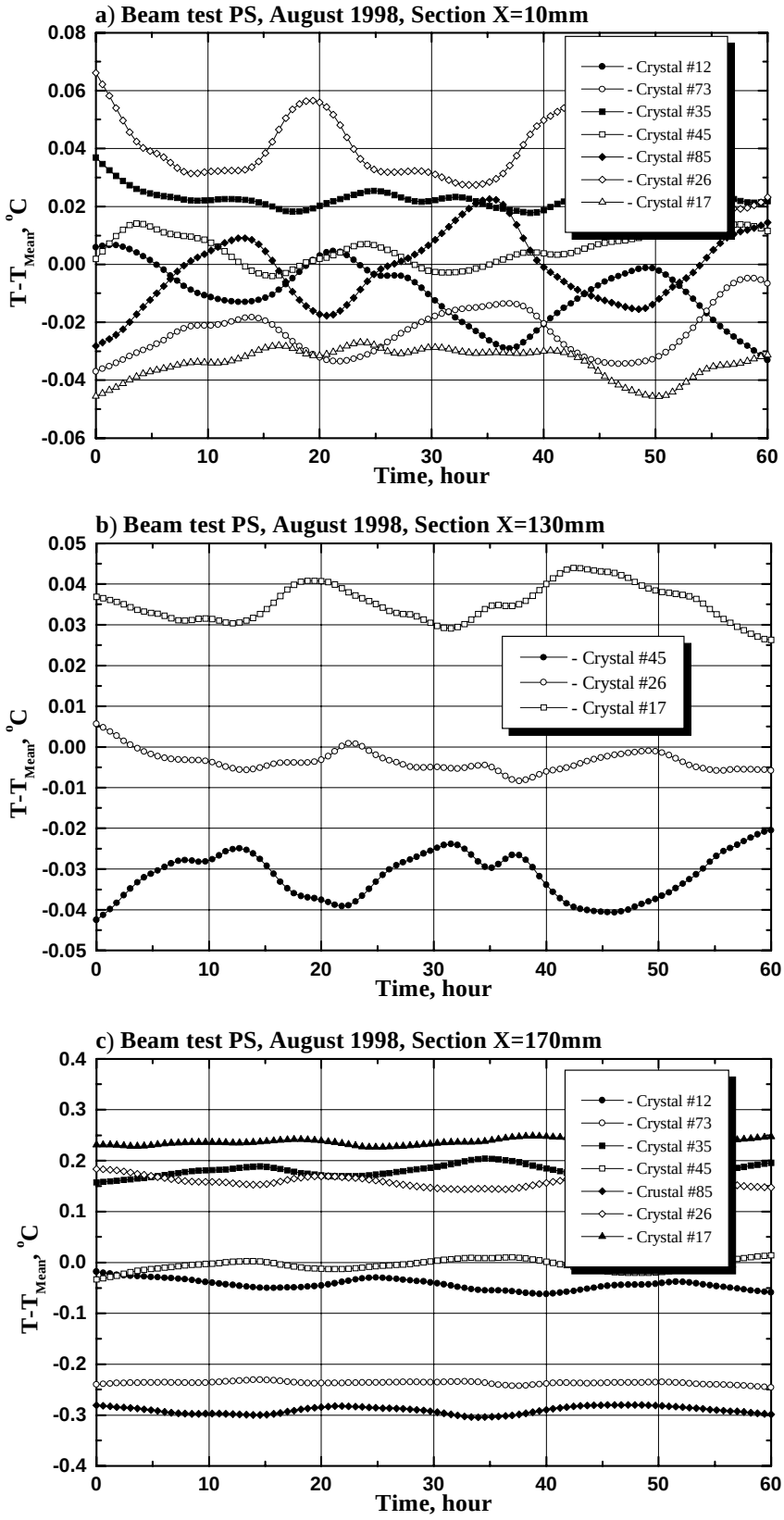

Figure 3.20: Stationary cooling mode of the detector matrix module prototype in beam test experiment at the CERN PS. Temperature deviation from the mean value in the crystal matrix at a) $x = 10$ mm, b) $x = 130$ mm and c) $x = 170$ mm.

is close to the main cooling panel. This effect is caused by slightly different temperatures in the adjacent cooling channels.

After completion of the beam test experiment at the CERN PS, the equipment was moved to the CERN SPS accelerator, reassembled and activated. During the period between the switching off and on again of the cooling system the crystal matrix was warmed up to about -20°C.

The temperature oscillations in the SPS experimental zone were less than at the PS and did not exceed 2.5°C. The thermostabilization system functioned better in these conditions, and in the stationary mode the stability and homogeneity of temperature in the crystal matrix were also better. The temperature inhomogeneity in the crystal matrix 130 mm from the front plane did not exceed 0.1°C.

The analysis of the experimental data (Figs. 3.19 and 3.20) and the comparison with calculated values shows good agreement between the calculated and measured temperatures at different points over the crystal volume.

3.4 The architecture of the front-end electronics and read-out

The PHOS detector comprises four modules with a total of 17 280 channels. The calculated (GALICE) occupancies for a central Pb–Pb event (with dn/dy = 8000 charged particles at midrapidity) are shown in Table 4.5 on page 116. The data are digitized in 12 or 13-bit ADCs. The average event size is estimated to be 11 Kbyte [2]. This small event size means that the readout does not constitute a critical element of the detector.

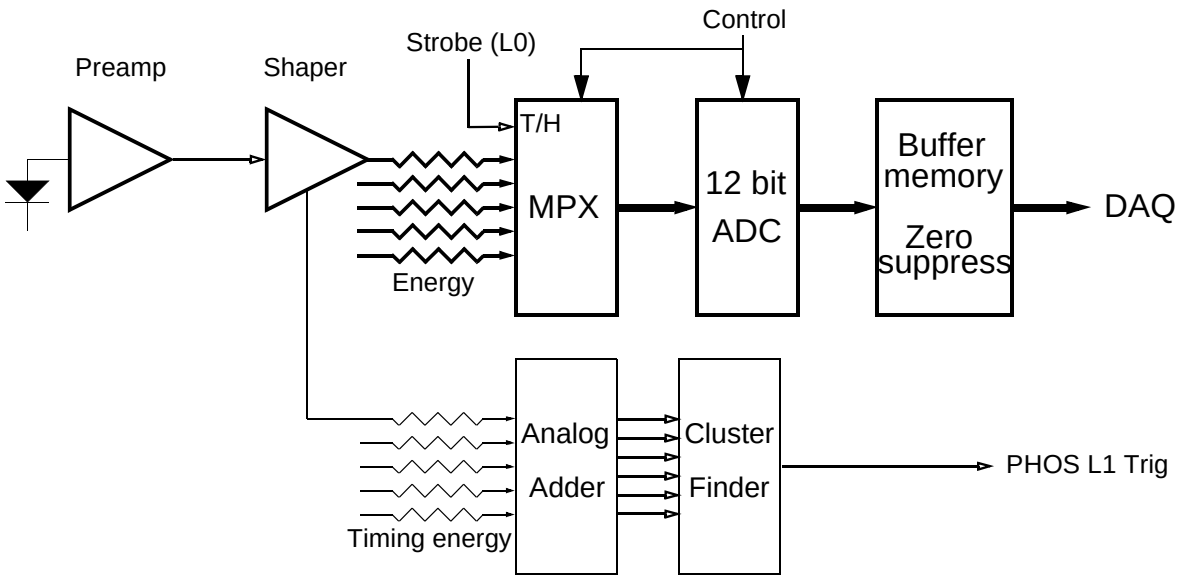

Figure 3.21: The PHOS readout chain. The option for generating an L1 PHOS trigger is under study.

The electronics chain is schematically shown in Fig. 3.21. The preamplifier is integrated with the PIN photodiode. The shapers, multiplexer, and ADC are mounted on cards placed in the 'warm' volume of the PHOS module. The cards containing the buffer memory and zero suppression are either placed in the same 'warm' volume or in crates under the PHOS cradle. The output signals from the preamplifier and the shaper are shown in Fig. 3.22.

3.4.1 The PIN photodiode

The output signals from the PIN photodiodes are bundled into groups of eight through a connector on the detector strip printed circuit board (see Fig. 3.2). The signals are transferred to shapers on readout cards

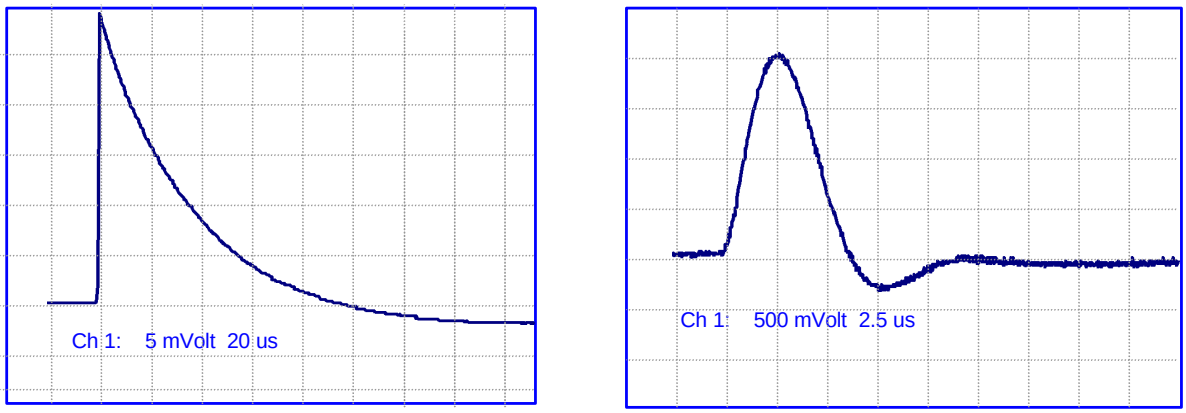

Figure 3.22: Oscilloscope traces of output signals from the photodiode preamplifier and the shaper, the time axis in μs/div is shown below the trace

located in crates in the 'warm' volume of the PHOS module. There are no T/H or RESET signals from the readout electronics back to the PIN preamplifiers. A calibration/test signal to the preamplifier may be included, but the system is more easily calibrated and monitored by means of the LED monitoring system (see Section 3.5).

3.4.2 Preliminary description of the readout chain

3.4.2.1 PHOS readout cards – PHROC

The PHOS readout card (PHROC) comprises a number of shapers, track-and-hold (T/H) circuitry, analog multiplexers, and 12-bit ADCs. The data encoding (zero suppression) circuitry may also be implemented on the PHROC. The L0 trigger signal provides the T/H signal to the PHROCs. Prototypes of the shaper and ADC are described in Chapter 2. A Monolithic shaper and ADC circuits will be used, both for minimizing the board area and for keeping the power budget as low as possible.

The height of the 'warm' volume is less than 20 cm (see Fig. 3.6), which limits the size of the electronic cards that can be placed inside.

The shaper must be strictly matched to the characteristics of the preamplifier in order to maximize the signal-to-noise ratio (see Chapter 2), and the monolithic version will be developed under an on-going PHOS R&D project. For the ADC, a commercial chip will probably be available.

The PHROCs will be placed in the 'warm' volume under the PHOS module. The design and prototyping of the PROC will take place in the years 1999–2001, with production starting in 2002.

3.4.2.2 PHOS trigger electronics

The various ALICE detectors have different triggering requirements. Furthermore, the relative low event rate in ALICE has led to the choice of track-and-hold (T/H) electronics for most of the detectors. In order to accomodate these demands, the trigger system generates an early strobe (L0) about 1.2 μs after the interaction has taken place. This strobe is used by the PHOS for sampling the amplitude of the signals from the photodetectors. A following L1 trigger is generated by the ALICE trigger system at about 2.7 μs. The overall ALICE trigger architecture is shown in Fig. 3.23, taken from Ref. [2].

The PHOS detector could contribute to the trigger L1 with the generation of a fast summing of energy signals to find an energy deposition above a threshold in a cluster of adjacent channels. It may also be sufficient to trigger on a single high-energy cell. The current version of the front-end electronics for PHOS does not supply an energy signal sufficiently fast for a L1 decision. It will therefore require a revised shaper design with a fast output energy signal in addition to the current low-noise energy signal

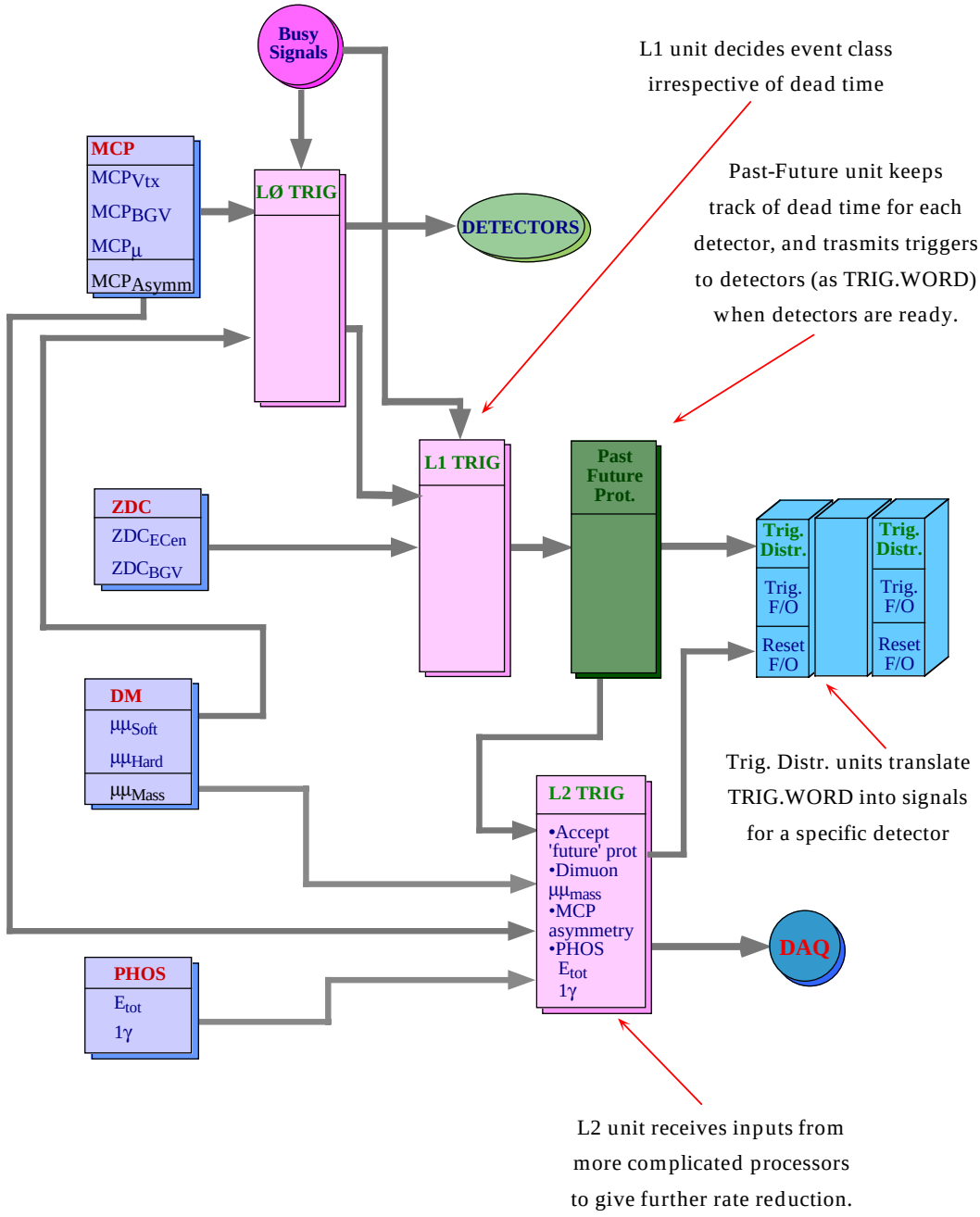

Figure 3.23: ALICE trigger block diagram.

that has a peaking time at around 2 μs. For an energy summing circuitry a concept similiar to the one developed for the PHENIX experiment will be studied [3].

The option of generating a PHOS trigger to enhance high p_T events during pp operation is currently under discussion. In this case, the PHOS has to contribute to a L2 decision in less than 100 μs.

3.4.2.3 The read-out architecture and interface to the ALICE DAQ system

The general architecture of the PHOS readout system is shown in Fig. 3.24. The analog signals from the PIN photodetectors of a PHOS module are routed to, and processed by a group of PHROCs. The data are zero suppressed and stored in a memory buffer before being moved to the ALICE DAQ system.

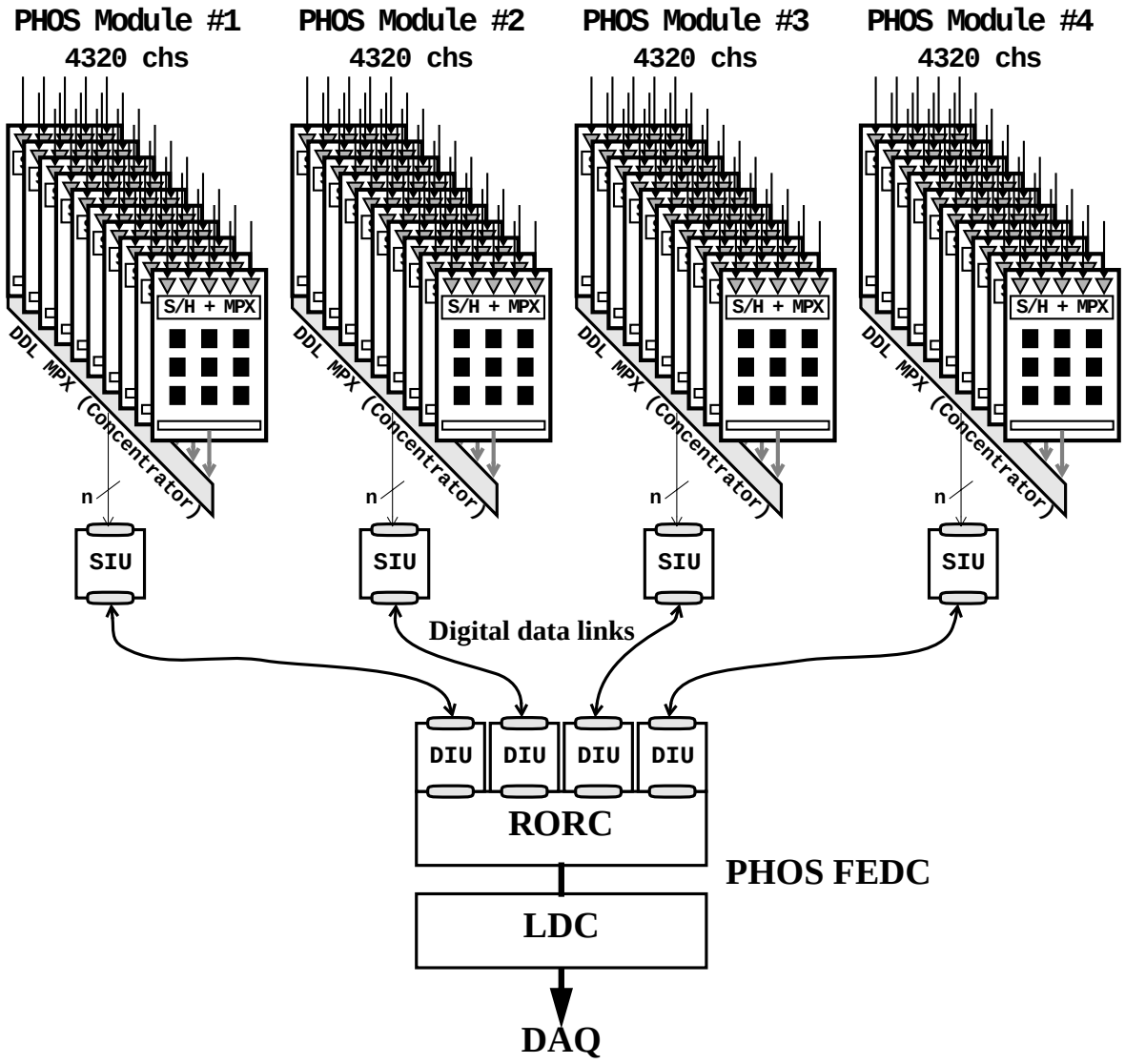

Figure 3.24: The general architecture of the PHOS FEE and readout system. *This figure corresponds to the TP version of the PHOS detector, twice as wide as the present version.*

The architecture conforms to the scheme described in Ref. [2]. The output from the memory buffers are merged by a Digital Data Link (DDL) concentrator, and transferred over the DDL to an ALICE Read-Out Receiver Card (RORC) in the ALICE DAQ system Front-End Digital Crate (FEDC). A RORC will support four DDL ports, therefore one RORC can handle the data from all four PHOS modules.

Since the PHROC is currently only in a specification phase, the on-board data buffer storage and the interconnection to the readout link is not yet defined. Furthermore, an evaluation has started within the ALICE DAQ project regarding the implementation of a readout architecture for ALICE with multiple buffering at the detector front-end level [2]. Such a feature will also influence the design of the PHOS readout chain.

The DAQ system of the PHOS will consist of one FEDC, containing one RORC, one Local Data Concentrator (LDC), and a crate processor. The crate processor will be used for local debugging, testing and data collection during calibration, integration and commissioning of the PHOS modules. The architecture of the FEDC is shown in Ref. [2].

3.5 LED Monitoring System

Although the PIN photodiodes chosen as the photodetectors in the PHOS do not require a gain monitoring, and the preamplifiers have their own calibration input, a monitoring system which can test simultaneously all the components of the PHOS channels would be very useful, especially for a general test of the PHOS modules after assembly and/or before cooling. This will allow us to check the channel matching, the optical contacts between crystals and PIN photodiodes, the transparency of the crystals, the gain factors and their stability for all PHOS channels, and the linearity of the electronic chain including preamplifier, shaper, and ADC.

The LED monitoring system is an essential part of the PHOS spectrometer. It uses Light Emitting Diodes (LED) in junction with stable current generators. It is controlled by an autonomous host computer which has the following tasks:
- control the LEDs;
- initiate a special PHOS monitoring trigger;
- synchronize it with the the trigger system.
The PHOS monitoring system is relying on the ALICE central trigger, for the distribution of the PHOS monitoring trigger and the ALICE central DAQ system to collect the monitoring data. The system will be used during and between the data-taking periods.

The Monitoring System (MS) consists of two kinds of modules; the Master Module (MM) and the Control Module (CM). The MM is located in the control room and connected by an optical link with the CMs which are located inside the PHOS.

The MMs will be produced as 9U VME modules. One MM can drive all CMs in one PHOS module. The complete monitoring system includes four MMs (which can operate in parallel) and 40 CMs (10 CMs per PHOS module), each of them consisting of 432 LED channels.

The monitoring system is controlled by a special host computer, which is connected with the MMs through the VME crate. There are three main operational modes of the monitoring system:

- 'ON/OFF' mode, i.e. the mode when each channel of the PHOS is tested for amplitude stability. The test of all PHOS channels without changing the LED intensity takes $\simeq 10$ min for 10^3 flashes per channel. This mode is used more often during a physics run.

- Amplitude scan and different pattern loading. The main purpose of this mode is a total test of the cable connections, quality of the optical contacts and the electronics chain. This test takes about 20 min for a full amplitude scan of all channels. This mode is intended for the installation stage of the PHOS and for periods between runs for checking its performance.

- Loading of the *shower pattern* and the *physical event image*. In this mode the physical performance of the PHOS based on Monte Carlo minimum bias events (which are loaded into the CM) can be estimated. The performance of PHOS will be taken 'in vitro' without beams.

3.5.1 Master Module

A block diagram of the Master Module is shown in Fig. 3.25. The pattern of the tested channels is downloaded from the host computer to the local memory of the MM. After a command from the host computer the signals are sent from the MM to the CMs. The functions of the MM are as follows:

- Loading of channel pattern into the memory of MM. In this case the PHOS channels will be checked in ON/OFF mode;

- Amplitude scan for the test of the linearity of the electronic chain. For this function the Digital-to-Analog Converter (DAC) of the CM (see Fig.3.26) is loaded with a set of special codes;

- Coding the packet function – pattern loading or 'FIRE' command;

- 'Parallel-in-serial-out' – conversion for sending the packet to the CM;
- Sending the packet to the CM.

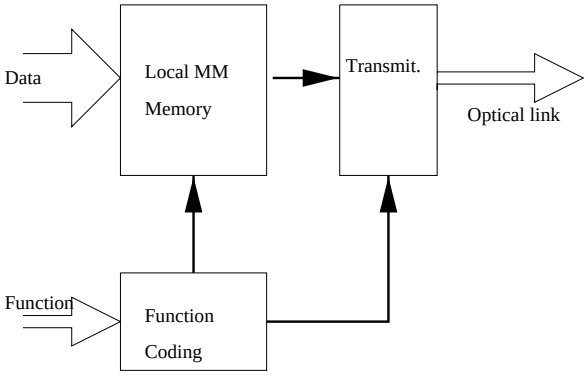

Figure 3.25: Functional diagram of the MM (Master Module).

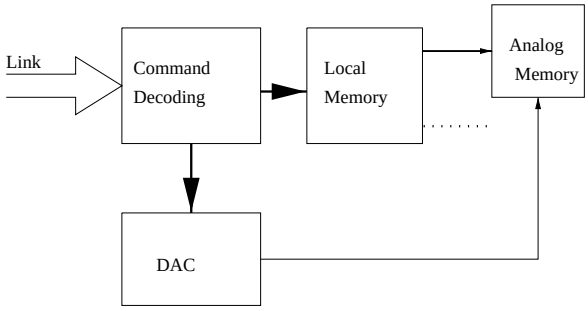

Figure 3.26: Functional diagram of the CM (Control Module).

3.5.2 Control Module

The Control Module of the monitoring system is a printed circuit board with 24 $\times$ 18 LEDs positioned centrally over the front face (beam side) of the crystals. The control circuits are mounted on the same board. A functional diagram of the CM is shown in Fig. 3.26.

The functions of the Control Module are as follows:

- decoding of the input packet from the MM;
- decoding of the received function code;
- loading of the pattern for channel testing to the local memory;
- loading of the DAC value;
- FIRE of the pattern.

The link protocol is one-directional and has the following format:

- start packet;
- type of operation (LOAD or FIRE);
- N $\times$ (DAC code, channel address), where N is the total number of channels to be tested;
- -1 (end of the packet).

The time needed for full loading of the CM is about 100 μs without changing the DAC codes. When loading a *shower pattern* the time is about 4 μs per channel and is limited only by the DAC output setting time.

For the analog part of module the following requirements have been taken into account for the CM design and the selection of the LED. The wavelength spectrum and duration of the LED flash should be similar to the one generated by the $PbWO_4$ crystals. This means that one does not need to make the light flash too short. Because the typical duration of the $PbWO_4$ scintillation is less than 100 ns and the shaping time of the PHOS preamplifiers is ~ 1 μs, the ultrabright green LED HLMP-8505 from Hewlett

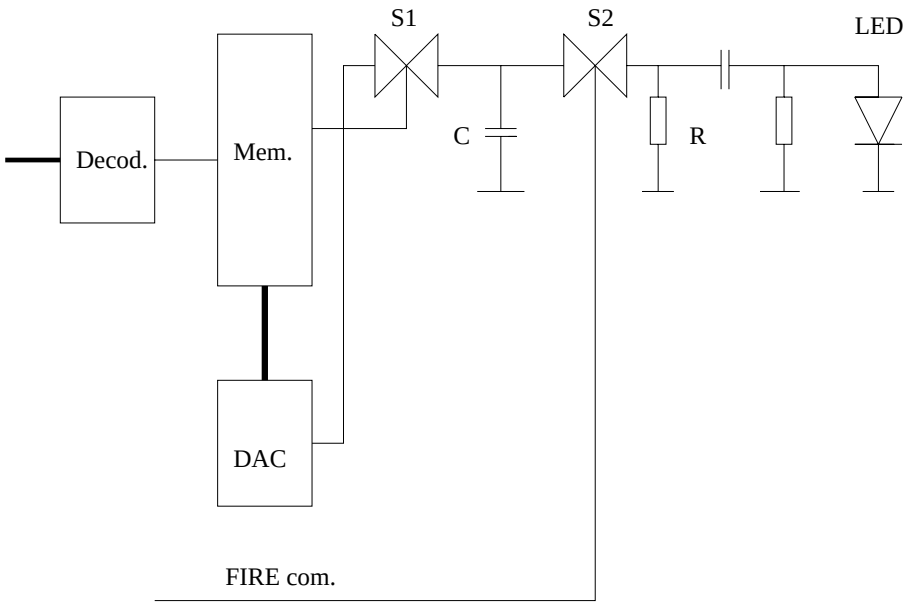

Figure 3.27: Electronic block diagram for the Control Module.

Packard is used for matching the $PbWO_4$ wavelength spectra. To minimize the difference between the LED pointlike light emission and the real distribution from an electromagnetic shower the LED surface should be diffuse.

The principal scheme of the LED driver part is shown in Fig. 3.27. The capacitance C is charged by the DAC through the connected analog switch 74HCT4066. In this case the capacitance is used as an analog memory and should have a low leakage current and high stability. After charging all channels the CM is ready to fire. The whole amount of LED light is defined by the charge kept by the capacitance C and can be changed by the DAC (in the prototype the AD5310 [4] was used). The range of the voltage on the capacitance overlaps with the whole dynamical range of the PHOS.

By the command 'FIRE' the switch $S1$ is disconnected and the switch $S2$ is connected, and the capacitance is discharged through the LED. The duration of the leading edge of the LED flash is defined by the speed of the switch, and the trailing edge is defined by the CR time constant. The spread of the light flash is $\simeq 10^{-3}$.

There are three different operational modes of the CM:

- loading pattern and DAC code in the local CM memory;
- LED 'FIRE';
- idle state with minimal power consumption.

3.5.3 Mechanical construction and assembly

The CM plates are located inside the PHOS module, directly over the crystal faces. One CM covers a region of 24×18 crystals, and is shown in Fig. 3.28. The side view of the CM plate together with the PHOS crystals are shown in Fig. 3.29. All LED, control and decoding circuits of the CM are mounted on the same PCB. The circuits are in microSOIC packages. The connector for the cable is located in the centre of the PCB. The LED monitoring system for one PHOS module consists of 10 CM boards glued on a NOMEX plate with a thickness of 15 mm.

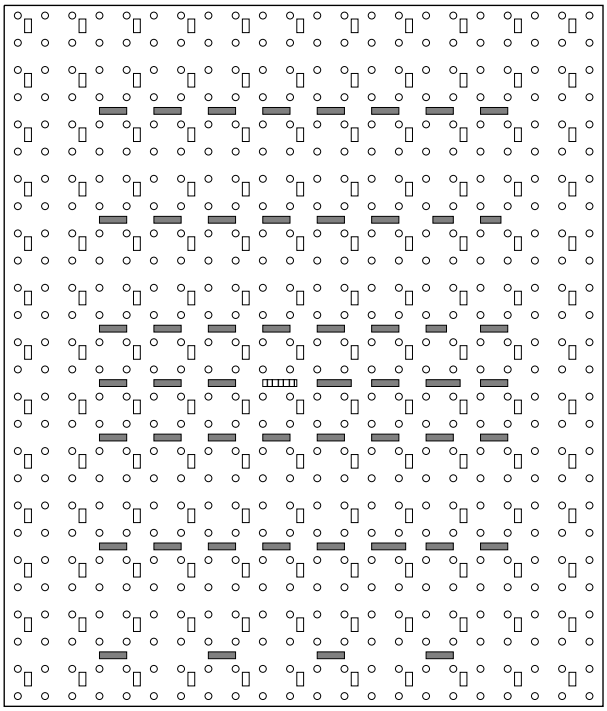

Figure 3.28: Control Module mechanical layout (front view).

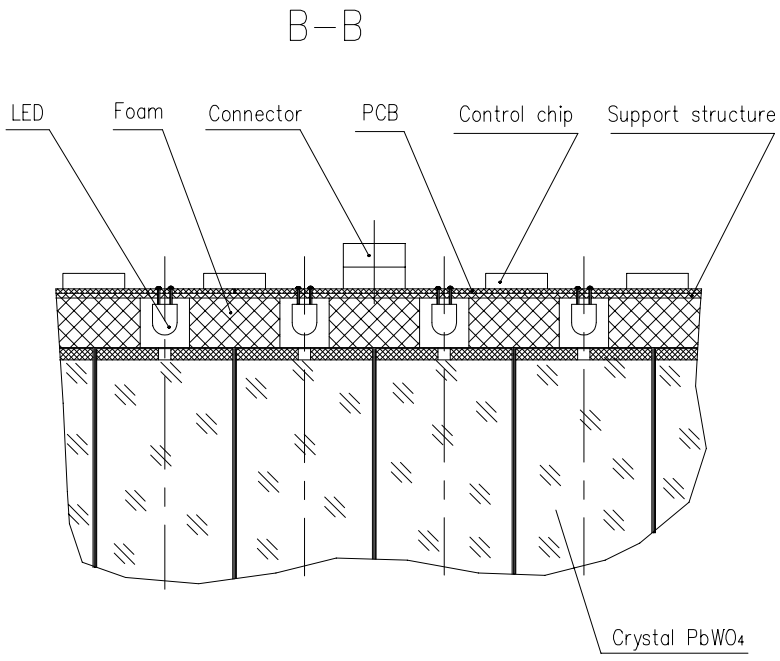

Figure 3.29: Control Module mechanical layout (side view).

The production of the PCBs for Control Modules (40 boards in total for the full PHOS) as well as assembly will be performed at IHEP. The produced and tested modules will be delivered to CERN where they will be glued onto the NOMEX plate. The final assembly of the monitoring system will be performed together with the PHOS modules.

3.6 Calibration and monitoring

In order to keep the PHOS energy and space resolution at the required level the PHOS channels have to be calibrated and monitored. The energy resolution declared in Ref. [5] and achieved at beam tests of the PHOS prototype (see Chapter 2), assumes that the gain factors will be known with a precision better than 0.5 %. Therefore the calibration coefficients obtained during the calibration procedure, as well as the monitoring coefficients used for the calibration coefficient corrections, have to be known with a precision of ~ 0.35 % during a physical run.

To fulfil the requirements mentioned a special calibration/monitoring procedure of the PHOS is proposed. Each PHOS module will be calibrated separately. The full calibration procedure includes beam test calibration/monitoring of the PHOS modules at several energies, coefficients monitoring during the data-taking, and independent PHOS calibration during the data-taking by two different methods. As it was shown at the beam tests of the PHOS prototype and in the laboratory tests of the PHOS monitoring system, the combined calibration/monitoring procedure of the PHOS provided the required level of calibration coefficient precision.

3.6.1 PHOS calibration at test beams

PHOS calibration at test beams is the essential stage of the PHOS calibration procedure. The main goals of the calibration are: monitoring the coefficients at several energies and crystal temperatures.

3.6.1.1 Calibration line

The diagram of the beam line is presented in Fig. 3.30. This line consists of the special table *Sup* for the PHOS module *PHOS* support, and the telescope of beam counters S_1–S_3 with a sensitive area $\sim 3 \times 3$ cm^2. It also includes two threshold Cherenkov counters $\check{C}_1$–$\check{C}_2$ for electron identification, two Drift Chamber blocks DC^1_{xy}, DC^2_{xy} with an aperture of 15×15 cm^2 as the coordinate detectors, trigger electronics, slow control electronics of the PHOS module and the cooling machine *CM*.

For calibration, the PHOS module, installed on the table, should be moved within limits ± 120 cm in the horizontal and ± 75 cm in the vertical direction, respectively. Positioning the table with a precision of 0.5 mm is required.

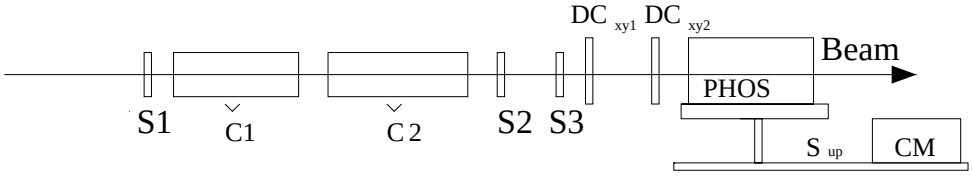

Figure 3.30: Beam-line setup for the calibration of the PHOS: $S_1 - S_3$: beam scintillation counters; $\check{C}_1 - \check{C}_2$: threshold Cherenkov counters; DC_{xy}: blocks of drift chambers, *PHOS*: PHOS module; *CM*: cooling machine.

3.6.1.2 Calibration in the electron beam

The method of electromagnetic calorimeter calibration in a wide electron beam is described in Ref. [6]. The PHOS module will be installed on a special calibration table at an angle of 30° to the beam direction (working position of two of the four PHOS modules in the ALICE environment). The calibration table will be moved by computer control across the beam to provide uniform irradiation of the crystals. As an electron shower in PHOS module will occupy several crystals, and the coordinates of the electron are not actually known, the gain factors α_i can be found by minimization of the function:

$$F(\alpha) = \Sigma_{k=1}^{N} (\Sigma_i \alpha_i A_i^k - E_{\text{beam}})^2 \,, \tag{3.1}$$

where the sum over k is spread over events N of the module, i is the crystal number with amplitude A_i^k above threshold in the k-th event, and E_{beam} is the beam energy. The system of linear equations Eq. (3.1) can be solved by iteration methods (see Ref. [6])

The module calibration can be performed at the PS test beam T9 or T10. The optimal energy of the electron beam for the PHOS calibration is 2–4 GeV. To achieve the required accuracy of the calibration coefficient, one will need to accumulate on average 500 hits of electrons in each crystal. The peripheral crystals of the module will be additionally calibrated by a narrow beam with electron coordinate measurements, because for these nodules the procedure based on Eq. (3.1) gives an overestimation of the coefficient values due to shower leakage. At a beam intensity of 100 electrons/sec we will need about 30 h for the calibration of a full PHOS module at a given energy.

3.6.1.3 Calibration/Monitoring procedure

Each module will be calibrated at room temperature at three beam energies (1, 4, and 7 GeV) and at the nominal PHOS temperature of -25° C at five beam energies (1, 2, 4, 5 and 7 GeV). Before and after the calibration at each energy/temperature the special monitoring scan of the module will be performed with the LED monitoring system. The sets of monitoring and calibration coefficients will be obtained and written into a database.

The monitoring coefficients obtained will be used for the control and correction of the PHOS calibration coefficients in future physics runs. The monitoring procedure will be repeated at the LHC during accelerator cycles (i.e. after each 20 h).

3.6.2 PHOS calibration in the ALICE environment

After the installation of PHOS the monitoring of the PHOS channels with further interpolation is the only way to correct initial calibration coefficients.

We are considering two methods in order to obtain the calibration coefficients independently from the calibration at test beams. These are: a) calibration on the base of physical events during the data-taking, and b) cosmic muon ray calibration of the PHOS between physical runs.

3.6.2.1 Calibration during data-taking

The average amplitude from a PHOS cell depends only on the geometrical position (z-coordinate) of this cell relative to the interaction point. The truncated mean of the amplitude spectrum, corrected for a geometrical factor, can thus be used for the relative calibration of cells. For the absolute calibration the π^0 peak position can be used.

At a trigger rate of 40 Hz (central trigger) one will need $\sim$ 50 min to estimate the calibration coefficient ratios with $\sim$ 1 % statistical accuracy. The systematical errors can be estimated only during real data-taking.

3.6.2.2 Cosmic muon calibration of the PHOS modules

This calibration procedure relies on the trigger properties of the charged particle veto detector CPV (see the next section for the construction details) as well as the scintillator counter, analogous to the L3 muon scintillation counter [7].

The coincidence between the signals from the CPV anode wires and the scintillator counter will select cosmic muons within angles of $\pm 15^\circ$ compared to the normal CPV plane directions. A muon passing through a PWO crystal longitudinally will deposit $\sim$ 250 MeV energy which will be readout with $\sim$ 10 % resolution. About 40 % of the muons will hit PIN-diodes and will distort signals from the PHOS cells. To suppress these muons, the coordinate information from the CPV will be used.

The intensity of the hard penetrating component of cosmic rays crossing a horizontal area is $\sim 0.8 \times 10^2$ m^{-2} s^{-1} sterad^{-1} [8] at sea level. In this case, the rate for one PHOS module will be ~ 50 s^{-1} and 10 days will be needed to accumulate a few thousand tracks to define the peak position with an accuracy of $\sim 0.5\,\%$.

3.7 Charged Particle Veto

The Charged-Particle Veto detector (CPV) is an essential part of the PHOS spectrometer. Its aims are an efficient detection of the charged particles at the front of PHOS and the measurement of their coordinates with an accuracy of about 3 mm. The CPV detector is based on the MWPC with pad readout. The CPV consists of four separate modules which are placed on the top of each PHOS module. The material budget of the CPV module is less than 5 % of X_0, which does not actually distort the photon shower development in the PHOS. The CPV materials are not sensitive to the large neutron fluxes expected in the ALICE experiment. The CPV modules are positioned approximately 5 mm above the PHOS modules.

3.7.1 Principles of operation

The CPV module is a multiwire proportional chamber with a cathode pad readout. A schematic diagram is shown in Fig. 3.31. The anode wires are oriented along the direction of the magnetic field in ALICE. The wire diameter is 30 μm. The MWPC geometry is chosen as follows: the wire pitch is 5.5 mm, the cathode-anode gap is 5 mm, and the size of the cathode pads is 22 $\times$ 11 mm^2 (22 mm along the wires and 11 mm across the wires). The gas mixture is 80 % Ar + 20 % CO_2. Further details can be found in Ref. [9].

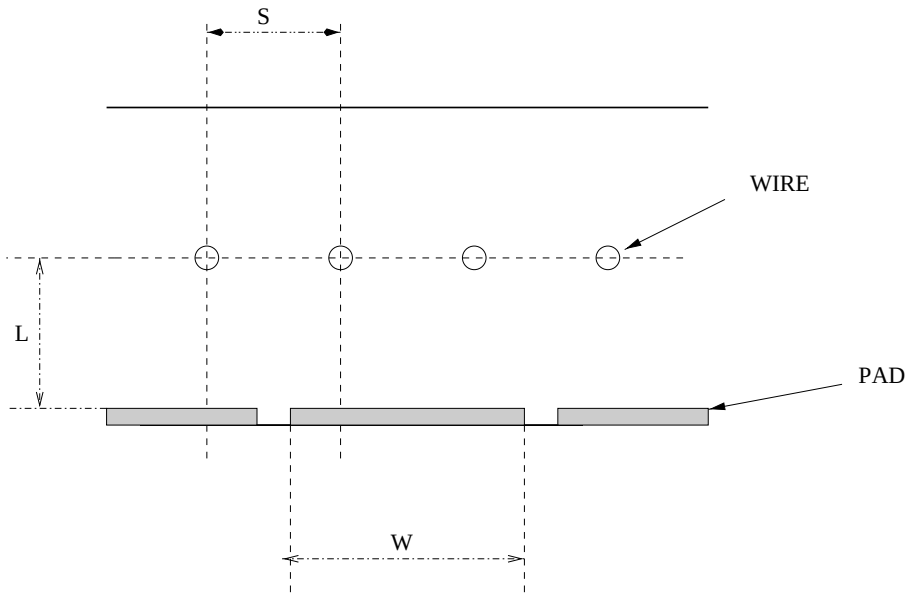

Figure 3.31: Schematic diagram of the CPV.

The two-dimensional readout is achieved by segmenting the cathode into pads and detecting the charge induced on the adjacent pads. The pad response function (PRF) relates the pad charge with the position of the avalanches relative to the pad centre. The width of the PRF is a key point for the spatial resolution of two tracks in the CPV, as well as for the accuracy of the track coordinate measurements.

The Pad Response Function (PRF) corresponding to our geometry has been calculated (see Refs. [10, 11] for details on the calculation) and the result is shown in Fig. 3.32.

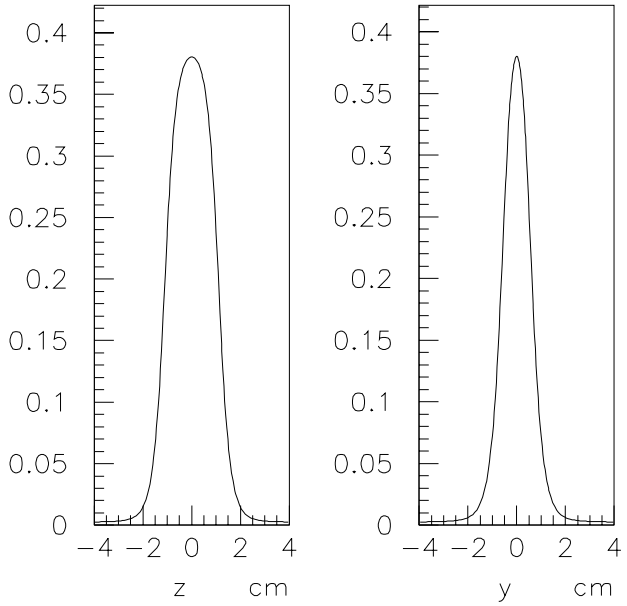

Figure 3.32: Pad Response Function. Left: $P(z,0)$; right: $P(0,y)$.

3.7.2 Mechanical design and construction

3.7.2.1 CPV design

The view of the CPV detector is shown in Fig. 3.33. Low-mass construction materials will be used for CPV production to minimize the material budget and detector weight. Each module of the CPV consists of two flat rigid panels, one of which (at the top) is made of a 20 mm thick sheet of foam and of two 0.8 mm thick copper-clad G10 foils. The outer copper cladding plays the role of the detector electromagnetic shield. The inner copper cladding forms the cathode. The cathode sheet has a fine pad structure. Schematically the pad plane is shown in Fig. 3.34.

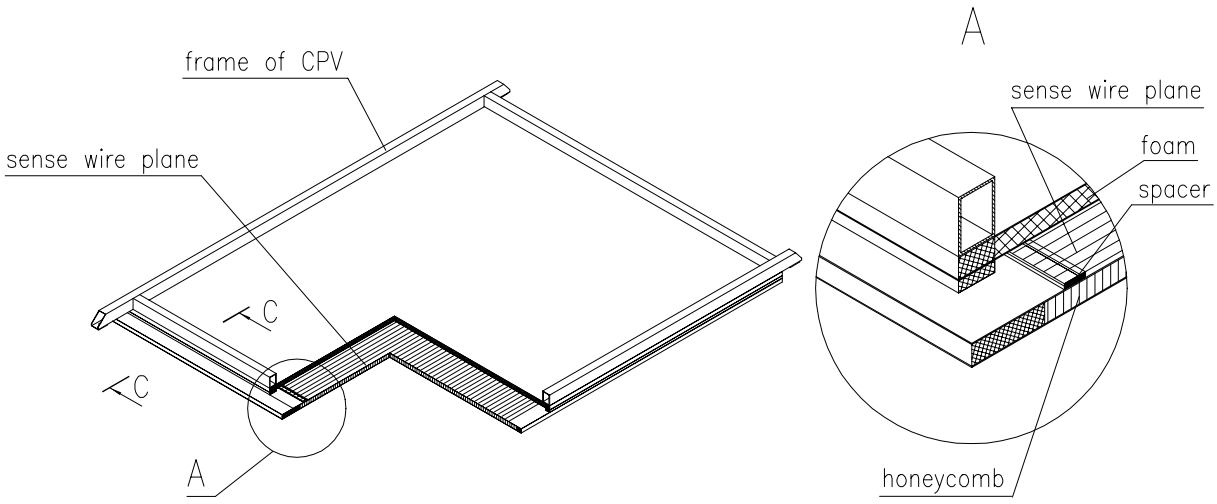

Figure 3.33: View of the CPV detector for one PHOS cradle (pad readout electronics not shown).

The other panel (at the bottom) is a composite type structure (copper-clad G10 foil, nomex HEXEL honeycomb) inserted in a metallic frame. This technology was selected in order to provide a stiff structure of the pannel with a minimum of material.

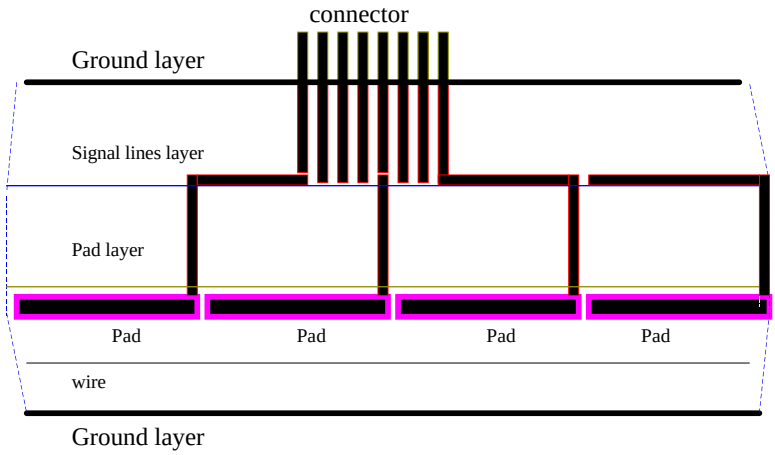

Figure 3.34: Cut-off view of the CPV cathode plane showing schematically the pad connections.

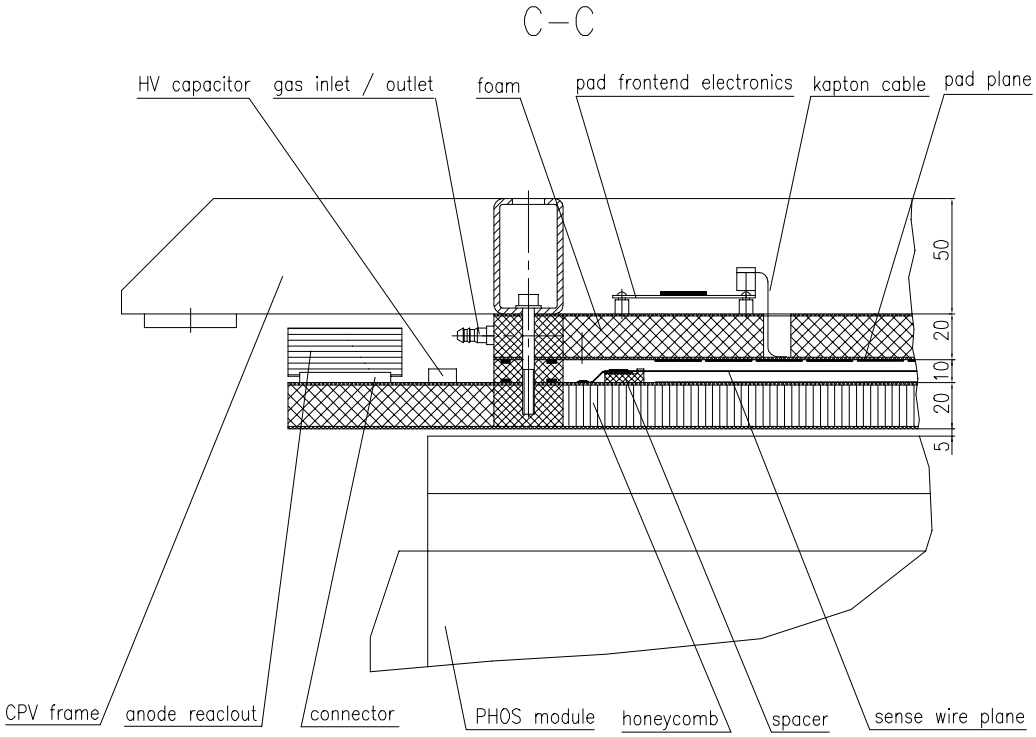

Figure 3.35: Cut-off view of the CPV module showing construction details.

The general CPV structure is shown in Fig. 3.35. The CPV consists of the pad PCB with Kapton circuits spaced by a 20 mm thick foam plate from another circuit referred to as the ground PCB. Kapton foils are soldered onto the pad PCB in rows, leaving a free space of about 20 mm between them for placing foam strips of that width. The grooves thus formed allow the Kapton foils to come out through apertures created in the ground PCB. Signals from the pads are transferred via these Kapton cables to the electronic readout board located on the top chamber panel.

Below the pad plate is the anode wire plane. The anode wires are made of gold-plated tungsten with 3 % rhenium. The wire's diameter is 30 μm. A pitch between the anode wires is achieved with a precise spacer glued on the bottom cathode plane. In order to pass over the frame region, the wire trace is enclosed between two G10 foils of 1 mm thickness ensuring HV insulation. Outside the chamber, at each end of the anode wires, traces are pulled in groups of eight to a well-insulated flat connector. On

one side of the chamber the special PCB is used to make the HV distribution. A rubber gasket between two adjacent planes provides the gas seal for the assembly.

3.7.2.2 Assembly procedure

The key construction elements of the CPV are the lithographically produced pad cathode and the board with the readout electronics located on the other side of the cathode plane. The other important element of the CPV construction is the layout for the fixation of the anode wires, which includes anode wire supports of machinable ceramic Macor and support lines in the middle of the modules. These support lines are made from wire, coated with a slightly conductive material.

The assembly of the CPV module will be performed on a granite table. First the cathodes are placed face down on the table. The honeycomb sheet is epoxied to the cathode. During the epoxy curing time, the honeycomb is pressed on the cathode.

The PCB pad is glued to the frame on a granite table and then the necessary ground connections are made with conductive glue. After this, the elements are stacked and glued together under proper load, keeping the PCB pads in contact with the granite table. A flatness of ± 50 μm is achieved over an area of $\sim$ 60×60 cm^2. The ground of the PCB makes good grounded electromagnetic shielding. The pins necessary for plugging the FEE boards are implemented in the last step.

3.7.3 The CPV gas system

The CPV detector is relatively insensitive to gas parameters and is therefore immune to modest variations in temperature and pressure. It operates with a non-flammable gas mixture containing 80 % argon and 20 % carbon dioxide. Two facts make the CPV insensitive to neutron background: the gas mixture has a small volume and does not contain hydrogen. The total gas volume of the CPV is 0.095 m^3. This volume is split into four chamber Modules. Each module has volume a of $1175 \times 1990 \times 10$ mm^3 and is supplied individually with the gas.

The proposed design consists of a single pass gas system that distributes the gas to each Module at a flow rate of 4 l/h (four volume changes per day) at a pressure of 2 mbar above atmosphere. The design parameters are shown in Table 3.3.

Table 3.3: Design parameters of the gas system.

Total volume	0.095 m^3
Number of modules	4
Module volume	0.024 m^3
Gas mixture	80 % Ar+20 % CO_2
Volume exchanges/day	4
Total flow rate	16 l/h
Working pressure	2 mbar

Primary pressure regulation and system purge will be located in the surface gas building (SG). The final distribution and flow control to the individual Modules will take place on the shielding plug area in the shaft (PX24), which is accessible during LHC machine operation. Return gas will be exhausted to air in the shielding plug area. An overview of the system can be seen in Fig. 3.36.

3.7.3.1 Pressure regulation and mixing unit.

A standard LHC gas mixing unit is proposed. A three-way valve is incorporated into each supply line which will allow a small volume of gas to flow via the exhaust for purging purposes (see Fig. 3.37).

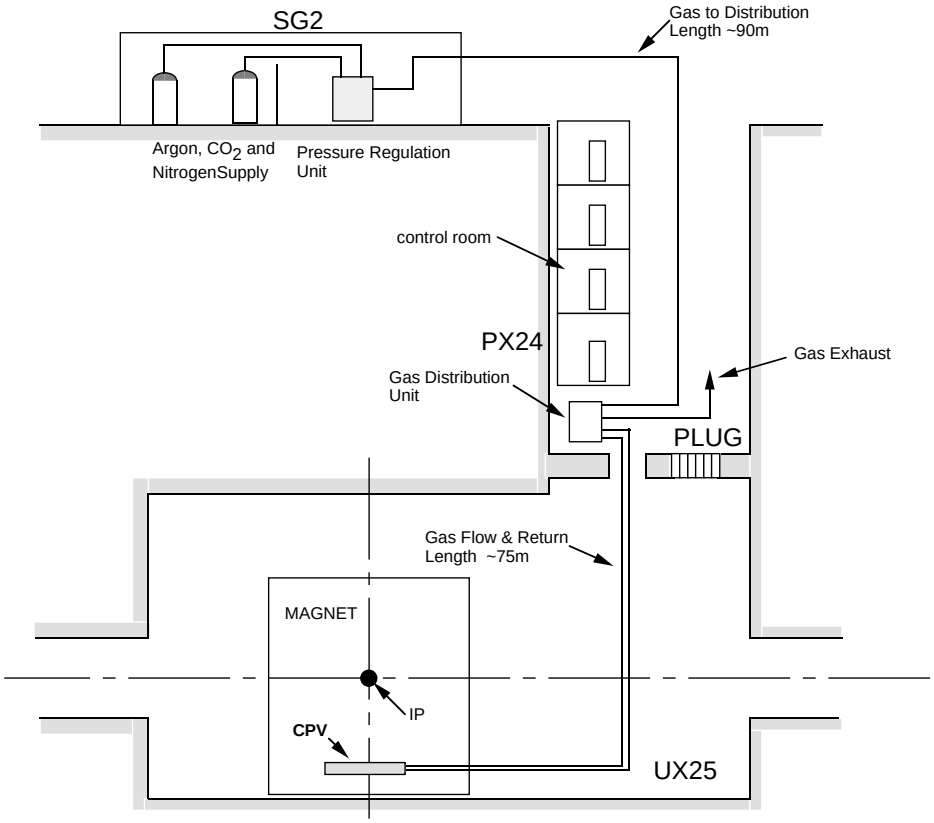

Figure 3.36: Overall view of the gas system.

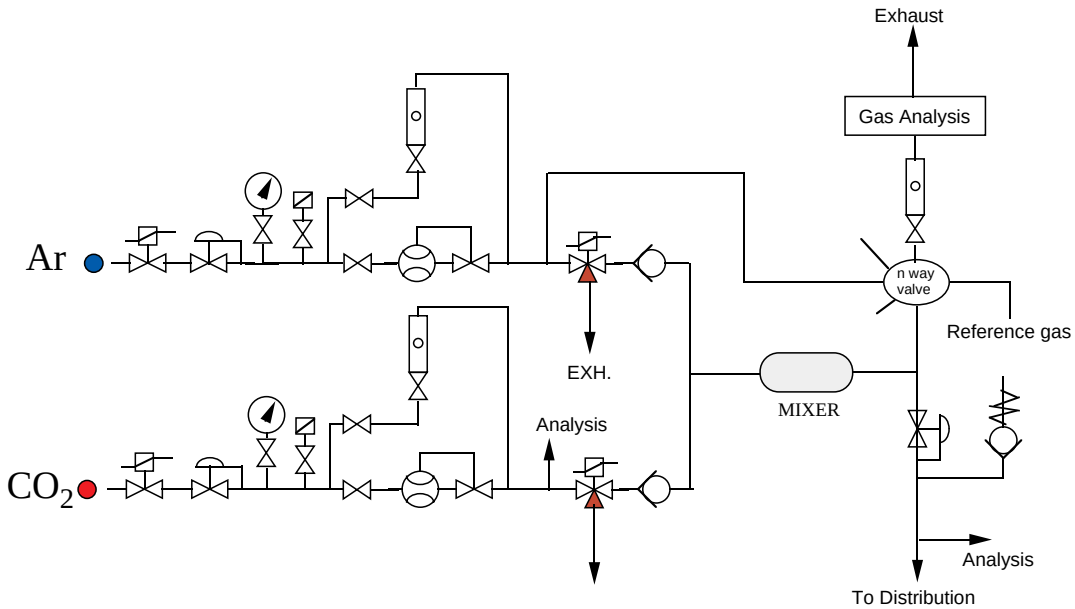

Figure 3.37: Gas mixer unit.

The gas flows are metered by mass flow controllers, with an absolute precision of 0.3 % (in constant flow conditions). Flows are monitored by a process control computer. If a second component is added, the mixing unit can either work in a constant ratio mode or, alternatively, may be derived from comparison of the running mixture with a reference gas mixture in an analysis instrument. Normal flow rates are typically about 30 % of full-scale flow. Detector filling and purging would generally be at maximum flow rate, resulting in a volume exchange time of 0.6 h. The medium-term stability (in constant flow conditions) is better than 0.1 %. Absolute stability will depend on the absolute precision of the analysing instrument.

3.7.3.2 Gas analysis

The quality of argon and carbon dioxide supplied from the CERN stores is considered adequate as far as impurities are concerned. Sampling points can be incorporated in the distribution system for the on-line measurement of oxygen and moisture in the incoming gases.

On the distribution rack, sampling points on the return gas flow from each of the four Modules will monitor gas for impurities of oxygen and moisture.

3.7.3.3 Flow distribution

Final pressure regulation and flow distribution to the four Modules will take place in the shielding plug area. Gas arriving from the surface building will pass through a pressure regulator, before being distributed and passing through individual throttle valves, Fig. 3.38. A safety relief unit is incorporated into the manifold to prevent over-pressure of the Modules. This unit will either be a simple relief valve or a rupture disk depending on the pressure limits.

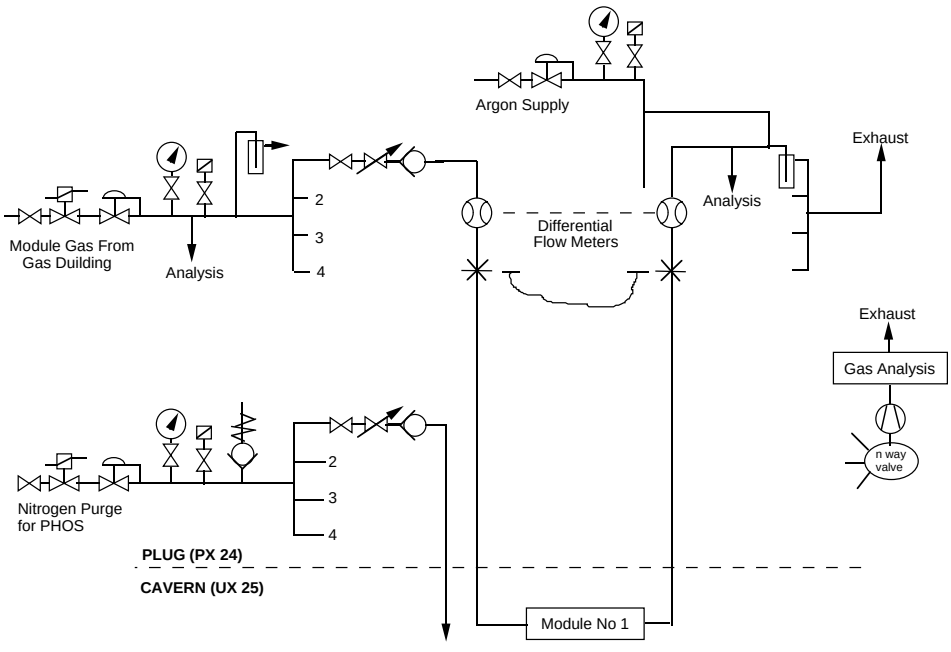

Figure 3.38: Schematics of the gas distribution system.

Differential flow meters are integrated in the flow and return lines which will allow us to adjust individual channel flows using the throttle valves.

The bubbler oil levels at the oulet will allow us to maintain the module pressure between 1 and 2 mbar above atmospheric pressure.

To prevent excess stressing of the Modules due to fluctuations in atmospheric pressure and in case of a loss of the primary gas supply, a system of back-filling with argon gas is proposed. This allows us to fill or ballast gas to keep the Modules at bubbler pressure. As gas is fed in near the exhaust outlet no dilution of the module gas will occur.

3.7.3.4 Distribution pipework

All tubes, valves, and fittings within the system will be made of stainless steel. Existing gas pipes at Point 2 will be reused as far as possible. Table 3.4 shows an overall view of the main piping parameters. At the shielding plug end they will be modified to link up with the new position of the distribution rack. In the Experimental Area (UX25) they will be extended into the L3 Solenoid Magnet, and onto the PHOS cradle. A patch panel, equipped with self-sealing quick connectors will allow disconnection for removal of the modules.

Table 3.4: Main piping parameters.

	No.	Dia.	Length
SG2-Distribution	1	22/20	90 m
Distribution-Module	4	10/8	75 m
Module-Exhaust	4	16/14	75 m

3.7.4 Electronics

The low interaction rate in ALICE allows us to use an electronics scheme with the following specific features:

- a charge-sensitive preamplifier with a large shaping time > 800 ns,
- analog charge measurements,
- multiplexed operation (MPX).

To achieve sub-millimetric accuracy of charged particle localization, for pad readout we are planning to use the HPMID electronics designed to satisfy the system requirements specific to the ALICE operational modes:

- maximum trigger interaction rates of 10 kHz and 100 kHz in ion and proton collider modes, respectively;
- the possibility to mount the detectors with a surface density of 4 kchannel/m^2. The adopted multiplexed analog schematic is composed of two parts:
- an analog part based on the CMOS VLSI front-end chip GASSIPLEX, providing 16 analog multiplexed channels,
- a digital part performing the digitization and synchronized zero suppression.

3.7.4.1 Front-end chip GASSIPLEX and its operation

The 16-channel GASSIPLEX chip is composed of several function blocks per channel (see Fig. 3.15 of Ref. [12]) a charge sensitive amplifier (CSA), a switchable filter (SF), a shaping amplifier (SH) and a Track/Hold stage (T/H). The measured performances of the GASSIPLEX 1.5 and 0.7 μm versions are shown in Table 3.5, taken from Ref. [12], which should be consulted for further details.

Table 3.5: Measured performances of the GASSIPLEX 1.5 and 0.7 μm versions

		GASSIPLEX V. 1.5 μm	GASSIPLEX V. 0.7 μm
Silicon area	mm^2	$4.2 \times 4.6 = 19.3$	$3.46 \times 4 = 13.8$
VDD/VSS	V	± 3.5	± 2.5
Noise at P.T.* = 500 ns	r.m.s. e	630 at 0 pF	485 at 0 pF
Noise slope at P.T. = 500 ns	e r.m.s./pF	16	15.8
			12.0 at P.T. = 1 μs
Noise at P.T. = 1 μs	r.m.s. e		585
Linear dynamic range	fC	-75 to 150**	-250 to 300
Conversion gain	mV/fC	12.3	4.9
Base line recovery		$< 0.5\%$ μs after 3	$< 0.5\%$ after 3 μs
Range peaking time	ns	400 to 650	400 to 1000
Power consumption	mW/chan	6	6
Analog readout speed	MHz	10	10 max

* P.T. = Peaking Time.

** $\times 2$ when operated in silicon mode.

The GASSIPLEX is an ungated, asynchronous device, which means that its inputs/outputs are always sensitive. Therefore, when the T/H signal is set, each output is raised at constant DC level. Measuring the fluctuation of the pedestal level gives the noise level of this channel which is the r.m.s. of a pedestal distribution. Calling PED(i) and SIG(i) the average and r.m.s. values of the pedestal distribution, the operating threshold of the channel (i) is defined as:

$$TH(i) = PED(i) + N * SIG(i) \ ,$$

where N is a selectable constant, usually ≥ 3.

This procedure has the essential advantage of attributing the correct threshold value to every channel, regardless of the gain, noise figure, and pedestal spread among the channels and is, in fact, the prime reason to have chosen an analog-based operation.

In order to exploit the physics data correctly, the basic state of the system, i.e. the pedestal and noise tables of all the channels, must be known, and their stability should be under control. This operation is referred to as a 'pedestal run' providing the necessary pedestal and threshold tables which are stored in the memories of the digitizer/zero suppressor modules. The pedestal distributions are recorded with a pulse generator as the trigger, in the absence of any other detector signal.

In ALICE, the detectors are irradiated in a DC-mode for periods lasting a few tens of hours without beam interruption. At low interaction rates, pedestal runs could be taken in interaction mode, but as few times as possible, implying a good stability of the pedestal values between measurements, i.e. in a way similar to be used for the HMPID [12].

3.7.4.2 MultiChip Module

In order to satisfy the trigger and data flow rates expected in pp and Pb-Pb operational modes at ALICE, the final electronic system will be organized in a serial/parallel architecture based on a modular array composed of three GASSIPLEX chips (48 channels), and a MultiChip Module (MCM) composed of one ADC and one zero-suppressor chip, referred to as DILOGIC. The analog part will still be implemented at the back of pad panels, whilst the multiplexed analog signals will now be propagated in parallel on

a bus PCB to the frame of the module where the MCMs are concentrated on a motherboard. The data transfer to the DAQ is achieved by a serial optical link (see Fig. 3.34 on p. 124 of Ref. [12]).

The data-transfer system of the CPV will be included in the HPMID data system. This system will consist of a single Front-End Digital Crate (FEDC) including four read-outreceiver boards (RORC) and one local Data Concentrator. This crate will also contain the RORCs of the CPV detector. A standard computer is also included in the system.

3.7.4.3 Anode readout and trigger capabilities of the CPV

The anode readout can be used for the PHOS cell calibration with cosmic muons. The total number of anode channels per CPV module is 352. The coincidence of the OR signals from the anode wires and the signal from the scintillation counters on top of the L3 magnet will be used for triggering the pads readout. The anode readout system similar to PCOS-III, can be used [13].

3.7.4.4 Building of the CPV Electronics

The CPV electronics contains 34 560 readout channels for pads and around 1400 for wires. The 3-GASSIPLEX cards (48 channels) are mounted on the ground PCB. The analog output signals are transferred through Kapton cables to eight power/slow control boards (Fig. 3.39). The total amount of components for the pad readout are shown in Table 3.6.

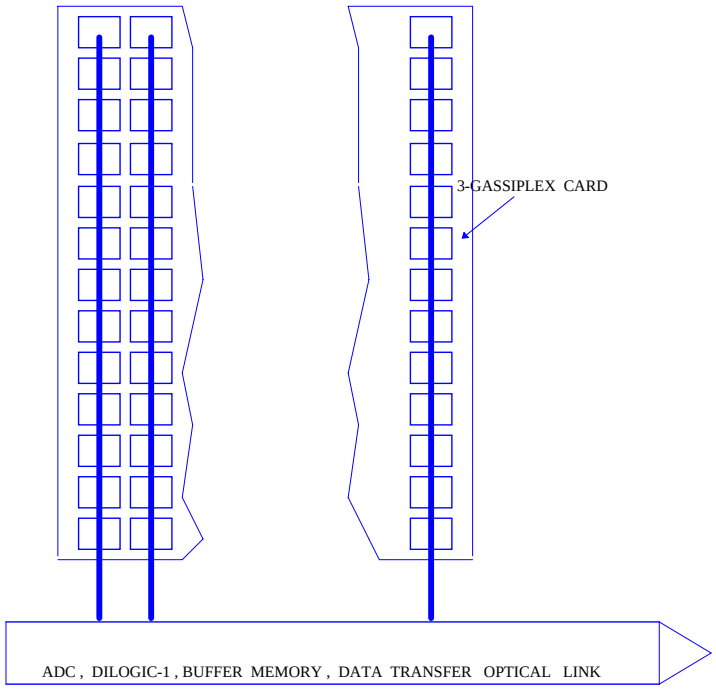

Figure 3.39: Schematic cable communications between the electronics units for the pad read-out in one CPV cradle.

3.8 Slow control

The ALICE detector control system (DCS) is characterized in Ref. [2] and will be described in detail later in the ALICE Computing Technical Proposal. The signals to be controlled and monitored for the PHOS and CPV are listed in Tables 3.7 and 3.8, respectively.

Table 3.6: Electronics for the CPV pad readout.

ASIC chips:	
GASSIPLEX-0.7-1	2288
DILOGIC-1	764
Cards and Boards:	
3-GASSIPLEX card	764
MCM processor card	154
Column bus card	78
CMRW protocol card	764
Power/slow control board	8

Table 3.7: Main parameters of the detector control system for the PHOS.

Systems Subsystems	Location	Controlled parameteres	Number	Type	Parameters	Control
Nitrogen	PX24	Primary flows	4	Analog	Flow	Read
filling and	PX24	Primary pressure	4	Analog	Pressure	Read
FEE cooling	PX24	Safety switch	1	Binary	Voltage	On/Off
	Detector	Temperat.	4	Analog	Temperat.	Read/Write
	Detector	Pressure	4	Analog	Pressure	Read
LV supply	UX25	Voltage	36	Binary	Voltage	On/Off
for PIN	UX25	Temperature	36	Analog	Temp.	Read
and preamp.	UX25	Current limit	36	Digital	Threshold	Read/Write
-6,+12,+80V	UX25	Voltage limit	12	Digital	Threshold	Read/Write
	UX25	Voltage	24	Analog	Voltage	Read
	UX25	Voltage	12	Analog	Voltage	Read/Write
LV supply	UX25	Voltage	36	Binary	Voltage	On/Off
$\pm$6,12,24	UX25	Temperature	36	Analog	Temp.	Read
FEE	UX25	Current limit	36	Digital	Threshold	Read/Write
Crystal	PX24	Voltage	12	Binary	Voltage	On/Off
temperature	PX24	Temperature	12	Analog	Temp.	Read
measurement*)	PX24	Current limit	12	Digital	Threshold	Read/Write
	PX24	Voltage	12	Analog	Voltage	Read
	Detector	Temperature	616	Analog	Temper.	Read
Cooling	PX24	Voltage	3	Binary	Voltage	On/Off
and	PX24	Coolant level	4	Analog	Voltage	Read
thermo-	Detector	Coolant temp.	14	Analog	Temper.	Read
stabilization	Detector	Coolant flow	2	Analog	Voltage	Read
	Detector	Temperature	32	Analog	Voltage	Read
	PX24	Voltage	4	Binary	Voltage	On/Off

*) To reconstruct temperature fields inside a module with a precision of 0.1°C one will need to install 154 T-sensors in each module. ADCs for the T-sensors, readout will be integrated in the FEE electronics. Data will be passed to the main DAQ and at the same time to a stand-alone data aquisition system for temperature monitoring.

Table 3.8: Main parameters of the detector control system for the CPV.

Systems Subsystems	Location	Controlled parameters	Number	Type	Parameters	Control
Gas supply	PX24	Primary flows	10	Analog	Flow	Read
	PX24	Primary pressure	7	Analog	Pressure	Read
	PX24	Purity control	2	Serial IF	Complex	Read
	PX24	Safety switch	1	Binary	Voltage	On/Off
	UX25	Gas press MWPC	8	Analog	Pressure	Read
	UX25	Gas flow MWPC	4	Analog	Flow	Read
	UX25	Current limits	4	Analog	Threshold	Read
	Detector	Temperat.	20	Analog	Temperat.	Read/Write
LV	PX24	Readout electronics	24	Analog	Voltage	Read/Write
	PX24	RO sign.CNtrl	24	Binary	Voltage	On/Off
	PX24	FEE	24	Binary	Voltage	ON/OFF
	PX24	MWPC FEE supply	16	Analog	Voltage	Read/Write
	PX24	FEE current monitoring	16	Analog	Current	Read
	PX24	Current limits	16	Binary	Thresholds	Read/Write
	PX24	Chamber	16	Binary	Voltage	Read/Write
	PX24	Chamber	16	Binary	Current	Read
HV	PX24	Chamber voltage	4	Analog	Voltage	Read/Write
	PX24	Chamber current	4	Analog	Current	Read
	PX24	Current limits	4	Analog	Voltage	Read/Write

The validation of the design choices for the overall ALICE DCS is being performed with different sub-systems in the context of a common control project for all LHC experiments: Joint Controls Project [14]. The architecture of the ALICE detector control system will be based on a commercial supervisory system and off-the-shelf controller hardware connected through standard communication systems.

3.8.1 PHOS slow control

The slow control system of the PHOS detector will provide the following functions:

- Monitoring of the temperature field in the crystals of the detector modules;
- Control and monitoring of the cooling and thermostabilization systems;
- Monitoring of the nitrogen purging (filling) system;
- Temperature monitoring of the front-end electronics;
- Control and monitoring of power and bias supplies for the PIN photodiodes and preamplifiers;
- Control and monitoring of the front-end electronics power supplies.

3.8.2 CPV slow control system

The slow control system of the CPV detector will provide the following functions:

- Control and monitoring of the CPV gas system;
- Control and monitoring of power supplies for the CPV front-end electronics;
- Control and monitoring of the HV power supplies.

4 Detector performance

4.1 Introduction

In this chapter the results of simulations of the PHOS and CPV performance are presented.

The following studies have been carried out via simulations:

- extraction of π^0 and η mass peaks from the two-photon invariant mass spectra obtained with the PHOS in the high multiplicity environment of central Pb–Pb collisions;
- PHOS occupancy in the ALICE experiment;
- light propagation in lead-tungstate using a specially developed code;
- energy and position resolution of a prototype PHOS calorimeter for different incidence angles and different gaps between the crystals;
- unfolding overlapping showers to identify photons and to discriminate charged hadrons, neutrons and antineutrons using the first version of the PHOS hit reconstruction algorithm;
- performance of the CPV detector.

4.2 Light propagation in the lead tungstate crystals

A simulation study of the scintillation light propagation in the lead-tungstate crystals of different lengths has been performed using a specially developed Monte Carlo code. The description of the approach and detailed discussions of the results can be found in Ref. [1]. Here a brief summary is presented.

In the simulation, a light collection efficiency ε has been calculated for different crystal areas, different types of optical coupling between the crystal and PIN-diode, different types of crystal wrappers, and different qualities of the crystal surface. This quantity was defined as follows:

$$\varepsilon = \frac{N_{\mathrm{phdet}}}{N_{\mathrm{phtot}}} , \tag{4.1}$$

where N_{phdet} is the number of the crystal scintillation photons which reach the PIN-diode and therefore are detected and N_{phtot} is the total number of scintillation photons produced due to the deposited energy.

In the simulation, the lead tungstate crystal experimental emission spectrum (see Chapter 2), as well as absorption length were used. The quantum efficiency of the PIN-diode was also taken into account.

The dependence of the light collection efficiency on the distance from the scintillating volume to the PIN-diode was obtained via Monte Carlo simulation and then parametrized by the function

$$\varepsilon(d) = \varepsilon_0 \times \exp(-kd) , \tag{4.2}$$

where d is the distance (along the crystal length) from the scintillating point to the PIN-diode, ε_0 is the light collection efficiency for the scintillation occuring at zero distance and k is the effective light absorption coefficient of the lead-tungstate crystal. The parameter ε_0 depends on the crystal area.

A fit to the Monte Carlo simulated dependence of ε on d for the 20 cm length crystal, gave the following values for the parameters ε_0 and k:

$k = 0.009$; $\varepsilon_0 = 0.018$ for the PIN-diode of 0.5 cm^2 area,
$\varepsilon_0 = 0.057$ for the PIN-diode of 1 cm^2 area,
$\varepsilon_0 = 0.16$ for the PIN-diode of 2 cm^2 area.

The dependence of the light collection efficiency on coordinates x and y in the (x,y) plane (perpendicular to the crystal length) at distance d was parametrized by the function:

$$\varepsilon(x,y,d) = A(d) + \frac{B(d)}{1+\exp[(x^2+y^2-C(d)]/D(d)} \ , \tag{4.3}$$

where the parameters A, B, C, and D depend on the distance from the PIN-diode and on the PIN-diode area.

This parametrization allows us to perform a rather simple simulation of the light propagation in the crystal by using Eqs. 4.2 and 4.3 instead of a time-consuming full Monte Carlo simulation.

In Fig. 4.1 the result of simulations of the light collection efficiency for different wrappers is shown. In the simulation it was assumed that the scintillating volume is a layer of thickness 1 cm. The light efficiency is plotted vs. the layer distance from the front end of the crystal (the PIN-diode is glued to the back end). As can be seen, no visible effect on the wrapper was observed. This simulation result is in good agreement with the experimental test result (see Chapter 2). On the other hand, a quite significant effect of the refraction index of the optical coupling material was observed in the simulation: increasing the refraction index from 1.5 to 1.7 leads to increasing the light collection efficiency by a factor of 1.55.

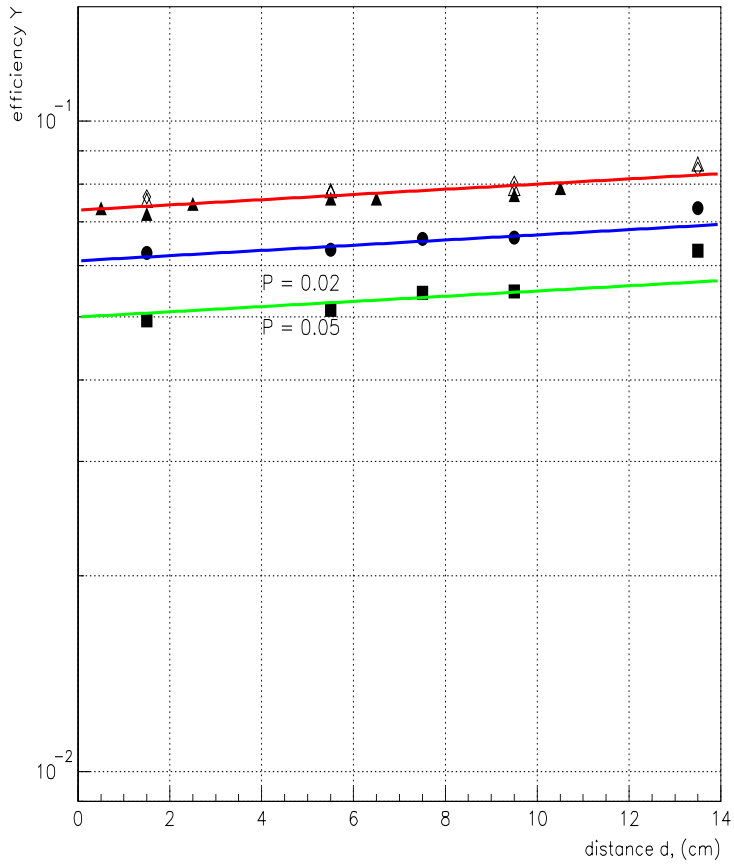

Figure 4.1: Light collection distribution vs. distance from the generation point to the crystal front for different wrappers (open triangles – Tyvek, full triangles – Mylar and open rhombus – paper) and different diffusion value P of the crystal surface (full circles and squares). $P = S_d/S_k$, where S_d is the area of scratches and S_k the crystal's area.

4.3 Energy resolution

A number of effects contribute to the resolution of electromagnetic calorimeter. The different effects are dominating in different energy regions. At intermediate and low energies the most important are:

- electronics coherent and incoherent noises in readout channels;
- light yield and scintillation light collection efficiency;
- overlapping background hits.

Usually, the energy resolution can be parametrized as:

$$\frac{\sigma_E}{E} = \sqrt{\left(\frac{b}{\sqrt{E}}\right)^2 + \left(\frac{a}{E}\right)^2 + c^2}\,, \tag{4.4}$$

where the energy E is in GeV, b represents the stochastic term, a represents the system noise, and c represents the constant or systematic term.

The low-energy regime is characterized by the importance of the value of a which is caused by the contribution from the coherent and incoherent electrical noise in the readout channels. Soft particle background also contributes to the noise term and is quite important at low energies.

The stochastic term dominates at medium energies ($\sim$ 5–10 GeV) and represents the influence of photoelectronic statistics on energy resolution.

For crystals with a high refraction index it is crucial to optimize the detector's construction from the point of view of light collection, surface treatment and optical coupling between the crystal and the PIN-diode (see previous subsection).

The constant term becomes very important at very high energies. It is defined by geometry effects (including shower leakage, inactive materials), shower fluctuations and intercalibration errors. The influence of this term on the properties of the PHOS detector in the energy range of interest is negligible.

4.3.1 The simulations of the energy resolution

To study the performance of the PHOS calorimeter, a part of it has been simulated using GEANT 3.21 [2]. The simulated detector corresponds to the actual one which was assembled and then tested at the CERN PS and SPS beam lines. The prototype is an 8×8 array of $PbWO_4$ modules. Each module consists of an $2.2 \times 2.2 \times 18$ cm^3 $PbWO_4$ crystal wrapped with a 100 μm thick Mylar layer. The front of the crystal and its two opposite sides are covered with 50 μm thick titanium. The remaining gap between the two adjacent modules is filled with air, so that the total thickness of inactive material between the crystals amounts to 600 μm.

The simulation of the prototype was performed in the energy range 0.2–10 GeV. As a first step, the simulations of the relative energy resolution, defined as σ_E/E for the sum of nine modules were performed without taking into acccount the electronic noise. Thus, a lower limit on the energy resolution was estimated. The results for the configuration with 100 μm gaps between crystals show that the constant and stochastic term may be as low as 0.78 ± 0.03 % and 2.48 ± 0.02 %, respectively. An increase of the gap thickness from 100 μm to 1.0 mm deteriorates the relative energy resolution at 0.5 GeV by 20%. On the other hand, when we include 10 MeV noise (corresponding to the 1997 year tests results), there is almost no dependence of the energy resolution on the width of the gaps, because at low energies the electronics noice dominates. The simulation of the energy resolution has also been performed for different angles of incidence. Almost no influence of the angle of incidence for angles up to 13° on the energy resolution was found.

4.4 Simulation of PHOS response in the ALICE environment

An event generator which produces the highest rapidity density expected in Pb–Pb collisions, i.e. 8000 charged particles per unit of rapidity, was used for the simulation of the yields and spectra of the primary particles. The complete response of the ALICE experiment to these particles was simulated, including the material budget of all the detectors, using the GALICE [3] and FLUKA [4] packages. The simulation gives also the yields and spectra of the secondary particles which irradiate the PHOS detector in addition to the primary particles. Then the response of the PHOS detector to the total radiation, which is the sum of these two components, was found by simulating the energy depositions in every detecting channel using the GALICE package.

4.4.1 GEANT description of the PHOS

To simulate the performance in the ALICE radiation environment, a description of the PHOS has been implemented in the ALICE detector simulation code [3] based on GEANT 3.21. The PHOS geometry in GALICE was described as follows. The PHOS consists of four modules situated at 4.6 m from the interaction point on the bottom of the ALICE experiment. The module has a 90×48 PWO crystals' matrix positioned inside a cooled volume filled with air. The crystal size is $22 \times 22 \times 180$ mm. The

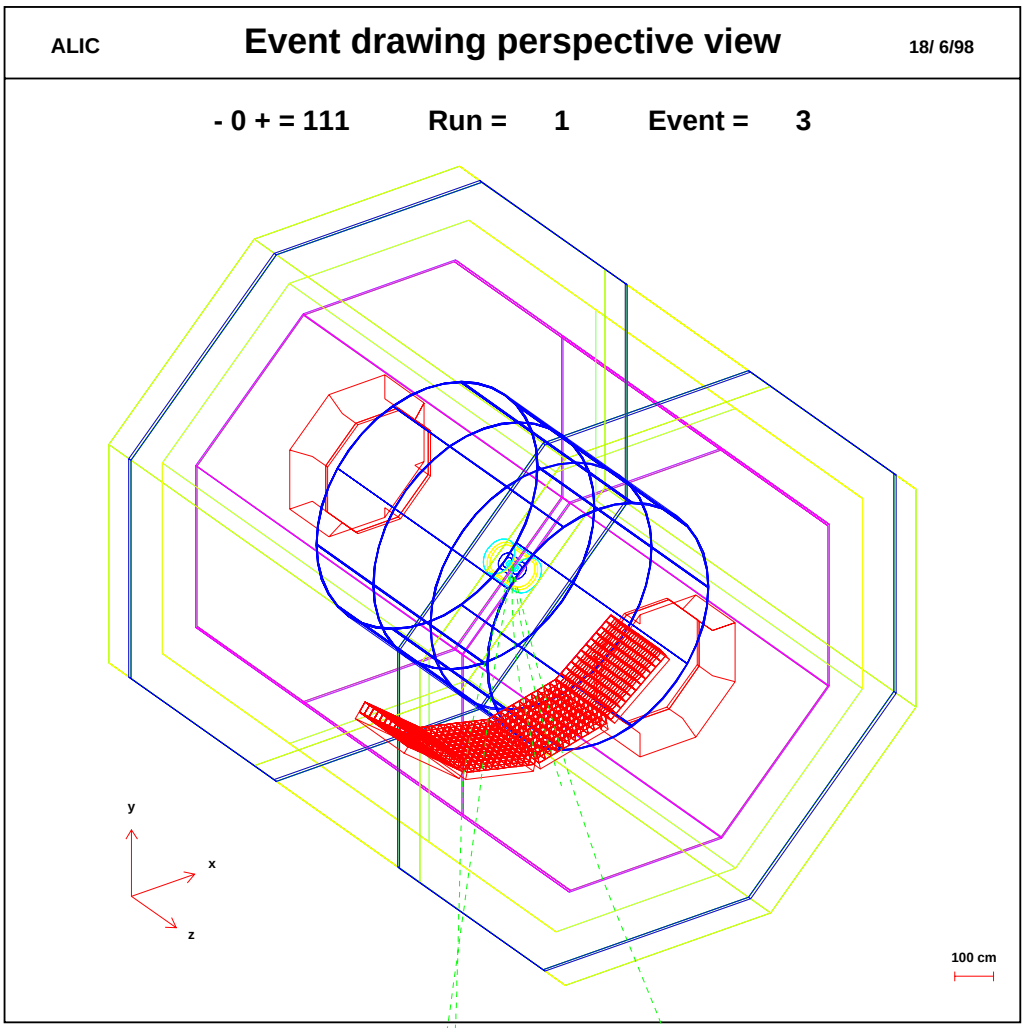

Figure 4.2: PHOS description in GALICE package. For simplicity, only PHOS is shown.

Table 4.1: Particle fluxes (in particles/m^2) obtained with FLUKA.

Particle	all η	From magnet	$\|\eta\| < 0.21$	$\eta < -1.5$	$\eta > 1.5$
π	40	0.4	32	1.4	1.7
K	0.7	–	0.7	–	–
μ	13	0.4	8.0	0.9	0.4
e	31	4.4	11.0	2.3	7.5
p	5.2	0.4	1.5	0.5	1.8
charged	90	5.6	53	5.1	11.4
γ	1100	220	120	180	560
n	2500	700	190	150	2000

Table 4.2: Particle fluxes (in particles/m^2) obtained with FLUKA. Data with different energy thresholds on the particles' energy are presented.

Energy threshold, MeV	Gammas	Neutrons	Charged
0	1100	2500	90
10	77	100	71
20	71	77	68
30	64	65	66
40	60	50	63
50	56	42	61

cooled volume is formed by a thin Al box and thermoinsulating foam pads. On the top of the Al box lies the CPV detector. The crystals are wrapped with Tyvek and clamped to an Al support plate with stainless-steel straps. A PIN-diode is attached to the rear of the crystal. This geometry is described in detail in Chapter 3. The PHOS is shown in Fig. 4.2. For simplicity, the other detectors are not shown. Some particle tracks are also shown.

4.4.2 Background simulations

The simulations were performed for central events with about 84 000 particles in the whole ALICE detector. GEANT and FLUKA simulations were performed to calculate the expected flux of background particles. The results of the FLUKA simulations are shown in Table 4.1 without any energy threshold. In Table 4.2 the particle fluxes with different energy thresholds are presented. One can conclude that most of the neutrons and γ's come from the high pseudorapidyty region, mainly from the muon absorber, and 95% of them have energy less than 10 MeV. About 20% of the γ's and 25% of the neutrons come from the bottom (from the L3 magnet). The γ flux amounts to 1100 per m^2 and most of the γ's are products of secondary interactions.

Calculations of the particle fluxes also have been performed with the GALICE package. The results are shown in Table 4.3. They are in a good agreement with the FLUKA ones, except for the low-energy neutrons which are not included correctly in the GALICE simulations. The results of the GALICE flux simulations performed only for particles emitted into the PHOS acceptance are presented in Table 4.4. The comparision of the results presented in these tables shows that most of all neutrons and low-energy γ's were produced in the surrounding PHOS structures and the L3 magnet. It should also be mentioned that the energy of most of the background particles is well below the energy deposited by a minimum ionizing particle passing the crystal along its axis ($\sim$ 250 MeV).

Table 4.3: Results of calculations of particles fluxes (in particles/m^2) obtained with GALICE. In total 84 000 primary particles were simulated in the ALICE detector.

Energy threshold, MeV	Gammas	Neutrons	Charged	Electrons	Muons	Pions
0	1126.5	1560.5	91.4	30.5	13.0	40.6
10	124.7	213.3	78.4	17.5	13.0	40.6
20	85.2	123.0	76.8	16.4	13.0	40.6
30	71.6	84.1	74.0	14.7	13.0	40.6
40	68.3	66.6	72.8	14.1	12.4	40.6

Table 4.4: Results of calculations of particles fluxes (in particles/m^2) obtained with GALICE. Only particles emitted into the PHOS acceptance are taken into account.

Energy threshold, MeV	Gammas	Neutrons	Charged	Electrons	Muons	Pions
0	63.5	29.6	42.3	8.5	5.9	25.1
10	30.5	7.9	41.2	7.5	5.8	25.1
20	27.8	4.9	40.9	7.3	5.8	25.1
30	26.2	2.7	40.6	7.1	5.8	25.1
40	25.3	2.0	40.0	6.8	5.6	25.0

The PHOS occupancy is presented in Tables 4.5 and 4.6 for different energy thresholds. All data were simulated with GALICE. In the simulation the lower energy cut for the electrons was 100 keV and the energy cut for gammas was 50 keV. The the other cuts have standard GEANT values. The module response is smeared with 10 MeV noise.

In Table 4.5 an occupancy of the PHOS in presence of all the ALICE detectors and with 84 000 primary particles in one event is shown. In Table 4.6 the results of the occupancy simulation for particles emitted in the PHOS solid angle are shown.

Table 4.5: Occupancy for PHOS (in %) in the presence of all ALICE detectors. In total 84 000 primary particles were simulated in the ALICE detector.

Energy threshold, MeV	Mod#1	Mod#2	Mod#3	Mod#4
10	39	40	41	40
20	21	23	24	22
30	15	15	16	15
40	11	12	13	12

Table 4.6: Occupancy for PHOS (in %) in the presence of all ALICE detectors. Only primary particles emitted into PHOS acceptance taken into account.

Energy threshold, MeV	Mod#1	Mod#2	Mod#3	Mod#4
10	24	28	30	27
20	9.5	13	15	11
30	5.8	8.4	9.6	7.1
40	4.7	6.8	7.8	5.6

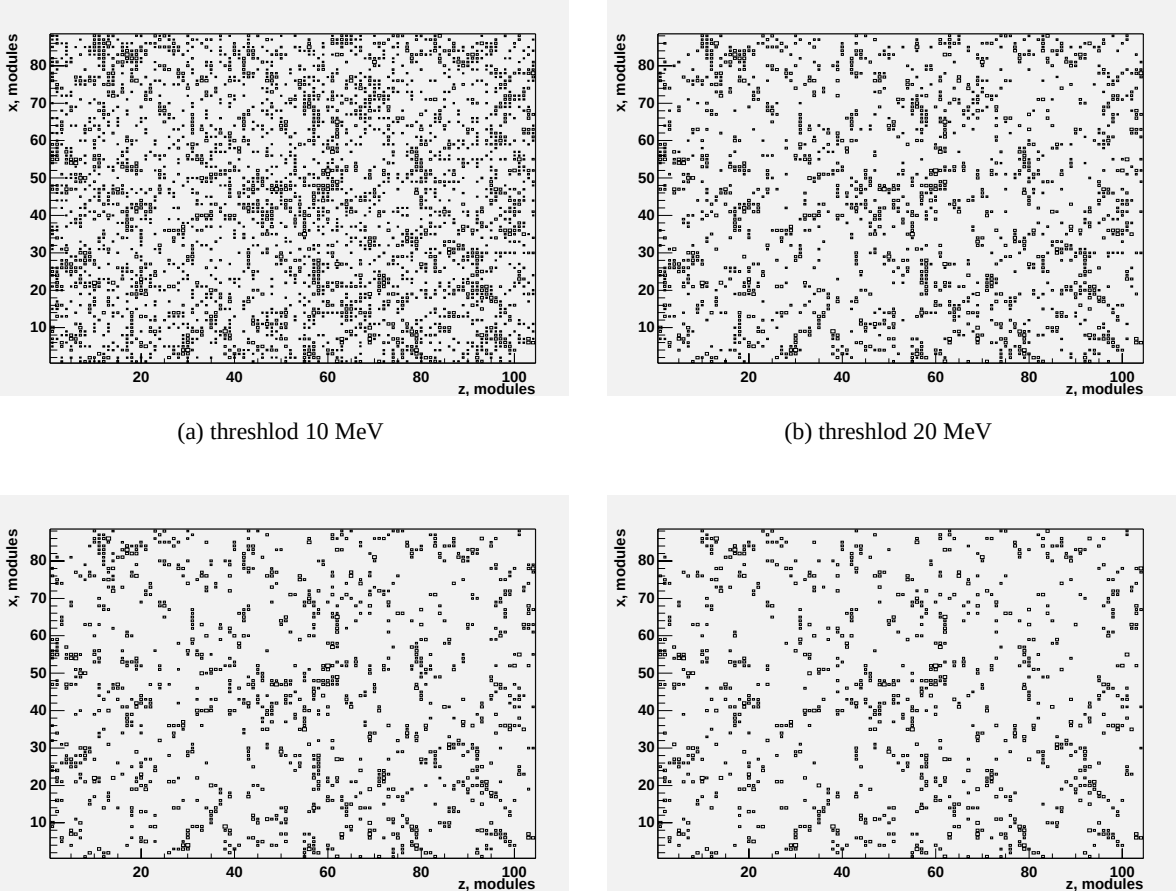

(a) threshlod 10 MeV

(b) threshlod 20 MeV

(c) threshlod 30 MeV

(d) threshlod 40 MeV

Figure 4.3: Displays corresponding to one Pb–Pb central event in one of the PHOS modules for different energy thresholds: 10 Mev (a); 20 MeV (b); 30 MeV (c) and 40 MeV (d). Each square represents one cell. The area of the square is proportional (in logarithmic scale) to the energy deposited in this cell.

The simulated event display for one Pb–Pb central event can be seen in Fig. 4.3 for different energy thresholds applied in every cell.

4.5 Reconstruction procedure

4.5.1 Reconstruction algorithm

In this chapter the study of the particle identification capabilities of the ALICE PHOS detector is presented. For the high particle density environment of a heavy-ion experiment the following points have to be considered:

- identification of single electromagnetic showers and misidentification of single hadronic ones as photons;
- recognition and unfolding of two or more overlapping electromagnetic showers;
- recognition of overlap between an electromagnetic and a hadronic shower.

Thus the reconstruction algorithm of a modular electromagnetic calorimeter consists of the following steps:

- cluster finding;
- unfolding of clusters resulting from overlapping showers;
- hit coordinate reconstruction;
- shower identification.

The electromagnetic showers were generated in the energy range 0.2–10 GeV. The data analysis was performed using the clustering algorithm described in Section 4.5.2. A detector energy threshold of 30 MeV was applied during clustering. Unless otherwise stated, incident particles were distributed randomly and uniformly over the square centred on the axis of one of the central cells so, that all the possible incidence angles which would occur in the full detector system are represented equally.

4.5.2 Cluster finding algorithm

The main part of the PHOS reconstruction procedure is the clustering algorithm. Figure 4.4 shows a block diagram representing the cluster-finding routine that was used to analyse the test-beam data obtained with the PHOS prototype (see Section 2.4, Chapter 2) and simulated data. This routine was implemented based on the ROOT and RALICE software packages [5].

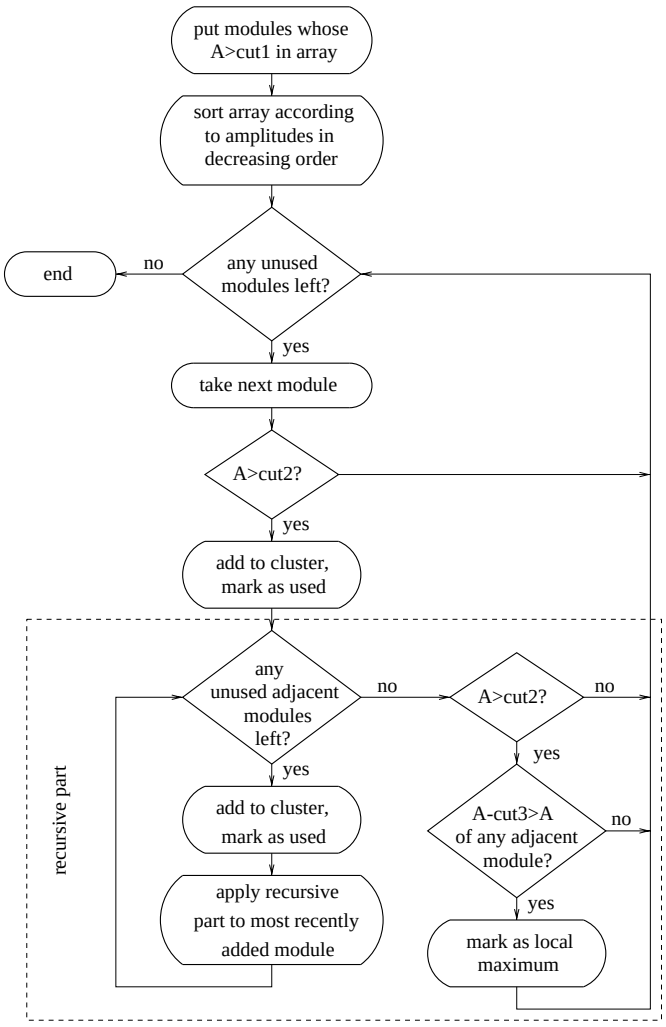

Figure 4.4: The cluster-finding algorithm. *A* is the ADC value of a cell. The meaning of the thresholds *cut1*, *cut2* and *cut3* is explained in the text.

A cluster is a group of adjacent cells whose ADC values are greater than the noise threshold, considering as adjacent any two modules that share a common side or corner. First, all cells with signal amplitudes above the noise threshold (*cut1*) are arranged according to their amplitudes in decreasing order and a cluster is formed around the first one whose ADC value is greater than *cut2*. Then the next unused cell is taken as a cluster centre, a cluster is formed around this one and so on. If one of the cells belonging to a cluster has an ADC value greater than *cut2* and at the same time its signal is higher than the signals of all the adjacent cells at least by a certain value *cut3*, this cell is marked as a local maximum. It turned out that the efficiency of the procedure is not very sensitive to the values of *cut2* and *cut3*. For this study they were 100 MeV and 60 MeV, respectively.

Further analysis depends on the number of local maxima in the cluster. If the cluster has only one maximum, it is considered as originating from a single particle, whilst if there are several maxima in the cluster, it is considered a superposition of multiple showers. In the latter case it is necessary to perform unfolding of the cluster according to the number of maxima.

4.5.3 Unfolding of overlapping electromagnetic showers

A classic method of cluster unfolding used in the WA98 experiment for the LEDA spectrometer data is described in detail in Ref. [6]. This method is based on the knowledge of lateral distribution in electromagnetic showers. The lateral distribution of electromagnetic showers as given by GEANT 3.21 is presented in Figure 4.5. The triangles in the same plot represent the experimental data. The energy deposition in one cell relative to the total energy deposited is plotted vs. the distance between the cell centre and the incident point for 10 GeV gammas at normal incidence. The solid line superimposed on the data points represents the function which provides parametrization for the data:

$$f(r,E) = \begin{cases} A \cdot \exp(-r^4/2.32) & \text{if } r < 0.5 \\ A \cdot \max[\exp(-r^4/2.32), d \cdot \exp(-r^{0.6}/s)] & \text{if } r \geq 0.5\ . \end{cases} \tag{4.5}$$

Here d = 1.97, s = 0.385, r is in cm, and f is a function which has to be normalized to the measured response by the parameter A. Unfortunately, GEANT 3.21 yields the same lateral shape for gammas

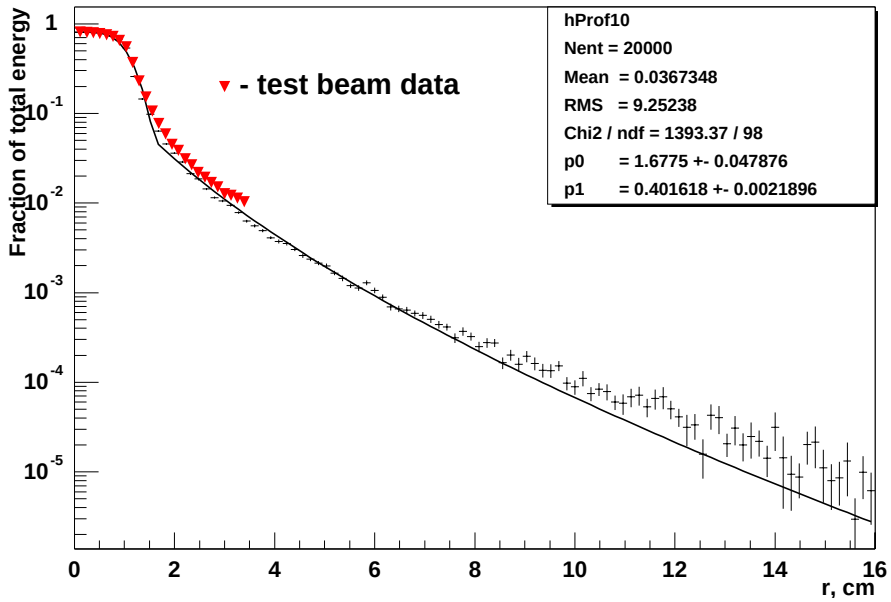

Figure 4.5: Response in one cell relative to the total energy deposit vs. the distance to the incident point of a 10 GeV gamma (normal incidence). The solid line represents parametrization according to Eq. 4.5 and the triangles show the test beam data.

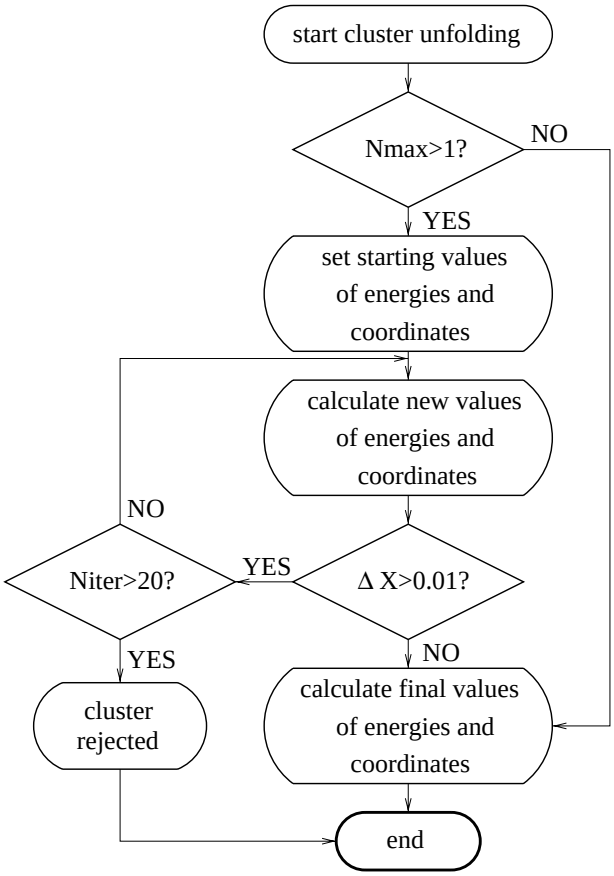

Figure 4.6: The cluster unfolding algorithm.

regardless of the energy, hence the dependence on E is contained in the normalization parameter only. Experience of WA98 shows that parameters d and s depend slightly on the shower energy. It can be seen from Figure 4.5 that the range of the test beam measurements is not sufficient to parametrize the distribution's tail. Later, when this tail will be measured to a greater extent, these dependences will be studied.

A flow chart of the unfolding algorithm is shown in Figure 4.6. The unfolding procedure itself needs the estimated energies and positions of the single showers involved as input parameters. Initial seeds for these are given by the energies and the positions of cells found to be local maxima of the cluster, i.e. the positions of the showers are given by the centres of these cells and their pulse heights are used for normalization of Eq. 4.5. Assuming that there are N local maxima in the cluster, the pulse height A_i of the ith cell is subdivided into $A_i^1, A_i^2, \ldots A_i^N$ according to the following formula:

$$A_i^k = A_i \cdot \frac{f(r_{ik}, E_k)}{\sum_{j=1}^{N} f(r_{ij}, E_j)} \; . \tag{4.6}$$

Here $f(r,E)$ is the normalised response function from Eq. 4.5. Only relative normalisation of the showers is needed in this algorithm. For the unfolded hits, new energies and positions are calculated, which are used as the input parameters for the next iteration. The next iteration is only performed if at least one of the coordinates of any shower changed by more than 0.01 cell size units, otherwise the unfolding procedure is considered to have converged. Usually 4–5 iterations are enough, but if there are more than 20 iterations needed, the cluster is not considered anymore.

According to the clustering routine, the problem of two overlapped showers was divided into two cases:

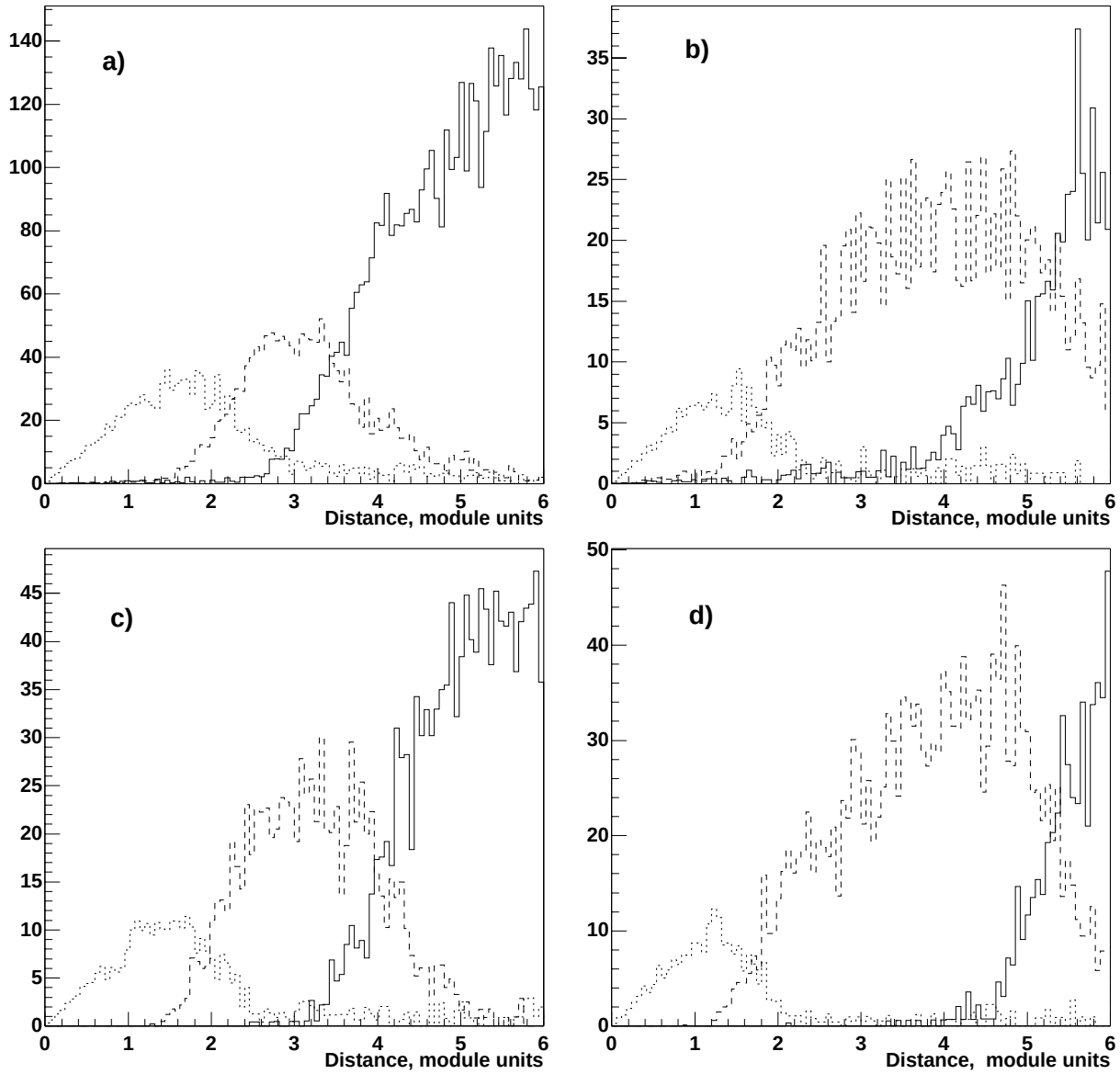

Figure 4.7: Resulting cluster type for two superimposed showers as a function of the distance between the two incident particles. The dotted line corresponds to one cluster with one maximum, the dashed line to one cluster with two maxima, and the solid line to two clusters with one maximum each. (a) 10 GeV γ + $\leq$ 1.4 GeV π^-; (b) 10 GeV γ + 2-6 GeV π^-; (c) 10 GeV γ + 1 GeV γ; (d) 10 GeV γ + 10 GeV γ. The distributions are normalized according to the distance between the two hits to reflect the phase-space density for cluster pairs.

- the resulting cluster has only one maximum;
- there are two or more maxima.

If not otherwise mentioned, the results presented in this section were obtained with a simulated 17$\times$17 cells prototype otherwise similar to the one described in Section 4.3. Pairs of particles were generated and overlapped so that all possible incident positions are presented. Figure 4.7 illustrates for different particle combinations and for different energies that clusters with one maxima occur only for small distances between the two particles ($\leq$ 2 cell size units, dotted line). Clusters with two maxima are observed at distances from 2 to 5 cell size units (dashed line) and two well separated clusters with one maximum each appear at distances larger than 5 cell size units.

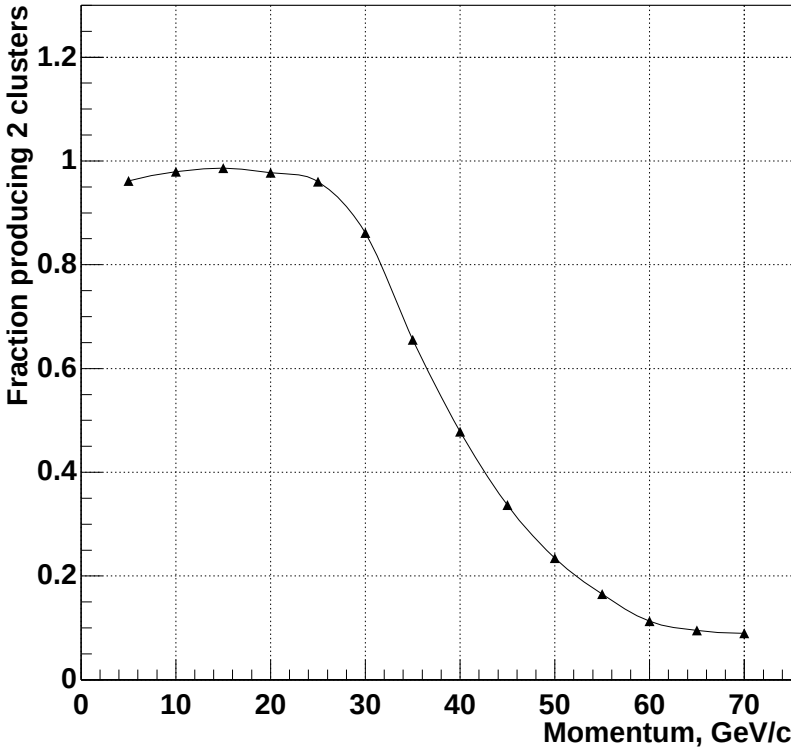

Figure 4.8: The fraction of π^0 producing two hits in the PHOS.

Figure 4.8 shows what fraction of neutral pions of different momenta decaying into two gammas produces such response in PHOS that is recognized by the reconstruction program as two hits. The data were obtained using the GALICE package [3]. Primary particles were distributed randomly and uniformly over the solid angle covered by PHOS. A pion was taken into account only if both of its gammas hit the detector. The general behaviour of the curve is easily understood: the higher the momentum of the π^0 the smaller is the most probable angle between the gammas. However, even for relatively low momenta (below 15 GeV/c) the probability of finding two hits belonging to two gammas is less than 100%. It is explained by the fact that as the momentum of the gamma decreases the probability that one of the gammas falls below the registration threshold increases.

The rest of the section is concerned with the reconstruction of clusters having multiple maxima. First, the overlap of two electromagnetic showers and then the overlap of an electromagnetic with a hadronic shower were studied. The issue of rejection of overlapping showers resulting in clusters with only one maximum is discussed in Section 4.6.1.

Electromagnetic showers of different energies were unfolded and the reconstructed position and energy were compared with the original single shower values. Four energy combinations were studied:

- 1 GeV γ + 0.5 GeV γ ;
- 1 GeV γ + 1 GeV γ ;
- 10 GeV γ + 1phantom.0 GeV γ ;
- 10 GeV γ + 3phantom.0 GeV γ .

Table 4.7 shows the results for the unfolding of these combinations. The distributions were weighted according to the distance between the two hits in order to account for the phase–space density of the

Table 4.7: Energy resolution and spatial resolution of unfolded gammas compared with single-particle resolutions.

γ energy, GeV		Energy resolution			Spatial resolution	
		Single-hit, %	Unfolded hits, %	γ energy, shift, MeV	Single-hit, mm	Unfolded hits, mm
1+0.5	1	4.78 ±0.03	5.4 ±0.3	17 ±3	3.02 ±0.04	3.3 ±0.2
	0.5	7.43 ±0.04	8.2 ±0.6	12 ±3	4.00 ±0.06	4.2 ±0.3
1+1	1	4.78 ±0.03	4.9 ±0.2	14 ±3	3.02 ±0.04	3.02±0.17
10+1	10	1.478±0.014	1.60±0.04	40 ±4	0.972±0.011	0.99±0.03
	1	4.78 ±0.03	5.33±0.14	26.1±1.8	3.02 ±0.04	3.03±0.13
10+3	10	1.478±0.014	1.62±0.05	47 ±3	0.972±0.011	1.00±0.03
	3	2.62 ±0.03	2.86±0.05	44.4±1.8	1.75 ±0.08	1.83±0.05

Table 4.8: Energy resolution and spatial resolution of unfolded gammas from an overlap between 0.5, 1 and 10 GeV gammas and pions of two different deposited energy ranges compared with single-particle resolutions.

π^- energy deposit, GeV	γ energy, GeV	Energy resolution			Spatial resolution	
		Single-hit, %	Unfolded hits, %	γ energy, shift, MeV	Single-hit, mm	Unfolded hits, mm
1– 3	0.5	7.43 ±0.04	13.4 ±0.9	77± 5	4.00 ±0.06	6.9 ±0.2
	1	4.78 ±0.03	7.7 ±0.4	88± 6	3.02 ±0.04	5.1 ±0.3
	10	1.478±0.014	2.43±0.05	179± 6	0.972±0.011	1.04±0.03
5–10	0.5	7.43 ±0.04	13.3 ±1.5	106± 8	4.00 ±0.06	8.1 ±0.6
	1	4.78 ±0.03	8.1 ±0.6	101±13	3.02 ±0.04	5.0 ±0.4
	10	1.478±0.014	3.11±0.19	203±12	0.972±0.011	1.13±0.04

cluster pairs. The energy and spatial resolution of unfolded clusters are similar to the single-particle resolutions. The sum of signals of overlapping clusters is greater than the sum of the single hits. This is because signals which are below noise threshold for single clusters may contribute to the sum if the energy of the second hit is deposited in the same cell.

Electromagnetic showers induced by 0.5, 1 and 10 GeV gammas were overlapped with ones induced by pions. Two cases were analysed:

- pion deposits of 1 to 3 GeV of energy;
- pion deposits of 5 to 10 GeV of energy.

The distributions were weighted in the same way as in the previous case. The energy resolution and spatial resolution of the gammas are influenced more by pions depositing more energy (see Table 4.8). If the charged pion deposits a large amount of energy, the gamma parameters worsen significantly. Energy deposited by the pion is carried to the gamma.

4.5.4 Incident position reconstruction

The most straightforward method to estimate the coordinate of an incident particle is to calculate the centre of gravity of the shower [7]

$$x_{\mathrm{Rec}} = \frac{\sum x_i w_i}{\sum w_i} \ , \tag{4.7}$$

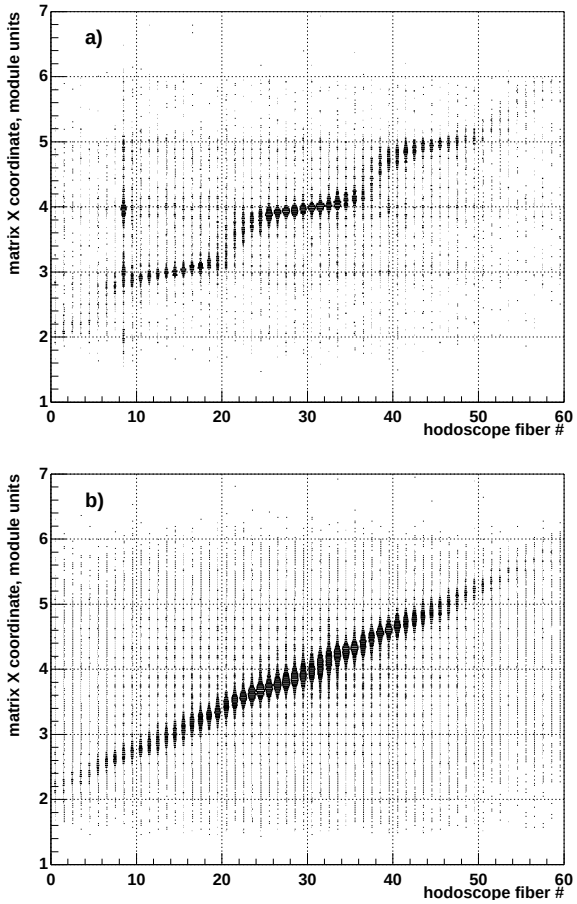

Figure 4.9: The reconstructed coordinate vs. incident coordinate. Beam test data for 2 GeV/c electrons. (a) Linear weights. (b) Logarithmic weights, w_0 = 4.5. The incident coordinate corresponds to the hodoscope fibre number. The distance between two adjacent fibres is 1.3 mm.

where x_i is the x coordinate of the centre of module i. Taking $w_i = E_i/E_{\mathrm{T}}$, where E_i is the energy deposited in ith module and $E_{\mathrm{T}} = \sum E_i$, one obtains the well-known S-shaped curve (see Figure 4.9) for the x_{Inc} vs. x_{Rec} graph [8]. Dependence of x_{Rec} on x_{Inc} can be approximated with the function

$$x_{\mathrm{Rec}} = F(x_{\mathrm{Inc}}) = \beta + d \cdot \left[\frac{x_{\mathrm{Inc}} - \alpha}{d} + 1\right] - \frac{d}{2} + c \cdot \sinh \frac{x_{\mathrm{Inc}} - \alpha - d \cdot \left[\dfrac{x_{\mathrm{Inc}} - \alpha}{d} + 1\right] + \dfrac{d}{2}}{\mu}, \qquad (4.8)$$

where square brackets represent the Gauss bracket symbol (the largest integer number less than the argument), $c = d/[2 \cdot \sinh(d/2\mu)]$ is the condition of consistency at cell boundaries, $d = 2.26$ cm is the transverse cell size and α, β, μ are the fit parameters. $\hat{x}_{\mathrm{Inc}} = F^{-1}(x_{\mathrm{Rec}})$ is an estimator for x_{Inc}.

There is another much simpler method for estimating the incident coordinate. Rather than fitting the S-curve, it is proposed to use Eq. 4.7, but instead of linear weights, the weights to be used are given by the following expression [8]:

$$w_i = \max\left\{0, \left[w_0 + ln\left(\frac{E_i}{E_T}\right)\right]\right\}, \qquad (4.9)$$

where w_0 is a free parameter.

This method is preferable than the former one since it does not require as many fitting parameters and the extremely accurate knowledge of the detector geometry, which makes it easier to apply to large

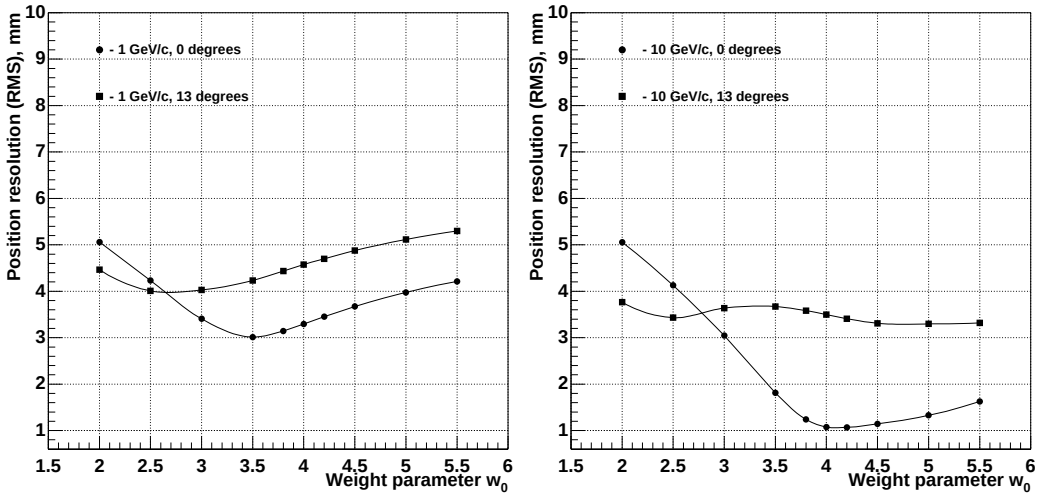

(a) 1 GeV gammas (b) 10 GeV gammas

Figure 4.10: Dependence of the position resolution on w_0. The position resolution value corresponds to the r.m.s. of the $x_{\mathrm{Rec}} - x_{\mathrm{Inc}}$ distribution.

systems. It is necessary to make the right choice of the parameter w_0 and to estimate the average difference $\langle x_{\mathrm{Rec}} - x_{\mathrm{Inc}} \rangle$ for non-perpendicular incidence. This method was chosen by the WA98 collaboration for the LEDA spectrometer data analysis. Figure 4.9 shows its effect on the test beam data.

Figure 4.10 shows the dependence of the resolution on the parameter w_0 for gammas of 1 and 10 GeV and different angles of incidence. The resolution values correspond to the r.m.s. of the distribution of differences between the reconstructed and incident positions. For each combination of incident energies and angles a minimum in the position resolution is observed at different values of w_0. A constant (energy- and angle-independent) value of w_0 = 4.0 may be used with only a small loss of position resolution at low energies and large angles.

The dependence of the position resolution on the angle of incidence is presented in Figure 4.11 for 1

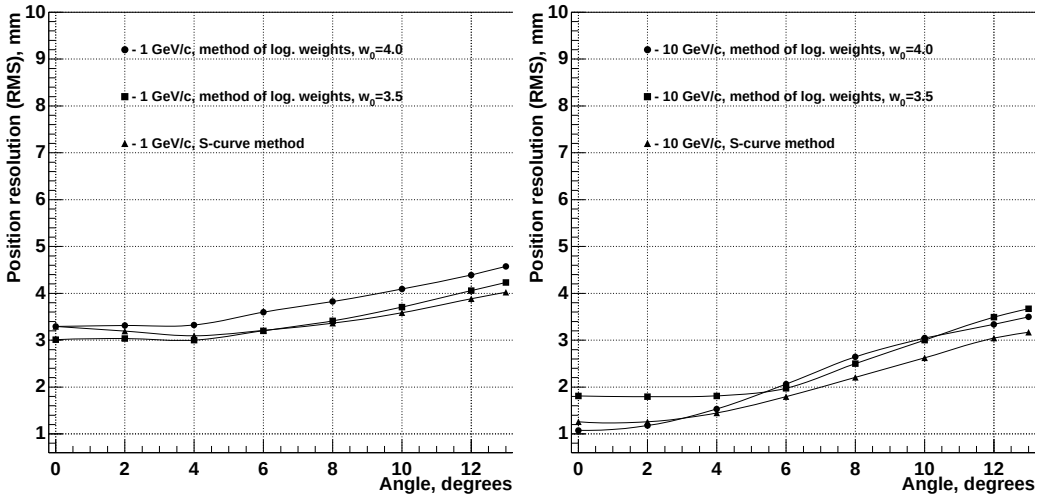

(a) 1 GeV gammas (b) 10 GeV gammas

Figure 4.11: Dependence of the position resolution on the angle of incidence. The position resolution value corresponds to the r.m.s. of the $x_{Rec} - x_{Inc}$ distribution.

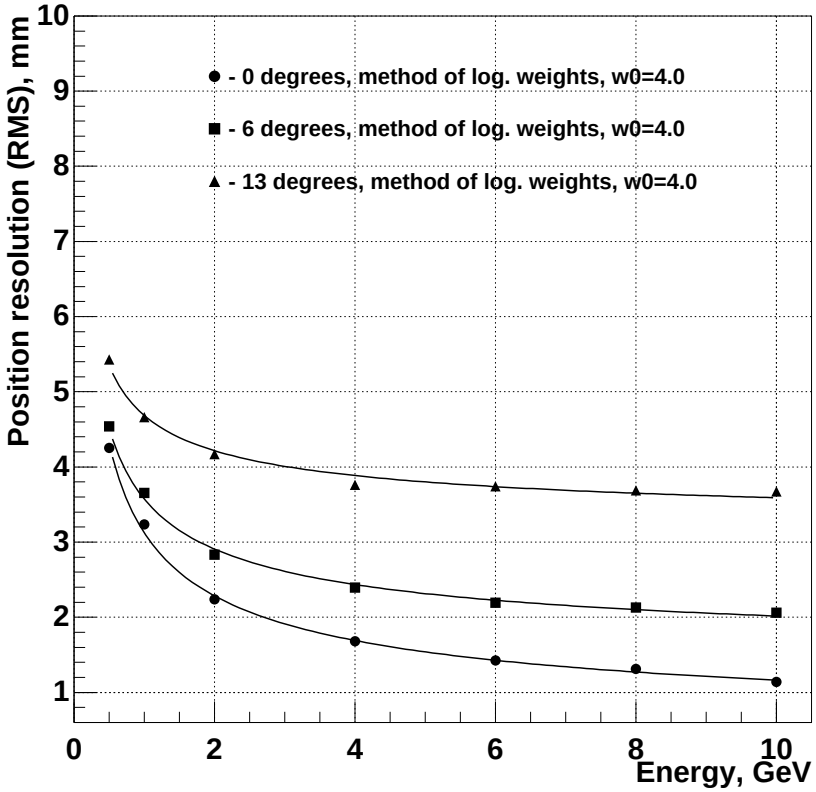

Figure 4.12: Dependence of the position resolution on the energy for incident angles of 0°, 6° and 13°.

and 10 GeV gammas between 0° and 13° and for two different values of w_0. The results obtained with the 'S-curve' method for the same data are also shown. It is clear that both methods give quite similar results. A more detailed comparison of the two methods can be found in Ref. [9].

Figure 4.12 shows the dependence of the position resolution on the energy of incident gammas at 0°, 6° and 13°. All sets of data were parametrized as follows

$$\sigma_x(E) = \frac{A}{\sqrt{E}} + B\,, \tag{4.10}$$

where the energy E is in GeV and A and B are fit parameters. Table 4.9 contains values of the parameters for different angles of incidence.

Comparison with the test-beam results is shown in Figure 4.13. The experimental data were obtained using a wide electron beam at normal incidence distributed over the front face of the detector. Here the σ of the Gaussian fit was chosen to be the measure of the position resolution, since at small incident angles and reasonable values of w_0 the $x_{\mathrm{Rec}} - x_{\mathrm{Inc}}$ distribution is well described by such fit. These data were also parametrized with Eq. 4.10 and the values of the parameters for the simulated and test-beam data are presented in Table 4.10. The discrepancy between the values of the parameters has most probably two reasons:

Table 4.9: Values of fit parameters from Eq. 4.10 obtained for gammas at different angles of incidence.

Angle of incidence	A, mm	B, mm
0°	2.87 ± 0.03	0.257 ± 0.015
6°	2.28 ± 0.04	1.30 ± 0.02
13°	1.60 ± 0.05	3.08 ± 0.03

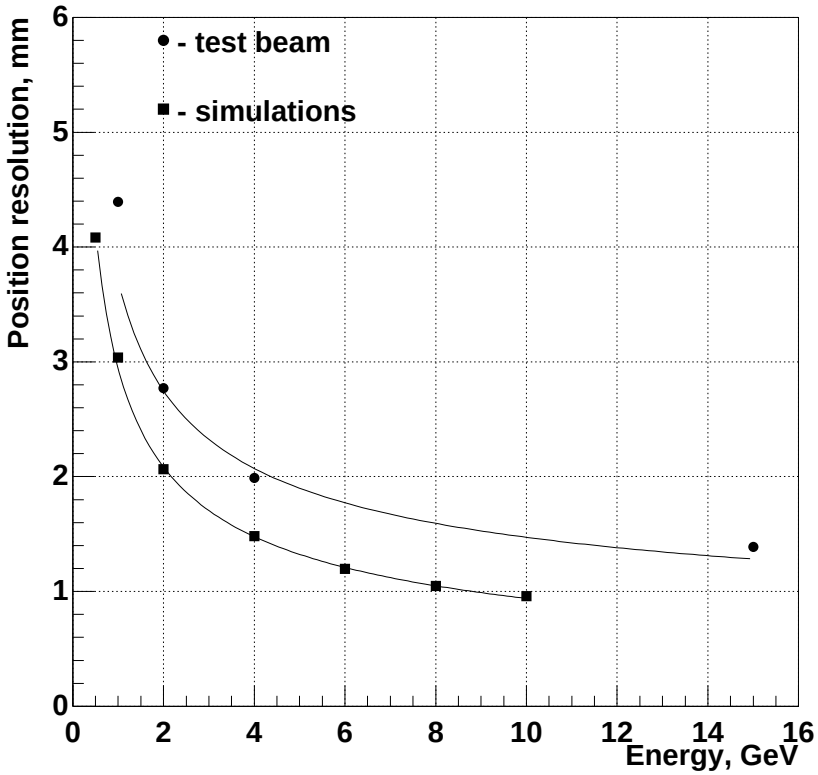

Figure 4.13: Dependence of the position resolution on the energy for normal incidence. Simulated and test-beam results. The resolution values correspond to the σ values obtained from Gaussian fits.

- the light collection efficiency of PIN-diodes and/or the light yield of $PbWO_4$ crystals was slightly overestimated;
- no attempt was made to correct the test-beam results for the position resolution of the beam detector.

At normal incidence there is no shift in the average difference $\langle x_{Rec} - x_{Inc} \rangle$. But at 13° for 10 GeV gammas the shift of 19 mm is observed. Such a shift is expected since the extracted position corresponds to a position located at some depth within the $PbWO_4$ array where the energy is deposited. Therefore, after reconstructing the position with Eqs. 4.7 and 4.9 it is necessary to apply a position correction for non-zero incidence angle. The effective depth of the shower, which is the reason for this correction, increases logarithmically with energy. It was found that this shift can be approximated by the following function:

$$\Delta_x(\text{mm}) = -[a \ln(E(\text{GeV})) + b] \cdot \sin\alpha \,, \tag{4.11}$$

where α is the angle between the normal to the detector and incident particle, a = 9.25 and b = 65.2 for $PbWO_4$ crystals. The values of these parameters depend only on the radiation length of the material, but do not depend on the detector granularity or cell size.

Table 4.10: Values of fit parameters from Eq. 4.10 obtained for test-beam and simulated data.

	A, mm	B, mm
Beam test	3.26 ± 0.03	$(4.40 \pm 0.14) \times 10^{-1}$
Simulations	2.93 ± 0.02	$(0.15 \pm 0.09) \times 10^{-1}$

Histograms in Figure 4.14 were obtained using the GALICE package. Five hundred 4 GeV gammas originating from the interaction point were distributed randomly and uniformly over the polar and azimuthal angles within the surface of one of the PHOS mudules. The incident position of a single gamma was reconstructed using Eqs. 4.7 and 4.9 and then its polar angle θ and azimuthal angle ϕ were calculated. Figures 4.14a and 4.14b represent the distribution of differences between the calculated and simulated θ and ϕ of a gamma without the shift correction and Figures 4.14c and 4.14d show the same distribution after applying the angle- and energy-dependent shift according Eq. 4.11.

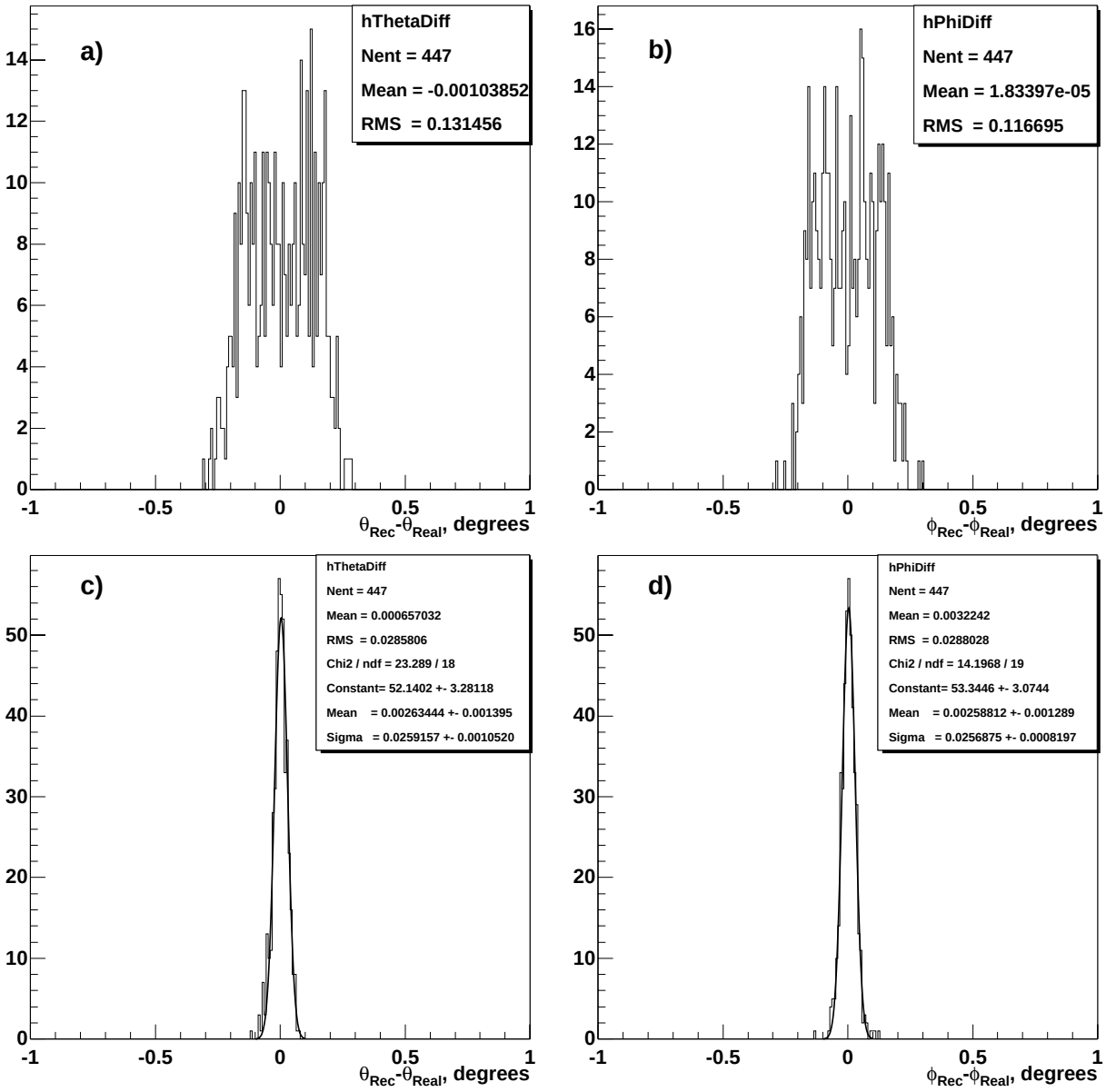

Figure 4.14: Distribution of differences between the calculated and simulated polar and azimuthal angles before (a) and (b), and after (c) and (d) the shift correction by Eq. 4.11 was applied. 4 GeV gammas were distributed over one of the PHOS modules. The histograms in (c) and (d) were fitted with Gaussians.

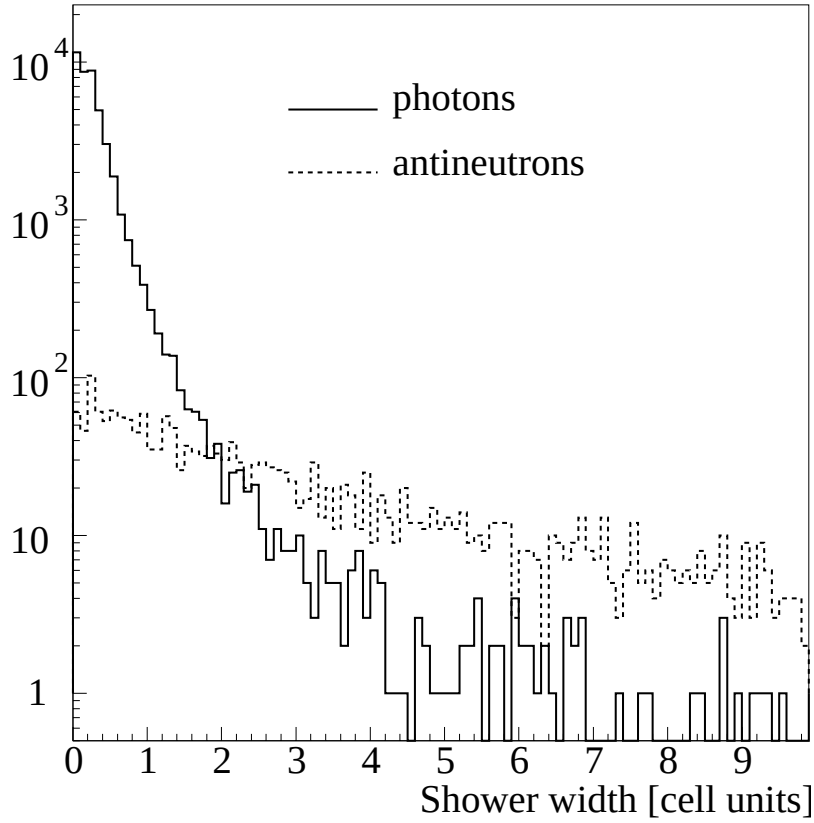

Figure 4.15: Shower width distributions for photons and anti-neutrons (GEANT simulation).

4.6 Hadron rejection using shower shape

In order to separate electromagnetic and hadronic showers, different methods will be used in ALICE. The first two make use of the PHOS only and are based on a shower shape analysis, which works equally well for identification of both neutral and charged hadrons. The other two, described in a following section, make use of the CPV in order to identify the charged particle contamination of the photon spectrum. A comparison of the final results between the different methods will be used to estimate the systematic errors related to photon misidentification.

4.6.1 Shower dispersion analysis

The fact that electromagnetic showers have a smaller radial energy profile than hadronic ones (see Fig. 4.15) allows us to discriminate against the latter except for the lowest energies. Thus the shower dispersion D is commonly used as a mean to obtain this discrimination [8]. Similar to Eq. 4.7, the second central moment is calculated as

$$D_x^2 = \frac{\sum w_i x_i^2}{\sum w_i} - \left(\frac{\sum w_i x_i}{\sum w_i}\right)^2 , \tag{4.12}$$

where x_i is the coordinate of module i and the weights w_i are usually taken as being equal to the energy deposited in that module, $w_i = E_i$.

However, as in the case of the first moment, when using weights linear in energy it is necessary to apply position-dependent corrections [6]. It may be expected that the calculation of the second moment using Eq. 4.12 with the logarithmic weights of Eq. 4.9 can provide a measure of the shower dispersion which is independent of the detector's granularity. An example of the calculated shower dispersion,

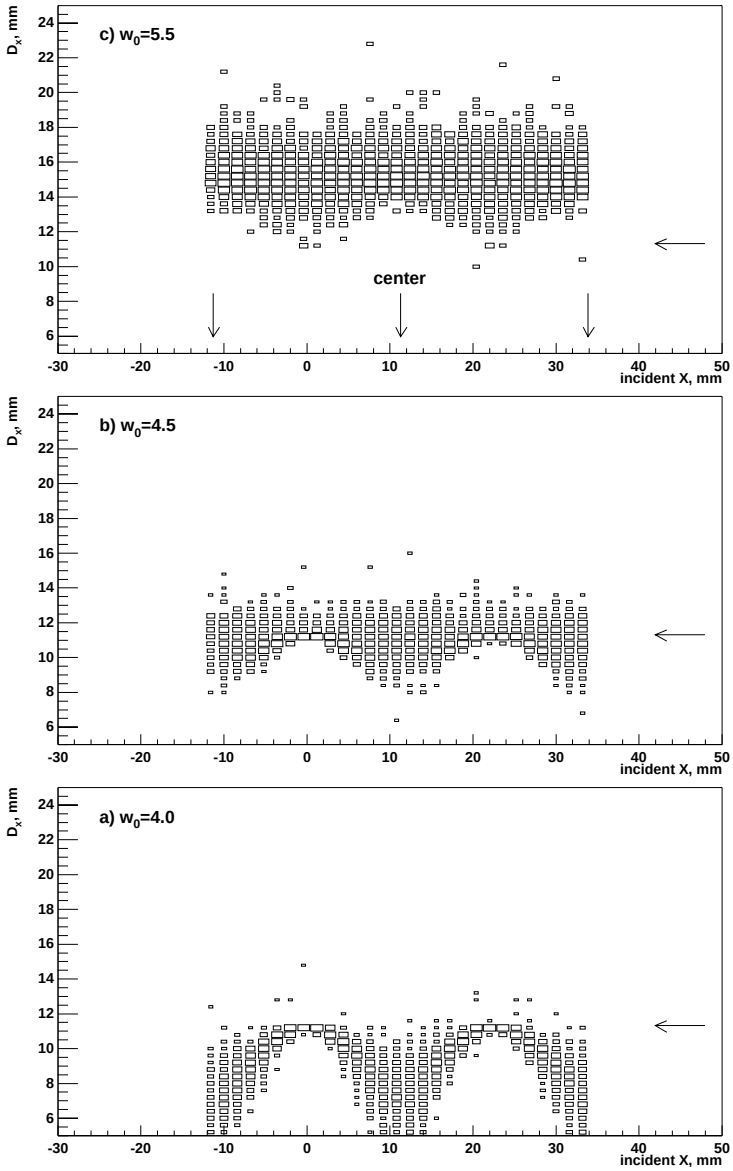

Figure 4.16: The shower dispersion D_x, calculated using Eq. 4.12 with the logarithmic weights of Eq. 4.9, as a function of the incident position for 10 GeV gammas. The coordinates of $PbWO_4$ cell's centres are indicated by the vertical arrows shown in (c). The horizontal arrows indicate a dispersion value which would correspond to one cell half-width.

using the weights logarithmic in energy, is shown in Figure 4.16 as a function of the incident position for 10 GeV gammas incidenting normally over the area of 2×2 cells centred on the axis of one of the central cells. The results are shown for weight parameter values of w_0 = 4.0, 4.5 and 5.5. Although the weight parameter value of w_0 = 4.0 gives the optimum results for the calculation of the shower location, this value of w_0 results in a calculated shower dispersion that shows strong incident position dependence. The position dependence begins to disappear at w_0 = 4.5 and is negligible when w_0 = 5.5.

In Fig. 4.17 the total shower dispersion $D = \sqrt{D_x^2 + D_y^2}$ is plotted vs. the energy deposited in the $PbWO_4$ array for gammas and pions of various incident momenta. The dispersion is calculated using the logarithmic weights with the weight parameter of $w_0 = 4.5$. From this figure it can be seen that the average value of the dispersion $\overline{D}$ is rather independent of the energy deposited, while the variation in the dispersion σ_D increases for the low deposited energy.

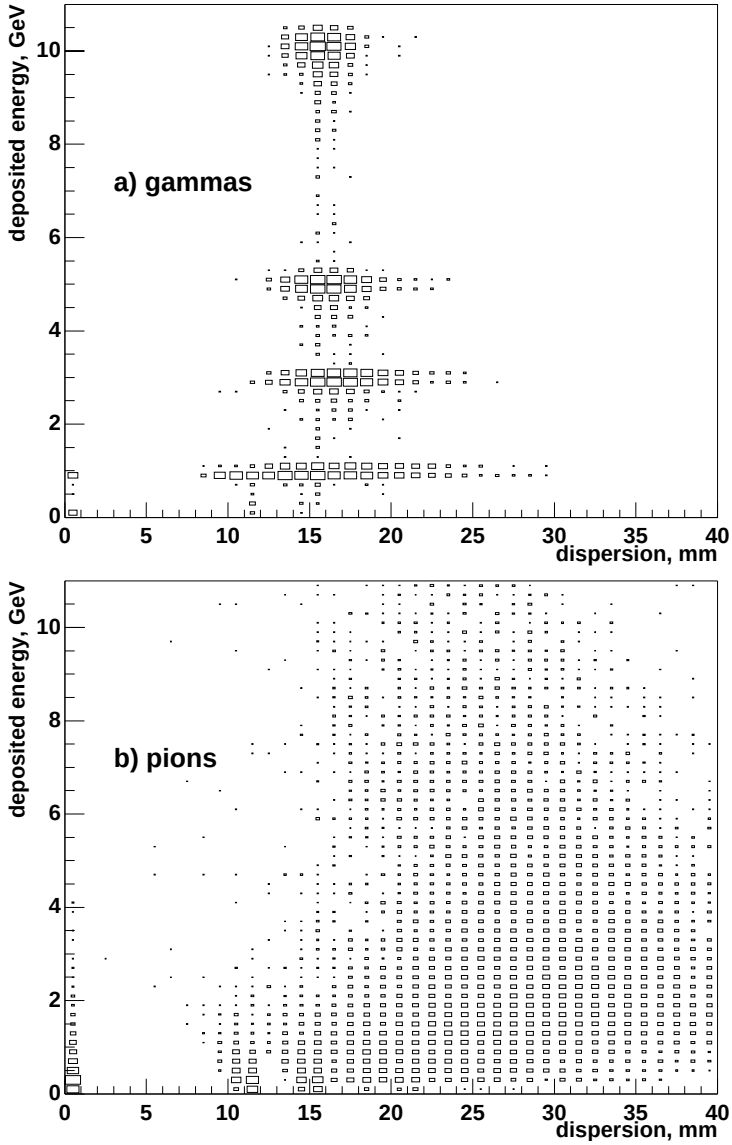

Figure 4.17: The correlation between the total dispersion of the shower $D = \sqrt{D_x^2 + D_y^2}$ and the amount of deposited energy for (a) gammas and (b) pions. The results are shown for incident gamma momenta of 1, 3, 5 and 10 GeV/c and incident pion momenta of 1, 3, 5, 10 and 20 GeV/c. The dispersion is calculated using Eq. 4.12 with weights given by Eq. 4.9 and the weight parameter of $w_0 = 4.5$.

In order to obtain a good separation of electromagnetic and hadronic showers it is desirable to have a large difference between their respective average dispersions $\overline{D_e}$ and $\overline{D_\pi}$ with variations in their individual dispersions σ_e and σ_π as small as possible. Therefore, the value of the weight parameter w_0 should be chosen so that these parameters are optimized. This can be seen in Figure 4.18a where the average dispersions are plotted for various values of w_0 for gammas with momenta 1 and 10 GeV/c and for pions which deposit from 1 to 10 GeV in the $PbWO_4$ array. The width of the dispersion distributions is indicated by the vertical bars on the data points.

A measure of the e/π separation can be constructed from these quantities by calculating an e/π resolving power as

$$R = \frac{(\overline{D_\pi} - \overline{D_e})^2}{\sigma_{D_\pi}\sigma_{D_e}} \,. \tag{4.13}$$

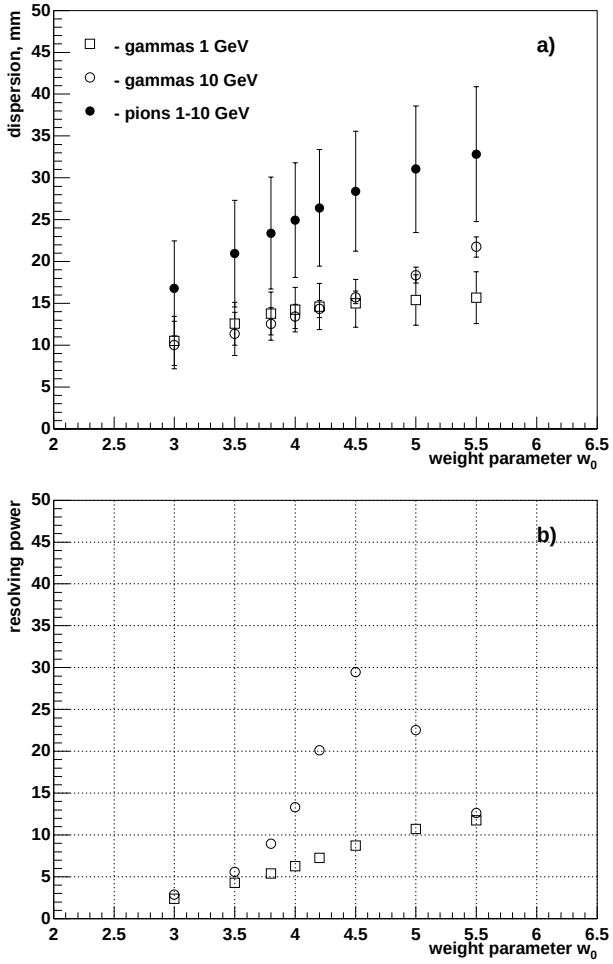

Figure 4.18: (a) the dependence of the mean of the shower total dispersion $D = \sqrt{D_x^2 + D_y^2}$, calculated using Eq. 4.12 with the weights given by Eq. 4.9, on the weight parameter w_0. The results are shown for gammas with momenta 1 and 10 GeV/c with the open squares and circles, respectively. The full circles show the results for 1, 3, 5, 10 and 20 GeV/c pions with deposited energies between 1 and 10 GeV (see Figure 4.17b). The vertical bars indicate $\pm\sigma_D$ of the distribution of shower dispersions. (b) The dependence of the resolving power between gammas and pions on the weight parameter w_0. The resolving power is calculated with Eq. 4.13 using the results shown in (a).

The resolving power between 1 or 10 GeV/c gammas and pions depositing 1 to 10 GeV of energy is shown as a function of w_0 in Fig. 4.18b. From these results it can be seen that the resolving power is greater for higher energy showers because of the smaller width of the shower dispersion distribution. It is observed that the resolving power is the greatest when using a weight parameter of $w_0 = 4.5$, which corresponds to a gamma shower dispersion which is a slightly larger than a single cell halfwidth and therefore position independent (see Fig. 4.16).

The level of e/π separation that may be obtained by applying dispersion cuts is presented in Fig. 4.19a. Here the fraction of particles having dispersion value less than varying cut as a function if this cut is shown. The result is shown for gammas and pions at normal incidence which are distributed uniformly over the square of 2×2 cells centred on the axis of one of the central cells. A weight parameter value of $w_0 = 4.5$ was used for calculating the weights according to Eq. 4.9. As an example: with a dispersion cut of $D < 18.0$ mm, more than 86% and 99% of the gammas with incident momenta 1 and 10 GeV/c are respectively accepted, whilst less than 11% and 8% of pions depositing 1–3 and 5–10 GeV are accepted, respectively. It can be seen that a dispersion cut which depends on the energy deposited can be used to

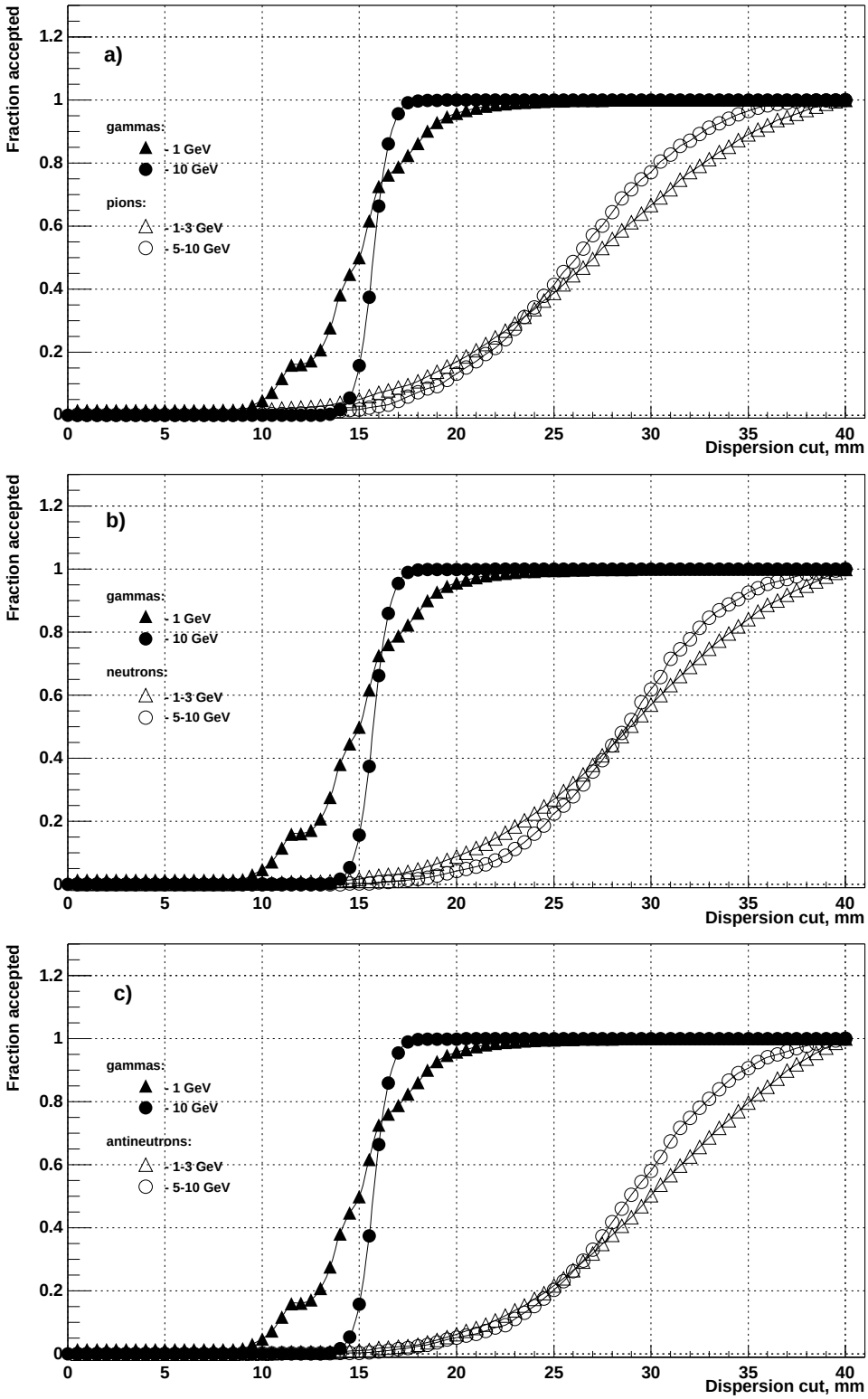

Figure 4.19: The fraction of gammas and hadrons accepted for varying upper limit on the total shower dispersion $D = \sqrt{D_x^2 + D_y^2}$ as a function of this cut. The dispersion is calculated using Eq. 4.12 with weights given by Eq. 4.9 using an optimum weight parameter of $w_0 = 4.5$. Results are shown for gammas of 1 and 10 GeV momentum and for (a) pions, (b) neutrons, and (c) antineutrons, depositing 1–3 and 5–10 GeV of energy.

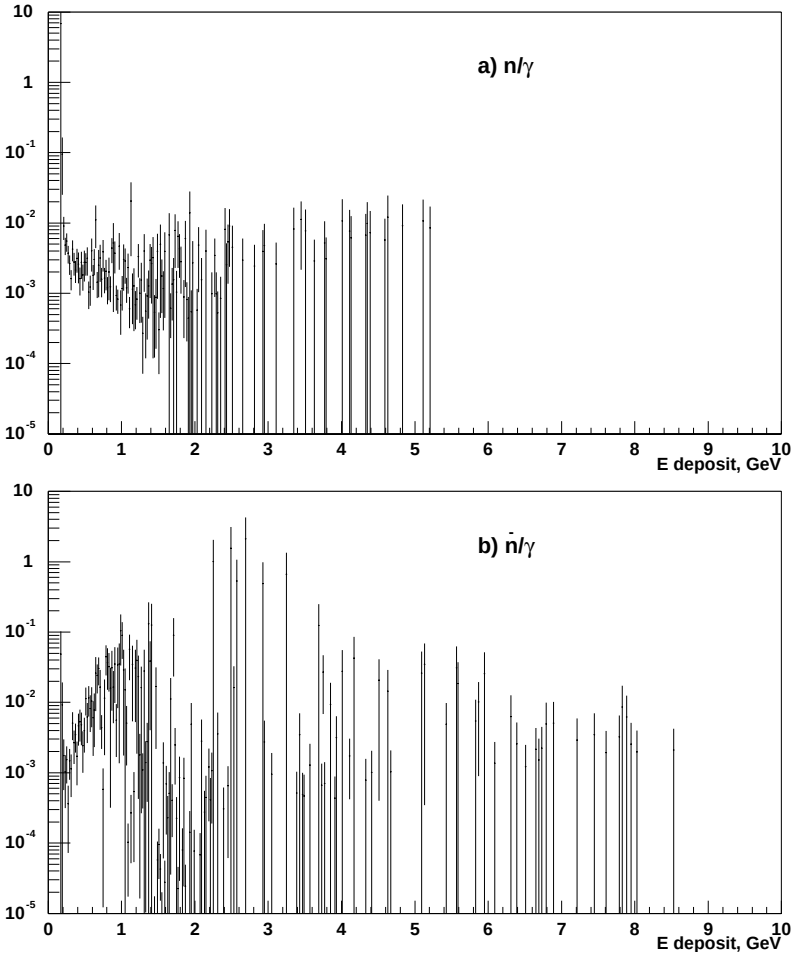

Figure 4.20: Neutron/gamma (a) and antineutron/gamma (b) ratios vs. deposited energy (GEANT simulations). Shower width cut 18 mm.

obtain an energy-independent acceptance level for electromagnetic showers while providing a maximum hadronic shower rejection.

While the charged hadron rejection capability of the spectrometer can be improved by using a charged particle veto, this is not the case for neutral particles. K_L^0's, neutrons and antineutrons will interact in the calorimeter with a probability of $\sim$ 50% and PHOS will record a fraction of the total energy (K_L^0) or kinetic energy (neutron). Antineutrons can annihilate in the detector and deposit correspondingly more energy. Here the dispersion analysis is the major means of particle discrimination. Figures 4.19b and 4.19c show the level of separation that may be achieved using various dispersion cuts for neutrons and antineutrons, respectively. Applying the dispersion cut of $D < 18.0$ mm allows less than 5% of neutrons depositing 1–3 GeV and less than 2% of them depositing 5–10 GeV to be accepted. With the same cut we have less than 3% of antineutrons accepted within all considered interval of depesited energy. Figure 4.20 shows the results of the dispersion cut of 18 mm on n/γ and $\overline{\text{n}}/\gamma$ ratios. The neutron contamination stays well below 1% at all energies while antineutron one reachs the level of almost 4% at $\sim$ 1 GeV of deposited energy compare to 20% without this cut [10].

4.6.2 Shower topology analysis

As an alternative to the method described above, one can also discriminate photons by analysing the shape of the shower in more detail. The major source of the background in PHOS consists of charged pions and antineutrons which also develop a shower. The energy deposition in a cluster, shown in Fig. 4.21

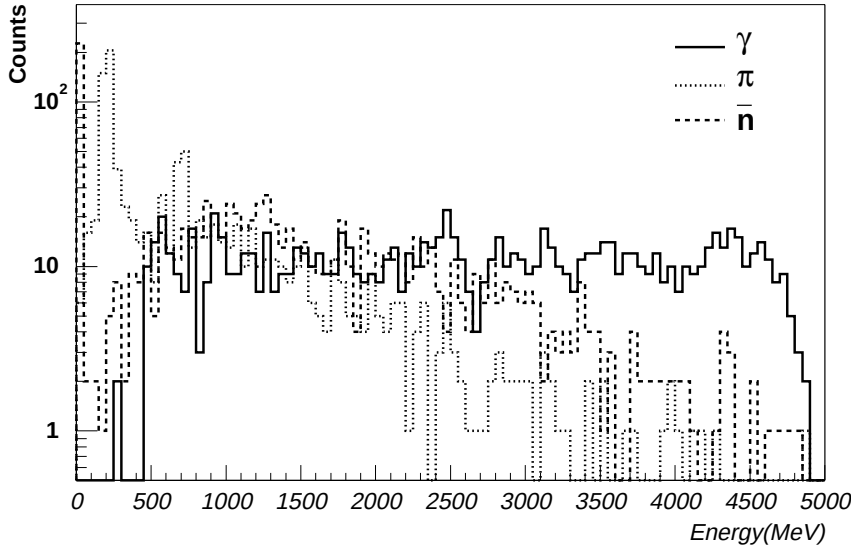

Figure 4.21: Deposited energy spectra in PHOS module simulated for photons, charged pions and antineutrons generated with a flat p_T distribution between 0.5 and 5 GeV.

for photons, charged pions and antineutrons, provides a first criteria. A cut at about 500 MeV eliminates most of the pions contributing mostly to the minimum ionizing peak at 200 MeV. This cut, however, does not remove neither the antineutrons nor the pions which traverse the photodiode and hence deposit an additional 500 MeV to the measured signal. However, the shower profile for the different kind of particles is different. It is measured by calculating (λ_1, λ_2), the eigen-values of the 2×2 sphericity tensor which represents the two axes of the ellipse delimiting the shower on the surface of the PHOS modules:

$$S_{xx} = \sum_i E_i x_i^2 \ , \qquad S_{xy} = S_{yx} = \sum_i E_i x_i y_i \ , \qquad S_{yy} = \sum_i E_i y_i^2 \ , \tag{4.14}$$

where x_i, y_i are the coordinates of the cell centres in within the shower intersection with the front face of the detector. As can be seen in Fig. 4.22, antineutrons and photons lead to very different distributions in the (λ_1, λ_2) representation providing a clear criterium to discriminate photons. The selection can be

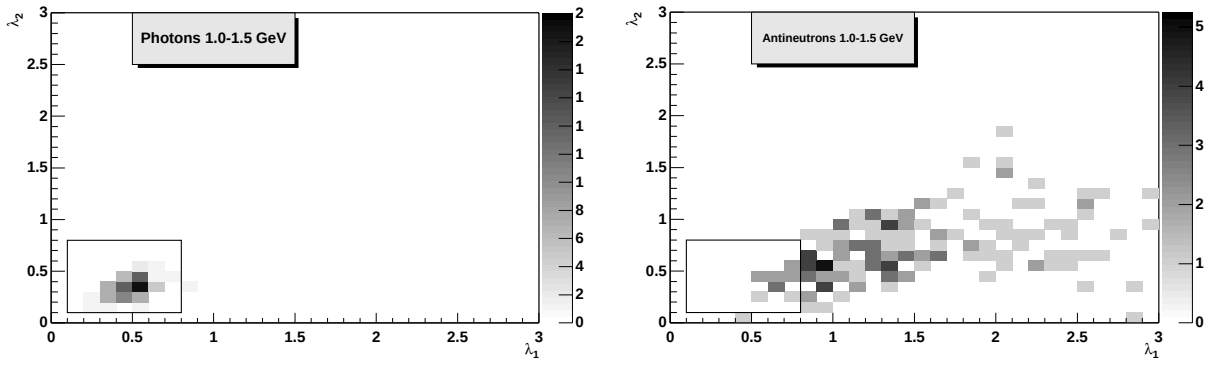

(a) photons (b) antineutrons

Figure 4.22: Shape of the shower generated in a PHOS module by photons (a) and antineutrons (b) characterized by two eigenvalues of the sphericity tensor. The rectangular contour indicates the selected cut to isolate photons.

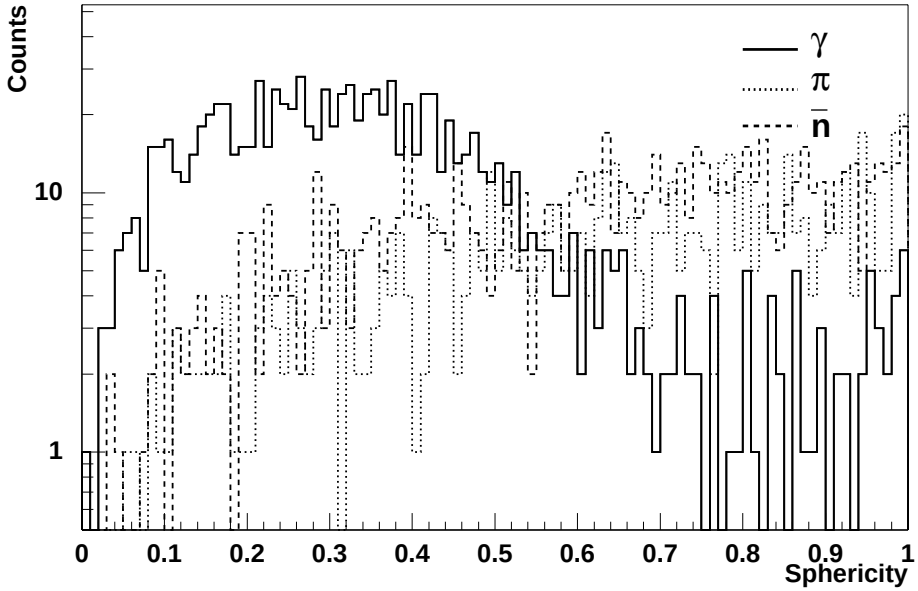

Figure 4.23: Sphericity factor L of the shower calculated for photons, charged pions and antineutrons generated with a flat p_{T} distribution between 0.5 and 5 GeV.

further improved by setting a cut on the sphericitiy factor L (Fig. 4.23) defined as:

$$L = \frac{|\lambda_1 - \lambda_2|}{\lambda_1 + \lambda_2} \, . \tag{4.15}$$

The resulting rejection factors calculated from a simulation where particles are generated following a flat p_{T} distribution between 0.5 and 5 GeV (Table 4.11) indicate that only 10% of photons are accidently removed and that the selected photons are contaminated by at most 6% of left-over antineutrons and 15% of charged pions.

Table 4.11: Rejection factor calculated for photons, charged pions and antineutrons by applying the conditions, $0.2 < \lambda_{1,2} < 0.8$; $0.1 < L < 0.6$

Rejection factor, %		
Photons	Charged pions	Antineutrons
10±3	85±5	94±2

4.7 CPV performance

4.7.1 CPV simulation model

Beam tests of the CPV prototype discussed in Section 2.4 (see Chapter 2) allow one to formulate and tune a realistic simulation model of the CPV detector. The model is based on the pad response function parametrized in terms of the charge density function. Athough the last can be expressed as an infinite series and calculated using the distance between the CPV wires and cathode plane (see Ref. [11]), the realistic parametrization of the charge density function $\sigma(z,y)$ in a finite form has been obtained in the CPV beam tests

$$\sigma(z,y) = \frac{Q}{2\pi} \cdot \frac{\beta}{(z^2 + y^2 + \beta^2)^{3/2}} \, , \tag{4.16}$$

where $\beta = 0.915 \pm 0.003$ [11]. Thus the charge density induced on a pad plate in a real experiment can be calculated for any pointlike charge Q located near the CPV wires.

Apart from induced charge density (Eq. 4.16), the CPV model takes into account the effects of the inclined tracks which lead to distortion of the avalanche charge along the wires. It can be even shared among several wires in the case of tracks with large angles which often happens due to the track bending in the ALICE magnetic field. Another important effect incorporated in the model is the overlapping of CPV clusters for neighboured charged tracks at small distances. For example, the charge distortion along the wires for inclined tracks is evaluated numerically by integrating the corresponding charge density along the wires.

Another important parameter of the CPV model — the value of equivalent electronic noise in the CPV channels — was chosen in such a way that the coordinate resolution along the wires for single normal tracks will be the same as the one measured in the beam tests of the CPV prototype (≈ 1.3 mm). Thus the model is virtually parameter free.

4.7.2 Charged track reconstruction

The reconstruction procedure of the CPV hits includes several steps:

- search clusters amongst the CPV pads with amplitudes A_i above some threshold, $A_i > A_{\rm thr}$;
- identification of the single-hit clusters and determination of the hit coordinates;
- unfolding of the overlapping hits in clusters and determination of each hit amplitude and coordinates;
- suppression of the low-amplitude hits ($A^{\rm hit} > A^{\rm hit}_{\rm thr}$) and recombination of the small-distance hits into one;
- projection of the CPV hits on the PHOS crystal plane.

The hits unfolding in a cluster are based on the comparison of the amplitude distribution observed on the pads with that expected in a cluster for single- or multi-particle hits. In the latter case one adds the amplitude in the pads affected by several particles. As for the expected amplitude distribution on the pads for a single particle hit with arbitrary incident angles in the CPV, we use the pad response function corresponding to the charge density function (Eq. (4.16) obtained in the beam tests for charged particles with normal incident angles. Then the χ^2 criteria is used for unfolding the track multiplicity in such clusters.

The reconstruction program was tuned for a sample of Monte Carlo events in the magnetic field of 0.2 T with the charged particle flux of 90 particles/m^2 expected in ALICE for Pb–Pb central collisions, including background hits. The events generated were tracked through the real detector medium by the GALICE package. The CPV response was recorded and reconstructed.

The quality of the event reconstruction in the CPV is illustrated in Figs. 4.24–4.26. In particular, the unfolding efficiency for two-hit clusters is almost perfect (see Fig. 4.24). Actually the tracks at distances greater than 2.5 cm (the transverse size of one PHOS crystal is 2.2 cm) are resolved with a probability better than 80%.

The present tuning of the reconstruction programme provides a very high detection efficiency for charged particles in the CPV. The reconstructed CPV multiplicity is shown in Fig.4.25a, whereas in Fig.4.25b the deviation of the reconstructed hit multiplicity from the generated one is presented. Taking into account that the average CPV multiplicity in central events is ~ 1500 (see Fig.4.25a) one can obtain CPV multiplicity in central collisions reconstructed with an accuracy better than 3%.

The coordinate resolution of the CPV at high occupancy can be estimated by looking at the distance between the generated hit and the closest reconstructed one. The corresponding distributions over the z (along wires) and y (across wires) coordinates are shown in Fig. 4.26. The accuracy of the coordinate

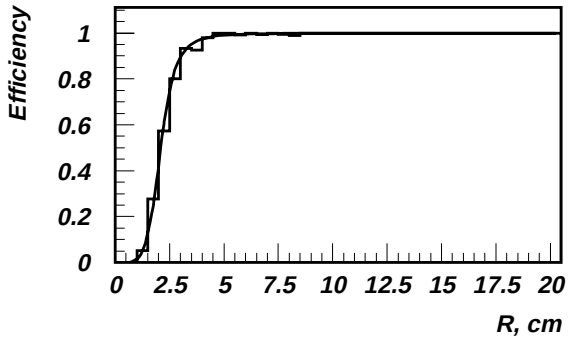

Figure 4.24: Unfolding efficiency for two hits in the CPV as a function of the distance between them, solid line shows a smoothing function.

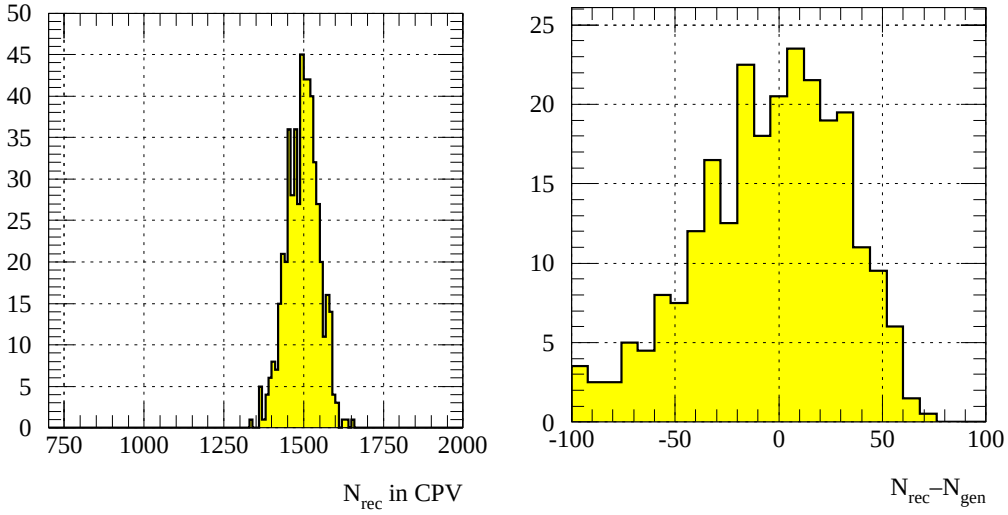

(a) (b)

Figure 4.25: Multiplicity of reconstructed hits in the CPV (a). Deviation of the reconstructed multiplicity N_{rec} from the generated one N_{gen} (b). For central Pb–Pb collisions.

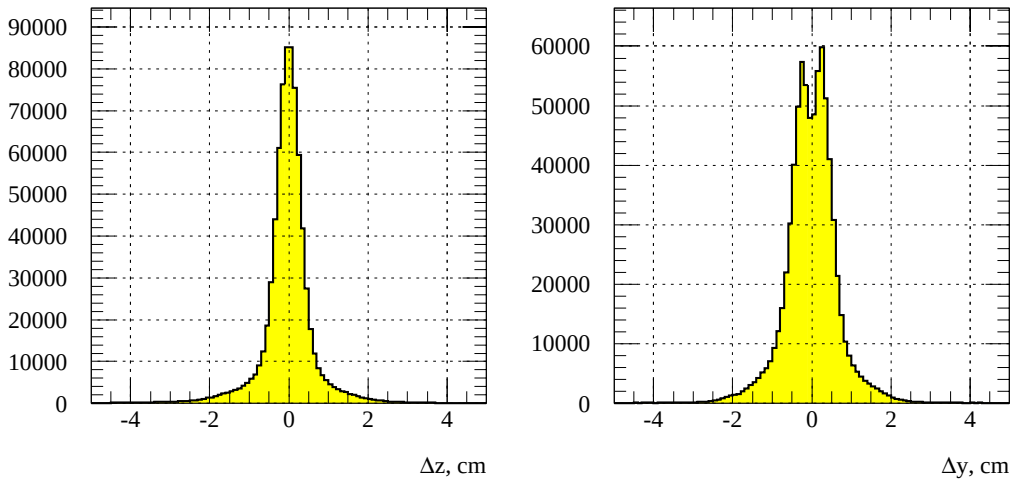

(a) (b)

Figure 4.26: Resolution of z (along wires) (a) and y (across wires) (b) coordinate reconstruction in the CPV for central Pb–Pb collisions.

measurements of hits will be of the order of 3 mm along, and 4.5 mm across the CPV wires, respectively. These numbers take into account the track inclinations, cluster overlapping, electronics noise, occupancy, and influence of the unfolding procedure.

4.8 Hadron rejection using the CPV

There are two methods of charged particle rejection using the CPV detector. The first one was described in Ref. [10] and allows us to separate charged and neutral particles inclusively, i.e. to separate the total inclusive spectrum of all detected hits into the spectra of charged and neutral particles. The second method attempts a separation into charged and neutral particles for each individual shower.

4.8.1 Inclusive separation of charged particles

This method was used in the WA80 experiment data analysis. The charged particle hit in the CPV is projected onto the photon detector and for each shower the distance to the closest projection point is calculated (R_{veto}). Since the efficiency of the CPV is less than 100% and both the CPV and the photon detector have finite space resolution, it is not attempted to determine for each hit if it comes from a charged particle or not. Some fraction of the charged particles will always escape detection in the CPV and has to be subtracted from the photon spectrum.

The basic idea of the inclusive separation is that neutral particles can be vetoed only by accident (because some charged particle hit the detector close to it) and that the dependence of the probability to be accidentally vetoed on R_{veto} is different from that of charged particles, which are vetoed 'non-accidentally'. Then one can separate all particles into accidentally vetoed and 'non-accidentally' vetoed. The latter represent a fraction of all charged particles. An example of the separation of the charged from neutral particles is shown in Fig. 4.27. This method does not impose any strict requirements on the position resolution or the charged-particle veto efficiency.

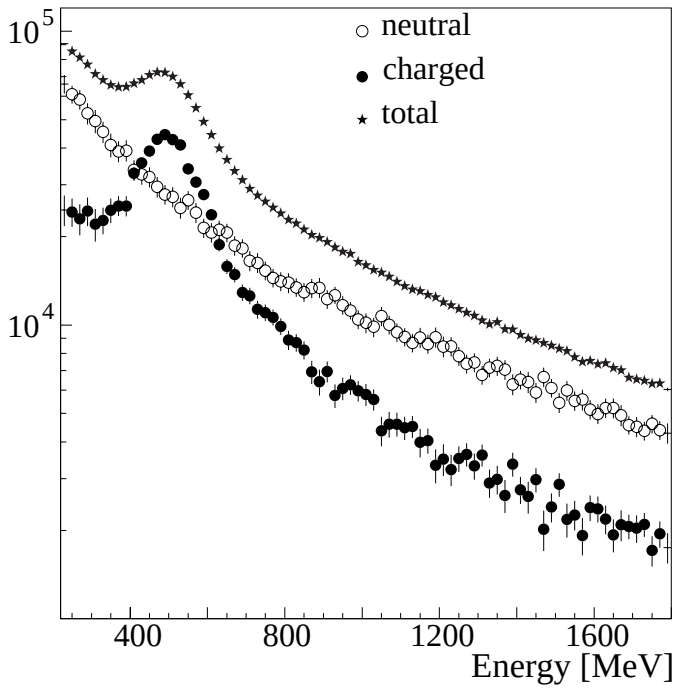

Figure 4.27: Separation of neutral and charged particl contributions to the mesured energy spectrum in WA80.

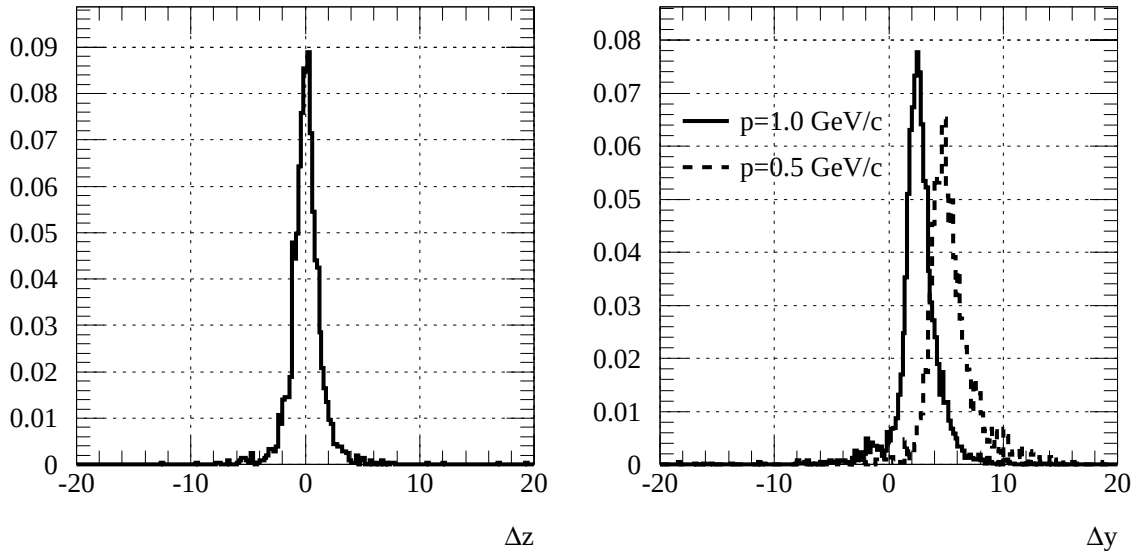

Figure 4.28: Difference in cm between the exact π^--coordinate in the CPV plane and the shower coordinate in the PHOS (a) along the magnetic field (z) and across the magnetic field (y), $B = 0.2$ T.

4.8.2 Individual separation of charged particles

In order to separate individual showers into hadronic and electromagnetic ones, the coordinates of the charged particle hits in the CPV are projected onto the PHOS and compared with the coordinates of the showers in the PHOS. If the reconstructed shower in the PHOS is accompanied by a charged track in the CPV within some minimum distance, this shower can be produced or distorted by a charged particle hit and is therefore rejected.

For single particles (or at very low occupancy), the matching between CPV and PHOS is very good. This is illustrated in Fig. 4.28, where the difference of the coordinates on the CPV plane and the reconstructed coordinates in the PHOS for 0.5 and 1 GeV/c charged pions are presented. The shift observed in the y-coordinate (across the magnetic field) is caused by the inclination of charged tracks in the magnetic field which can only be corrected if the track inclination is known (e.g. from the TPC).

In order to study the efficiency of tagging charged particles with the CPV at high multiplicity, the event generator SHAKER [12] was used. The charged particle density per unit rapidity was taken to be $\mathrm{d}N_{\mathrm{ch}}/\mathrm{d}y = 8000$. The events contained $\pi^0, \pi^{\pm}, \mathrm{K}^{\pm}$, p and $\overline{\mathrm{p}}$ were tracked through the real detector medium by the GALICE package and the corresponding signals in the CPV and PHOS were simulated and reconstructed. As a result, the array of the shower coordinates in the PHOS and the array of the hit coordinates in the CPV were obtained for each event.

For each reconstructed shower in the PHOS, the distance from the shower coordinate to the closest reconstructed hit of the charged particle in the PHOS was found. The reconstruction of the charged particle hit in the PHOS can be performed by extrapolating the charged track from the reconstructed hit in the CPV. Using the CPV as a stand-alone device, such an extrapolation can be made assuming that the track comes from the beam interaction point. This assumption defines the direction of the track which produced a hit in the CPV, and thus, a coordinate of the hit in the PHOS. Figure 4.29 and shows the distance from the shower coordinate to the closest charged particle hit on the PHOS along the z- and y-coordinates, using this extrapolation. In Fig. 4.29a there is a single peak near $\Delta z = 0$ which corresponds to the PHOS showers caused by the charged particles. The PHOS showers not correlated with the charged tracks give the wide background on this plot. Along the y-coordinate, the influence of the magnetic field on the charged particles results in the shift between the PHOS shower from the charged particle and the corresponding CPV hit. This effect is seen as two peaks (positive and negative particles) in Fig. 4.29b.

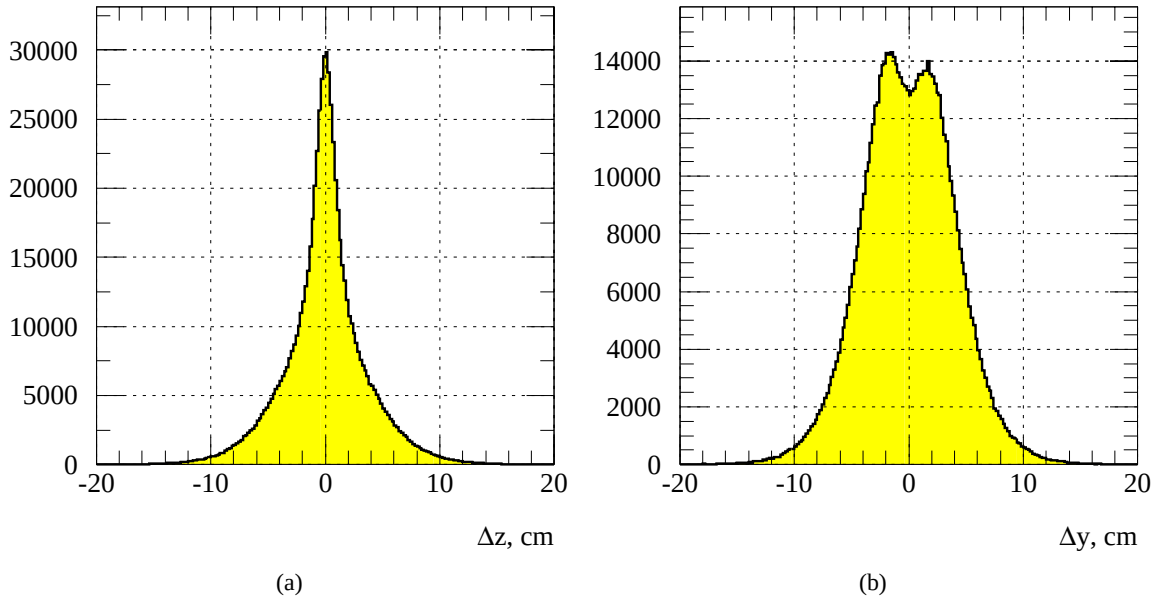

Figure 4.29: Distance of the shower coordinate to the closest charged track in the PHOS: (a) along the *z*-coordinate and (b) along the *y*-coordinate. The track is assumed to come from the interaction point.

At high momentum ($\sim$ 1 GeV) the information from the TPC can be used to define the direction of the tracks coming to the CPV more precisely. The extrapolation of the CPV hit to the PHOS using this direction gives a more narrow distribution of the deviation of the PHOS shower from the charged track coordinate along the *y*-axis which is shown in Fig.4.30.

These distributions give the criterion of the photon isolation in the PHOS. The reconstructed shower in the PHOS not accompanied by a charged track hit closer than Δz_0 ($\min|\Delta z| > \Delta z_0$) along the *z*-coordinate and along the *y*-coordinate closer than Δy_0 ($\min|\Delta y| > \Delta y_0$) is determined as an isolated shower and is caused by a photon. The numerical values of Δz_0 and Δy_0 are defined from Figs.4.29a and 4.30. The value of Δy_0 is energy dependent because soft charged particles are bent more on their path from the CPV to the PHOS than particles with higher momenta. The choice of the Δz_0 value is not

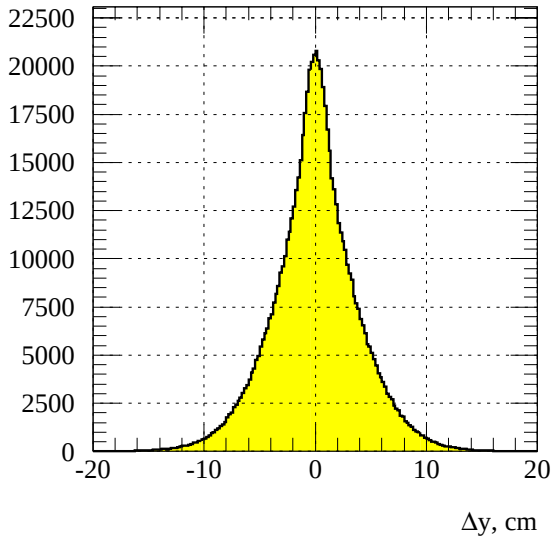

Figure 4.30: Distance from the PHOS shower coordinate to the closest charged track in the CPV along the *y*-cordinate. The track direction is used from the TPC.

Table 4.12: Numerical values of Δy_0 and Δz_0.

p, GeV/c	Δy_0, cm	Δy_0, cm
< 0.5	2.8	1.5
$0.5 - 1.0$	2.2	1.5
> 1.0	1.8	1.5

influenced by the particle momentum. In Table 4.12 the values of Δy_0 and Δz_0 are given for three ranges of the closest PHOS shower mometum.

Figure 4.31 and shows the ratios of the p_T-spectra of the reconstructed to the generated photons without and with charged track rejection. From Fig. 4.31a it follows that the number of reconstructed showers in the PHOS is about double and for small momenta up to three times greater than the real number of photons hitting in the PHOS. This double load of the PHOS is caused by the hadrons. After selecting the genuine photon showers in the PHOS, the number of reconstructed photons amount to $\sim 80\%$ compared with the generated ones caused by partial photon conversion and CPV rejection. Thus, the Charged Particle Veto detector provides an effective tool for selecting genuine photons in the PHOS.

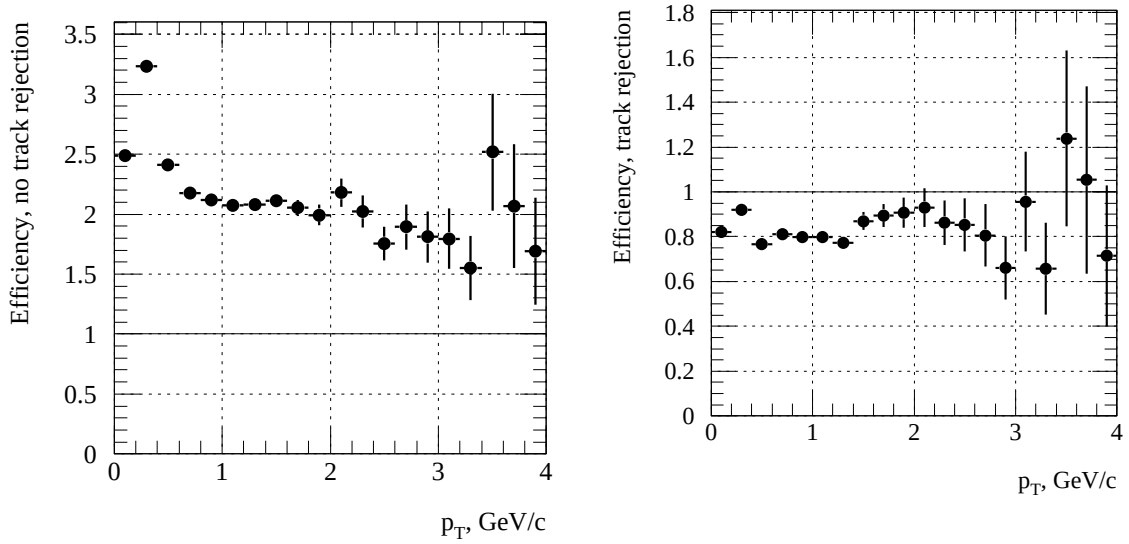

(a) without rejection (b) with rejection

Figure 4.31: Ratio of p_T-spectra: (a) without charged track rejection and (b) with charged track rejection.

4.9 Photon reconstruction efficiency

In PHOS main physics goal, the measurement of direct photons, ALICE will be limited by systematic rather than statistical errors. One of the main sources of systematic errors is the accuracy with which the photon reconstruction efficiency, and in particular its multiplicity dependence, is known. The absolute value of the efficiency, defined as the ratio between generated and reconstructed spectra (see below), is less crucial and is typically between 0.8 at low p_T and 1.2 at high p_T.

The efficiency will be evaluated with methods developed for the WA80/93/98 experiments which are described below. By using different methods, and by varying the cuts, the systematic error can be estimated from the actual data. The systematic errors we expect in ALICE are based on these SPS results, suitably extrapolated to LHC in Section 4.11.

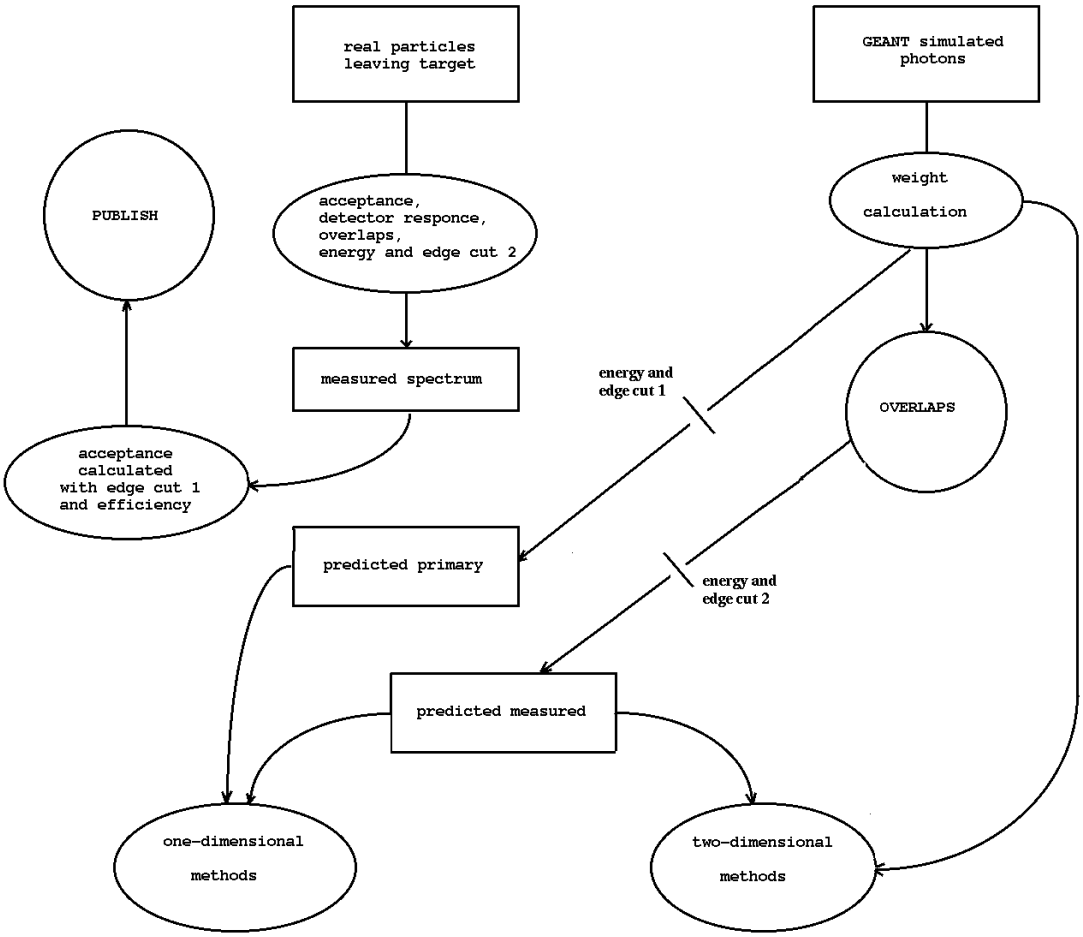

Figure 4.32: Efficiency calculation algorithm.

In a high multiplicity environment one of the main sources of systematical errors is the overlap of photon showers. Because of overlap some photons are lost and some change their energy or coordinate. This leads to a decrease of the photon registration efficiency and a distortion of the photon spectrum's shape. In heavy-ion central collisions at SPS energies [13] (200 GeV/nucleon, experiments WA80/93/98) the detector occupancy reaches 20%, which means that the probability of overlapping is very high. In WA80/93/98 the distortion of the photon spectrum caused by overlaps was calculated by adding single test photons to real events. The procedure was as follows. A test event containing single GEANT simulated photons was analysed using the same algorithm as the one used for real data analysis. Then a test event was added to a real event by summing up the ADC values of each module in real and test events. After this, the new sum event was analysed and a search for an overlayed test photon was made. As the same algorithm was used for data analysis before and after overlapping of the test photon, one can expect that all imperfections of the cluster unfolding procedure are taken into account. The efficiency calculation algorithm is shown in Fig. 4.32

Test photons used for efficiency calculation were simulated using GEANT. Photons were simulated with uniform distribution in transverse momentum $P_\perp$ and rapidity Y. $P_\perp$ and Y-dependent weights $W(P_\perp)$ and $W(Y)$ were used to reproduce true photon distributions. As a first approximation these weights were taken from experimentaly measured distributions and corrected in subsequent iterations as is described below. An additional weight, equal to multiplicity M of the event on which the test photon was overlapped, was introduced to reproduce correctly the probability of a photon being in an event with multiplicity M.

Thus, all histograms were filled with weight W equal to:

$$W = rtw \cdot W(Y) \cdot W(P_\perp) \cdot M \,, \tag{4.17}$$

where *rtw* is the trigger weight.

There are several ways to calculate efficiency using the overlap of test photons.

4.9.1 Single particle 'one-dimensional' method

The simplest way is to look around the spot where the test photon was added to a real event and if one can find exactly the same test photon as was added to the real event, then it means that there was no overlap. If no exact match is found, then one should look at the closest hit and if the energy of this hit is between the energy of the test photon before overlap and twice of this value, this hit can be considered as a test photon which changed its energy and/or coordinate because it overlapped with another hit; otherwise the test photon is considered lost.

The efficiency ε_1 was calculated according to the formula:

$$\varepsilon_1 = N_{\text{found}}/N_{\text{total}} \,, \tag{4.18}$$

where N_{total} is the original spectrum of the test photons and N_{found} is the spectrum of the test photons found using the procedure described above.

In both N_{total} and N_{found} spectra, a 750 MeV energy cut was used (the same as in the experimental data analysis).

4.9.2 Multiparticle 'one-dimensional' method

A shortcoming of the method described above is that one has to decide somehow if an overlapped test photon is lost or has just changed its energy and/or coordinate. This shortcoming could be eliminated if all the hits which appear and disappear after the overlap of a test photon are taken into account. In this case the efficiency could be calculated as the difference between the spectrum of all the hits which appeared and the spectrum of all the hits which disappeared after the overlap of a test photon, divided by the original spectrum of test hits. One should note here that the number of appearing hits is not always equal to one. Thus, the efficiency is calculated as:

$$\varepsilon_2 = \frac{(N_{\text{new}} - N_{\text{lost}})}{N_{\text{total}}} \,. \tag{4.19}$$

Double counting is eliminated in this case by using an additional energy-dependent weight for filling all the histograms. This weight is calculated as:

$$W_E = \frac{E_{\text{testhit}}}{E_{\text{testhit}} + \sum E_{\text{losthits}}} \tag{4.20}$$

where E_{losthits} is the energy of the hits which disappeared after the overlap of a test photon with energy E_{testhit}. The introduction of this weight is in a way similar to the cut on energy change in the single particle method. If a test photon with high energy overlapped with a low-energy hit in a real event, this weight will be close to 1. If a low-energy test photon overlapped with a high-energy hit in real event, this weight will be close to 0.

The main shortcoming of both of the methods is that the calculated efficiency depends on the shape of the spectrum of the test photons which are used for the overlaps. Simple simulations show that for the exponential spectrum a change in the slope of the spectrum by 5% leads to $\approx$ 5% change in the value $(1-\varepsilon)$, where ε is the efficiency. As the measured spectrum is already distorted by overlaps, several iterations (2–4) were necessary to obtain the correct efficiency.

There is, however, an efficiency calculation method which does not depend on the test photon spectrum shape and does not require iterations.

4.9.3 'Two-dimensional' methods

The true spectrum of photons can in principle be calculated by solving the integral equation:

$$F_{\mathrm{m}}(P_{\perp}) = \int A(P_{\perp}, P'_{\perp}) \cdot F_{\mathrm{t}}(P'_{\perp}) \mathrm{d}P'_{\perp} \ , \tag{4.21}$$

where F_{m} is the measured photon spectrum, F_{t} is the true photon spectrum and $A(P_{\perp}, P'_{\perp})$ is the probability of a photon with original transverse momentum $P'_{\perp}$ having transverse momentum $P_{\perp}$ after overlap.

As all the spectra are in the form of histograms with finite bin size, the integral equation is transformed into a set of linear equations.

Matrix $A(P_{\perp}, P'_{\perp})$ can be calculated by overlapping test photons on real events. As with the 'one-dimensional' method, there are two ways of filling this matrix. The first is to search for the closest neighbour of the overlapped test photon and the second is to take into account all the new and disappeared after overlap hits and use an energy-dependent weight according to Eq. (4.20).

A typical shape of matrix $A(P_{\perp}, P'_{\perp})$ is shown in Fig. 4.33

The main problem with this method is the calculation of errors. As the relation between measured and true spectrum is rather complicated, we used a Monte Carlo method for error calculation. Each point of the measured spectrum was smeared randomly according to a gaussian distribution with an average equal to the spectrum value at this point and sigma equal to its error. After this smearing, Eq. (4.21) was solved again. This procedure was repeated several times and the dispersion of results at a given point was taken as an error at this point. Of course, this method does not take into account the uncertainty of

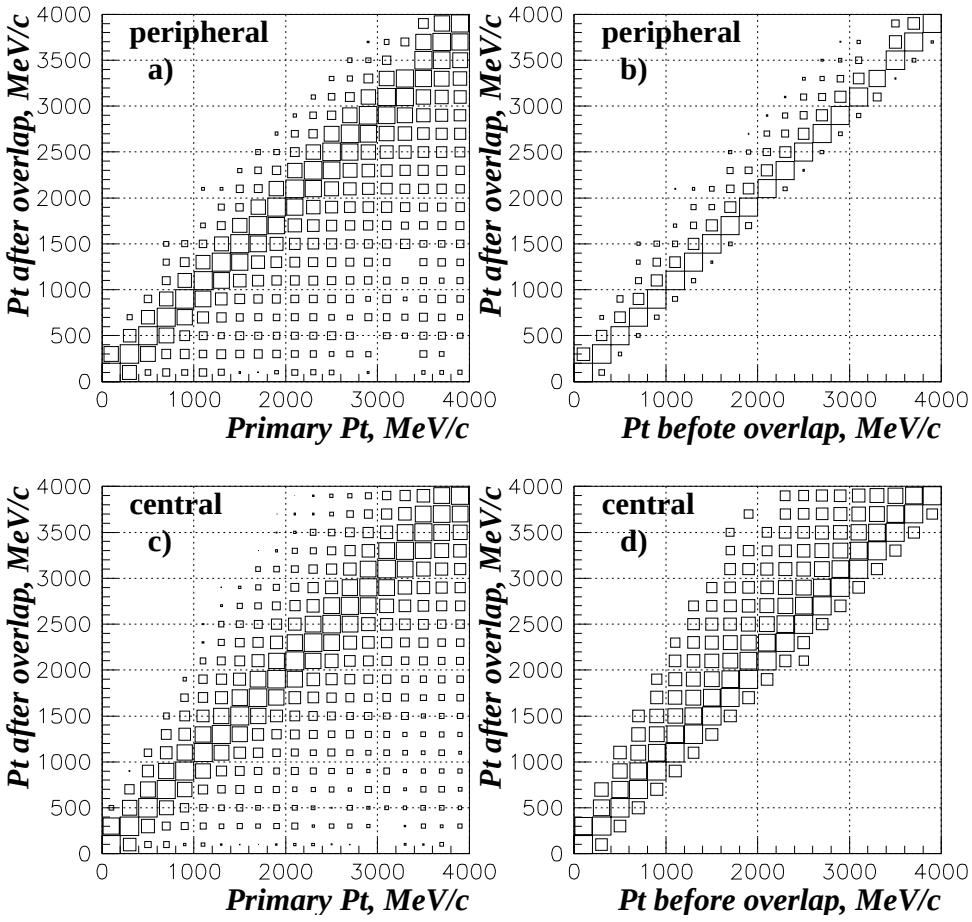

Figure 4.33: Probability of a photon changing its transverse momentum in peripheral (a and b) and central (c and d) collisions due to overlaps only (b and d) and due to overlaps and detector response (a and c).

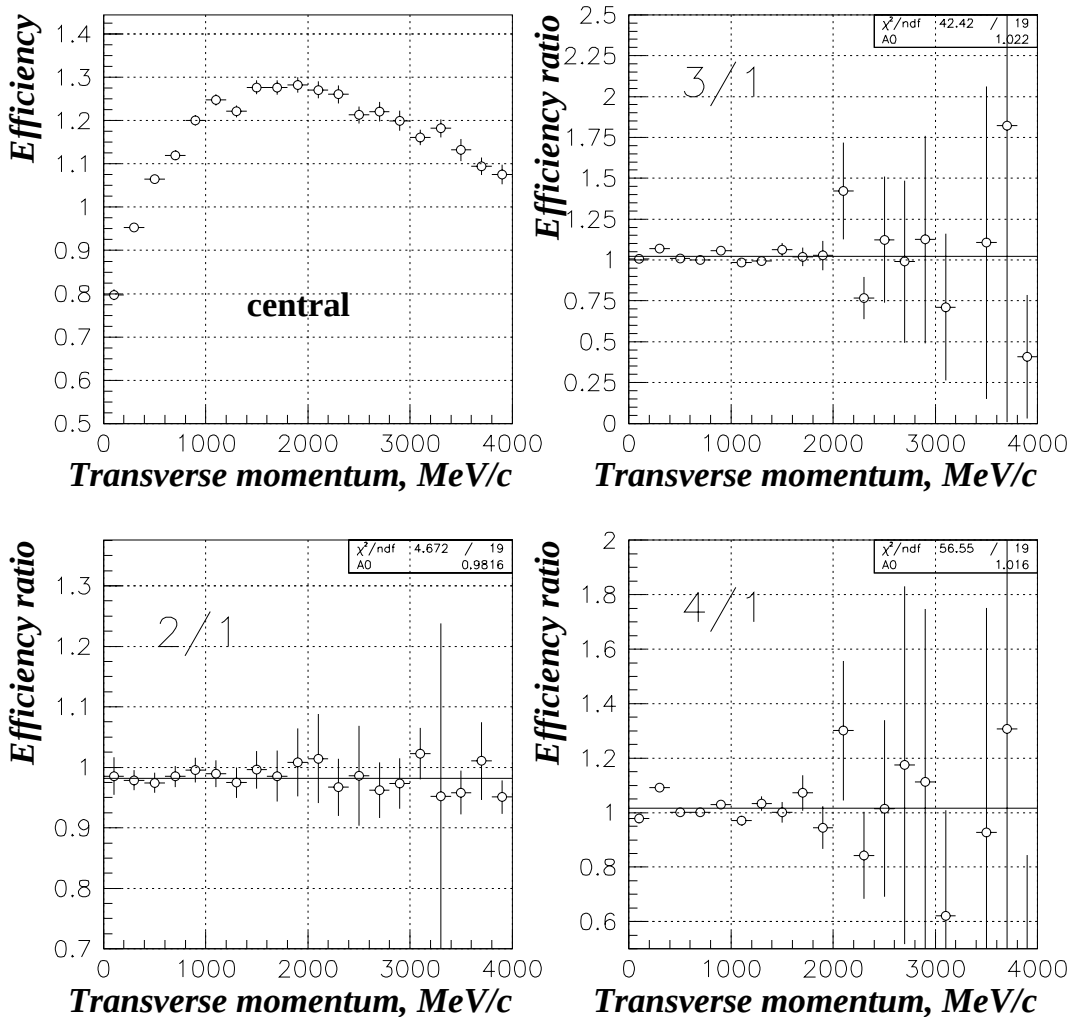

Figure 4.34: Photon registration efficiency calculated using the single particle one-dimensional method (upper-right) and ratios of efficiencies calculated using other methods to the single particle one-dimensional method (other three) in central collisions.

matrix A, and the error calculated in this way can be considered only as a lower limit. In fact, the errors in 'two-dimensional' efficiency turned out to be higher than those obtained in the 'one-dimensional' calculations, especially at high $P_\perp$. Consequently, the efficiency calculated by solving Eq. (4.21) was used only to check the other methods. As can be seen in Figs.. 4.34 and 4.35, the 'two-dimensional' efficiencies ε_3 and ε_4 are in good agreement with the 'one-dimensional' efficiencies ε_1 and ε_2.

4.9.4 Results

The efficiencies calculated using four different methods are shown in Figs. 4.34 and 4.35. The good agreement between the 'one-dimensional' and 'two-dimensional' methods shows that the final distributions for test photons were correct and that the iterations converged. Agreement between single particle and multiparticle methods indicates that there was no significant systematic error made. From the difference between the efficiencies calculated by the different methods one can estimate the systematic error of the efficiency which in the SPS experiment turn out to be $\approx 2\%$ in central and $\approx 0.5\%$ in peripheral collisions.

The fact that the efficiency becomes greater than 1 at some $P_\perp$ in central collisions is explained by the photon energy change caused by overlap. As can be seen in Fig. 4.33, the overlaps mostly increase

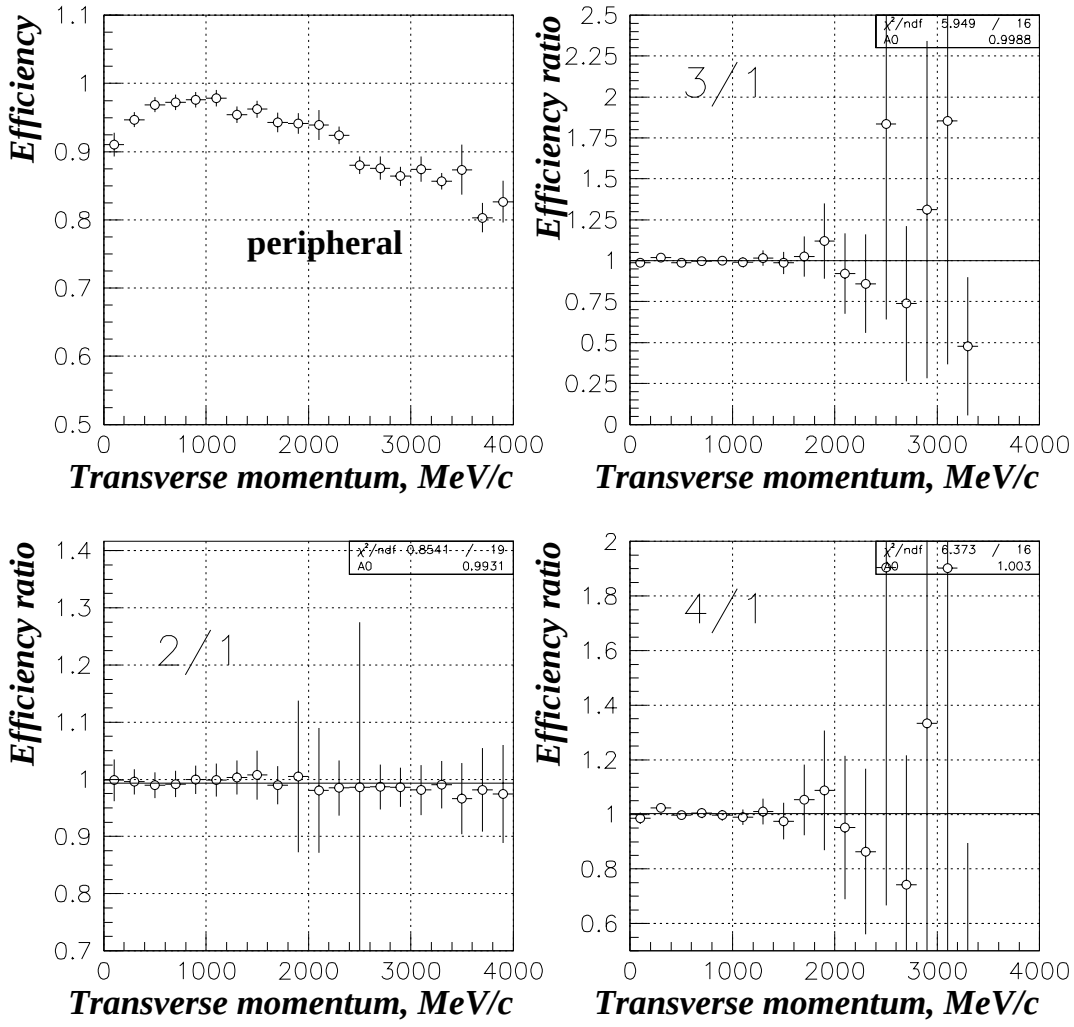

Figure 4.35: The same as Fig. 4.34 for periphepral collisions.

photon energy. As the photon spectrum has an exponential shape, the number of photons which left a certain $P_\perp$ bin is much smaller than the number of photons which moved to this bin from the higher $P_\perp$ bin. This causes the number of detected photons at some $P_\perp$ to be greater than the actual number of these photons. At high $P_\perp$ the photon spectrum flattens out, which causes a drop in efficiency.

One additional problem, which is associated with the efficiency calculation using the overlap of test photons, is that the efficiency is actually calculated for multiplicity $M+1$, where M is the average multiplicity for a given centrality. And since the probability of shower overlap increases with increasing multiplicity this could introduce the systematic error in efficiency calculated in this way. In Fig. 4.36 a ratio of efficiencies calculated for different event multiplicity is shown. One can see that the addition of seven particles (approximately 10% increase) leads to a 2–3% change in efficiency. Thus, the addition of one particle should not lead to more than 0.3–0.4% efficiency change and can be neglected.

4.10 π^0- and η- meson production

The neutral mesons will be reconstructed via their $\gamma\gamma$ decay channel. In central Pb–Pb collisions at LHC energy, the number of particles produced in each collision is very high, as is the combinatorial background (B) in the two-photon invariant mass spectrum, due to the many possible photon pairs.

Because of the large background, meson yields can only be determined inclusively. True π^0 and η

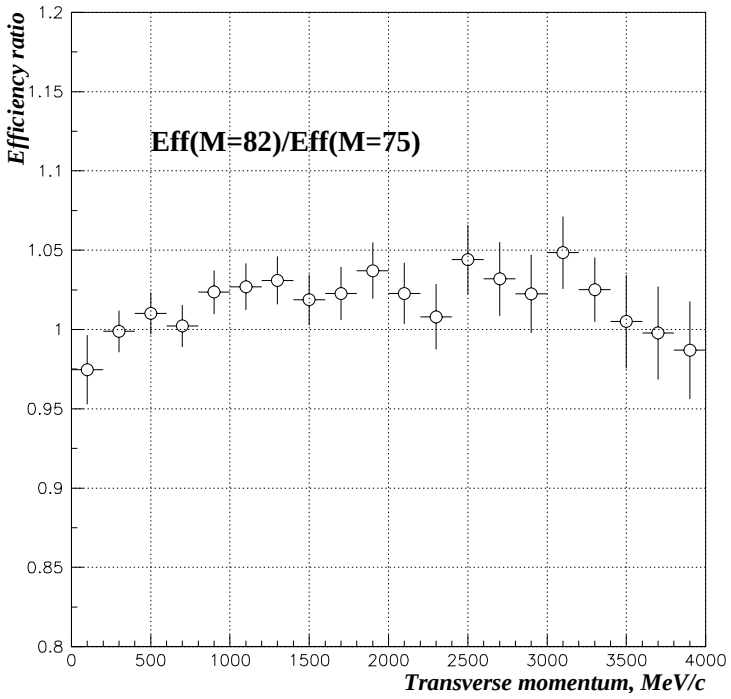

Figure 4.36: Ratio of efficiencies calculated for different average multiplicities.

yields (S) must be extracted from the respective mass peaks which sit on the combinatorial background. The signal fraction $[S/(S+B)]$ in such plot decreases inversely with the phase–space density of the photons. This problem worsens in heav-ion collisions with respect to pp or p–A collisions because of the much higher multiplicity of the photons produced. The combinatorial background problem also becomes worse at low p_{T}, both due to the increased phase–space density of low-energy photons, and the fact that at low p_{T} the true photon pairs open up to encompass a larger region of acceptance, which allows a larger number of combinatorial possibilities.

4.10.1 Statistical accuracy

The statistical accuracy of π^0 and η yield measurements, $(\sigma_N/N)_{\pi^0,\eta}$, is determined by the numbers of accumulated mesons, $N_{\pi^0,\eta}$, as well as by the signal fractions $[S/(S+B)]_{\pi^0,\eta}$, and can be expressed as follows:

$$\left(\frac{\sigma_N}{N}\right)_{\pi^0,\eta} = \sqrt{\left[2\cdot\left(\frac{S+B}{S}\right)_{\pi^0,\eta} - 1\right]\cdot\frac{1}{N_{\pi^0,\eta}}}\,. \tag{4.22}$$

The expected π^0 and η multiplicities in the PHOS calorimeter for central Pb–Pb collisions are shown in Fig. 4.37. The numbers of π^0's and η's per event per GeV/c detected by the PHOS calorimeter at a photon-energy threshold of 250 MeV are plotted vs. the meson transverse momentum, p_{T}. These plots are the result of a simulation using the HIJING event generator.

The signal-to-total ratios for the π^0 and η mesons in central Pb–Pb collisions, shown in Fig. 4.38, were simulated with the SHAKER event generator, assuming the rapidity density of produced charged particles $\mathrm{d}N_{\mathrm{ch}}/\mathrm{d}y$ =8000 (which implies the same density for photons). The energy and position resolutions found in the beam tests with the prototype (see Section 2.4, Chapter 2) were used in the simulation. The ratio $S/(S+B)$ for π^0 mesons is at the level of a few per cent for $p_{\mathrm{T}} \sim$1 GeV/c , and it is getting to a level of a few tens per cent for $p_{\mathrm{T}} > 2$ GeV/c. For the η mesons this ratio is at a level of a few

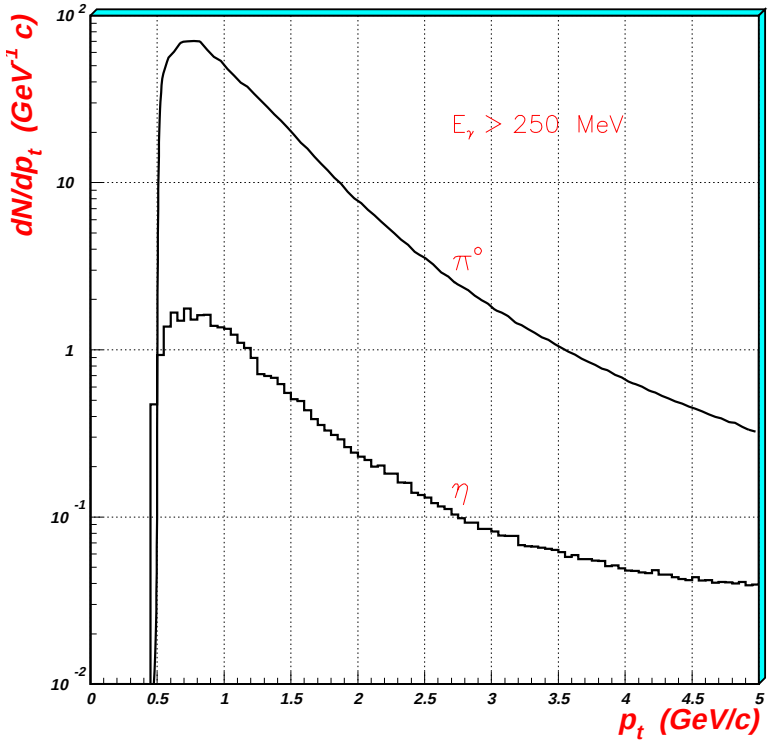

Figure 4.37: The number of π^0's and η's per event per GeV/*c* detected by the PHOS calorimeter at a γ-energy threshold of 250 MeV.

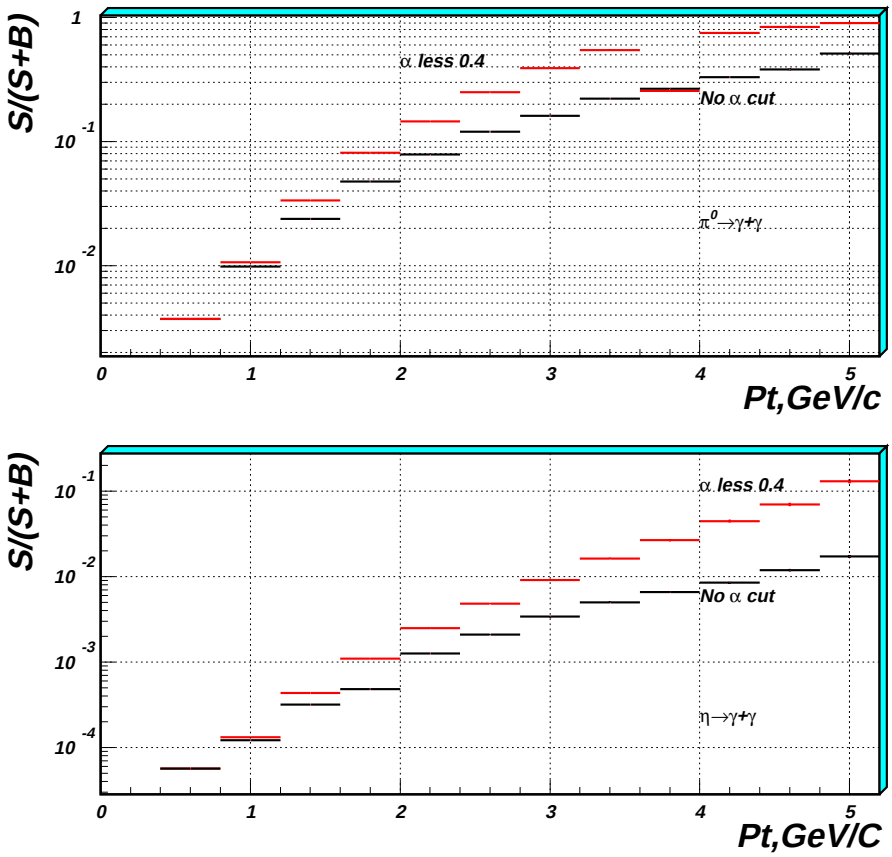

Figure 4.38: Signal-to-(signal+background) ratio vs. transverse momentum.

tenths of a per cent for p_T in the range 2–4 GeV/c, and it is getting to a per cent level for $p_T > 4$ GeV/c. Applying proper cuts to the asymmetry in the energy of the photon pairs, $\alpha \equiv |E_{\gamma 1} - E_{\gamma 2}|/(E_{\gamma 1} + E_{\gamma 2})$, the signal-to-total ratio is improved, as it is demonstrated in Fig. 1.2, where the result obtained with $\alpha < 0.4$ is presented.

However, as already mentioned, even at the signal-to-total ratios of this level, the π^0 and η mass peaks can be extracted with the required precision.

The number of π^0 and η mesons which have to be detected in order to achieve a required statistical accuracy, $a^{\rm req} \equiv (\sigma_N/N)^{\rm req}$, can be found by using the following formula:

$$N = \left[2 \cdot \left(\frac{S+B}{S}\right) - 1\right] \cdot \left(\frac{1}{a^{\rm req}}\right)^2 . \tag{4.23}$$

Then the number of events to be accumulated for achieving a required statistical accuracy is readily found as

$$N^{\pi^0,\eta}_{\rm event} = \frac{1}{M_{\pi^0,\eta}} \cdot \left[2 \cdot \left(\frac{S+B}{S}\right)_{\pi^0,\eta} - 1\right] \cdot \left(\frac{1}{a^{\rm req}_{\pi^0,\eta}}\right)^2 , \tag{4.24}$$

where $M_{\pi^0,\eta}$ is the multiplicity (per event) of π^0's or η's in a given p_T range detected by the PHOS calorimeter

$$M_{\pi^0,\eta} \equiv \frac{1}{N_{\rm event}} \cdot \frac{{\rm d}N_{\pi^0,\eta}}{{\rm d}p_T} . \tag{4.25}$$

We have evaluated the number of events needed to reach a given accuracy for the meson cross-section based on the signal fractions, $[S/(S+B)]_{\pi^0,\eta}$, and the meson multiplicities, $M_{\pi^0,\eta}$, shown in Fig. 4.38 and Fig. 4.37, respectively.

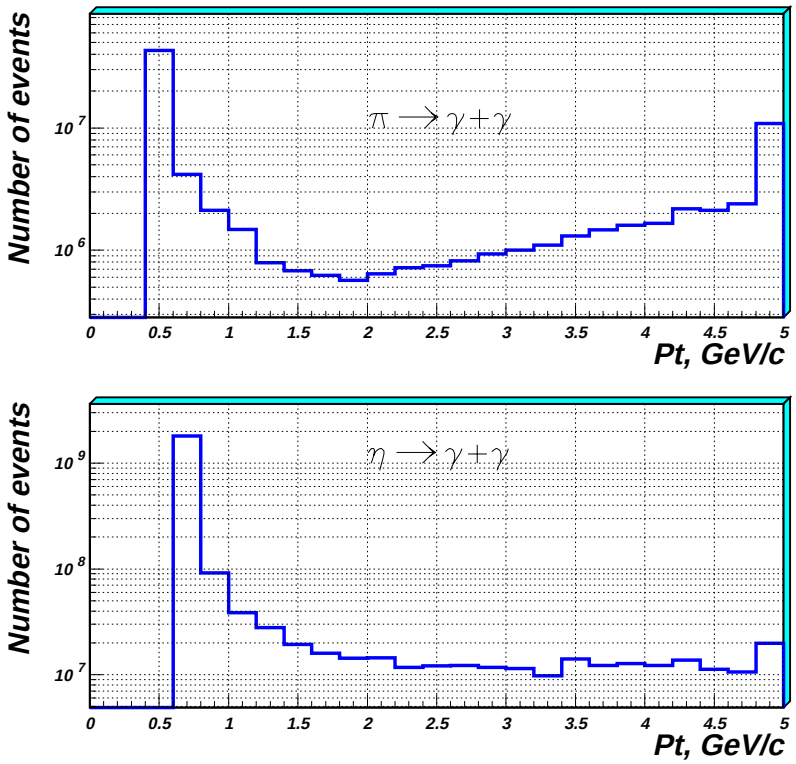

Figure 4.39: Total number of events necessary for achieving a statistical accuracy of 1% per 200 MeV/c bin in the π^0 yield (top figure) and 10% per 200MeV/c bin in the η yield (bottom figure), plotted vs. transverse momentum.

The results of the simulation are presented in Fig. 4.39. It shows, for each p_T bin, the total number of events which must be accumulated if one wants to achieve 1% statistical accuracy in the π^0 yield and 10% accuracy in the η yield. In ALICE we expect to collect about 5×10^7 central Pb–Pb events per year.

4.10.2 Extraction of meson spectra

The combinatorial background is evaluated by the so-called event mixing technique (see, for example Refs. [13])

Hits in the PHOS detector will be combined in pairs to provide distributions of pair invariant mass vs. pair transverse momentum for all possible combinations, satisfying the chosen cuts.

These distributions will be obtained both for the real events (REAL$(m_{\rm inv}, p_{\rm T})$) and for so-called mixed events (MIXED$(m_{\rm inv}, p_{\rm T})$), where a hit from one event is combined with a hit from another event of the same centrality class. MIXED$(m_{\rm inv}, p_{\rm T})$ provides a good description of the combinatorial background.

The properly normalized mixed event distribution is then subtracted from the real event distribution to obtain the invariant mass distributions of the neutral mesons.

Simulations have been performed to evaluate the capabilities of the event mixing method in the ALICE experiment multiplicity environment. The SHAKER event generator with the highest rapidity density expected in central Pb–Pb collisions, i.e. 8000 charged particles per unit of rapidity, has been used to produce π^0's and η's. The JETSET package has been used to simulate the decays of the produced mesons. In total 1.5 million of such events were simulated. The REAL and MIXED two-photon invariant mass spectra were obtained using the procedure described above, both with and without a cut on α. The ratios REAL/MIXED in a p_T range of 2–3 GeV/c for the two cases are shown in Fig. 4.40.

As can be seen in the figure, in both cases even the η mass peak is clearly seen with these statistics, although the ratio $S/(S+B)$ for this peak is smaller than $\sim 0.2\%$.

This technique was successfully applied in the analysis of the CERN SPS photon data, obtained

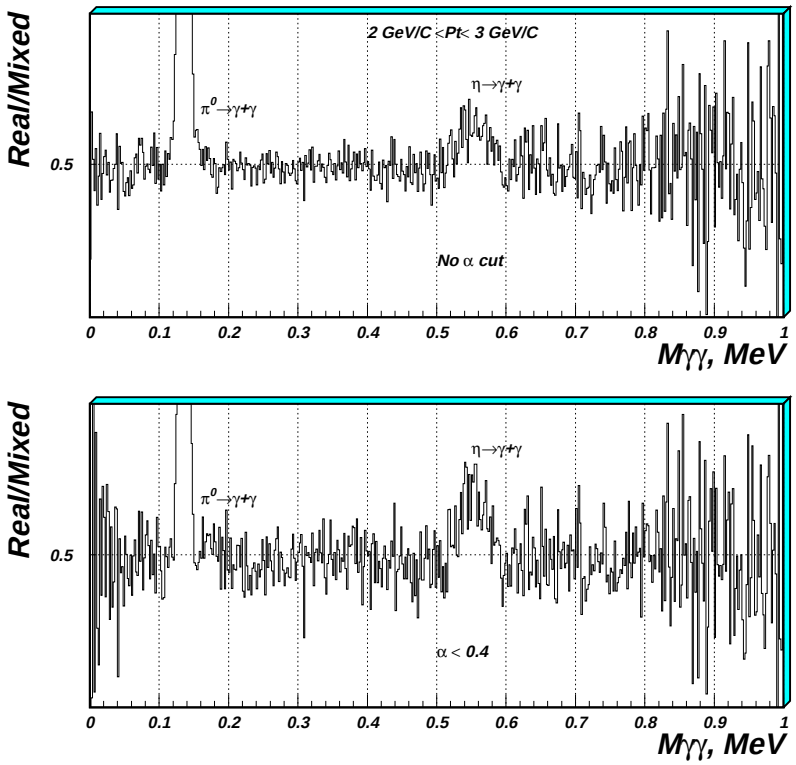

Figure 4.40: Extraction of π^0 and η signals with the event-mixing technique.

by the WA80 and WA98 experiments with highly-granulated electromagnetic calorimeters of $\sim$ 4000 (WA80) and $\sim$ 10000 (WA98) lead glass detectors [13]. It was demonstrated in these experiments that the event mixing technique appears to work, with values of the signal-to-background ratio as low as a few tenths of a per cent with the statistics of a few million events. There was little or no systematic errors in determination of the combinatorial background.

4.11 Direct Photons

We aim at a sensitivity, limited by systematic errors, of $\sim$ 5% for the measurement of direct photons in the energy range $\sim$ 2–5 GeV. We will be able to collect sufficient number of central events so that the measurement of direct photons will be limited by systematic rather than statistical errors over most of the relevant p_{T} range. While statistical errors can be reasonably estimated, a good *a priori* estimate of systematic errors by Monte Carlo simulation is difficult.

We will try to relate most systematic errors to quantities which can be controlled with the actual data. Possible sources of systematic errors expected in ALICE are listed below. This list, to a large extent, is based on the experience from the direct-photon analysis of the CERN WA80 experiment [14], although some of the sources which have to be taken into account in ALICE are of no importance for the SPS experiment (e.g. antineutrons). A large part of the listed systematic errors are independent of centrality.

- **Photon reconstruction efficiency:** This error depends on the cell occupancy and hence on centrality. It can be esimated by comparing efficiencies calculated using different methods. Error in WA80 was $\sim$ 2%. In ALICE one could expect this error to be less or at least not greater, since the cell occupancy is lower by almost a factor of 2.

- π^0 **yield extraction and efficiency:** This is expected to be the largest contribution to the systematic error, which also depends on centrality. It can be estimated by applying different cuts to the photons used for invariant mass calculation (e.g. different energy thresholds, shower width cut, CPV cut, use of clusters with a single maximum). Different methods of background normalization, as well as different invariant mass ranges for summing up of π^0, should be used. Error in WA80 was $\sim$ 5%. In ALICE it should be less due to the smaller cell occupancy and also due to significantly higher statistics, which allows the combinatorial background to be evaluated with better accuracy. Thus, this error can be estimated as $\sim$ 4%.

- **Detector acceptance:** This error is independent of centrality and is determined by uncertainties in geometry. Therefore, it can be reduced to a minimum if the PHOS geometry is measured with high accuracy. Error in WA80 was $\sim$ 0.5%.

- **Energy nonlinearity:** The nonlinearity, which is centrality independent, has to be controlled with data by measuring the π^0 peak position for different p_{T}. Error in WA80 was $\sim$ 1–2%.

- **Binning effects:** Centrality independent, in WA80 visible ($<$ 1%) only for low p_{T}.

- **Charged vs. neutral shower separation:** Error in WA80 was $\sim$ 1%. In ALICE this error should be comparable or less since the cell occupancy is smaller and a quite similar method of separation will be used. This error is centrality independent.

- γ **conversion correction:** Error in WA80 was $\sim$ 1%. In ALICE this error, centrality independent, can even be reduced if the exact amount of matter between the interaction point and the PHOS is known.

- **Neutrons:** Error in WA80 was $\sim$ 1%. In ALICE the neutron contribution to the photon spectrum is negligible.

- **Antineutrons:** Error in WA80 was negligible. In ALICE the antineutron contribution to the photon spectrum can be reduced to $\leq 10\%$. The remaining error is determined by how well the yield and detector response can be extracted from p and $\overline{\mathrm{p}}$ spectra. This should be possible to much better than 10% accuracy, leading to a residual error of $\leq 1\%$.

- **Other neutral mesons:** This error is determined mostly by the knowledge of the η-meson yield. We plan to measure η yield with 10% accuracy and η mesons contribute $\sim 15\%$. Thus, the uncertainty in the final result should be $\leq 1.5\%$.

- **π^0's from strange-particle decay.** Since strange paricles have a long lifetime, they may decay into π^0's far from the interaction point, which are therefore reconstructed with the wrong mass, leading to an underestimate of the π^0 cross-section. A simulation shows that this effect is very small. Error in WA80 was $\sim 0.1\%$.

The quadratic sum of all errors is 5.6%. It should be noted that the PHENIX Collaboration has evaluated the performance of a detector similar to PHOS for RHIC and estimates a systematic error below 5.5% [15].

4.12 Hanbury-Brown and Twiss correlations in π^0–π^0 system

The correlation of gammas into π^0 and the subsequent study of the π^0–π^0 correlation function is impractical in the ALICE environment due to the limited PHOS acceptance and the enormous combinatorial background. We therefore investigated the problem of whether the π^0–π^0 Bose–Einstein correlations also called Hanbury-Brown and Twiss (HBT) correlations survive in the π^0 decay products and addressed the question of the quantitative reproduction of the π^0 HBT parameters by analysing the gamma–gamma correlation function. In the following we will demonstrate that it is perfectly feasible to reconstruct the π^0 source-size and its 'coherence' factor from the gamma–gamma correlation function [16]. The simulations presented did not include effects caused by resonance decays.

To define the two-gamma correlation function, let us consider a correlated pair of π^0 which in a fixed laboratory frame has momenta $\mathbf{k}$ and $\mathbf{l}$, respectively. Each of the two pions subsequently decays into two gammas and the momentum conservation yields $\mathbf{k} = \mathbf{k}_1 + \mathbf{k}_2$ and $\mathbf{l} = \mathbf{l}_1 + \mathbf{l}_2$, where $\mathbf{k}_j$ and $\mathbf{l}_j$ ($j = 1,2$) are the momenta of the photons. We wish to investigate only the correlations between two photons descending from different parent pions and for this purpose it will be convenient to introduce a relative two-photon momentum $\Delta = 1/2 \cdot (\mathbf{k}_1 - \mathbf{l}_1)$ supplemented with their total momentum $\mathbf{s} = \mathbf{k}_1 + \mathbf{l}_1$. Having established the notation, the two-gamma correlation function $C_\gamma(\Delta)$ can now be written as the ratio

$$C_\gamma(\Delta) = \frac{\int \Pi(\mathbf{k})\,\Pi(\mathbf{l})\,C_\pi(1/2\cdot\mathbf{k} - 1/2\cdot\mathbf{l})\,\mathrm{d}\rho}{\int \Pi(\mathbf{k})\,\Pi(\mathbf{l})\,\mathrm{d}\rho}\,, \tag{4.26}$$

where C_π is the two-pion correlation function, the functions Π describe the initial momentum distribution of the pions, and $\mathrm{d}\rho$ denotes the phase–space element

$$\begin{aligned}\mathrm{d}\rho = \mathrm{d}^3k\,\mathrm{d}^3l\,\mathrm{d}^3s \quad &\times \quad \delta(\sqrt{m^2+k^2} - |1/2\cdot\mathbf{s} - \Delta| - |\mathbf{k} + \Delta - 1/2\cdot\mathbf{s}|) \\ &\times \quad \delta(\sqrt{m^2+l^2} - |1/2\cdot\mathbf{s} + \Delta| - |\mathbf{l} - \Delta - 1/2\cdot\mathbf{s}|)\,,\end{aligned} \tag{4.27}$$

with m being the pion mass. The azimuthal angle integrations are trivial because of the presence of the delta functions expressing energy conservation and can be carried out analytically so that ultimately we are left with six dimensional integrations which have to be performed numerically. We used the following C_π correlation function: $C_\pi(\Delta) = 1 + 1/[1 + (|\Delta|\cdot R)^{\mathbf{2}}]^{\mathbf{2}}$, where R is the π^0–π^0 source-size. The initial momentum distribution of pions was taken in the form $\Pi(\mathbf{k}) = k\exp(-\alpha k)$ with $\alpha = 3\ (\mathrm{GeV}/c)^{-1}$.

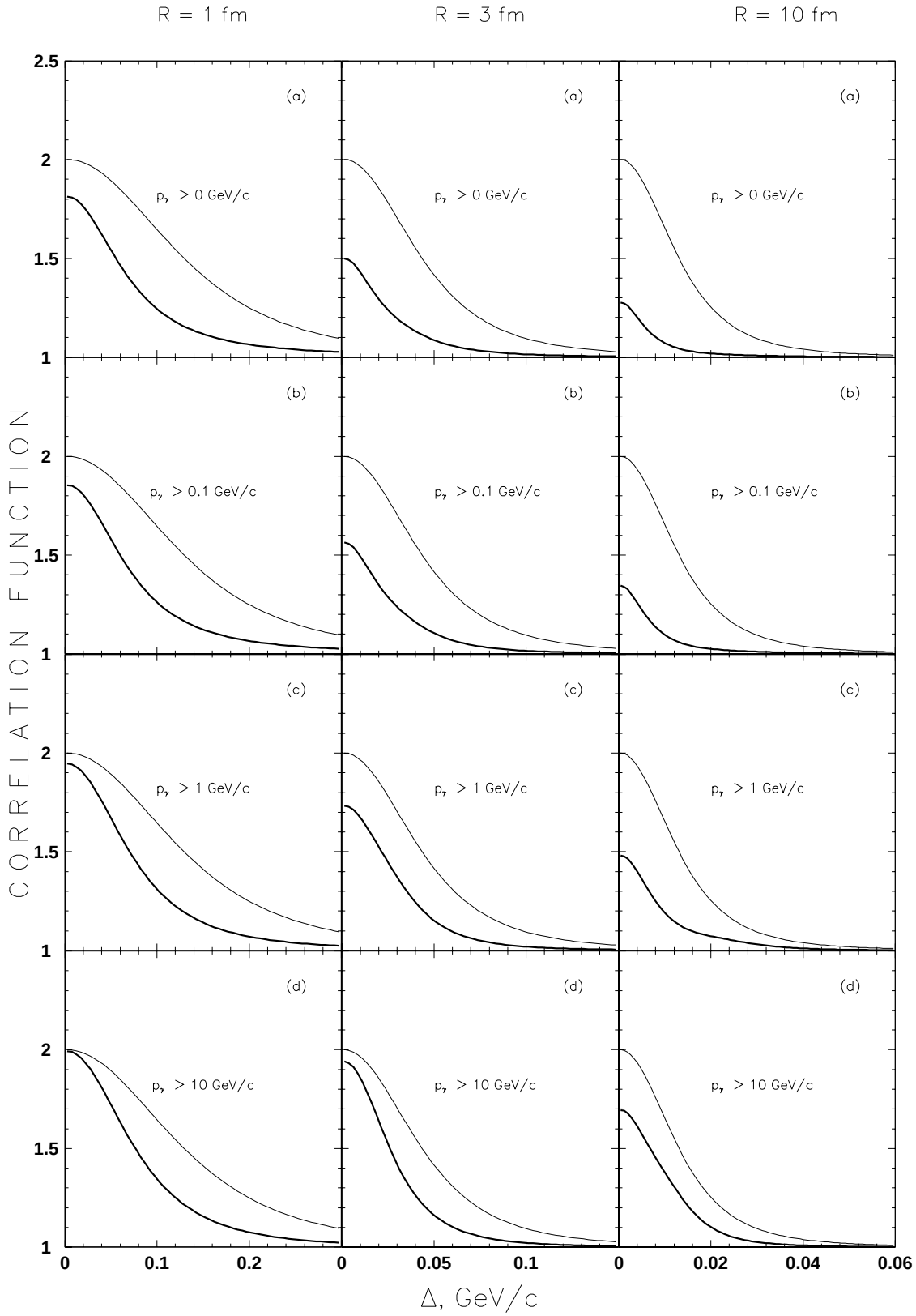

Figure 4.41: Correlation function for the π^0–π^0 and γ–γ systems calculated for three (1, 3 and 10 fm) source-sizes. Labels (a), (b), (c) and (d) correspond to the whole photons' spectrum and a cut of 0.1, 1, and 1 GeV$/c$ on the photon momentum, respectively. The thin curve refers to π^0–π^0 and the thick one to the γ–γ correlation function.

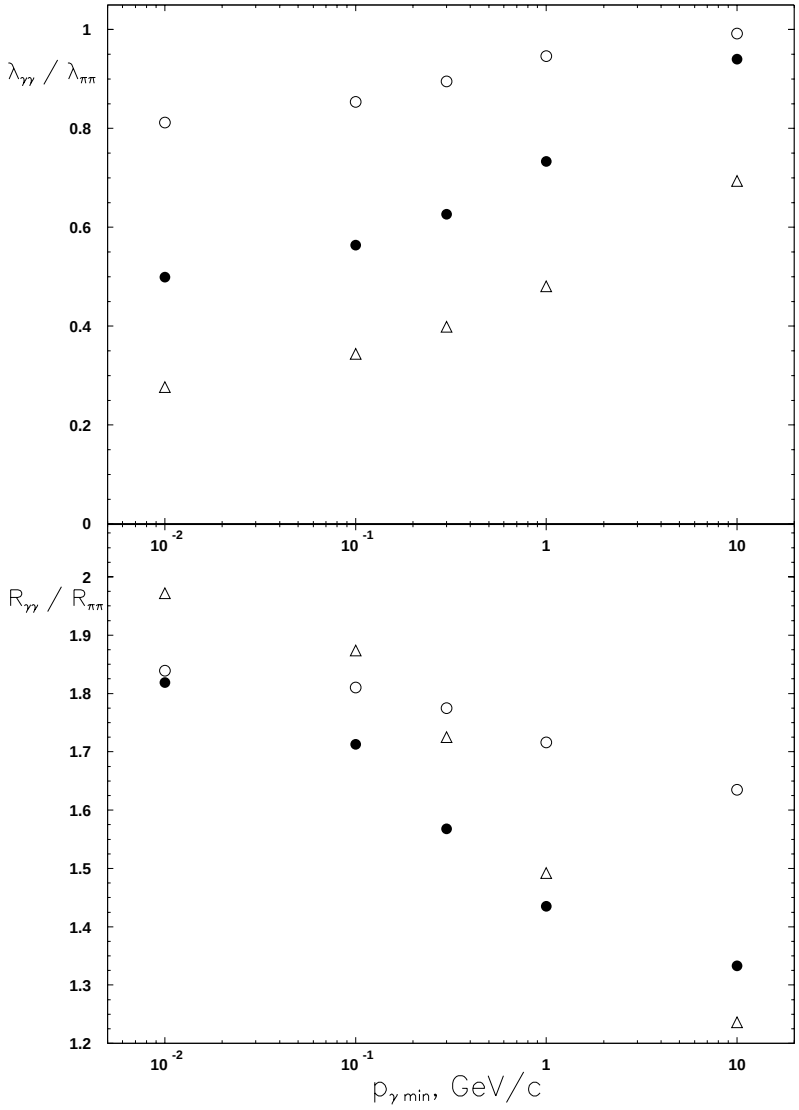

Figure 4.42: Ratios of source-sizes and coherence factors of γ–γ to those of π^0–π^0 as a function of the minimal photon momentum. The open, filled circles and triangles refer to the π^0–π^0 source-sizes of 1, 3 and 10 fm, respectively.

Figure 4.41 shows the π^0–π^0 correlation function (thin curve) compared with the γ–γ correlation function (thick curve) for three source-sizes of 1 fm, 3 fm and 10 fm, and various cuts applied to the photons, momenta. The figure labelled (a) refer to all gammas, whereas those labelled (b), (c) and (d) represent selections with minimal γ momentum of 0.1, 1 and 10 GeV/c, respectively. In the upper and lower panels of Fig. 4.42 we show the corresponding ratios of $\lambda_{\gamma\gamma}/\lambda_{\pi\pi}$ and $R_{\gamma\gamma}/R_{\pi\pi}$, respectively, as a function of the cut applied on the gamma momentum. Inspection of Figs. 4.41 and 4.42 reveals the following regularities:

(i) The value of the intercept (coherence factor) of the two-gamma correlation function gets consistently larger with the increase of the $p_{\gamma\min}$, approaching for $p \geq 10$ GeV/c the coherence factor of a π^0 source for 1 fm and 3 fm sources. This would require a cut of about 50 GeV/c for the 10 fm source to reach the π^0–π^0 coherence factor.

(ii) The source-size extracted from the two-gamma correlation function roughly doubles the two-π^0 source-size if the whole gamma-spectrum is used to construct the γ–γ correlation function. It decreases when the cut is imposed on the gamma momentum, but even for the largest cut applied ($p_\gamma > 10$ GeV/c),

the γ–γ source-size exceeds somewhat the π^0–π^0 source-size, the ratio being between 1.2 and 1.6. The practical prescription to evaluate the $R_{\pi\pi}$ from the γ–γ correlation function will consist in inserting into (4.26) the $\Pi(\mathbf{k})$ extracted from the experiment and subsequent calculation of $R_{\gamma\gamma}/R_{\pi\pi}$ as a function of $p_{\gamma\min}$.

5 Installation and organization

5.1 ALICE experimental area

The ALICE detector will be installed at Point 2 of the LHC accelerator. The Point 2 experimental area was designed for the L3 experiment. The main access shaft, 23 m in diameter, provides a 15×7 m^2 installation passage and space for counting rooms. The counting rooms are separated from the experimental area by a concrete shielding plug (see Fig. 5.1). The experimental cavern is 21.4 m in diameter and will be re-equipped with a 2×20 t crane having a clearance of about 3 m over the L3 magnet.

The L3 magnet provides a 11.6 m long and 11.2 m diameter solenoidal field of up to 0.5 T. The endcaps have a door-like construction. The door frames will support large beams traversing the L3 magnet, from which the ALICE central detectors will be supported.

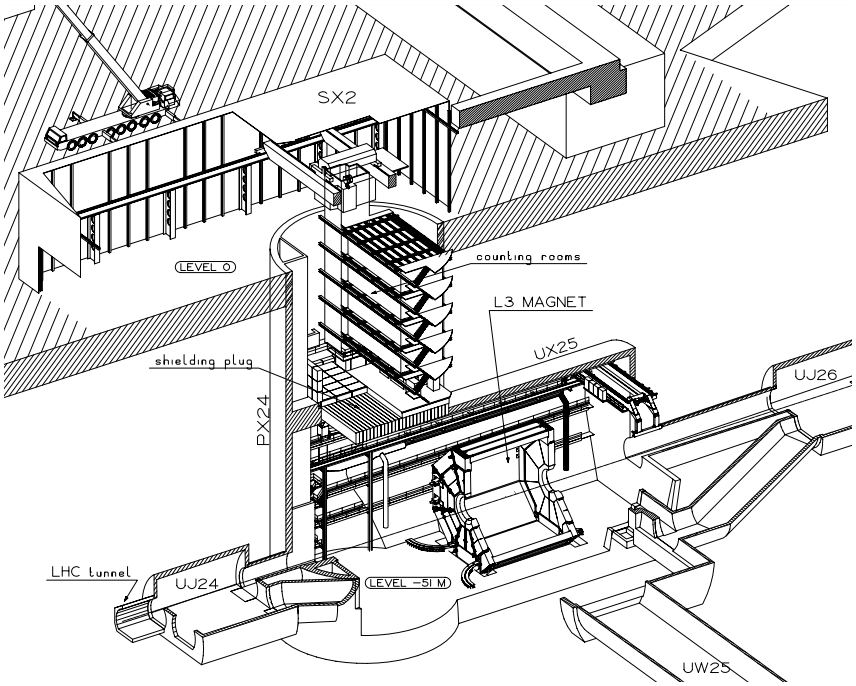

Figure 5.1: General layout of the basic underground structures at Point 2, showing the L3 magnet and the counting rooms.

5.2 Installation of the PHOS and CPV detectors

The PHOS and CPV detectors will be mounted in two separate support cradles (see Fig. 5.2), which will be supported by four large beams traversing the complete length of the L3 magnet. The cradles can be displaced on rails fixed to the support beams and, by adding extensions, the complete detector can be installed or removed independently of the space frame supporting the central detector unit.

The support beams are fixed to the L3 magnet door frames and have been dimensioned to undergo a maximum deflexion of 20 mm [1]. As it is not possible to provide any intermediate support points over the length of the L3 magnet coil (12.3 m), the relatively large size of the beams (height 55 cm for the full PHOS) restricts the available space for the PHOS/CPV detector and the support cradles.

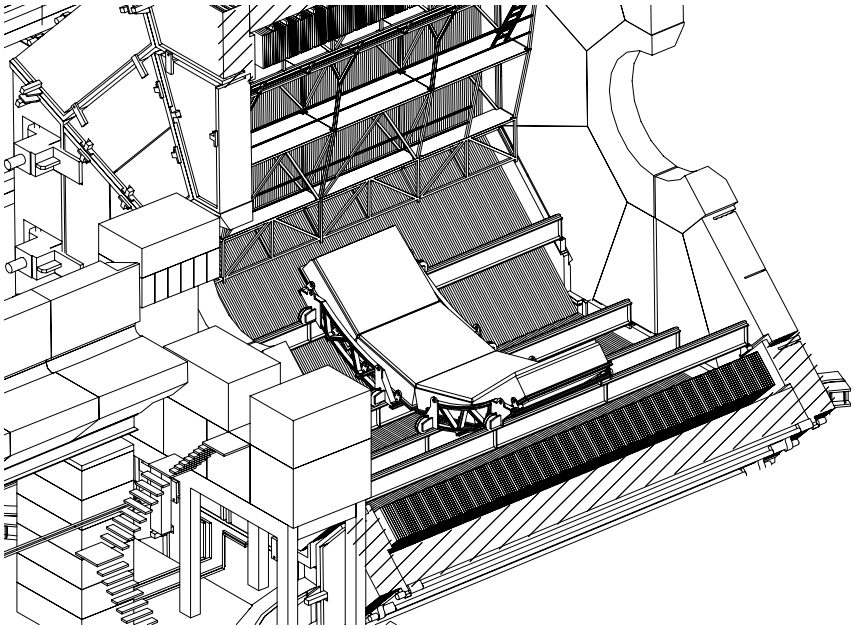

Figure 5.2: The PHOS/CPV detector supported by four beams inside the L3 magnet.

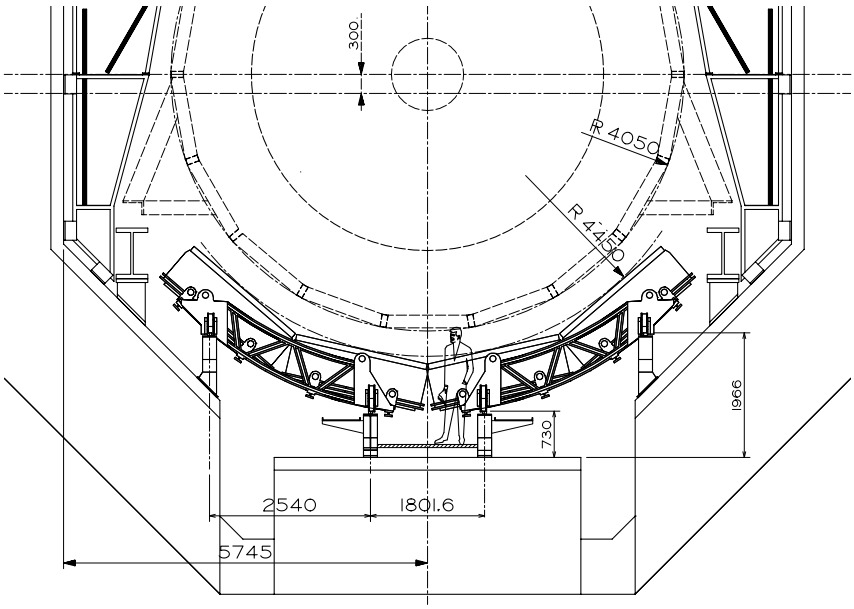

Figure 5.3: Front view of the position of the PHOS/CPV detector situated below the space frame for the central detectors.

The maintenance access to the PHOS/CPV, once installed inside the L3 magnet, is not difficult and it will be possible to reach most parts of the detector during a short access. A gangway will be installed between the two central beams to permit access even when the magnet doors are closed (see Fig. 5.3). If a complete module has to be removed for repair it will be necessary to open the magnet doors, which will require a partial removal of the beam line shielding and, therefore, require a longer shutdown.

A system of two independent cradles, each supporting two PHOS/CPV modules, has been chosen in preference to a single support cradle. The two-cradle system provides for easy installation and removal procedures, completely independent of the central detectors and the beam line (see Fig. 5.4).

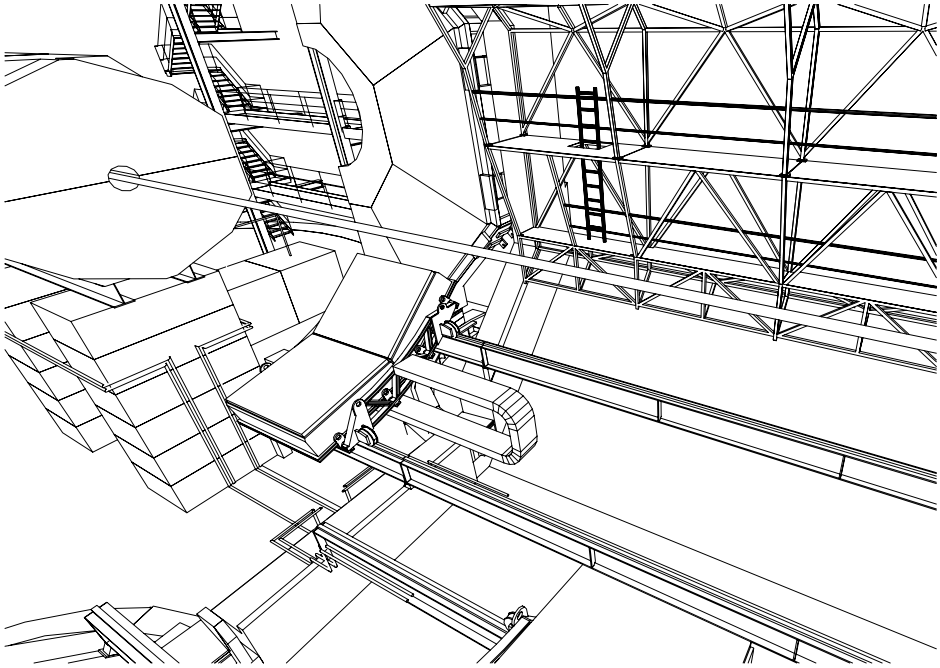

Figure 5.4: Temporary rail support for the PHOS/CPV. The detector is shown in an installation/maintenance position outside the L3 magnet. Part of the concrete shielding has been removed in order to open the magnet doors.

Because of the presence of a magnetic field, it is foreseen to move the support cradles using hydraulic motors. All services for the moving system and detectors will be placed in a flexible cable tray, and therefore all connections and disconnections can be made outside the L3 magnet.

The final assembly of the modules will be made at CERN. The large support beams and the cradle mechanics will be installed and tested inside the L3 magnet in June 2003. The cradles will, thereafter, be placed on temporary supports in the SXL2 hall ready to receive the PHOS/CPV modules. This will allow the PHOS/CPV detector to be completely assembled and tested before it is installed in the L3 magnet. The complete detector assembly will be lowered down into the UX25 area (see Fig. 5.5) and lifted onto the temporarily installed rail extensions, from which the detector can be rolled into its final position.

5.3 Services

The cooling units for the PHOS will be located as close as possible to the L3 magnet so as to reduce the length of pipes to a minimum, since each additional metre increases the heat input into the cooling liquid. The tubes will be insulated to reduce the heat input to a minimum. Heat produced by the cooling units (estimated to be of the order of 40 kW) will be removed by circulating water at $\sim 12\,^{\circ}$C. An additional mixed water circuit will remove heat produced by the front-end electronics. It is expected that the fraction of heat removed by the cooling water will be higher than 90 %.

All services will pass into the internal volume of the L3 magnet through a gap between the door and the barrel (see Fig. 5.2). In this way, the magnet doors can be opened without disconnecting and removing the services.

The HV and LV power supplies will be located in racks in the UX25 experimental area, close to the L3 magnet. All power supplies will be remotely controlled from the counting rooms. It is estimated that four standard racks will be required in close proximity to the L3 magnet.

Argon gas for the mixture and purging is supplied from a liquefied storage dewar, with reserve batteries, which will ensure an interruption-free supply at a nominal pressure of 5 bar.

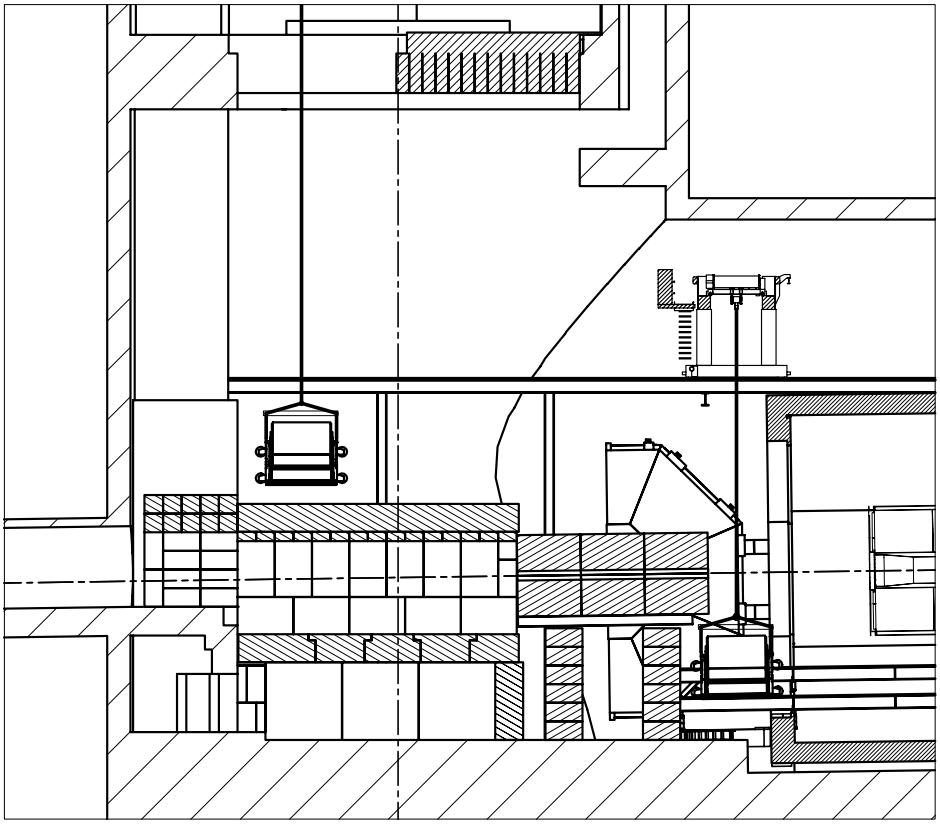

Figure 5.5: The PHOS/CPV detector is lowered down via the PX24 access shaft to an intermediate position on top of the beam radiation shielding. From this position it can be moved by the cavern crane and placed on the extension rails just outside the L3 magnet.

Carbon dioxide gas is supplied from standard batteries, each battery having a capacity of approximately 30 kg. Two batteries will be installed in parallel. Automatic changeover and primary pressure regulation will ensure an interruption-free supply of gas to the panel in the mixing room, at a nominal pressure of 5 bar.

5.4 Safety aspects

The PHOS/CPV detector was the subject of a recent Initial Safety Discussion (Ref. TIS/GS/WW/99–014). The outcome of this review was that the concept of the detector did not include any particular safety risks.

The gas in the CPV detector is not flammable and the relatively small volume of gas, compared to the total volume inside the L3 magnet, does not justify any particular safety precautions. The closed volume of the L3 magnet will be monitored separately for both flammable gas and oxygen deficiency, and access to the inside of the magnet will be restricted.

As the mixture of the cooling liquid for the modules (a solution of propylene glycol in water) has a high flash point and is non-toxic, no precautions are required with respect to leakages and personnel protection. The installation will be designed and built to the highest industrial standards and all tubes will be made of stainless steel. Troughs will be placed under the cooling units and storage tanks to recover any spilt liquid.

All insulation materials will conform to the CERN Safety Instruction TIS IS41 (The use of plastic and other non-metallic materials at CERN with respect to fire safety and radiation resistance).

5.5 Milestones and construction programme

The crystals, after delivery from the producers, will be tested on test-benches in the participating institutes. The crystals' characteristics will be written into a database. The crystal strip units will be assembled and then delivered to CERN. The modules will be assembled from the crystal units and calibrated at CERN.

An overall time schedule for the PHOS is shown in Fig. 5.6. During 1999 and the first half of 2000 the design of the main components will be finalized. Production of the crystals will start in the second quarter of 1999 and finish in the middle of 2004.

During the middle of 2001 the main orders for the electronics should be placed so as to start the module assembly from the middle of 2002. The preproduction of the PIN-diodes and preamplifiers will start in the autumn of 2000, and production will continue between the middle of 2001 and the end of 2003. The FEE prototype study will start in the middle of 2000. FEE production will begin in 2002 and will continue for 1.5 years, until the middle of 2003.

Construction of the LED monitoring system will start in the middle of 2001, and will continue up to the end of 2002. The mechanics and cooling will be produced and delivered to CERN, in several batches, before the middle of 2003. The completion of the CPV design is foreseen for the middle of 2000. The first two CPV modules will be delivered to CERN in the second quarter of 2003.

The assembly of the modules will start in the middle of 2002. The modules will be assembled one after the other. About four months will be necessary to assemble one module. The PHOS installation in UX25 will start from the beginning of 2005. Before this time, all the modules should be calibrated with an electron beam.

In the middle of 2000 a programme for the creation of the electromagnetic shower database will be started. During 2000–2005 an accumulation of a total of 100,000,000 well-defined electromagnetic showers is foreseen. To fulfil the requirements of the programme, the total beam time needed is ~ 9 months, at the CERN PS accelerator, using the energy range 0.5–10 GeV.

Figure 5.6 is based on the following technical milestones:

- end of 2000: finalize the engineering design of the mechanical structure and cooling system;
- end of 2002: assembly of the first PHOS module;
- middle of 2003: calibration of the first PHOS module;
- third quarter of 2004: assembly of the fourth PHOS module;
- end of 2004: calibration of the fourth PHOS module;
- beginning of 2005: installation of the PHOS detector in UX25 and its commissioning.

5.6 Organization

5.6.1 Participating institutes

The following institutes will participate in the construction and operation of the PHOS detector:

- China Institute of Atomic Energy, Beijing, China.
- University of Bergen, Department of Physics, Bergen, Norway.
- CERN, Geneva, Switzerland.
- Russian Research Center 'Kurchatov Institute' (KI), Moscow, Russia.
- Westfälische Wilhelms Universität, Institut für Kernphysik, Münster, Germany.
- Laboratoire de Physique Subatomique et des Technologies Associées, Nantes, France.

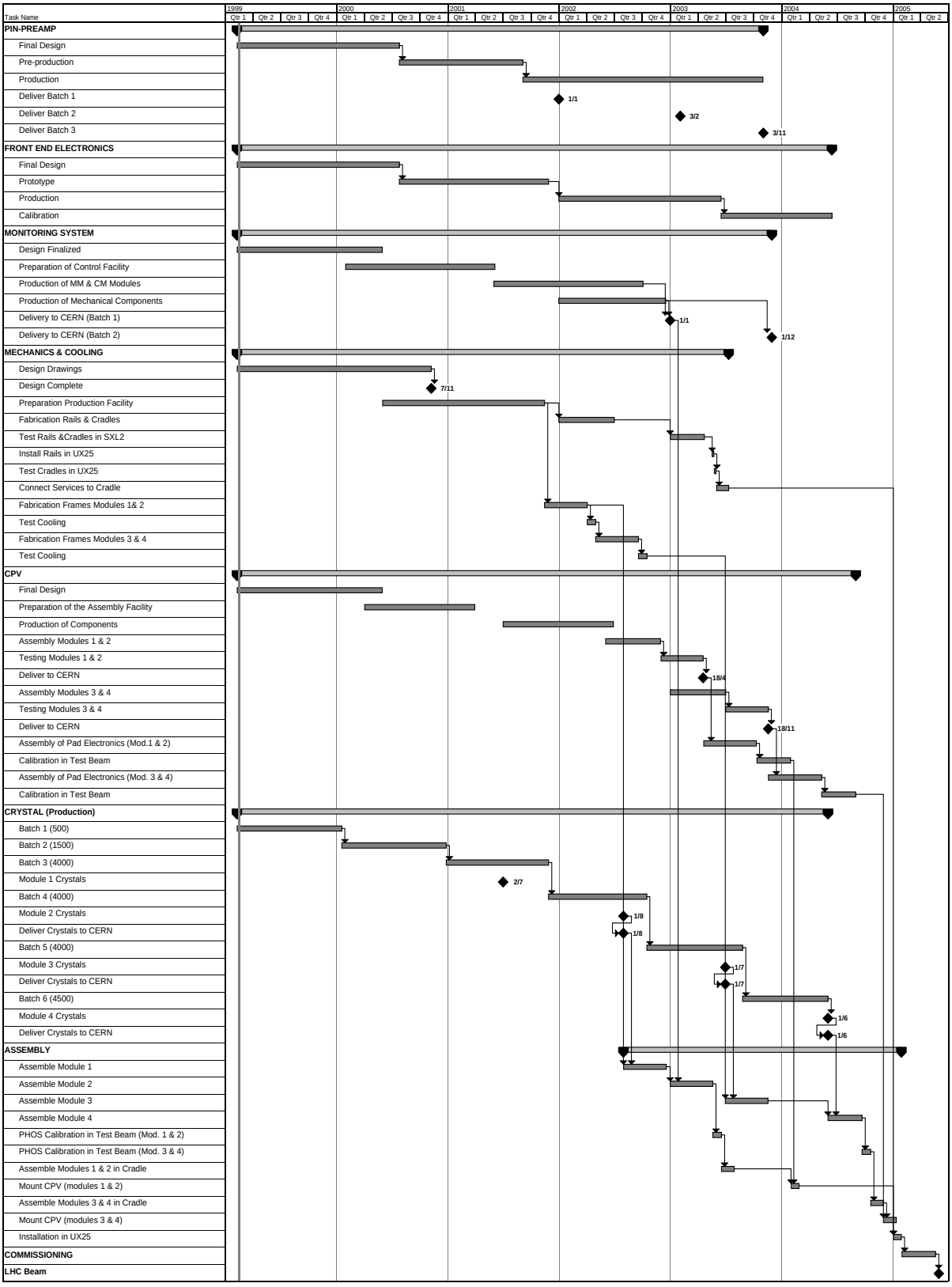

Figure 5.6: General schedule for production, testing and installation of the PHOS/CPV detector.

- University of Oslo, Department of Physics, Oslo, Norway.
- Academy of Sciences of the Czech Republic (ASCR), Institute of Physics, Prague, Czech Republic.
- Institute for High Energy Physics (IHEP), Protvino, Russia.
- Russian Federal Nuclear Center (VNIIEF), Sarov, Russia.
- Soltan Institute for Nuclear Studies, Warsaw, Poland.

The participation of the following two laboratories is under discussion:

- Oak Ridge National Laboratory, Oak Ridge, U.S.A.
- Huazhong Normal University, Institute for Particle Physics, Wuhan, China,

5.6.2 Responsibilities

The proposed sharing of responsibilities during the construction and operation of the PHOS detector is shown in Table 5.1.

Table 5.1: Sharing of responsibilities.

Item	Institutions
Crystals	Beijing, Moscow, Prague, Protvino, Sarov, Warsaw
PIN+preamplifier	Bergen
FEE	CERN, Moscow, Oslo
Mechanics and cooling	Moscow, Sarov
LED monitoring	Protvino
CPV	Nantes, Protvino
On-line	Moscow, Nantes, Oslo
Off-line	Moscow, Münster, Nantes, Protvino, Warsaw

5.7 Cost estimate and resources

The costs of the major systems of the PHOS are presented in Table 5.2. They are based, whenever possible, on industrial quotations.

The total cost of the PHOS spectrometer is 8.6 MCHF. It is foreseen that the required manpower will be provided by the participating institutions, except installation manpower, which will be partially provided by CERN. The manpower from participating institutes amounts to approximately 90 man years.

Table 5.2: Cost estimate of the PHOS spectrometer.

System	amount	unit price	cost (MCHF)
Crystals	18 500	209 CHF	3.87
PIN-preamp. units	18 500	112 CHF	2.07
Mechanics, cooling			0.80
FEE		42 CHF/ch	0.78
Monitoring system			0.09
CPV			0.29
Prototypes			0.18
Tools			0.36
Transportation			0.10
Data transfer			0.06
Total			8.60

Appendix A: CPV with MICROMEGAS gas chambers

A.1 The structure of the detector

The basic element of the CPV consists of a large MICROMEGAS detector, 432×392 mm^2, with an active area of 415×375 mm^2. The detector is an asymmetric two-stage parallel plate detector. The first stage, the 3 mm thick conversion gap, is separated from the second one, the 100 μm thick amplification gap, by a micromesh frame resting on insulating spacers. By applying adequate voltages to the three electrodes one can achieve a very high electric field in the amplification region (100 kV/cm) and a quite low electric field in the drift region. The passage of a charged particle through the conversion gap generates primary electrons which are multiplied in the small amplification gap. The ion cloud is quickly collected on the micromesh, providing the possibility of a fast trigger signal. The electrons are collected on an anode and the two-dimensional localization is provided by a pad layout. The detector elements are shown in Figs. A.1 and A.2.

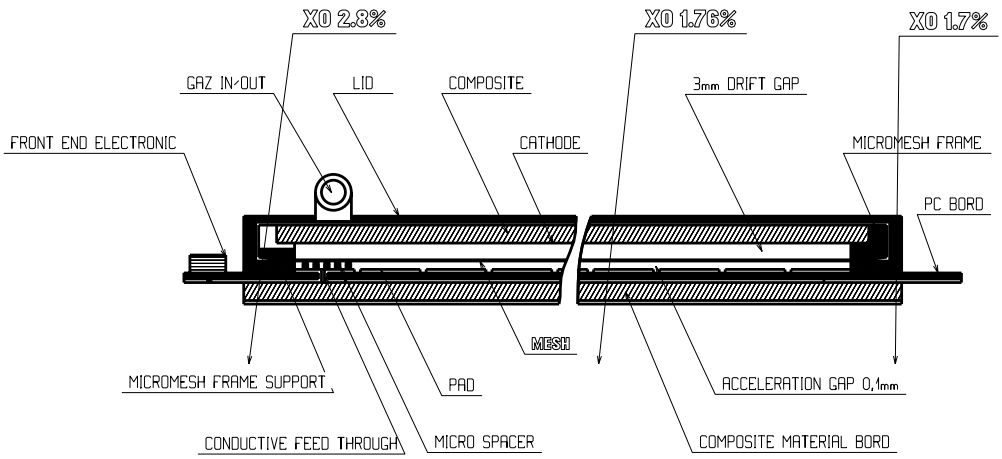

Figure A.1: Principle design of a MICROMEGAS detector for the PHOS CPV: view of an assembled detector seen from the side.

- The anode electrode is made of a 1.0 mm thick electronic board (GI180). On one side with rectangular 22×22 mm^2 copper pads, and on the other side with the signal collecting strips; each pad is pierced by a conductive pine hole which will allow readout through the board; the rigidity of the board is provided by an additional 3 mm thick support made of low X_0 composite material (EPOXY glass and ROHACELL); micro spacers 100 μm high are deposited on the pads with a pitch of 2 mm in the z and y directions.

- The electroformed mesh, made of pure Ni, forms a 3 μm thick grid matrix; the grid consists of 39 μm^2 squared holes outlined by 11 μm of Ni in steps of 50 μm, providing a maximum transparency of 59 %; it is stretched on a Plexiglas frame and rests on the microspacers.

- The cathode electrode is glued on a 3 mm thick plate made of composite material sandwiched between two 300 μm thick GI180 boards covered with a 9 μm layer of copper.

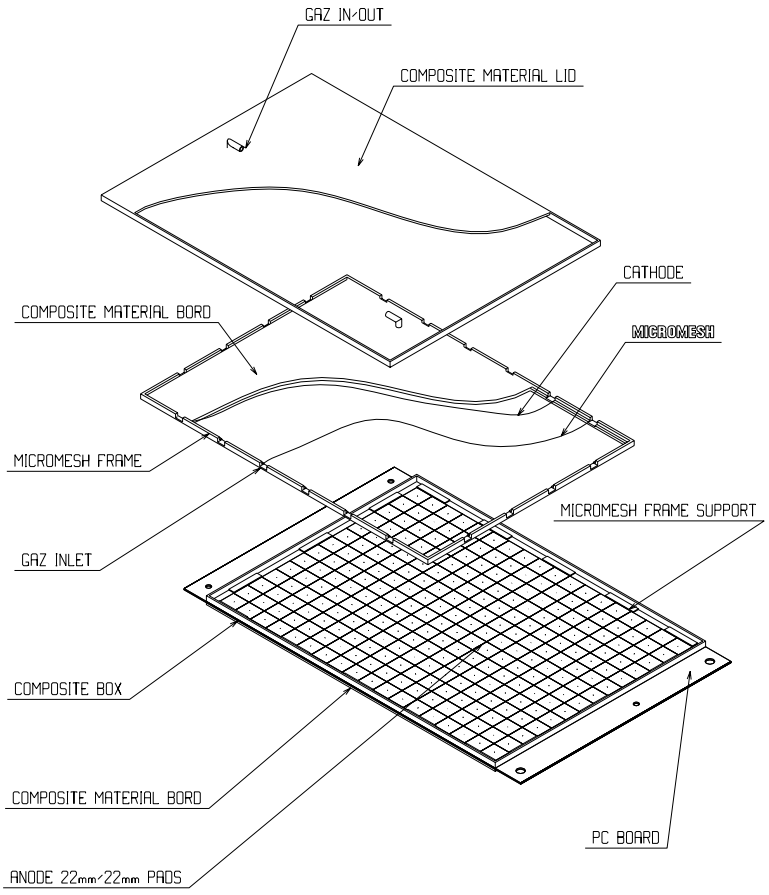

Figure A.2: Principle design of a MICROMEGAS detector for the PHOS CPV: enlarged view showing the various components.

The gas, a mixture of Argon and 5% isobutane, flows through the detector with a pressure slightly above atmospheric pressure. The leak tightness of the detector is ensured by a 2 mm thick composite material box with the lid pierced for the gas inlet. The total thickness of the detector is 13 mm, corresponding to 1.76 % of X_0 throughout the active area and at most 2.8% at the edge of the detector. When overlapping, the maximum X_0 stays below 5 %. The measured efficiency for a detector of this kind is better than 95 %.

The signals of the individual pads are collected at the backplane of the amplification electrode by individual strips and transported to the front-end electronics located on the two opposite sides of the detector. The electronics add 1 % of X_0 to the 1.76 % in the active area.

Such a module with its 256 pads will cover four PHOS modules of 64 crystals with a one-to-one correspondence between the pad and the crystal. The total active area of the CPV will be 9.3 m^2.

CPV layout

Each CPV module will be equipped with 15 elementary units, overlapping by up to 36 mm in order to reduce the dead-zone to zero. They will be fixed on a staggered platform (see Fig. A.3) so that the detectors will be positioned on four different levels at an average distance of 150 mm from the front face of the PHOS crystals. The platform is made of a 5 mm thick composite material introducing an additional 0.3% of X_0. This design is not yet optimized and in its final version the distance to the crystals will be reduced.

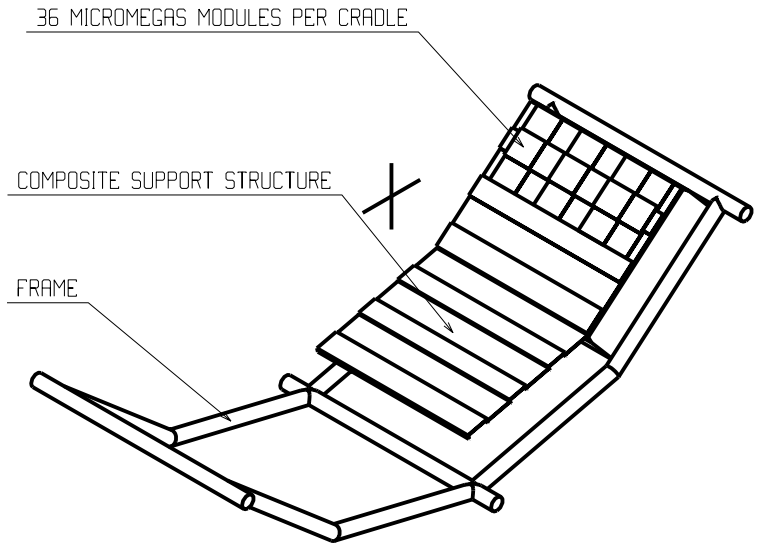

Figure A.3: Schematic view of the layout of the individual MICROMEGAS detectors on top of the modules.

A.2 From electronics to DAQ

Preamble

This novel detector belongs to the family of proportional counters and benefited from the elaborate developments that followed the GASSIPLEX paradigm. It is premature to give a full description of the electronics implementation but some important details should be mentioned.

Preamplifier and protection

It should be remembered that the pad capacitance (with reference to the mesh grid) is 39 pF. The sensitivity to be selected in the GASSIPLEX family will be investigated during the first tests of this MMPC (MicroMegas Pad Chamber). To prevent sparks or possible heavy discharges (unlikely with a large pad area), GASSIPLEX inputs have to be protected by their own resistance network, either implanted on the MMPC board or on an easily changeable hybrid circuit. The choice will have to take into account the eventual excess in X_0.

GASSIPLEX and mapping on boards

There are 252 pads per MMPC module: this number is not a multiple of the number of GASSIPLEX inputs. Nevertheless, it is essential to have each MMPC module independent of the others. For the sake of robustness and reliability, the GASSIPLEX connections should be of the TAB type.

Interconnections, driving GASSIPLEX logic and ADC chaining

The tiling of the various MMPC modules must be known before designing the optimum way of interconnecting the various GASSIPLEX towards the external world (in parallel, in daisy chain, or a mixture of both). However, the tiling will not be known before the final choice of the MMPC geometry. In any event, all the extra boards (ADCs, etc.) should be outside the PHOS acceptance and all the interconnections should be made with flexible cables (Kapton flexibles) and with connectors having a minimum of mass. The flexible paths have to be optimized to be as short as possible.

A.3 Cost

The cost calculation was based on the development costs of a prototype presently under construction, and is shown in Table A.1. (This table corresponds to the TP version of the PHOS detector, twice as wide as the present version). The cost per unit of active surface is ~ 2.18 CHF/cm^2 and per PHOS crystal is ~ 13.5 CHF.

Table A.1: Cost estimate (values in CHF).

	Unit	Module	CPV
Detector	2 716	97 785	391 140
Mechanics		750	3 000
Electronics	698	25 146	100 609
Total	3 414	123 681	494 724

A.4 Discussion on the resolution

From simulations we learn that photons can be discriminated from hadrons through a shower topology analysis algorithm with an efficiency of 90 % (see Chapter 4). In the analysis, the events attributed to photons contain at most 20 % of misidentified charged hadrons. The purpose of the CPV is to measure this contamination level and subsequently eliminate these events. Two factors enter the discussion. First the occupancy, which has been deduced from simulations (central HIJING collision) to be 215 hits per module and per event. The second factor is the bending of charged particles due to the magnetic field between the CPV and the front active face of the PHOS cradle (15 cm for the MICROMEGAS CPV). The effect on charged particle identification has been studied through a simulation in which positive pions with a flat p_{T} distribution between 0.5 and 5 GeV illuminate one PHOS cradle. We then calculate the distance between the z (beam direction) and y (transverse direction) coordinates of the hit in the PHOS cradle and the corresponding coordinates in the CPV. The width of the distribution in the y direction (see Fig. A.4, bottom) reflects the width of one cell of PHOS. The displacement with respect to zero and the width in the x direction (see Fig. A.4, top) results from the bending of charged particles in the magnetic field. Only simulations for positive pions are represented in Fig. A.4. One needs to symmetrize the distribution with respect to zero to take into account negative pions, so that the final distribution will be about 4 cm wide, i.e. the equivalent of two pads. In these figures are also displayed the two possible CPV pad configurations considered to veto charged particles. The random rejection factor of true photon events can then be calculated as

$$R_{\mathrm{random}} = \frac{S_{\Sigma\mathrm{pad}}}{S_{\mathrm{cradle}}} \times \mathrm{occupancy}\ .$$

This number is 7 % (19 %) when considering three (four) pads in the y direction and one (two) pad in the z direction.

In conclusion, within the geometry of the MICROMEGAS CPV, the leftover charged hadrons can be removed from the set of photon candidates with an efficiency better than 95 %, while at most 19 % of true photons are wrongly tagged as charged particles.

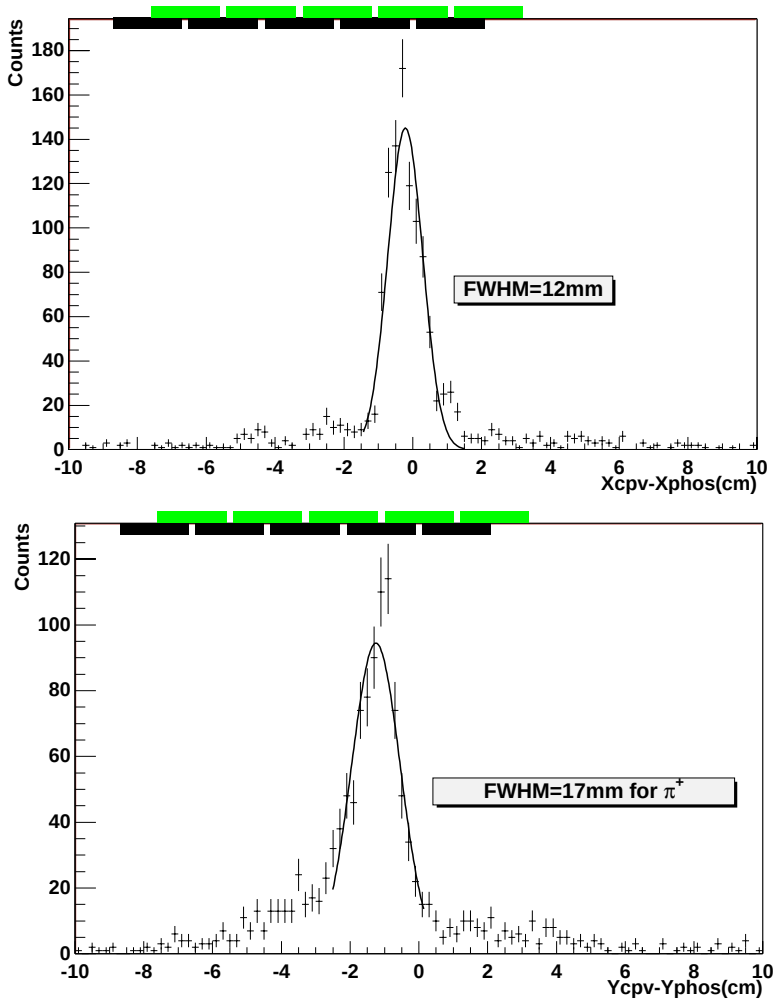

Figure A.4: Distance between CPV hit position and PHOS hit position calculated for positive pions with a flat p_T distribution between 0.5 and 5 GeV in the *x* direction (top) and in the *y* direction (bottom). The rectangular boxes indicate the possible layout of the CPV pad viewed by the event.

References

Chapter 1

[1] ALICE Collaboration, Technical Proposal, CERN/LHCC/95–71 (1995).
[2] See, for example, P.V. Ruuskanen, Nucl. Phys. **A544** (1992) 169c, and references therein.
[3] A. Dumitru and N. Hammon, *Effect of quark-jet energy loss on direct photons in ultrarelativistic heavy-ion collisions*, hep-ph/9807260.
[4] J.I. Kapusta, Nucl. Phys. **A566** (1994) 45c.
[5] WA80 Collaboration, R. Albrecht *et al.*, Phys. Rev. Lett. **76** (1996) 3506.
[6] V.I. Manko for the WA98 Collaboration, talk given at the International Nuclear Physics Conference INPC98 (Paris, August, 1998), to appear in the proceedings.
[7] WA80 Collaboration, R. Albrecht *et al.*, Phys. Lett. **B361** (1995) 14.
[8] WA80 Collaboration, R. Albrecht *et al.*, Eur. Phys. J. **C5** (1998) 255.
[9] WA98 Collaboration, M.M. Aggarwal *et al.*, Phys. Rev. Lett. **81** (1998) 4087.
[10] M. Hentschel *et al.*, Z. Phys. **C75** (1997) 333.
[11] S. Sarkar *et al.*, Phys. Lett. **B402** (1997) 13.
[12] M.M. Aggarwal *et al.*, *Freeze-Out Parameters in Central* $158 \cdot A\ GeV\ ^{208}Pb + ^{208}Pb$ *Collisions*, nucl-ex/9901009.
[13] M. Gyulassy and M. Plümer, Phys. Lett. **B243** (1990) 432;
X.-N. Wang and M. Gyulassy, Phys. Rev. Lett. **68** (1992) 1480.
[14] M. Gyulassy and X.-N. Wang, Nucl. Phys. **B420** (1994) 583;
X.-N. Wang, M. Gyulassy and M. Plümer, Phys. Rev. **D 51** (1995) 3463;
R. Baier, Yu.L. Dokshitzer, S. Peigné and D. Schiff, Phys. Lett. **B 345** (1995) 277;
R. Baier, Yu.L. Dokshitzer, A. Mueller, S. Peigné and D. Schiff, Nucl. Phys. **B484** (1997) 265.
[15] X.-N. Wang, Phys. Rev. Lett. **81** (1998) 2655.
[16] See, for example, T.K. Nayak, Nucl. Phys. **A638** (1998) 249c, and references therein.
[17] M. M. Aggarwal et al., Phys. Lett. **B420** (1998) 169.
[18] J. Kapusta, D. Kharzeev and L. McLerran, Phys. Rev. **D53** (1996) 5028.
[19] Z. Huang and X.-N. Wang, Phys. Rev. **D53** (1996) 5034.
[20] D. Kharzeev, R.D. Pisarski and M.H.G. Tytgat, *Parity odd bubbles in hot QCD*, hep–ph/9808366.
[21] R.M. Weiner *Bose-Einstein Correlations in Particle and Nuclear Physics – A Collection of Reprints*, John Wiley & Sons (1997).
[22] U. Heinz, *HBT interferometry in high energy nuclear and particle physics*, overview talk given at CRIS'98 (Acicastello, Italy, June 8–12, 1998) to appear in *CRIS'98: Measuring the sizes of things in the Universe: HBT interferometry and heavy ion physics*, (S. Costa *et al.* eds.), World Scientific, Singapore, 1998; cf. also hep–th/9806512.
[23] U. Heinz, in *Correlations and Clustering Phenonena in Subatomic Physics*, (M.N. Harakeh *et al.*, eds.), NATO ASI Series **B359** (Plenum, New York, 1997) p. 137.
[24] G. Baym, Acta Phys. Polon. **B29** (1998) 1839.
[25] A. Deloff and T. Siemiarczuk, Internal Note ALICE 98–50.
[26] CMS Collaboration, The Electromagnetic Calorimeter Technical Design Report, CMS TDR 4, CERN/LHCC 97–33 (1997).
[27] Results of recent developments in this field can be found in the Proceeding of the International Workshop on Tungstate Crystals, Roma, October 12–14, 1998 (to be published).
[28] F. Binon *et al.*, Nucl. Instrum. Methods **188** (1981) 507.

[29] S.S. Frank, C.L. Britton Jr., A.L. Wintenberg, G.R. Young, Trigger Circuits for the PHENIX Electromagnetic Calorimeter, 1997 IEEE Nuclear Science Symposium.
[30] ALICE Collaboration, High Momentum PID Technical Design Report, ALICE TDR 1, CERN/LHCC 98–19 (1998).

Chapter 2

[1] ALICE Collaboration, Technical Proposal, CERN/LHCC/95–71 (1995).
[2] S. Burachas *et al.*, Journ. of Crystal Growth **186** (1998) p.175.
[3] L. Luke, Y. Chang, J. Amer. Society **54** (1971) 357.
[4] S.F. Burachas *et al.*, Kristallografia **39** (1994) 544.
[5] S.F. Burachas *et al.*, Atomnaya energiya **79** (1995) 464.
[6] M. Ishii *et al.*, Nucl.Instrum. Methods **A378** (1996) 203.
[7] M. Nikl *et al.*, Phys. Status Solidi (b) **196** (1996) K7.
[8] W. van Loo, Phys. Status Solidi (a) **27** (1979) 565; **28** (1979) 227.
[9] E. Auffray *et al.*, Proc. of SCINT 95, Aug. 28–Sept.1, 1995, Delft, The Netherland, p. 282.
[10] P. Lecoq *et al.*, Nucl. Instrum. Methods **A365** (1995) 291.
[11] M. Nikl *et al.*, Chem. Phys. Lett. **291** (1998) 300.
[12] G. Tamulaitis *et al.*, Phys. Stat. Sol. (a) **161** (1997) 533.
[13] A.N. Belsky *et al.*, Chem. Phys. Lett. **243** (1995) 552.
[14] R.Y. Zhu *et al.*, Nucl. Instrum. Methods **A376** (1966) 319.
[15] M. Nikl *et al.* Phys. Stat. Sol (b) **195** (1996) 311;
V. Murk *et al.*, J. Phys. Cond. Mat **9** (1997) 249;
M. Martini *et al.*, Chem. Phys. Lett. **260** (1996) 418.
[16] M. Nikl *et al.*, Appl. Phys. Lett. **71** (1977) 3755.
[17] G. Born *et al.*, Phys. Stat. Sol. **37** (1970) 255.
[18] G. Born *et al.*, Phys. Stat. Sol. **28** (1968) 583.
[19] S. Baccaro *et al.* Phys. Stat. Sol. (a) **160** (1997) R5;
M. Kobayashi *et al.* Nucl. Instrum. Methods **A399** (1997) 261.
[20] J.A. Groening, H. Binsma, J. Sol. St. Chem. **29** (1979) 227.
[21] S. Baccaro *et al.*, Rad. Phys. and Chem. **52** (1998) 635.
[22] V.V. Lagute *et al.*, J. Phys. Cond. Mat. **10** (1998) 7293.
[23] CMS Collaboration, The Electromagnetic Calorimeter Technical Design Report, CMS TDR 4, CERN/LHCC 97–33 (1997).
[24] R. Rongved, A. Klovning, O. Mæland, and I. Sibiriak, ALICE Internal Note 99–11.
[25] H. Den Hartog and F.A. Muller, Physica **13** (1947).
[26] M.L. Purschke and B.W. Kolb. QDAC–A Quick Data Aquisition System, Version 2.03, Internal Report WA98/93–4 July 1994.
[27] B. Skaali *et al.* Prototype DAQ System for the ALICE Experiment Based on SCI. Talk presented at RT–97, Beaune, France, September 1997.
[28] Cascade manual, CERN ECP/FEX–CA–96–1.
[29] F. Berger *et al.* Preprint IKP–MS–92/102, Institute fur Kernphysic Universitat Munster.
[30] S. Abramovitch *et al.*, Internal Note ALICE 99–12, in preparation.
[31] ALICE Collaboration, High Momentum PID Technical Design Report, ALICE TDR 1, CERN/LHCC 98–19 (1998).
[32] A. Blick *et al.*, ALICE Internal Note 99–08.

Chapter 3

[1] S. Abramovitch *et al.*, Internal Note ALICE 99–12, in preparation.
[2] O. Villalobos *et al.*, Internal Note ALICE 98–23.
[3] S.S. Frank, C.L. Britton Jr., A.L. Wintenberg, G.R. Young, Trigger Circuits for the PHENIX Electromagnetic Calorimeter, 1997 IEEE Nuclear Science Symposium.
[4] Analog Device Application Selection Guides.
[5] ALICE Collaboration, Technical Proposal, CERN/LHCC/95–71 (1995).
[6] S. Donskov *et al.*, Preprint IHEP 85–80, 1985, Protvino, Russia.
[7] P. Le Coultre, L3, a New Tool for Cosmic Ray Muon Reserch, Durban Conference, 1997.
[8] R.M. Bartnett *et al.* Phys. Rev. **D64** (1996) 1.
[9] A.M. Blick *et al.* Internal Note ALICE 99–08.
[10] H. Buchholz, Elektrise und magnetische Potentialfelder, Springer (1957).
[11] I. Enddo *et al.*, Nucl. Instrum. Methods **188** (1981) 51.
[12] ALICE Collaboration, High Momentum PID Technical Design Report, ALICE TDR 1, CERN/LHCC 98–19 (1998).
[13] LeCroy Nuclear Products Catalog.
[14] Joint Controls Project (JCOP), CERN.

Chapter 4

[1] V. G. Antonenko, ALICE Internal Note 99–15.
[2] R. Brun *et al.*, CERN Program Library Long Write-up W5013, GEANT Detector Description and Simulation Tool, 1994.
[3] http://www.cern.ch/alice/Projects/offline/Simulation/galice.
[4] A. Fasso *et al.*, Proc. IV Int. Conf. on Calorimeters and their Applications, World Scientific, Singapore, 1994, p.493.
[5] http://root.cern.ch
[6] F. Berger *et al.*, Nucl. Instrum. Methods **A321** (1992) 152.
[7] G.A. Akopjanov *et al.*, Nucl. Instrum. Methods **140** (1977) 441.
[8] T.C. Awes *et al.*, Nucl. Instrum. Methods **A311** (1992) 130.
[9] K.H. Kampert *et al.*, Preprint IKP–MS–94/0301 University of Münster, A high resolution BGO calorimeter with longitudinal segmentation.
[10] ALICE Collaboration, Technical Proposal, CERN/LHCC/95–71 (1995).
[11] A.M. Blick *et al.*, ALICE Internal Note 99–08.
[12] N. van Eijndhoven *et al.*, ALICE Internal Note 95–32.
[13] WA80 Collaboration, R. Albrecht *et al.*, Phys. Lett. **B361** (1995) 14.
WA80 Collaboration, R. Albrecht *et al.*, Eur. Phys. J. **C5** (1998) 255.
WA98 Collaboration, M.M. Aggarwal *et al.*, Phys. Rev. Lett. **81** (1998) 4087.
[14] WA80 Collaboration, R. Albrecht *et al.*, Phys. Rev. Lett. **76** (1996) 3506.
[15] Phenix Collaboration, *PHENIX Conceptual Design Report*, 1993.
[16] A. Deloff and T. Siemiarczuk, ALICE Internal Note 98–50.

Chapter 5

[1] V. Souzdalev, ALICE Internal Note 99–10.